THEORETICAL MODELS OF CHARGED PARTICLE ACCELERATION MOTIVATED BY SOLAR FLARES

Alexei Borissov

A Thesis Submitted for the Degree of PhD
at the
University of St Andrews

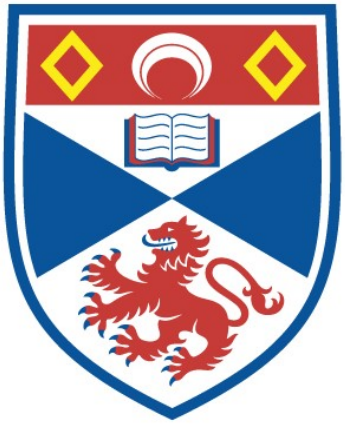

2018

Theoretical models of charged particle acceleration motivated by solar flares

Alexei Borissov

University of
St Andrews

This thesis is submitted in partial fulfilment for the degree of
Doctor of Philosophy
at the University of St Andrews
March 2018

Abstract

In this thesis we examine non-thermal particle behaviour in the presence of modelled electromagnetic fields motivated by various aspects of solar flares.

We first investigate particle dynamics in magnetic reconnection scenarios, in particular 2D reconnection in force-free current sheets and 3D separator reconnection. The electromagnetic fields are obtained by performing resistive magnetohydrodynamic (MHD) simulations with a non-zero anomalous resistivity specified in regions where the local current density exceeds a specified threshold. Test particle orbits and energy spectra are computed in the resulting electromagnetic fields using the relativistic guiding centre equations. Motivated by the enhanced anomalous resistivity, which is several orders of magnitude greater than the Spitzer resistivity, pitch angle scattering linked to the resistivity is introduced into guiding centre formalism when the test particle is located in regions of non-zero resistivity.

In 2D reconnection, pitch angle scattering modifies the particle trajectories, energy gain and orbit duration. In certain cases, pitch angle scattering allows test particles to gain more energy than would be possible in the absence of scattering due to particles traversing the reconnection region multiple times, hence experiencing a parallel electric field component along a greater portion of their orbits. We observe many of the same phenomena in 3D separator reconnection simulations, however changes in particle energy spectra are minimal in comparison to the 2D case.

We also investigate test particle behaviour in an analytical model of a collapsing magnetic trap with the inclusion of a jet braking region at the loop apex, which consists of an indentation in the loops caused by an interaction of a reconnection outflow with low lying magnetic field. New types of particle orbits that are not observed in the absence of the braking jet are characterised. The effects of different trap parameters on particle energisation and orbit behaviour are also examined.

PhD supervisor:

Prof Thomas Neukirch, University of St Andrews

Viva examiners:

Dr Vasilis Archontis, University of St Andrews

Prof Silvia Dalla, University of Central Lancashire.

Candidate's Publications

From the different research projects in my doctoral studies, the following papers have been published, or have been submitted:

1. A. Borissov, T. Neukirch, and J. Threlfall. Particle Acceleration in Collapsing Magnetic Traps with a Braking Plasma Jet. *Solar Physics*, 291:1385-1404, May 2016. DOI:10.1007/s11207-016-0915-0.

2. A. Borissov, E. P. Kontar, J. Threlfall. and T. Neukirch. Particle acceleration with anomalous pitch angle scattering in 2D magnetohydrodynamic reconnection simulations. A&A, 605, A73, Sept 2017. DOI:10.1051/0004-6361/201731183.

Acknowledgements

There are many people I have to thank for their help and support throughout the last 3 and a half years, without whom this PhD would have been very much more difficult.

Firstly, thank you Thomas for guiding me through this PhD, for helping me develop research skills, and for showing a very broad physical picture of solar physics.

To James, thank you for putting up with me with the endless programming issues I had, for editing much of my written work (I hope it's getting more comprehensible), and for helping me find my way in academia.

To Ben, Craig and Tom for the distractions (both scientific and not) from my particle work, making days filled with staring at a computer screen more bearable.

And last but certainly not least, to Yun You. Thank you for encouraging me at every step on this journey, for pushing me to pursue my interests, and for comforting me when things got tough. I am incredibly grateful for your sacrifices and hope I will be able to make them worthwhile soon.

I would also like to thank the School of Mathematics and Statistics of the University of St Andrews for financial support throughout my PhD, and the Royal Astronomical Society for financial support for my attendance at the AGU fall meeting in 2017.

Candidate's Declarations

I, Alexei Borissov, do hereby certify that this thesis, submitted for the degree of PhD, which is approximately 33,000 words in length, has been written by me, and that it is the record of work carried out by me, or principally by myself in collaboration with others as acknowledged, and that it has not been submitted in any previous application for any degree.

I was admitted as a research student at the University of St Andrews in September 2014.

I received funding from an organisation or institution and have acknowledged the funder(s) in the full text of my thesis.

Date: 19/10/18

Signature of candidate:

Supervisor's Declaration

I hereby certify that the candidate has fulfilled the conditions of the Resolution and Regulations appropriate for the degree of Ph.D in the University of St Andrews and that the candidate is qualified to submit this thesis in application for that degree.

Date: 19/10/18

Signature of supervisor:

x

Underpinning Research Data or Digital Outputs Candidate's declaration

I, Alexei Borissov, understand that by declaring that I have original research data or digital outputs, I should make every effort in meeting the University's and research funders' requirements on the deposit and sharing of research data or research digital outputs.

Date: 19/10/18

Signature of candidate:

Permission for publication of underpinning research data or digital outputs

We understand that for any original research data or digital outputs which are deposited, we are giving permission for them to be made available for use in accordance with the requirements of the University and research funders, for the time being in force.

We also understand that the title and the description will be published, and that the underpinning research data or digital outputs will be electronically accessible for use in accordance with the license specified at the point of deposit, unless exempt by award of an embargo as requested below.

The following is an agreed request by candidate and supervisor regarding the publication of underpinning research data or digital outputs:

No embargo on underpinning research data or digital outputs.

Date: 19/10/18

Signature of candidate:

Date: 19/10/18

Signature of supervisor:

Permission for publication

In submitting this thesis to the University of St Andrews we understand that we are giving permission for it to be made available for use in accordance with the regulations of the University Library for the time being in force, subject to any copyright vested in the work not being affected thereby. We also understand, unless exempt by an award of an embargo as requested below, that the title and the abstract will be published, and that a copy of the work may be made and supplied to any bona fide library or research worker, that this thesis will be electronically accessible for personal or research use and that the library has the right to migrate this thesis into new electronic forms as required to ensure continued access to the thesis.

I, Alexei Borissov, have obtained, or am in the process of obtaining, third-party copyright permissions that are required or have requested the appropriate embargo below.

The following is an agreed request by candidate and supervisor regarding the publication of this thesis:
Printed copy
No embargo on printed copy.

Electronic copy
No embargo on electronic copy.

Date: 19/10/18

Signature of candidate:

Date: 19/10/18

Signature of supervisor:

Contents

Chapter 1

Introduction

It is fortunate for humanity that the Earth's atmosphere is opaque to x-ray radiation. For astronomers, this is however a hinderance due to the wide variety of astrophysical processes which emit in the x-ray (and more energetic) parts of the electromagnetic spectrum. Due to humanity being confined to the Earth's atmosphere, it was not until the years after the second world war that the capability to observe space in the x-ray spectrum developed, first with rocket-borne detectors, and eventually with satellites [see e.g. Giacconi, 2009]. The first astronomical x-ray source observed was the Sun, which is not a surprise since it is the closest star to the Earth. Solar x-ray emission comes primarily from two sources: radiation from hot plasma, and due to collisions of highly energetic charged particles with other particles, both of which originate in the solar atmosphere.

The Sun is a ball of hot gas, consisting of approximately 73% hydrogen and 25% helium, along with trace amounts of heavier elements. The Sun produces energy by way of fusing hydrogen into helium in the centre of the Sun, known as the core, which has a radius of 20-25% of the Sun's radius. The energy is carried out of the core by photons through what is known as the radiative zone, which extends to approximately 0.7 solar radii. The remainder of the solar interior is the convective zone where the energy is carried outward by convection. The Sun becomes transparent to visible light in a layer a few hundred kilometres thick called the photosphere. The solar atmosphere extends above the photosphere and consists of the chromosphere and corona, in both of which the density decreases and temperature increases dramatically. Fluid motions in the interior of the Sun generate a magnetic field which extends into the solar atmosphere and permeates the solar corona.

The solar corona consists of hot gas at temperatures of the order of $10^6\,\mathrm{K}$, at which point the atoms in the gas (which are mostly hydrogen) have undergone some degree of ionisation, forming the fourth state of matter known as a plasma. The corona is also a very diffuse environment with typical plasma number densities

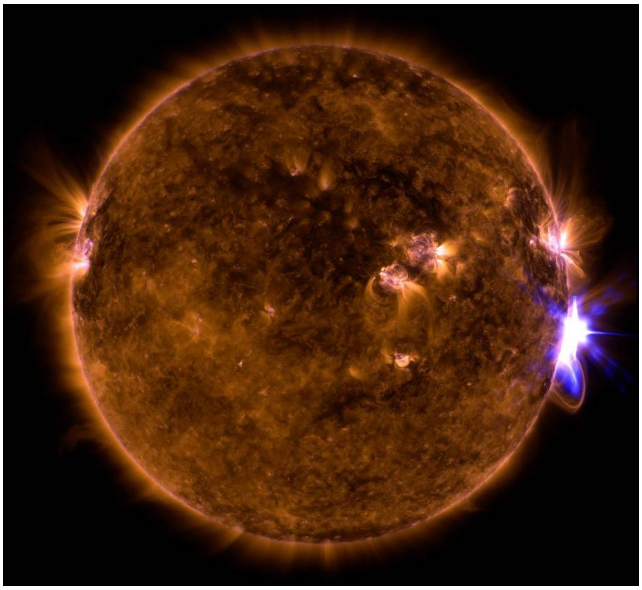

FIGURE 1.1: Flare (bright point on right hand side) observed by SDO on 10 September, 2017 shown in a composite of extreme ultra-violet wavelengths. (Credit: NASA)

of the order $10^{15}\,\mathrm{m}^{-3}$, which is between 1 and 8 orders of magnitude lower than in the chromosphere, the next least dense layer of the Sun. Because of the low densities and pressures, the dynamics of the corona are in many cases dominated by the magnetic fields. In the solar interior the situation is reversed and the fluid dynamics dominates the magnetic field. As a result, convective motions in and below the Sun's photosphere move the footpoints of the coronal magnetic field, causing stresses to build up in the corona which eventually need to be released. It is generally thought that this energy release involves a process called magnetic reconnection, in which the magnetic field lines change their connectivity. The energy stored in the magnetic field is then transferred to plasma heating, non-thermal particles, and bulk plasma flows. Magnetic reconnection is associated with some of the most powerful events in the solar system, such as solar flares [e.g. Cargill et al., 2012, see also Figure 1.1], which are the motivation for the work in this thesis.

Solar flares are transient localised brightenings of the Sun and are observed in all wavelengths from radio to ultraviolet (UV) and both hard and soft x-rays (abbreviated HXR and SXR corresponding to photons with energies $\gtrsim 10\,\mathrm{keV}$ and $\sim 1-10\,\mathrm{keV}$ respectively, see Figure 1.2), whose emission is caused by a variety of physical processes. The causes for brightenings in each of these bands can be quite

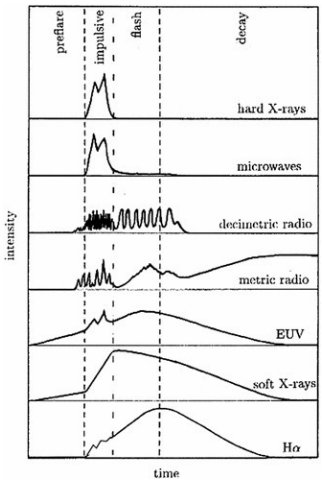

FIGURE 1.2: Time evolution of solar flare emission in a variety of wavelengths. (Credit: Benz [2008])

different. Ultraviolet and SXR emission is associated with thermal emission from hot plasma. Radio emission originates from the gyration of charged particles in the magnetic fields, but also from plasma waves and collisions of thermal charged particles. Finally, HXR emission originates from collisions of non-thermal charged particles. The presence of HXR emission implies that non-thermal charged particles need to reach energies greater than $10\,\mathrm{keV}$ (note that this is much greater than the thermal energy of a particle at typical coronal temperatures of $10^6\,\mathrm{K}$, which is $86\,\mathrm{eV}$). In this thesis we examine the dynamics and energetics of charged particles that could be responsible for producing the HXR emission, specifically by using numerical and analytical models for the coronal electromagnetic fields from which we can calculate particle orbit trajectories and energisation. However, before we continue with the physical aspects of particle acceleration in solar flares, we discuss the different approaches to studying plasma physics and how they relate to the solar corona.

1.1 Methods of plasma physics

1.1.1 What is a plasma

We are all familiar with three states of matter in our everyday lives: solids, liquids and gases. Generally speaking (if we use appropriate pressures and temperatures to avoid sublimation), heating up a solid will eventually result in a liquid, and

heating a liquid will produce a gas. Rigid molecular or atomic bonds are gradually broken for ever increasing temperatures causing a solid to melt into a liquid. Although individual molecules or atoms are more free to move in a liquid, there is still some bonding between them restricting the material from becoming gaseous. Increasing the temperature still further results in these bonds also breaking, with the liquid evaporating to become a gas. One might wonder then what happens to a gas if the temperature is increased. If the temperatures become high enough the atoms will become ionised to produce another state of matter called a plasma. For example, assuming thermodynamic equilibrium, in order to achieve 50% ionisation of hydrogen the temperature needs to only be approximately $10^4\,\mathrm{K}$, which is much lower than in the solar corona.

In contrast to a gas, where pressure forces dominate interactions, plasmas also exhibit interactions mediated by the electromagnetic force. This results in a wide range of phenomena that are unique to plasmas. Examples include a wide variety of waves, plasma instabilities, and collisionless shocks. Although relatively rare on the Earth, plasmas are ubiquitous in the universe, including examples such as the intergalactic medium, interstellar medium, solar wind, Earth's radiation belts, and, importantly for this thesis, the solar corona. Thus, to understand and be able to model the solar corona in general, and aspects of solar flares in particular, it is important to be able to understand plasma physics. A number of approaches to modelling plasmas are used, some of which, specifically those relevant to the solar flares, will be broadly described below.

1.1.2 Kinetic description

The interaction between two charged particles is given by the Coulomb force:

$$F_{12} = \frac{q_1 q_2}{4\pi\varepsilon_0 r_{12}^2}, \tag{1.1}$$

where q_j is the charge of the jth particle, r_{12} is the distance between the particles, and ε_0 is the electric permeability of free space. The motion of particles due to this force is reasonably straightforward to solve if the number of particles is (very) small, however the problem quickly becomes overwhelming when the number of particles required to accurately describe macroscopic plasmas with number densities comparable to the solar corona. In any case, we are not interested in the locations of all the individual particles in the corona, but in the macroscopic quantities, such as density and temperature. As a result it is worthwhile instead to use distribution functions, $f_s(\mathbf{r}, \mathbf{p}, t)$ to describe the macroscopic quantities, for

example the number density,

$$n_s = \int f_s(\mathbf{r}, \mathbf{p}, t) d\mathbf{p},$$

where **r** and **p** are the position and momentum of the particle respectively. Since the distribution function essentially is the number of particles in a phase space volume, and because the particles evolve in a Coulomb potential, from classical mechanics we can obtain an evolution equation for the distribution function. Due to Liouville's theorem the distribution function following phase space flow is conserved,

$$\frac{df_s}{dt} = 0.$$

When expressed in terms of position, **r** and velocity **v** this gives the Vlasov equation, which can be written as

$$\frac{\partial f_s}{\partial t} + \mathbf{v}\frac{\partial f_s}{\partial \mathbf{r}} + q_s \left(\mathbf{E} + \mathbf{v} \times \mathbf{B}\right) \frac{\partial f_s}{\partial \mathbf{p}} = 0. \tag{1.2}$$

For specified **E** and **B** the Vlasov equation gives an expression for the distribution function. However, the electromagnetic fields exist fundamentally as a result of the particles themselves. Expressions for the electromagnetic fields are given by Maxwell's equations,

$$\nabla \times \mathbf{B} = \mu_0 \left(\mathbf{j} + \varepsilon_0 \frac{\partial \mathbf{E}}{\partial t}\right), \tag{1.3}$$

$$\nabla \times \mathbf{E} = -\frac{\partial \mathbf{B}}{\partial t}, \tag{1.4}$$

$$\nabla \cdot \mathbf{B} = 0, \tag{1.5}$$

$$\nabla \cdot \mathbf{E} = \frac{\rho_e}{\varepsilon_0}, \tag{1.6}$$

where μ_0 is the magnetic permeability of free space,

$$\rho_e = \sum_s \int q_s f_s d\mathbf{p}$$

is the charge density, and

$$\mathbf{j} = \sum_s \int q_s / m_s \mathbf{p}_s f_s d\mathbf{p}$$

is the current density. Together with the Vlasov equation, Maxwell's equations create a system which can be solved in principle for the particle distribution function and electromagnetic fields. Unfortunately, this is a seven dimensional (six phase space and one time) non-linear system of partial differential equations, which makes it difficult to solve. When solving these equations numerically in a region on coronal length scales the computational cost can quickly become overwhelming if appropriate spatial and velocity space resolution is used.

One alternative to directly solving the Vlasov equation self-consistently with Maxwell's equations is the particle in cell (PIC) approach [e.g. Hesse et al., 2011]. In PIC simulations the trajectories of super-particles (particles whose mass to charge ratio is the same as physical electrons and ions, but with an actual mass many orders of magnitude higher) are solved subject to the Lorentz force with the fields being self-consistently calculated on a grid. To obtain a reasonable description of a plasma large numbers of these super-particles need to be simulated which, although promising for describing phenomena on small scales (such as magnetic reconnection), becomes too computationally expensive to consider simulations on coronal length scales. A simplification is required, and it is obtained by employing a fluid approach.

1.1.3 Magnetohydrodynamics

One common way to approach the task of modelling solar coronal plasma is to use a fluid description. This approach is called magnetohydrodynamics (MHD), which we will use later on to compute the background electromagnetic fields into which particles will be injected. The MHD equations may be derived through combining the Navier-Stokes equations (which describes the evolution of a non-conducting fluid) with Maxwell's equations and coupling the two sets of equations with the magnetic induction equation (Equation 1.10) and Ohm's law (Equation 1.11). A more direct method is to calculate moments of the distribution function and integrate Equation 1.2 with additional collision terms added to the right hand side. Here we will simply state the MHD equations and discuss the various regimes that are relevant to this thesis, however a more detailed discussion may be found in, for example, Fitzpatrick [2014].

The resistive MHD equations used in this thesis are given by [see e.g. Arber et al., 2001]:

$$\frac{\partial \rho}{\partial t} + \nabla \cdot (\rho \mathbf{u}) = 0, \tag{1.7}$$

$$\rho\left(\frac{\partial \mathbf{u}}{\partial t} + \mathbf{u}\cdot\nabla\mathbf{u}\right) = \mathbf{j}\times\mathbf{B} - \nabla P, \tag{1.8}$$

$$\frac{\partial \epsilon}{\partial t} + \mathbf{u}\cdot\nabla\epsilon = -\frac{1}{\rho}P\nabla\cdot\mathbf{u} + \frac{\eta j^2}{\rho}, \tag{1.9}$$

$$\frac{\partial \mathbf{B}}{\partial t} = \eta\nabla^2\mathbf{B} + \nabla\times(\mathbf{u}\times\mathbf{B}), \tag{1.10}$$

$$\mathbf{E} + \mathbf{u}\times\mathbf{B} = \eta\mathbf{j}, \tag{1.11}$$

where ρ is the plasma density, $\mathbf{u}$ is the plasma velocity, P is the pressure, $\epsilon = P/(\rho(\gamma_g - 1))$ the internal energy, $\gamma_g = \frac{C_p}{C_v}$ is the ratio of specific heats (the subscript differentiates it from the Lorentz factor used in the rest of this thesis), η the resistivity, and $\mathbf{j}$ is the current density. Additional terms, such as forces due to gravity and viscosity can be added to Equation 1.8. In addition to the above equations, we have the constraint $\nabla\cdot\mathbf{B} = 0$, Ampere's law, $\nabla\times\mathbf{B} = \mu_0\mathbf{j}$ and the ideal gas law, $P = \rho k_B T/\mu$, with μ the reduced mass (not to be confused with the magnetic moment). Simplified versions such as ideal MHD (assumes $\eta = 0$) can also be used when the conditions warrant them [see e.g. Török and Kliem, 2005]. In large parts of the solar corona ideal MHD is a good approximation because diffusion timescales are long compared to the plasma dynamics.

In this thesis we will focus on particle acceleration in regions of magnetic reconnection, as such, it is worthwhile to examine the equations which relate directly to this phenomenon. From the MHD perspective, magnetic reconnection corresponds to diffusion of the magnetic field with respect to the plasma. This can be seen in Equation 1.10 which is in the form of the heat or diffusion equation, with an additional term $\nabla\times(\mathbf{u}\times\mathbf{B})$ on the right hand side. By non-dimensionalising Equation 1.10 it emerges that the diffusive term on the right hand side is dominant when $\eta B_0/L_0^2 \gg B_0V_0/L_0$ (where variables with subscript 0 refer to the characteristic values of those quantities). This statement is also commonly expressed in terms of a magnetic Reynolds number, $R_m = \eta/(L_0V_0) \gg 1$. Some consequences of having a high resistivity are contributions to plasma heating (from the last term in Equation 1.9) and the presence of parallel electric fields (since taking the scalar product Equation 1.11 with $\mathbf{b}$ gives $E_\parallel = \eta j_\parallel$). From a physical perspective additional terms can be added to the energy equation (Equation 1.9) to handle effects such as heat conduction or radiation, however we leave these terms out in our simulations for simplicity.

In contrast, ideal MHD requires $\eta = 0$, which implies that the magnetic field is frozen into the plasma. This result is commonly known as Alfvén's theorem. Ideal MHD applies to the majority of the solar corona, and will be particularly relevant to our work on collapsing magnetic traps in Chapter 6. However, for the majority of this thesis we will be examining acceleration by parallel electric fields, which can only exist in non-ideal regions where $\eta \neq 0$.

1.1.4 Test particles

In this thesis we investigate the dynamics of individual particles based on prescribed electromagnetic fields originating from analytical models or MHD simulations. The reason for doing so is that MHD precludes any study of non-thermal particle populations since it is assumed that the plasma is well described as a fluid. Solving for the distribution function using the kinetic approach would in principle provide a population of accelerated particles (if present), so would be the ideal tool for examining particle acceleration. However, as mentioned in Section 1.1.2, self-consistently solving the Vlasov equation while resolving both electron and proton distribution functions in six dimensions quickly becomes too computationally expensive.

By integrating individual particle trajectories we avoid the limitations of both the MHD and distribution function approaches. The force on a charged paricle in electromagnetic fields given by $\mathbf{E}(\mathbf{r}, t)$ and $\mathbf{B}(\mathbf{r}, t)$ is given by the Lorentz force,

$$m\ddot{\mathbf{r}} = q_e \left(\mathbf{E}(\mathbf{r}, t) + \dot{\mathbf{r}} \times \mathbf{B}(\mathbf{r}, t)\right) \tag{1.12}$$

In principle to solve for the particle trajectories from prescribed fields **E** and **B** we simply integrate Equation 1.12 to solve for **r**. This approach is not very suitable for coronal parameters because the particle dynamics will be dominated by gyration and the numerical code will have to temporally resolve this motion. However, by averaging over this gyrational motion, particle orbits can be reasonably quick to integrate, and generally do not require large computing resources. By calculating many particle orbits we can not only estimate particle energy spectra, but also find common trajectories, final positions and orbit lifetimes. A more detailed discussion of the equations we use to compute the particle orbits is given in Chapter 2. There are limitations to this approach, mainly because of a lack of self-consistency. This is due to the fields dictating the particle evolution being derived only from MHD simulations or analytical approximations, which precludes the possibility of investigating the effect that the non-thermal particles have on the electromagnetic

fields. This is not a problem if only very few particles are accelerated, however this could present a significant problem if we want to model the whole of the non-thermal population in a solar flare [see e.g. Cargill et al., 2012]. Nevertheless, the test particle approach can provide a good idea of the physics governing the acceleration of non-thermal particles.

1.2 Solar flare observations

Flares come in many sizes with large flares, which will be the main topic of discussion here, having energy output of the order $10^{32}\,\mathrm{erg}$. However, much smaller flares also exist, all the way down to "nanoflares", which have a much smaller output. These nanoflares are postulated to occur much more frequently than large flares, and as a result, are thought to contribute to the heating of the solar corona to temperatures much higher than the photosphere and chromosphere [see e.g. Parker, 1988, Klimchuk, 2006, Testa et al., 2014].

Solar flares generally proceed in the following manner. In the pre-flare phase, which typically lasts on the order of minutes, there is a gradual heating of the coronal plasma, observed in soft x-rays and extreme ultraviolet (EUV) wavelengths. The pre-flare phase is followed by the impulsive phase, lasting approximately 3 to 10 minutes, where large numbers of charged particles (of the order of 10^{38}) are accelerated and emit in both the hard x-ray and radio parts of the electromagnetic spectrum. Soft x-rays are then emitted by the hot coronal plasma in the decay phase of the flare, which lasts for several hours [see e.g. Benz, 2008]. The HXR emission during the impulsive phase of the flare typically follows a power law spectrum ($f \propto E^{-\delta}$, where E is photon energy and δ the power law index) between approximately 10 and $100\,\mathrm{keV}$ [e.g. Benz, 2008, see also Figure 1.3]. What has become known as the thick target model (TTM) [see e.g. Brown, 1971, Brown et al., 2009] implies that the energy spectra of the energetic particles responsible for the HXR emission should also follow a power law. As mentioned previously, this model assumes that particles are accelerated high in the corona, propagate towards the chromosphere and emit hard x-rays through bremsstrahlung radiation. In addition to footpoint emission, looptop HXR emission is often observed for large flares [see e.g. Masuda et al., 1995, Petrosian et al., 2002].

Solar flares can occur in a variety of field configurations, however, large flares often occur within magnetic fields spanning a polarity inversion line (location of zero line of sight magnetic field) [e.g. Hagyard et al., 1990]. These are locations of strong sheared fields resulting in large amounts of energy being stored in the

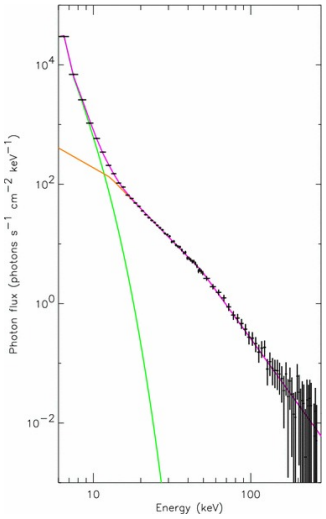

FIGURE 1.3: Example flare energy spectrum showing photon flux up to energies of 100 keV. Green curve is fitted Maxwellian at 16.7 keV, while orange curve is fitted power law component. (Credit: Benz [2008]).

magnetic field. This energy release involves magnetic reconnection, for example by way of flux emergence [see e.g. Choudhary et al., 1998, Archontis, 2008] .

The position of the footpoint HXR emission is also often seen to move along the footpoints of the flare arcade in anti-parallel directions on each side of the arcade as the flare progresses [see e.g. Krucker et al., 2003, Threlfall et al., 2017]. In some cases movement of the footpoint emission is observed perpendicular to the arcade also [e.g. Krucker et al., 2005].

It was noted by Neupert [1968] that the soft x-ray flux was proportional to the amount of radio emission since the start of the flare. Since both radio and HXR emission are associated with non-thermal particles, it is not a surprise that the SXR flux is also related to the cumulative amount of HXR emission. This is now known as the Neupert effect, suggesting that the plasma heating is related to the amount of particle acceleration. One possible scenario for this is precipitating energetic particles heat the chromospheric plasma, causing it to expand and producing what is known as chromospheric evaporation. This is essentially hot plasma flowing up the flare loops where it emits soft x-rays. Other scenarios include heat conduction from the corona causing heating of chromospheric plasma resulting in evaporation [see e.g. Johnston et al., 2017a,b], as well as heating caused by waves propagating along the flare loops and dissipating in the chromosphere, also causing heating [see e.g. Reep and Russell, 2016].

As mentioned previously, the HXR energy spectrum of solar flares tends to follow a power law at energies above approximately $10\,\mathrm{keV}$. This power law spectral index changes throughout the duration of the flare. The typical pattern is a soft-hard-soft progression [e.g. Parks and Winckler, 1969, Kane and Anderson, 1970], meaning an initial spectrum with a higher power law index, δ, resulting in fewer high energy particles and more low energy ones. As the flare progresses δ decreases, producing more particles at higher energies (compared to the initial soft spectrum). Towards the end of the impulsive phase of the flare the spectrum once again becomes softer. Although most flares follow this general pattern, some flares are observed to have a soft-hard-harder progression [see e.g. Kiplinger, 1995].

Radio emission from solar flares is associated with non-thermal particles. Specifically, the particle gyration causes synchrotron emission, which in the non-relativistic case has the same frequency as the gyration frequency of the particle. Spatially resolved radio observations show that the distribution of non-thermal particles is non-uniform throughout the flare loops, with particles being trapped at the looptop [e.g. Melnikov et al., 2002]. Solar flares are also associated with a variety of radio bursts. These are short duration radio emission events, ranging in duration from seconds to hours, and are sometimes clustered into so called storms. Radio bursts may be produced by electrons accelerated by shocks associated with coronal mass ejections, by non-thermal electrons travelling on open field lines away from the Sun, and by trapped electrons on flare loops [Gopalswamy, 2016].

1.3 Models for solar flares

So far we have not had a particular model in mind for how solar flares occur. Here we take a look at several scenarios which can lead to solar flares.

In the so called "standard model" for solar flares [see e.g. Shibata and Magara, 2011] a filament (this is a magnetic flux rope filled with relatively cool plasma suspended in the corona) erupts, causing reconnection to occur underneath it. Particles may then be accelerated at the reconnection site, at a shock occuring where the reconnection outflow encounters lower flare loops (known as the termination shock), or by turbulence throughout the flaring region. The accelerated particles then propagate down the flare loops, produce HXR emission at the footpoints and chromospheric evaporation then fills the loops producing the soft x-ray emission from the post-flare loops (see Figure 1.4). This model also suggests that looptop HXR emission can be produced either by the shock [e.g. Tsuneta and Naito, 1998], or by particles trapped at the looptop interacting with other energetic particles (this

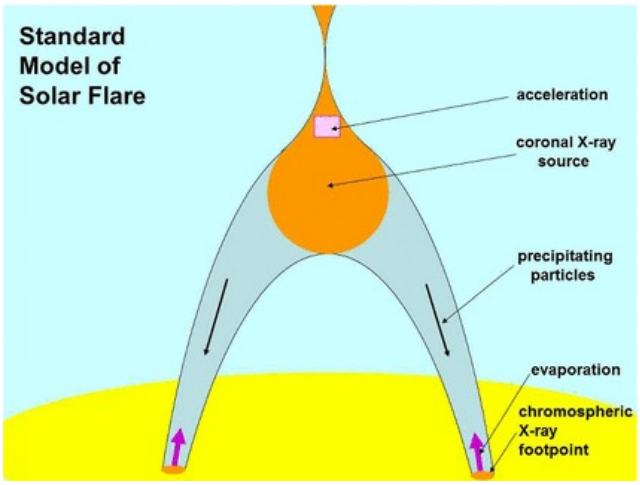

FIGURE 1.4: Cartoon of standard model of solar flares showing loop geometry, particle acceleration site (located below reconnection site, but particle acceleration can occur throughout a larger volume, including in the reconnection region), locations of coronal and chromospheric HXR emission, particle propagation, and chromospheric evaporation. Erupting filament not shown but located above reconnection site. [Credit: Benz, 2008].

motivates the collapsing magnetic trap model which will be discussed further in Chapter 6).

Flux emergence is another scenario where solar flares may occur. In this scenario a flux rope from the solar interior rises due to buoyancy (the increased magnetic field inside the flux rope combined with the requirements for pressure equilibrium and supposing that the plasma is isothermal requires the plasma inside the flux rope to be less dense than the surroundings). When it emerges into the solar corona it can reconnect with the overlying magnetic field, which will again cause particle acceleration, possibly leading to HXR emission and resulting in a flare. One difference to the standard model is that flux emergence can occur on both large and small scales. This explains the presence of smaller flares, as opposed to only the large ones described by the standard model [see e.g. Hansteen et al., 2017].

The convective motion on and below the solar surface can also twist magnetic flux ropes. When the amount of twist exceeds a certain threshold, a magnetic flux rope can become kink unstable, triggering reconnection and again resulting in particle acceleration and heating, [e.g. Gordovskyy et al., 2013, 2014]. Numerical experiments have shown that multiple loops can be triggered to reconnect if one neighbouring loop undergoes the kink instability [Tam et al., 2015, Hood et al.,

2016]. This process is reminiscent of the idea that solar flares can proceed on the basis of self-organised criticality (SOC) [for a review on this topic see Charbonneau et al., 2001], where energy is injected into the corona from footpoint motions until the amount of stress reaches a critical threshold at which point reconnection occurs to relieve the stresses, possibly causing nearby stressed fields to also reconfigure until the corona is in a lower energy state, at which point the process can begin again.

1.4 Mechanisms of particle acceleration

There are multiple models for the acceleration of charged particles to energies high enough to produce HXR emission, including acceleration caused by turbulence, shocks, and by parallel electric fields. Although in this thesis we will focus on the last method, here we give a brief description of the first two.

1.4.1 Turbulence

In the corona typical values of the Reynolds number, $Re = \frac{LV}{\nu}$, and the magnetic Reynolds number, $Re_m = \frac{LV}{\eta}$ (where L and V are the characteristic length and velocity scales for the corona, ν is the viscosity, and η the magnetic diffusivity or resistivity) are both much greater than unity, implying a turbulent environment. The turbulence will consist of a spectrum of wave modes with which particles can interact. Two interactions result in a change of energy: head-on collisions lead to particles gaining energy from the waves, while the particles can lose energy to the waves if the waves are overtaken. In general it is more likely that a head-on collision occurs rather than the particle overtaking a wave which results in the acceleration of the particle population. This model has been extensively developed [see e.g. Miller et al., 1997, Petrosian et al., 2006, Petrosian, 2012, and references therein] and can reproduce power-law energy spectra under certain assumptions, specifically, assumptions about the generation and location of turbulence and its spectrum.

1.4.2 Shocks

Particle acceleration can also occur at shocks, such as at the termination shock in solar flares. In general there are two types of shock acceleration: drift acceleration and diffusive acceleration. Drift acceleration involves particles being accelerated along the shock front due to the electric field component parallel to the shock front

[e.g. Ball and Melrose, 2001]. This type of acceleration has been observed in the magnetosphere, but is inefficient in the context of solar flares where only diffusive shock acceleration is relevant [e.g. Miller et al., 1997].

The mechanism of diffusive shock acceleration relies on considering the particle's momentum on different sides of the shock from the reference frame of the flow on the other side of the shock. For example, when the particle is upstream of the shock, in the reference frame of the downstream flow the particle's momentum is greater than its proper momentum by a factor proportional to the difference of flow speeds between the upstream and downstream flow. The same is true if the particle is downstream of the shock. Thus when the particle crosses the shock from upstream to downstream, and then back again it gains energy proportional to the difference in flow velocities on either side of the shock. With the requirement that there is sufficient scattering by magnetic fluctuations the particle can cross the shock multiple times to gain even more energy [e.g. Drury, 1983]. It turns out that the change in momentum per shock crossing is proportional to the particle's momentum. As a result, it is possible to show that a particle population will approach a power-law energy spectrum if the particles cross the shock sufficiently often and there is a sufficiently energetic seed particle population. The latter is known as the injection problem wherein the seed particles need to have a velocity much greater than the difference between the upstream and downstream flow velocities [e.g. Malkov and Völk, 1998].

1.4.3 Parallel (DC) electric fields

A magnetic field acting on a charged particle induces an instantaneous force perpendicular to the particle's velocity causing gyration of the particle in the plane perpendicular to the local magnetic field. As a result, for a given field strength, electric fields oriented parallel to the magnetic field are most effective at accelerating charged particles to the energies required for HXR emission. This is achieved if there are non-ideal terms, denoted by $\mathbf{R}$, on the right hand side of Ohm's law:

$$\mathbf{E} + \mathbf{u} \times \mathbf{B} = \mathbf{R}, \tag{1.13}$$

where $\mathbf{u}$ is the fluid flow velocity. By taking the dot product of Equation 1.13 with the unit vector in the direction of the magnetic field, $\mathbf{b} = \mathbf{B}/B$, a component of the electric field parallel to the magnetic field exists, provided $\mathbf{b} \cdot \mathbf{R} \neq 0$. One common form of non-ideal term is $\mathbf{R} = \eta \mathbf{j} = \frac{\eta}{\mu_0} \nabla \times \mathbf{B}$, which we will use throughout this thesis.

From a particle perspective the accelerating electric field can be calculated from Equation 1.13 for a given magnetic field structure and assuming that $\mathbf{R} = \eta\mathbf{j}$. The particle equations of motion (which also will be introduced in Chapter 2) can then be integrated to obtain the particle trajectories and energy evolution.

1.5 Magnetic reconnection

As mentioned in Section 1.1.3, ideal MHD is a good approximation for the plasma conditions found in many parts of the corona. However, in this formalism the magnetic field is frozen into the plasma, meaning that in some cases it is impossible for the magnetic field to reconfigure itself into a lower energy state (for example in ideal MHD, photospheric footpoint motions may twist the field arbitrarily as the field will not be able to change connectivity to restore itself to a straighter configuration). If the constraint of ideal MHD is relaxed locally, then magnetic reconnection can occur to relieve these stresses, reconfigure the magnetic field connectivity (or topology) and in so doing, allow for the conversion of the stored magnetic energy into other forms.

The topic of magnetic reconnection has been investigated for many decades, starting with two-dimensional (2D) Sweet-Parker [Parker, 1957, Sweet, 1958] and Petschek [Petschek, 1964] models [for more detailed discussions of 2D magnetic reconnection see textbooks by Biskamp, 2000, Priest and Forbes, 2002]. The Sweet-Parker model of reconnection (see Figure 1.5) consists of antiparallel magnetic fields being forced together by external plasma flows until a sufficiently strong current builds up between them (since $\mu_0\mathbf{j} = \nabla \times \mathbf{B}$, and $\nabla^2\mathbf{B} = \nabla(\nabla \cdot \mathbf{B}) - \nabla \times (\nabla \times \mathbf{B}) = -\mu_0 \nabla \times \mathbf{j}$, which when plugged into Equation 1.10 can give non-zero terms) such that magnetic diffusion becomes important locally. Due to pressure balance within the current sheet we get,

$$B^2/\mu_0 \sim \rho u_{out}^2,$$

where u_{out} is the outflow plasma speed. By rearranging this we get that

$$u_{out} = B/\sqrt{\mu_0\rho} = v_A,$$

which is the Alfven speed in the reconnection region. If we take the length of the current sheet to be Δ and the width δ then due to fluid continuity we must have $\Delta u_{in} = \delta u_{out}$, where u_in is the plasma inflow speed. We then define the reconnection rate as $M = u_{in}/u_{out} = \delta/\Delta$. However, in the ideal region Equation

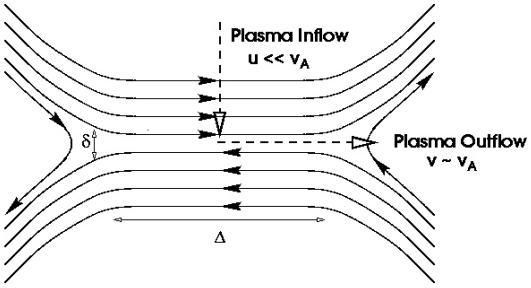

FIGURE 1.5: Sweet-Parker reconnection model, showing magnetic field lines, plasma inflow and outflow and dimensions of current sheet, which is located in the viscinity of the anti-parallel magnetic field lines. (Credit: http://mrx.pppl.gov/Physics/physics.html, retrieved on 30/01/2018).

1.13 has a zero right hand side, so in our simple geometry we get that $u_{in} = E/B$, where E is perpendicular to **u** and **B** (out of the page in Figure 1.5). This leads to

$$M = \frac{u_{in}}{u_{out}} = \frac{E}{Bv_A} = \frac{\eta B}{\mu_0 \delta B v_A} = \frac{\eta}{\mu_0 \delta v_A}.$$

By multiplying this result with $M = \delta/\Delta$ then taking a square root we get

$$M = \sqrt{\frac{\eta}{\mu_0 v_A \Delta}}$$

For the solar corona M typically has values in the range $10^{-4} - 10^{-5}$ [see e.g. Biskamp, 2000, Fitzpatrick, 2014]. Such values imply reconnection timescales of hours to days, much slower than those typically seen in solar flares.

Motivated by the slow timescale of the Sweet-Parker model, another model was developed by Petschek [Petschek, 1964], which uses a shorter diffusion region to obtain a higher reconnection rate with slow shocks set up at the outflow.

Other methods of increasing the reconnection rate have also been proposed, such as introducing a value of resistivity which is many orders of magnitude higher than the physical resistivity. This will be further discussed in Section 1.6. Investigations into magnetic reconnection in 2D are numerous, see for example Biskamp [2000], Loureiro et al. [2007], Markidis et al. [2012], Loureiro and Uzdensky [2016], Tenerani et al. [2016] and references therein, which present a more detailed narritive of 2D reconnection studies.

Not surprisingly in 3D magnetic reconnection can occur in many more different configurations than in 2D. Whereas in 2D there is only one way of changing the

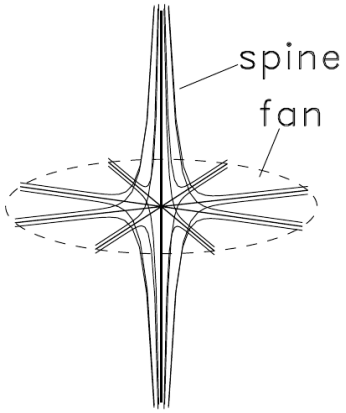

FIGURE 1.6: Structure of a 3D magnetic null point showing the spines and fan plane. (Credit: Brown and Priest [2001], used with permission).

connectivity of magnetic field lines (at an X-type null point), magnetic field line connectivity can change in 3D in multiple topologies including, but not limited to, null points, separators, and quasi-separatrix layers [for reviews of 3D magnetic reconnection see e.g. Priest and Forbes, 2000, Pontin, 2012]. Although reconnection is studied in these configurations to great detail, in general reconnection can occur in the absence of any specific topological configuration. In fact, the distinguishing feature of all 3D reconnection scenarios is that the integral $\int E_{\parallel} dl$ along field lines in the reconnection region must be non-zero, rather than requiring locations where the magnetic field vanishes [Schindler et al., 1988, Hesse and Schindler, 1988, Hesse, 1995].

Magnetic null points are locations where the magnetic field strength is zero [see e.g. Craig et al., 1995, Parnell et al., 1996, Priest and Titov, 1996, Pontin et al., 2004, 2005b, 2011]. Null points have field lines both entering and exiting them, of which one group forms a plane intersecting the null, called the fan plane, and the others, two spine field lines, are oriented out of the plane [e.g. Priest and Forbes, 2000, see also Figure 1.6]. Spine field lines point into the null and the fan plane field lines out of the null, in which case it is a positive null point, or vice versa, in which case it is a negative null. Furthermore, the field lines in the fan plane can be either radial, or curved, and the fan plane can be both perpendicular to the spine as well as inclined. Reconnection at 3D magnetic null points can occur either around the spine, or the fan, which are described in more detail in, for example, Parnell et al. [1996], Priest and Titov [1996], Priest and Forbes [2002], Pontin et al. [2011], Wyper et al. [2012].

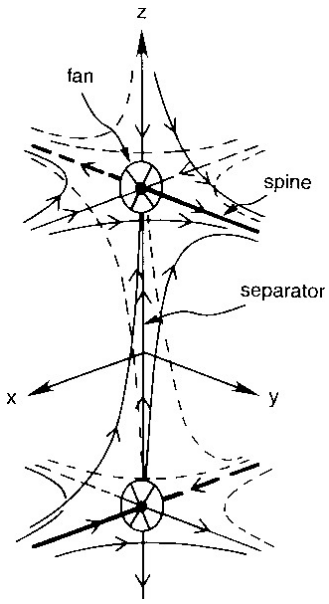

FIGURE 1.7: 3D separator structure, showing two null points, the associated spines and fan planes. The magnetic field line which is the intersection of the two fan planes is the separator. (Credit: Eric Priest, `http://www-solar.mcs.st-and.ac.uk/~eric/3dre.html`, retrieved 30/01/2018, used with permission).

A positive and negative pair of magnetic null points are linked by a special magnetic field line known as a magnetic separator (see Figure 1.7), along which reconnection can occur [see e.g. Priest and Forbes, 2002, Metcalf et al., 2003, Longcope et al., 2005, Parnell et al., 2010a,b]. In this case a current sheet builds up around the separator, which allows reconnection of field lines to occur due to a non-zero resistivity. Prior to reconnection field lines running parallel to one spine of one of the nulls twist through 180° while going up along the separator before exiting along a spine belonging to the other null. During reconnection they change connectivity to exit along the other spine [Stevenson and Parnell, 2015a].

Quasi-separatrix layers are locations where there is a strong gradient in the field line mapping, where magnetic reconnection can also occurs [see e.g. Priest and Démoulin, 1995, Aulanier et al., 2005, Aulanier et al., 2006]. This reconnection, similar to the separator case, is caused by a build up of current, which, when a non-zero resistivity is applied, also causes reconnection [Pontin et al., 2005a].

From a particle perspective the requirement that $\int E_{\|} dl \neq 0$ along field lines is precisely what is required for efficient acceleration, prompting investigation of particle dynamics for example in separator reconnection [Threlfall et al., 2015,

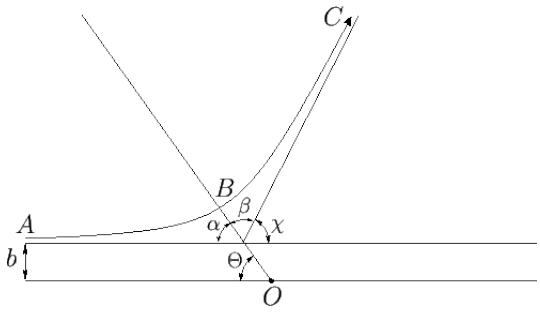

FIGURE 1.8: Trajectory of charged particle (starting at A) undergoing a Coulomb collision (at B) with a charged particle located at O. The impact parameter, b, and particle scattering angle, χ, are shown. (Credit: Fitzpatrick [2014], used with permission).

2016b]. On the other hand, particles can also be accelerated in the absence of parallel electric fields in certain situations, for example, at at 3D null points [see e.g. Dalla and Browning, 2005, 2006, 2008, Browning et al., 2010] and in collapsing magnetic traps.

1.6 The causes of resistivity

We have so far considered magnetic reconnection as a macroscopic process involving diffusion at a rate given by the resistivity. This macroscopic picture omits certain vital aspects of reconnection that can only be found by a microscopic treatment of individual particles. To do so we must recall that particles do not propagate in a vacuum, and that collisions between particles can occur. One type of interaction is Coulomb collisions, caused by the Coulomb interaction between pairs of charged particles (see Figure 1.8).

If we suppose that the probability that a particle is scattered into the solid-angle range $[\Omega, \Omega + d\Omega]$ is $p(\Omega)d\Omega$ (where $d\Omega = 2\pi \sin\chi d\chi$, with χ the scattering angle in Figure 1.8), then the scattering cross-section, $\frac{d\sigma}{d\Omega}$ for a particle with speed v incident onto particles with number density n is defined as

$$\frac{d\sigma}{d\Omega} n v d\Omega = p(\Omega) d\Omega.$$

The scattering cross-section is thus a measure of how likely a particle is to scatter into a particular solid angle. It can be shown [see e.g. Fitzpatrick, 2014] that for

Coulomb collisions the scattering cross-section is given by

$$\frac{d\sigma}{d\Omega} = \frac{1}{4}\left(\frac{q_1 q_2}{4\pi\varepsilon_0 \mu_{12} v^2}\right)^2 \frac{1}{\sin^4\left(\frac{\chi}{2}\right)},$$

where q_i are the particle charges, and $\mu_{12} = m_1 m_2/(m_1 + m_2)$ is the reduced mass. The important point here is that the cross-section decreases for higher relative velocities (and for larger scattering angles), so Coulomb collisions become less effective at higher energies. As a result Coulomb collisions are often neglected when performing simulations of particle acceleration in reconnection scenarios [e.g. Giuliani et al., 2005, Gordovskyy et al., 2010a,b, Threlfall et al., 2015, 2016b].

For every scattering process (including Coulomb collisions) there is an associated resistivity. We demonstrate this by considering the action of an electric field acting on a particle which experiences a drag force proportional to $\langle\nu\rangle\, v$, where v is the particle velocity and $\langle\nu\rangle$ is the average scattering rate experienced by the particle. In this case we have,

$$m\frac{dv}{dt} = qE - m\langle\nu\rangle\, v.$$

By multiplying this equation by qn (where n is the number density of the particles) and assuming a steady state we balance the accleration due to the electric field with the scattering, yielding

$$nq^2 E = m\langle\nu\rangle\, vqn = m\langle\nu\rangle\, j.$$

Hence from Ohm's law we obtain

$$\eta = \frac{m\langle\nu\rangle}{nq^2}.$$

Thus we get that there is a resistivity associated with every scattering process. For Coulomb collisions, the resistivity is called the Spitzer resistivity and is given by [e.g. Kuritsyn et al., 2006],

$$\eta_{sp} = \frac{\pi Z q^2 m^{1/2} \log\Lambda}{\left(4\pi\varepsilon_0\right)^2 \left(k_B T\right)^{3/2}}. \tag{1.14}$$

where Z is the ionisation state of the plasma, $\log\Lambda$ is the Coulomb logarithm [which for coronal conditions is in the range 10 to 20 Fitzpatrick, 2014], k_B is the Boltzmann constant and T is the plasma temperature. In the corona typical values of the

Spitzer resistivity are of the order $10^{-6}\,\Omega \cdot \mathrm{m}$ (note: this can be obtained by plugging in $Z = 1$, which assumes the corona is hydrogen, and $T = 10^6\,\mathrm{K}$ into Equation 1.14). Spitzer resistivity was assumed when discussing the low reconnection rates in Section 1.5.

One way to increase the reconnection rate would be to introduce a higher resistivity associated with another scattering process. This is an approach which is often used in MHD simulations of reconnection where a so-called anomalous resistivity is specified, sometimes with the criterion that the local current density exceeds a specified threshold [for example as in Stevenson and Parnell, 2015a] (note that this usage of the term anomalous resistivity is non-standardised, in many cases anomalous resistivity refers to a resistivity that has a more complex functional form depending on the current than as just a step function; as a result, in this thesis we refer to resistivity caused by Coulomb collisions as Spitzer resistivity, and to all other forms simply as resistivity, or MHD resistivity). This is motivated by particle scattering caused by turbulence as a result of plasma instabilities occuring due to high currents. Instabilities which likely contribute to resistivity are the ion-acoustic instability and the lower-hybrid drift instability [see e.g. Treumann, 2001]. Similarly to sound waves in a gas, ion-acoustic waves are compressive waves where the ions oscillate providing the wave inertia and the electrons move to ensure charge neutrality, providing the wave pressure [Fitzpatrick, 2014]. If the electron temperature is much greater than the ion temperature then the electrons do not neutralise the ion oscillations well enough. Under these conditions the instability can set in resulting in turbulence, particle scattering, and ultimately an resistivity [Treumann, 2001]. One key advantage of ion-acoustic turbulence is that it can occur in unmagnetised plasma [Petkaki and Freeman, 2008], which can be important if the reconnection region has very low magnetic field strength. On the other hand, the lower hybrid drift instability does require the presence of a magnetic field, which could make it applicable in the case of reconnection with a guide field where the magnetic field strength does not drop all the way to zero [Treumann, 2001]. Lower hybrid drift waves are oscillations of both electrons and ions in the direction perpendicular to the local magnetic field, which can grow unstable due to diamagnetic drifts (currents perpendicular to the magnetic field caused by pressure gradients, see e.g. Daughton et al. [2004], Fitzpatrick [2014]). There are multiple other instabilities which may play a role in producing resistivity, which are further discussed in Treumann [2001], Treumann and Baumjohann [1997] for instance.

Despite the complexities associated with producing different levels of resistivity

by way of different instabilities, since the work in this thesis is a proof of concept, for simplicity we follow a typical strategy from MHD simulations. Specifically we consider resistivity in the form of a step function with respect to current density, that is a constant value of resistivity wherever the current density exceeds a particular value, j_{crit} (to be specified depending on the MHD simulation), and zero otherwise. More complex dependency of the resitivity on current density is of course possible, and would be an interesting direction to extend the work in this thesis.

1.7 Particle acceleration and scattering

In motivating the dependence of the resistivity on particle scattering in Section 1.6 the average collisional scattering rate, $\langle\nu\rangle$, is defined by considering the whole particle population. The population of particles responsible for producing HXR emission in flares is a portion of the whole particle population in the corona, so an individual particle may not experience the average scattering rate. However, scattering is still possible, so ideally a scattering rate based on the instabilities mentioned above would be used where they are appropriate. For simplicity we take the following approach: since the Spitzer resistivity is caused by Coulomb collisions, which have a defined collision rate, and in general resistivities are proportional to the associated scattering rates, as a first approximation the scattering rate could be taken to be the Coulomb collision rate enhanced by a factor of the ratio of the MHD resistivity to the Spitzer resistivity. That is,

$$\nu_a = \frac{\eta_a}{\eta_{sp}}\nu_{ei},$$

where η_a is the MHD resistivity, η_{sp} is the Spitzer resistivity, and ν_{ei} is the Coulomb collision rate, which is given by Huba et al. [1998],

$$\nu_{ei} = 2.91 \times 10^{-6} \left(\frac{n_e}{\mathrm{cm}^{-3}}\right) \log\Lambda \left(\frac{T_e}{\mathrm{eV}}\right)^{-3/2} \mathrm{s}^{-1}.$$

Here n_e is the electron number density and T_e is the electron temperature.

Of course, it is not enough to simply know the scattering rate, one must know what happens to the particles during scattering events. For Coulomb collisions there is an energy loss [see e.g. Emslie, 1978]. In work done by Burge et al. [2014] the effects of not only a drag force, but also scattering of the pitch angle are considered on particle trajectories and energies in 2D reconnection simulations. The pitch

angle, given by,

$$\theta = \tan^{-1} \frac{v_{rot}}{v_{\parallel}}, \tag{1.15}$$

where v_{rot} is the rotational velocity of a particle, and $v_{\parallel}$ is its parallel velocity, is a measure of how much of the particle's velocity is oriented along the magnetic field. Particles with pitch angles close to $\theta = 90^{\circ}$ are primarily gyrating about the field lines, while particles with pitch angle close to 0° are primarily travelling along the magnetic field. Pitch angle scattering corresponds to redistribution of test particle velocity between directions parallel to the magnetic field and perpendicular to it. In this thesis we begin to account for the effects of scattering caused by resistivity on non-thermal particles. In this first step we only include pitch angle scattering at a constant rate (with respect to the cosine of the pitch angle) and neglect any drag terms that may arise due to the scattering.

1.8 Previous studies of particle acceleration in magnetic reconnection

Charged particle acceleration in the context of magnetic reconnection has been extensively studied in electromagnetic fields derived both analytically [e.g. Litvinenko, 1996] and numerically [e.g. Gordovskyy et al., 2010a,b, Burge et al., 2014, Threlfall et al., 2016b]. Of particular interest to the work in this thesis will be particle acceleration taking place in 2D magnetic reconnection [such as in Gordovskyy et al., 2010a], the effects of collisions [Burge et al., 2014], and particle acceleration in 3D separator reconnection [Threlfall et al., 2016b].

In studies of particle acceleration in fields derived from MHD simulations of 2D magnetic reconnection [e.g. Gordovskyy et al., 2010a,b] particles are advected with the fluid flow into the reconnection region where they are accelerated by the parallel electric field. Particles may exit the reconnection region by either being ejected along the separatrices (these are the "x"-shaped field lines leading to the corners of the box, for example in Figure 1.5), or being trapped in the reconnection outflow region, which gradually advects them out of the box. Particles may be accelerated to energies in excess of $1\,\mathrm{MeV}$, although this will depend on the strength of the parallel electric field and the size of the reconnection region.

As previously discussed, the addition of Coulomb collisions should not impact particle dynamics significantly for the most energetic particles in these 2D reconnection scenarios. However, the addition of pitch angle scattering at the Coulomb collision frequency was found to cause some particle orbits to traverse

the reconnection region multiple times, thus gaining more energy than is possible in the absence of scattering [Burge et al., 2014]. It was found that this effect occurred relatively infrequently as a result of the Coulomb collision rate being relatively low. We would expect to see this effect being more pronounced for the higher scattering rates we will be investigating.

The 3D separator reconnection scenario may be seen as an extension of 2D reconnection into 3D. In particular cuts perpendicular to the separator have magnetic field lines which resemble the 2D case. When investigating particle acceleration in the context of a 3D separator, Threlfall et al. [2016b] found that particles can indeed be accelerated to non-thermal energies with relatively small values of the parallel electric field. This was due to the potentially large size of these separators. Similarly to the 2D case, particle energy gains can be scaled with the length scale of the simulation. We extend the study done by Threlfall et al. [2016b], by investigating the effects of particle scattering on particle orbit trajectories and energy gain.

1.9 Collapsing magnetic traps

Although most of this thesis deals with particle acceleration and scattering in models of magnetic reconnection, in Chapter 6 we discuss aspects of particle acceleration applicable to events well described by the standard model for solar flares. Observations of large solar flares in hard x-rays show the presence of HXR emission high in the solar corona for certain flares [Masuda et al., 1995]. This is surprising since coronal densities are generally much lower than the chromosphere where footpoint HXR emission occurs, so some method of increasing particle densities or otherwise generating the observed emission is required. One such proposal is the collapsing magnetic trap (CMT) [e.g. Somov and Kosugi, 1997].

Collapsing magnetic traps may be investigated within the standard model of solar flares paradigm (see Figure 1.4). Here, an x-point like (2D) reconnection region high above the corona releases tension in highly stretched magnetic field lines allowing them to collapse into post flare loops. Energetic particles are trapped by the converging magnetic field at the loop footpoints (hence the name collapsing magnetic trap). Acceleration may be achieved in this scenario through Fermi acceleration, which occurs when particles are reflected by regions of strong magnetic field which move towards each other, or through betatron acceleration, which occurs due to a strengthening magnetic field (both of these methods will be discussed in more detail in Chapter 6).

Multiple models of CMTs have been developed. CMTs were first suggested by Somov and Kosugi [1997], where particles are accelerated due to Fermi effect either between opposite footpoints of the loops, or, if there is a termination shock, between the shock and looptop. Additional analytical investigations of the effects of electric fields [Kovalev and Somov, 2002] and the betatron effect [acceleration due to strengthening magnetic field Somov and Bogachev, 2003] were performed. Numerical simulations of particle acceleration in various models of CMTs were performed by, for example, Karlický and Kosugi [2004], Giuliani et al. [2005], Grady and Neukirch [2009], Grady et al. [2012], Eradat Oskoui et al. [2014], Eradat Oskoui and Neukirch [2014], investigating aspects such as Coulomb collisions, guiding centre drifts, and relativistic effects affecting particle acceleration. Here we extend the CMT model developed by Giuliani et al. [2005] with the addition of a compression and deformation of the magnetic field lines at the top of the loop, which may be caused by a reconnection outflow interacting with the upper loops. This is similar to work done in the context of particle acceleration in the Earth's magnetotail [see e.g. Khotyaintsev et al., 2011, Artemyev, 2014], in which context the reconnection outflow is called a braking jet. We incorporate the braking jet into the CMT model and investigate particle dynamics and trapping in the resulting electromagnetic fields.

1.10 Objectives and outline of thesis

The study of particle acceleration in the magnetic reconnection in the solar environment runs into many challenges. One of the greatest challenges is to address the relationship between particles and the background plasma environment. While taking background fields from MHD simulations for test particle studies is a common way of determining the fields the particles propagate through, this approach hides a lot of the microphysics going on in reconnection, specifically the instabilities that cause resistivity multiple orders of magnitude higher than what is caused by Coulomb collisions. The main objectives of this thesis are to investigate the effects of simple scattering models on particle acceleration by considering scattering rates multiple orders of magnitude higher than the Coulomb rate. We do this by considering particle acceleration and scattering in 1D, 2D and 3D, examining particle energy spectra, orbit durations and pitch angle distributions.

To do so, in Chapter 2 we will first describe the model we use to track particle trajectories and the implementation of pitch angle scattering. In Chapter 3 we

investigate the effects of pitch angle scattering on particle populations in the presence of a uniform electric field oriented parallel to a uniform magnetic field. We will vary the strength of the electric field and the scattering to emulate the effects a stronger resistivity would have in an MHD simulation of magnetic reconnection. In Chapter 4 we perform 2D MHD simulations of magnetic reconnection and compute test particle orbits both with and without pitch angle scattering. We extend our investigation of the effects of pitch angle scattering to 3D separator reconnection in Chapter 5. Here we obtain different reconnection rates for different applied resistivites in order to investigate the interaction between acceleration and scattering associated with resistivity. In Chapter 6 we introduce a model for CMTs which incorporates a deformation caused by the reconnection outflow into the collapsing loops. The aim is to investigate particle trapping within the indentation region which would correspond to the location where looptop HXR emission is observed. Surprisingly, we find that particle orbits are often confined outside of the indentation caused by the braking jet. We go on to classify the various orbits we see, and investigate the particle orbit trajectories and energy gain.

Chapter 2

Modelling energetic particles

2.1 Introduction

It is well known [see e.g. Boyd and Sanderson, 2003] that charged particles gyrate in the presence of a magnetic field. As mentioned in Chapter 1, this emerges from the expression of the Lorentz force on a single particle (Equation 1.12, reproduced here for convenience):

$$\mathbf{F} = q\left(\mathbf{E} + \mathbf{v} \times \mathbf{B}\right). \tag{2.1}$$

Here the $\mathbf{v} \times \mathbf{B}$ term produces a force perpendicular to both the velocity vector and the magnetic field, which results in a gyrational motion perpendicular to $\mathbf{B}$. By equating the centripetal force to the Lorentz force (and for the time being assuming $\mathbf{E} = 0$), it is possible to obtain the radius of the circle described by the particle in the plane perpendicular to the magnetic field:

$$r_g = \frac{m v_{rot}}{qB}, \tag{2.2}$$

where v_{rot} is the gyrational component of the particle velocity, $B = |\mathbf{B}|$ is the field strength, and m and q are respectively the mass and charge of the particle. It is also straightforward to compute the angular frequency (known as the gyrofrequency) of rotation of the particle:

$$\omega_g = \frac{v_{rot}}{r_g} = \frac{qB}{m}. \tag{2.3}$$

To get an idea for typical sizes of these quantities, we plug in typical values of $B = 0.01\,\mathrm{T}$ [see normalisations in e.g. Gordovskyy et al., 2010a] and $v_{rot} = 6 \times 10^6\,\mathrm{m/s}$ (approximate speed of electron at temperature of $100\,\mathrm{eV} \simeq 1.16 \times 10^6\,\mathrm{K}$), results in $r_g = 3.4 \times 10^{-3}\,\mathrm{m}$ and $\omega_g = 1.75 \times 10^9\,\mathrm{s}^{-1}$ for electrons (and $r_g = 1.4 \times 10^{-1}\,\mathrm{m}$, $\omega_g = 10^6\,\mathrm{s}^{-1}$ for protons). It is possible to track particle evolution by directly integrating the Lorentz force equation, however, this would result in having to temporally

resolve the gyration of the particles, resulting in a timestep of $dt < 10^{-9}\,\mathrm{s}$. For individual particle simulation lifetimes of up to the order of seconds this may be just about doable on modern computers (assuming the timestep does not need to be lowered due to stronger fields, and that the runtime scales as $1/dt$, we might expect a runtime per particle on the order of seconds to minutes), however an alternative, faster approach is necessary when computing the orbits of thousands of particles. One such method is to average the particle position over one gyration, which leads to the so-called guiding centre approach. The guiding centre approach requires that the electromagnetic fields do not change on lengthscales of r_g and timescales of $1/\omega_g$. In Section 2.2 we will derive the guiding centre equations describing the particle motion. We proceed to describe our additions to include pitch angle scattering into these equations in Section 2.3. Finally a description of the codes used throughout this thesis is given in Section 2.4.

2.2 Guiding centre equations

2.2.1 Charged particle motion in electromagnetic fields and examples of particle drifts

Before launching into a detailed discussion of the guiding centre equations, it is useful to consider the dynamics of particles in simple field configurations. For this part of the discussion we roughly follow the treatment of Boyd and Sanderson [2003].

We start with the simplest case: homogenous magnetic field, **B** and zero electric field. In this case the Lorentz force (Equation 2.1) becomes simply $\mathbf{F} = q\mathbf{v} \times \mathbf{B}$. If we align our coordinate system so that $\hat{\mathbf{z}} = \mathbf{b} = \mathbf{B}/B$ then we get $\dot{v}_z = 0$. Furthermore, by taking the scalar product of the Lorentz force with the velocity we get

$$m\dot{\mathbf{v}} \cdot \mathbf{v} = F \cdot \mathbf{v} = q\,(\mathbf{v} \times \mathbf{B}) \cdot \mathbf{v} = 0,$$

from which, by integrating, we get that the kinetic energy is constant,

$$E_k = \frac{1}{2}mv^2 = const.$$

This is to be expected as a constant magnetic field does no work on a charged particle. To solve for the position of the particle we rewrite the components of the Lorentz force as:

$$\dot{v}_x = -\omega_g v_y \qquad \dot{v}_y = \omega_g v_x. \tag{2.4}$$

It is easy to verify that the solution to this set of equations is $v_x = v_\perp \cos(\omega_g t + \phi), v_y = -v_\perp \sin(\omega_g t + \phi)$, where $v_\perp$ is the integration constant and corresponds to the velocity of the particle perpendicular to the magnetic field (note that this will be different from the gyrational velocity for more general fields because it includes components of perpendicular drifts that will be discussed below). The variable ϕ is also an integration constant representing the phase angle determined by the initial position of the particle with respect to the chosen coordinates. Together with $v_z = const$ this implies a helical motion of the particle. The next simplest case is to add a constant electric field perpendicular to the magnetic field, which, without loss of generality, we set to be along the $\hat{\mathbf{y}}$ direction. In this case Equation 2.4 is modified to:

$$\dot{v}_x = -\omega_g v_y \qquad \dot{v}_y = \omega_g v_x + \frac{qE}{m}. \tag{2.5}$$

Again, it is easily verified that $v_x = A\cos(\omega_g t + \phi) - \frac{qE}{m\omega_g}, v_y = -A\sin(\omega_g t + \phi)$ is a solution to these equations. In this case the integration constant, A, is not equal to the perpendicular velocity of the particle, as there is an additional drift in the $-x$ direction. This is known as the $\mathbf{E} \times \mathbf{B}$ drift, given by

$$\mathbf{v}_E = \frac{\mathbf{E} \times \mathbf{B}}{B^2}, \tag{2.6}$$

which in this case is $qE/m\omega_g = E/B$. The drifts associated with non-constant electric fields appear in the full guiding centre equations (see Equation 2.20), the derivation of which will be discussed in Section 2.2.2.

In a similar manner, for any arbitrary but constant force, F applied to the particle perpendicular to the magnetic field there is an associated drift perpendicular to both the magnetic field and the applied force. By substituting qE with F in Equation 2.5 we get the solutions $v_x = A\cos(\omega_g t + \phi) - \frac{F}{m\omega_g}, v_y = -A\sin(\omega_g t + \phi)$. The associated drift is then

$$v_D = \frac{\mathbf{F} \times \mathbf{B}}{qB^2}. \tag{2.7}$$

Note that in contrast to the $\mathbf{E} \times \mathbf{B}$ drift, the direction of the drift in Equation 2.7 depends on the charge of the particle, in particular as a consequence electrons and protons will drift in opposite directions. One example of such a force is the centripetal force acting on a particle as it follows curved field lines. The associated drift is called the curvature drift.

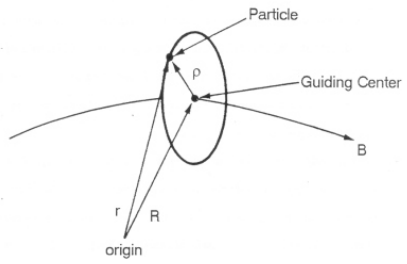

FIGURE 2.1: Particle gyration in magnetic field showing the locations of the particle and guiding centre with respect to some lab frame.

2.2.2 Non-relativistic guiding centre equations

It would be possible to enumerate all the possible drifts that a charged particle experiences and to add them together to gain an idea of the guiding centre motion, however a more direct way is described by Northrop [1963], which we present here. In this case the position of the particle is written as $\mathbf{r} = \mathbf{R} + \boldsymbol{\rho}$ (see Figure 2.1) where $\boldsymbol{\rho} = (m/qB)\mathbf{b} \times \left(\mathbf{v} - (\mathbf{E} \times \mathbf{B})/B^2\right)$ and a local coordinate system is set up with $\hat{\mathbf{e}}_1 = \mathbf{b}$, $\hat{\mathbf{e}}_2$ perpendicular to $\hat{\mathbf{e}}_1$ and $\hat{\mathbf{e}}_3 = \hat{\mathbf{e}}_1 \times \hat{\mathbf{e}}_2$. We will need to consider Taylor series expansions of the Lorentz force about $\mathbf{R}$ with $\epsilon = \frac{m}{q}$ being the smallness parameter. Note that $\boldsymbol{\rho}$ is of order ϵ, so it makes sense to expand about $\mathbf{R}$. This expression is substituted into Equation 2.1 and Taylor expanded to first order in ϵ.

$$\begin{aligned}\ddot{\mathbf{R}} + \ddot{\boldsymbol{\rho}} &= \frac{q}{m}\left[\mathbf{E}(\mathbf{r}) + \dot{\mathbf{r}} \times \mathbf{B}(\mathbf{r})\right] \\ &\simeq \frac{q}{m}\left[\mathbf{E}(\mathbf{R}) + (\boldsymbol{\rho}\cdot\nabla)\,\mathbf{E}(\mathbf{R}) + \left(\dot{\mathbf{R}} + \dot{\boldsymbol{\rho}}\right) \times \left(\mathbf{B}(\mathbf{R}) + (\boldsymbol{\rho}\cdot\nabla)\,\mathbf{B}(\mathbf{R})\right)\right] \qquad (2.8)\end{aligned}$$

Without loss of generality we can write $\boldsymbol{\rho} = r_g\left(\hat{\mathbf{e}}_2\cos\theta + \hat{\mathbf{e}}_3\sin\theta\right)$. By writing $\theta = \omega_g t$ and taking derivatives we obtain

$$\dot{\boldsymbol{\rho}} = \omega_g r_g\left(-\hat{\mathbf{e}}_2\sin\theta + \hat{\mathbf{e}}_3\cos\theta\right) + \frac{d}{dt}\left(r_g\hat{\mathbf{e}}_2\right)\cos\theta + \frac{d}{dt}\left(r_g\hat{\mathbf{e}}_3\right)\sin\theta, \qquad (2.9)$$

$$\begin{aligned}\ddot{\boldsymbol{\rho}} = {}& \omega_g^2 r_g\left(-\hat{\mathbf{e}}_2\cos\theta - \hat{\mathbf{e}}_3\sin\theta\right) + \frac{d\omega_g}{dt} r_g\left(-\hat{\mathbf{e}}_2\cos\theta - \hat{\mathbf{e}}_3\sin\theta\right) \\ &+ 2\omega_g\left[-\frac{d}{dt}\left(r_g\hat{\mathbf{e}}_2\right)\sin\theta + \frac{d}{dt}\left(r_g\hat{\mathbf{e}}_3\right)\cos\theta\right] + \frac{d^2}{dt^2}\left(r_g\hat{\mathbf{e}}_2\right)\cos\theta + \frac{d^2}{dt^2}\left(r_g\hat{\mathbf{e}}_3\right)\sin\theta.\end{aligned}$$

We could plug these results into equation 2.8, however the idea is to also average the particle motion over one gyroperiod, which could be done by integrating with respect to θ over the interval $[0, 2\pi]$. If we do so, the average values $\langle \boldsymbol{\rho} \rangle = \langle \dot{\boldsymbol{\rho}} \rangle = \langle \ddot{\boldsymbol{\rho}} \rangle = 0$, so we are left with

$$\ddot{\mathbf{R}} = \frac{q}{m}\left[\mathbf{E}(\mathbf{R}) + \dot{\mathbf{R}} \times \mathbf{B} + \frac{r_g^2 \omega_g}{2}\left(\hat{\mathbf{e}}_2 \times (\hat{\mathbf{e}}_3 \cdot \nabla)\,\mathbf{B} - \hat{\mathbf{e}}_3 \times (\hat{\mathbf{e}}_2 \cdot \nabla)\,\mathbf{B}\right)\right] \tag{2.10}$$

where we used $\int_0^{2\pi} \cos^2\theta d\theta = \int_0^{2\pi} \sin^2\theta d\theta = 1/2$. Note that by writing out the vector product and using chain rule we get

$$\begin{aligned}
\hat{\mathbf{e}}_2 \times (\hat{\mathbf{e}}_3 \cdot \nabla)\,\mathbf{B} &= \hat{\mathbf{e}}_1\,(\hat{\mathbf{e}}_3 \cdot ((\hat{\mathbf{e}}_3 \cdot \nabla)\,\mathbf{B})) - \hat{\mathbf{e}}_3\,(\hat{\mathbf{e}}_1 \cdot (\hat{\mathbf{e}}_3 \cdot \nabla)\,\mathbf{B}) \\
&= \hat{\mathbf{e}}_1\,(\hat{\mathbf{e}}_3 \cdot ((\hat{\mathbf{e}}_3 \cdot \nabla)\,\mathbf{B})) - \frac{B}{2}\,(\hat{\mathbf{e}}_3 \cdot \nabla)\,e_1^2 + \hat{\mathbf{e}}_3\,(\hat{\mathbf{e}}_3 \cdot \nabla B) \\
&= \hat{\mathbf{e}}_1\,(\hat{\mathbf{e}}_3 \cdot ((\hat{\mathbf{e}}_3 \cdot \nabla)\,\mathbf{B})) - \hat{\mathbf{e}}_3\,(\hat{\mathbf{e}}_3 \cdot \nabla B)\,.
\end{aligned} \tag{2.11}$$

By interchanging $\hat{\mathbf{e}}_2$ and $\hat{\mathbf{e}}_3$ (as well as a sign change due to the vector products) we get

$$\hat{\mathbf{e}}_3 \times (\hat{\mathbf{e}}_2 \cdot \nabla)\,\mathbf{B} = -\hat{\mathbf{e}}_1\,(\hat{\mathbf{e}}_2 \cdot ((\hat{\mathbf{e}}_2 \cdot \nabla)\,\mathbf{B})) + \hat{\mathbf{e}}_2\,(\hat{\mathbf{e}}_2 \cdot \nabla B)\,. \tag{2.12}$$

Taking the difference between Equations 2.11 and 2.12 and using $\nabla \cdot \mathbf{B} = 0$ we get

$$\hat{\mathbf{e}}_2 \times (\hat{\mathbf{e}}_3 \cdot \nabla)\,\mathbf{B} - \hat{\mathbf{e}}_3 \times (\hat{\mathbf{e}}_2 \cdot \nabla)\,\mathbf{B} = -\hat{\mathbf{e}}_1\left(\frac{\partial B}{\partial s}\right) - \hat{\mathbf{e}}_2\,(\hat{\mathbf{e}}_2 \cdot \nabla B) - \hat{\mathbf{e}}_2\,(\hat{\mathbf{e}}_2 \cdot \nabla B) = -\nabla B, \tag{2.13}$$

where $\frac{\partial B}{\partial s} = \hat{\mathbf{e}}_1 \cdot (\hat{\mathbf{e}}_1 \cdot \nabla \mathbf{B}) = \nabla \cdot \mathbf{B} - \hat{\mathbf{e}}_2 \cdot (\hat{\mathbf{e}}_2 \cdot \nabla \mathbf{B}) - \hat{\mathbf{e}}_3 \cdot (\hat{\mathbf{e}}_3 \cdot \nabla \mathbf{B})$. Plugging this result into Equation 2.10 we get

$$\ddot{\mathbf{R}} = \frac{q}{m}\left[\mathbf{E}(\mathbf{R}) + \dot{\mathbf{R}} \times \mathbf{B}\right] - \frac{\mu}{m}\nabla B(\mathbf{R}), \tag{2.14}$$

where $\mu = \frac{r_g^2 \omega_g q}{2} = \frac{m v_{rot}^2}{2B}$ is the magnetic moment of the particle. This is an important quantity as it is conserved in the guiding centre approximation. It is convenient to present the guiding centre equations in terms of components parallel and perpendicular to the magnetic field. To do this we take the cross product of equation 2.14 with $\mathbf{b}$ and rearrange to get

$$\dot{\mathbf{R}}_\perp = \frac{\mathbf{E} \times \mathbf{B}}{B^2} + \frac{\mu}{q}\frac{\mathbf{B} \times \nabla B}{B^2} - \frac{m}{q}\frac{\ddot{\mathbf{R}} \times \mathbf{B}}{B^2}. \tag{2.15}$$

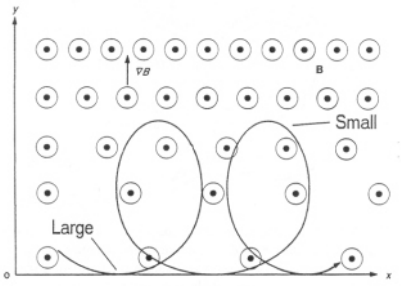

FIGURE 2.2: Path of particle in out-of-page magnetic field with a vertical gradient, demonstrating grad-**B** drift.

The second term on the right hand side is the gradient B drift, so called for occuring in regions of non-homogeneous magnetic field. This occurs because of the dependence of the gyroradius of the particle on the magnetic field strength. If there is a gradient of the magnetic field strength over a gyroradius the particle will travel along a smaller circle in the strong field region compared to the weak field region resulting in a drift perpendicular to the magnetic field and the gradient of the magnetic field strength. This drift is illustrated in Figure 2.2

To obtain an equation for the perpendicular drift in terms of known quantities we need to expression for $\ddot{\mathbf{R}}$. We note that since the term involving $\ddot{\mathbf{R}}$ in Equation 2.15 is proportional to $\epsilon = m/q$ we only need the zeroth order approximation of $\ddot{\mathbf{R}}$. By defining $v_\parallel = \dot{\mathbf{R}} \cdot \mathbf{b}$ as the parallel velocity of the guiding centre

$$\begin{aligned}
\ddot{\mathbf{R}} &\simeq \frac{d}{dt}\left(v_\parallel \mathbf{b} + \mathbf{v}_E\right) \\
&= \mathbf{b}\frac{dv_\parallel}{dt} + v_\parallel\left(\frac{\partial \mathbf{b}}{\partial t} + \left(v_\parallel \mathbf{b} + \mathbf{v}_E\right)\nabla \mathbf{b}\right) + \left(\frac{\partial \mathbf{v}_E}{\partial t} + \left(v_\parallel \mathbf{b} + \mathbf{v}_E\right)\nabla \mathbf{v}_E\right) \\
&= \mathbf{b}\frac{dv_\parallel}{dt} + v_\parallel \frac{\partial \mathbf{b}}{\partial t} + v_\parallel^2 \frac{\partial \mathbf{b}}{\partial s} + v_\parallel \mathbf{v}_E \cdot \nabla \mathbf{b} + \frac{\partial \mathbf{v}_E}{\partial t} + v_\parallel \frac{\partial \mathbf{v}_E}{\partial s} + \mathbf{v}_E \cdot \nabla \mathbf{v}_E. \qquad (2.16)
\end{aligned}$$

Plugging this into Equation 2.15 we get

$$\dot{\mathbf{R}}_\perp = \frac{\mathbf{b}}{B} \times \left[-\mathbf{E} + \frac{\mu}{q}\nabla B + \frac{m}{q}\left(v_\parallel \frac{\partial \mathbf{b}}{\partial t} + v_\parallel^2 \frac{\partial \mathbf{b}}{\partial s} + v_\parallel \mathbf{v}_E \cdot \nabla \mathbf{b} + \frac{\partial \mathbf{v}_E}{\partial t} + v_\parallel \frac{\partial \mathbf{v}_E}{\partial s} + \mathbf{v}_E \cdot \nabla \mathbf{v}_E\right)\right]. \qquad (2.17)$$

Similarly, by taking the scalar product of $\ddot{\mathbf{R}} \cdot \mathbf{b}$ we can get the parallel guiding centre equation:

$$\ddot{\mathbf{R}} \cdot \mathbf{b} = \frac{q}{m}\mathbf{E} \cdot \mathbf{b} - \frac{\mu}{m}\frac{\partial B}{\partial s}. \qquad (2.18)$$

By writing

$$\begin{aligned}\ddot{\mathbf{R}} \cdot \mathbf{b} &= \frac{d}{dt}\left(\dot{\mathbf{R}} \cdot \mathbf{b}\right) - \dot{\mathbf{R}} \cdot \frac{d\mathbf{b}}{dt} \\ &= \frac{dv_\parallel}{dt} - \dot{\mathbf{R}} \cdot \frac{d\mathbf{b}}{dt} \\ &\simeq \frac{dv_\parallel}{dt} - \mathbf{v}_E \cdot \frac{d\mathbf{b}}{dt} \\ &= \frac{dv_\parallel}{dt} - \mathbf{v}_E \cdot \left(\frac{\partial \mathbf{b}}{\partial t} + \left(v_\parallel \mathbf{b} + \mathbf{v}_E\right) \cdot \nabla \mathbf{b}\right).\end{aligned}$$

By plugging this into Equation 2.18 we get

$$\frac{dv_\parallel}{dt} = \frac{q}{m} E_\parallel - \frac{\mu}{m} \frac{\partial B}{\partial s} + \mathbf{v}_E \left(\frac{\partial \mathbf{b}}{\partial t} + v_\parallel \frac{\partial \mathbf{b}}{\partial s} + \mathbf{v}_E \cdot \nabla \mathbf{b}\right), \tag{2.19}$$

where $E_\parallel = \mathbf{E} \cdot \mathbf{B}$.

2.2.3 Adding relativistic effects

Equations 2.17 and 2.19 make up the guiding centre equations for a charged, non-relativistic particle. There is the possibility of adding a differential equation for the kinetic energy of the particle (as is done in Northrop [1963]), however this is not strictly necessary because it can always be updated in a numerical code by simply calculating it.

Hard X-ray emission in solar flares is in the energy range of $10 - 100\,\mathrm{keV}$, which means that the particles precipitating in the chromosphere to create this emission must have kinetic energies of at least this size. Since the electron rest mass is $511\,\mathrm{keV}$, the energies obtained in our simulations are mostly non-relativistic, however some particles do achieve relativistic energies. Just to be safe, an extension to the guiding centre equations is presented that takes into account relativistic effects, and is based on Northrop [1963], which in turn is based on the treatment of Vandervoort [1960]. The main idea is that for a relativistic particle the observed mass in the lab frame is $m = \gamma m_0$ where m_0 is the rest mass of the particle. Since $\gamma > 1$ and increases for higher energies, the observed mass increases, and hence so does the gyroradius. This results in modifications for many of the drifts, such as the gradient B drift as a result of the particle traversing a larger gyroradius than in the non-relativistic case. In addition to modifying the equations to accomodate a relativistic correction for the observed particle mass, a factor of $1 - E_\perp^2/B^2$ is included in terms involving the magnetic field to account for potentially relativistic

velocities involved in the $\mathbf{E}\times\mathbf{B}$ drift (it should be noted that since these drifts are not found in the simulations we perform, the factors are not included in the equations solved in the code, but are shown here for completeness). The relativistic guiding centre equations used throughout this thesis are given by:

$$\dot{\mathbf{R}}_\perp = \frac{\mathbf{b}}{B\left(1-E_\perp^2/B^2\right)}\times\left[-\left(1-E_\perp^2/B^2\right)\mathbf{E}+\frac{\mu}{\gamma e}\nabla\left[B\left(1-E_\perp^2/B^2\right)^{1/2}\right]\right.$$
$$\left.+\frac{mU}{e}\frac{d\mathbf{b}}{dt}+\frac{m\gamma}{e}\frac{d\mathbf{u}_E}{dt}+\frac{U}{\gamma}E_\parallel\mathbf{u}_E+\frac{\mu}{\gamma e}\mathbf{u}_E\frac{\partial}{\partial t}\left[B\left(1-E_\perp^2/B^2\right)^{1/2}\right]\right], \quad (2.20)$$

$$m\frac{dU}{dt} = m\gamma\mathbf{u}_E\cdot\frac{d\mathbf{b}}{dt}+eE_\parallel-\frac{\mu}{\gamma}\frac{\partial}{\partial s}\left[B\left(1-E_\perp^2/B^2\right)^{1/2}\right], \quad (2.21)$$

with

$$\gamma = \sqrt{1+\frac{U^2+u_E^2}{c^2}+\frac{2\mu B}{mc^2}}. \quad (2.22)$$

Here we define $U=\gamma v_\parallel$, $\mathbf{u}_E=\gamma\mathbf{v}_E$ and the magnetic moment is now

$$\mu = \frac{(p_\perp^*)^2}{2m_0B\left(1-\frac{E_\perp^2}{B^2}\right)}.$$

Here $p_\perp^*$ is the perpendicular component of the 4-momentum in the reference frame moving at the $\mathbf{E}\times\mathbf{B}$ drift, rather than the lab frame. Since in our case we assume that the $\mathbf{E}\times\mathbf{B}$ drift is small compared to the particle velocity we can simply use $p_\perp=\gamma m v_\perp$ instead. Note also that the definition of γ (Equation 2.22) differs from the typical definition due to the actual velocity of the particle not being explicitly stored by the particle code. This is a valid definition since by defining $u=\gamma v$ and rearranging $\gamma = 1/\sqrt{1-v^2/c^2}$ we get

$$\begin{aligned}\gamma &= \sqrt{1+\frac{u^2}{c^2}}\\ &= \sqrt{1+\frac{\gamma^2\left(v_\parallel^2+v_\perp^2\right)}{c^2}}\\ &\simeq \sqrt{1+\frac{\gamma^2\left(v_\parallel^2+v_E^2\right)}{c^2}+\frac{2\mu B}{mc^2}}\\ &= \sqrt{1+\frac{U^2+u_E^2}{c^2}+\frac{2\mu B}{mc^2}}.\end{aligned} \quad (2.23)$$

Note that to obtain the third line above we assume that to first order the particle

velocity can be decomposed into velocity parallel to the magnetic field, the $\mathbf{E} \times \mathbf{B}$ drift (as the highest order drift), and the rotational motion obtained through the magnetic moment.

2.2.4 Adiabatic invariants

Any discussion of the guiding centre equation would be incomplete without mentioning the three adiabatic invariants associated with charged particle motion in electromagnetic fields. We have already met one of them, namely the magnetic moment, associated with the particle gyration in a magnetic field. A simple proof [from Northrop, 1963] that this is in fact an invariant follows.

We assume that the fields do not vary with time. Using Equation 2.9 we can write the perpendicular velocity of a particle as

$$\mathbf{v}_\perp = \dot{\mathbf{R}}_\perp + \dot{\boldsymbol{\rho}} = \dot{\mathbf{R}}_\perp + \omega_g r_g \left(-\hat{\mathbf{e}}_2 \sin\theta + \hat{\mathbf{e}}_3 \cos\theta\right) + \frac{d}{dt}\left(r_g \hat{\mathbf{e}}_2\right)\cos\theta + \frac{d}{dt}\left(r_g \hat{\mathbf{e}}_3\right)\sin\theta.$$

Taking the mean square over one gyroperiod and noting that to leading order $\dot{\mathbf{R}}_\perp^2 \simeq v_E^2$ we get

$$\begin{aligned}\left\langle v_\perp^2 \right\rangle &= \dot{\mathbf{R}}_\perp^2 + \omega_g^2 r_g^2 \left(\sin^2\theta + \cos^2\theta\right) \\ &= v_E^2 + v_{rot}^2 \\ &= v_E^2 + \frac{2\mu B}{m}\end{aligned}$$

Note that when taking the dot product $\dot{\boldsymbol{\rho}} \cdot \dot{\boldsymbol{\rho}}$ we used $\hat{\mathbf{e}_2} \cdot \hat{\mathbf{e}_3} = 0$, $\frac{d\hat{\mathbf{e}_2}}{dt} = \frac{d\hat{\mathbf{e}_3}}{dt} = 0$, the fact that $\left\langle \dot{\mathbf{R}}_\perp \cdot \dot{\boldsymbol{\rho}} \right\rangle = \dot{\mathbf{R}}_\perp \cdot \langle \dot{\boldsymbol{\rho}} \rangle = 0$, and the fact that averaging over a full period of a sinusoidal function also gives zero. The result is also reassuring as it basically tells us that the average energy over a gyroperiod is (to first order) the sum of contributions from the $\mathbf{E} \times \mathbf{B}$ drift and the gyrational motion of the particle. If we denote the electric potential by ϕ then due to energy conservation we can write

$$\frac{d}{dt}\left[\frac{m\left(\left\langle v_\perp^2 \right\rangle + v_\parallel^2\right)}{2} + q\phi\right] = 0,$$

which can be rearranged to be

$$\frac{d}{dt}\left[\frac{m v_E^2}{2} + \mu B\right] = \frac{d}{dt}\left[\frac{m v_\parallel^2}{2} + q\phi\right]. \tag{2.24}$$

We note that if the fields are constant in time then $\frac{\partial \phi}{\partial t} = 0$, so to first order in ϵ

$$\begin{aligned}\frac{d\phi}{dt} &\simeq v_\parallel \frac{\partial \phi}{\partial s} + \dot{\mathbf{R}}_\perp \cdot \nabla \phi \\ &= -v_\parallel E_\parallel + \mathbf{v}_E \cdot \nabla \phi + \frac{\mathbf{b}}{B} \times \left(\frac{\mu}{q} \nabla B + \frac{m}{q} v_\parallel \frac{d\mathbf{b}}{dt} + \frac{m}{q} \frac{d\mathbf{v}_E}{dt} \right) \cdot \nabla \phi.\end{aligned}$$

Here we have used the guiding centre perpendicular drift equation. Since $\mathbf{E} = -\nabla\phi$, $\mathbf{v}_E \cdot \nabla \phi = 0$ and using the identity $\mathbf{A} \times \mathbf{B} \cdot \mathbf{C} = -\mathbf{A} \times \mathbf{C} \cdot \mathbf{B}$ we get

$$q \frac{d\phi}{dt} = -q v_\parallel E_\parallel - q \mathbf{v}_E \cdot \left(\frac{\mu}{q} \nabla B + \frac{m}{q} v_\parallel \frac{d\mathbf{b}}{dt} + \frac{m}{q} \frac{d\mathbf{v}_E}{dt} \right). \tag{2.25}$$

On the other hand, using the parallel guiding centre equation we get

$$\begin{aligned} m v_\parallel \frac{dv_\parallel}{dt} &= q v_\parallel E_\parallel - \mu v_\parallel \frac{\partial B}{\partial s} + m v_\parallel \mathbf{v}_E \cdot \left(\frac{\partial \mathbf{b}}{\partial t} + v_\parallel \frac{\partial \mathbf{b}}{\partial s} + \mathbf{v}_E \cdot \nabla \mathbf{b} \right) \\ &= q v_\parallel E_\parallel - \mu v_\parallel \frac{\partial B}{\partial s} + m v_\parallel \mathbf{v}_E \cdot \frac{d\mathbf{b}}{dt}. \end{aligned} \tag{2.26}$$

Plugging the results of Equations 2.25 and 2.26 into Equation 2.24 results in

$$m\mathbf{v}_E \cdot \frac{d\mathbf{v}_E}{dt} + \frac{d(\mu B)}{dt} = -q v_\parallel E_\parallel + \mu v_\parallel \frac{\partial B}{\partial s} - m v_\parallel \mathbf{v}_E \cdot \frac{d\mathbf{b}}{dt} + q v_\parallel E_\parallel + q \mathbf{v}_E \cdot \left(\frac{\mu}{q} \nabla B + \frac{m}{q} v_\parallel \frac{d\mathbf{b}}{dt} + \frac{m}{q} \frac{d\mathbf{v}_E}{dt} \right).$$

The coloured terms in the above equation cancel leaving us with,

$$\frac{d(\mu B)}{dt} = \mu v_\parallel \frac{\partial B}{\partial s} + \mu \mathbf{v}_E \cdot \nabla B = \mu \frac{dB}{dt},$$

which implies

$$\frac{d\mu}{dt} = 0.$$

A more general proof not requiring the fields to be constant in time is also presented in Northrop [1963], however is significantly more involved, and for reasons of conciseness is not presented here. The conservation of the magnetic moment can be used to explain important phenomena such as magnetic mirrors and the notion of particle trapping (which will be discussed in Chapter 6). Furthermore, when we are implementing scattering in Section 2.3, we will use it to determine the terms that need to be added to the differential equations governing pitch angle evolution to reflect geometrical effects of the electromagnetic fields on particle trajectories.

The magnetic moment (sometimes it is also called the first adiabatic invariant) is not the only adiabatic invariant of importance in space physics. The other

(somewhat) common one, called the second adiabatic invariant or longitudinal invariant, is associated with particle motion when trapped between two mirror points. This would apply for instance for the particles trapped on a field line in the Earth's magnetosphere, or in a collapsing magnetic trap [e.g. Grady, 2012]. It is given by

$$J = \int p_{\parallel} ds,$$

with the integral taken along a fieldline with the particle returning to the same point where it started. This invariant can also be used to explain Fermi acceleration, where mirror points getting closer together implies a shorter integration path, and hence necessitates a higher parallel velocity.

The third adiabatic invariant can, for example, be applied to particle motion around the Earth in the magnetosphere. It is given by

$$K = \int p_{\phi} ds,$$

where ϕ is the azimuthal coordinate. This invariant results in, for example, the expansion or contraction of the Earth's Van Allen belts due to different solar wind conditions [e.g. Fitzpatrick, 2014].

2.3 Pitch angle scattering

One approach to describing the particle population in a plasma is through the Vlasov equation:

$$\frac{df}{dt} = \frac{\partial f}{\partial t} + \mathbf{v} \cdot \frac{\partial f}{\partial \mathbf{r}} + \frac{q}{m} \left(\mathbf{E} + \mathbf{v} \times \mathbf{B} \right) \frac{\partial f}{\partial \mathbf{v}} = 0. \tag{2.27}$$

This is just a restatement of Liouiville's theorem in the context of particle distributions in a plasma. Liouiville's theorem fundamentally stems from the continuity equation in phase space, which means that changes in the amount of particles in a phase space element come from particles distribution flux into or out of this volume. This does not account for scattering processes (including collisional processes, such as Coulomb collisions) acting on particles. When the effects of scattering processes are non-negligible, Equation 2.27 is modified to be

$$\frac{df}{dt} = \frac{\partial f}{\partial t} + \mathbf{v} \cdot \frac{\partial f}{\partial \mathbf{r}} + \frac{q}{m} \left(\mathbf{E} + \mathbf{v} \times \mathbf{B} \right) \frac{\partial f}{\partial \mathbf{v}} = \left(\frac{\partial f}{\partial t} \right)_{coll}, \tag{2.28}$$

where the term on the right hand side denotes changes to the particle distribution function due to the effect of collisions. Although this gives the most accurate picture of particle populations throughout a plasma, it is difficult to solve numerically due to the fact that the distribution function has six phase space dimensions and one time dimension. With the test particle approach we are essentially trying to sample the distribution function to build up an understanding of the key features of particle phenomena in reconnection regions.

We start with a simple case of Equation 2.28 where we neglect the phase space terms (we are essentially solving $\partial f/\partial t = (\partial f/\partial t)_{coll}$, and we will eventually effectively include the velocity space terms, however physical space will be taken care of by the guiding centre equations). Since collisions correspond to diffusion in velocity space, the right hand side of Equation 2.28 is equal to the laplacian of f (with a constant of proportionality corresponding to the scattering rate). In this thesis we are only concerned with pitch angle diffusion, so we only consider terms relevant to pitch angle scattering. To describe the particle velocity we may use the coordinates (v, θ), which are analogous to spherical coordinates where the pitch angle, θ, is the polar angle (recall definition of the pitch angle θ in Equation 1.15). The terms related to θ give,

$$\frac{\partial f}{\partial t} = \frac{1}{\sin\theta}\frac{\partial}{\partial \theta}\left(\sin\theta \frac{\partial f}{\partial \theta}\right).$$

If instead the velocity coordinates are (v, β), where $\beta = \cos\theta$, then scattering occuring at a constant rate ν results in,

$$\frac{\partial f}{\partial t} = \frac{\partial}{\partial \beta}\left(\nu \frac{1-\beta^2}{2}\frac{\partial f}{\partial \beta}\right). \tag{2.29}$$

Equation 2.29 can be rewritten as

$$\frac{\partial f}{\partial t} = \frac{\partial}{\partial \beta}\left(\nu\beta f + \frac{\partial}{\partial \beta}\left[\nu \frac{1-\beta^2}{2} f\right]\right). \tag{2.30}$$

This is a Fokker-Planck equation, which in this form is still a little unhelpful as we cannot directly obtain a method for implementing any scattering with it (since we do not solve for the distribution function). It turns out that the Fokker-Planck equation can be easily transformed into a stochastic differential equation (SDE). The SDEs that are relevant for our purposes may be written in the form

$$dx = Adt + BdW$$

where we are solving for $x(t)$, with A, B possibly depending on x. The term proportional to dt may be viewed as a deterministic drift at the rate given by A. On the other hand dW is given by $dW = \zeta\sqrt{dt}$, where ζ is a random number with mean 0 and standard deviation 1, and this term specifies the stochastic evolution of the variable x at the rate given by the coefficient B. These SDEs may then be numerically integrated (for example with Euler's method).

The process of obtaining an SDE from a given Fokker-Planck equation is described in more detail in Appendix A as well as in textbooks, such as Gardiner [2004], however for practical purposes for a Fokker-Planck equation given by

$$\frac{\partial f}{\partial t} = \frac{\partial}{\partial x}\left(Af + \frac{\partial}{\partial x}\left[\frac{1}{2}Bf\right]\right),$$

the corresponding SDE is simply $dx = Adt + BdW$.

Thus the SDE corresponding to the Fokker-Planck equation 2.29 is

$$d\beta = -\nu\beta dt + \sqrt{\nu\left(1-\beta^2\right)}dW. \tag{2.31}$$

In Equation 2.29 we ignored the effects of the Lorentz force on the evolution of the distribution function. Since we are not tracking particles using the Lorentz force anyway, our modifications to Equation 2.31 to include the effects of external forces need to be motivated in a slightly different fashion. Since the stochastic part of SDEs comes from the dW term, any additional deterministic drifts need to be added into the dt term (this can also be seen in that any terms which are proportional to the first derivative with respect to $\mathbf{v}$, such as any external forces, will be in the dt term in the SDE also). Thus the SDE we solve is in fact

$$d\beta = \left(\dot{\beta} - \nu\beta\right)dt + \sqrt{\nu\left(1-\beta^2\right)}dW \tag{2.32}$$

These terms can be derived from considering the equation imposing the conservation of the magnetic moment. Since $\mu = \frac{mu^2\beta^2}{2B} = \frac{mU^2}{2B}\frac{1-\beta^2}{\beta^2}$ the conservation of the magnetic moment implies $\frac{d\mu}{dt} = 0$ so we have:

$$\begin{aligned} 0 = \frac{d\mu}{dt} &= \frac{mU}{B}\frac{1-\beta^2}{\beta^2}\frac{dU}{dt} + \frac{mU^2\beta}{B}\left(-\frac{2}{\beta^3}\right)\frac{d\beta}{dt} - \frac{mU^2}{2B^2}\frac{1-\beta^2}{\beta^2}\frac{dB}{dt} \\ &= \frac{2\mu}{U}\frac{dU}{dt} - \frac{2\mu}{\beta\left(1-\beta^2\right)}\frac{d\beta}{dt} - \frac{\mu}{B}\frac{dB}{dt}. \end{aligned}$$

Therefore, the time derivative, $\dot{\beta}$, can be expressed as:

$$\dot{\beta} = \left(\frac{1}{U}\frac{dU}{dt} - \frac{1}{2B}\frac{dB}{dt} \right) \beta \left(1 - \beta^2\right). \tag{2.33}$$

Although it is not strictly necessary, the update to the energy is implemented as

$$d\gamma = \dot{\gamma} dt, \tag{2.34}$$

where $\dot{\gamma}$ can be obtained by simply taking the time derivative of γ (Equation 2.23):

$$\gamma = \frac{\sqrt{1 + \frac{U^2}{c^2} + \frac{2\mu B}{mc^2}}}{\sqrt{1 - \frac{V_E^2}{c^2}}}. \tag{2.35}$$

Differentiating this with respect to time yields,

$$\begin{aligned} \dot{\gamma} = \frac{1}{2}\left(1 + \frac{U^2}{c^2} + \frac{2\mu B}{mc^2}\right)^{-1/2} \left(\frac{2U}{c^2}\frac{dU}{dt} + \frac{2\mu}{mc^2}\frac{dB}{dt}\right) \left(1 - \frac{V_E^2}{c^2}\right)^{-1/2} \\ + \frac{1}{2}\left(1 - \frac{V_E^2}{c^2}\right)^{-3/2} \left(1 + \frac{U^2}{c^2} + \frac{2\mu B}{mc^2}\right)^{1/2} \frac{2V_E}{c^2}\frac{dV_E}{dt}. \end{aligned} \tag{2.36}$$

Since $V_E \ll c$, the second term is negligible in comparison to the first term, so we get:

$$\dot{\gamma} = \frac{1}{2}\left(1 + \frac{U^2}{c^2} + \frac{2\mu B}{mc^2}\right)^{-1/2} \left(\frac{2U}{c^2}\frac{dU}{dt} + \frac{2\mu}{mc^2}\frac{dB}{dt}\right) \left(1 - \frac{V_E^2}{c^2}\right)^{-1/2}. \tag{2.37}$$

In practice a simple update for the value of γ would suffice, however this formulation adds the capability to add drag terms into the evolution of γ.

The integration of the pitch angle scattering SDE into the particle tracking code (as well as a description of the particle tracking code) will be given in subsection 2.4

2.4 Codes

In this thesis we use a particle tracking code which solves the relativistic guiding centre equations (as stated in Equations 2.20-2.22), which was written initially by Paul Wood [Wood and Neukirch, 2005], and has since been used and modified by Paulo Giuliani, Keith Grady, Solmaz Eradat-Oskoui, James Threlfall and most recently myself [see e.g. Giuliani et al., 2005, Grady and Neukirch, 2009, Eradat

Oskoui et al., 2014, Threlfall et al., 2016b, Borissov et al., 2016, 2017]. When necessary, the code will be referred to as the Giuliani code (or particle code). It updates the guiding centre position using an adaptive timestep Runge-Kutta 4th order method [in particular the Cash-Karp method described in Cash and Karp, 1990], with the possibility of specifying the electromagnetic fields either analytically or by reading in from various MHD code outputs. In the case when field input is taken from numerical MHD calculations the field values are linearly interpolated to the particle position from the nearest grid points. Particle orbits are evaluated until they either exit the computational domain or exceed a specified duration. The orbit trajectories and energies are output for further analysis.

My contribution to this particle code has been to implement routines to take care of pitch angle scattering as outlined in Section 2.3, improvements to the routines regarding relativistic energy calculation, as well as to parallelise the code with MPI. The interplay between the pitch angle scattering routines and the deterministic calculation of the particle trajectories is as follows. The pitch angle is updated according to Equation 2.32, and the capability to add a dynamical friction term through Equation 2.34 is implemented although not used. When scattering is switched on the code reverts to a fixed timestep and it updates the pitch angle using an Euler method at the beginning of the timestep, before recalculating the parallel and perpendicular velocities and solving for the guiding centre position using the 4th order Runge-Kutta scheme (although no longer with a variable timestep). To ensure that the chosen timestep is small enough to have a reliable solution, particles are run with different timesteps with the scattering rate, ν, artificially set to zero, ensuring that no scattering occurs. The results are then compared to the adaptive timestep code with scattering turned off, and the largest timestep which accurately reproduces particle orbit trajectories and energy evolution is taken. To ensure that pitch angle scattering is implemented correctly we ran multiple particles in multiple simple field configurations, as well as in snapshots taken from MHD simulations of magnetic reconnection, with scattering on and $\nu = 0$, and with scattering switched off. In all cases a fixed timestep was used. The orbit trajectories, energy gains and pitch angle evolution were then compared to ensure that the deterministic parts added to the SDE (i.e. $\dot{\beta}$) were accurately capturing the effects of the electromagnetic fields on the particles. To test the stochastic terms particles were set up in a uniform magnetic field and it was ensured that a population of particles approached a uniform distribution in the cosine of the pitch angle. The parallelisation was implemented as a simple task farm with the master process allocating individual particles orbits to run on separate processes. This way it

was possible to run hundreds of thousands of particles to obtain energy spectra in reasonable amounts of time.

The Giuliani particle tracking code is reasonably complex and is able to solve the full guiding centre equations with a variety of background fields, however in some of the investigations we are interested in performing, a simpler approach could also be appropriate. In this case we consider a 1D domain with an electric field aligned along it. The magnetic field is assumed to be strong enough so that the guiding centre approximation still holds. Equations 2.32 and 2.34 are solved with only the effects of parallel electric field causing changes in kinetic energy and the particle position updated simply as $x_{n+1} = x_n + v_{\|}dt$. The electric field is connected to the scattering rate through a parameter representing the resistivity, however the fields used (being a 1D simulation) are not self consistent and this is only meant as an exercise in examining the relationship between acceleration and pitch angle scattering. This code was then written in a way so as to be effectively accelerated with GPUs and written in CUDA, so we may refer to it as the CUDA code.

Finally a word needs to be said about the MHD code used to produce the reconnection simulations. We used the *Lare* code, in both 2D and 3D, developed by Tony Arber [Arber et al., 2001]. This code solves the resistive MHD equations on a staggered grid (that is where certain variables are located at the grid points, while others are centred on the grid faces or grid cells). *Lare* stands for *La*grangian *re*map which means that the quantities are advanced on a Lagrangian (i.e. moving with the fluid flow) grid and subsequently remapped back to the Eulerian grid at the end of each timestep. Further extensions to the MHD equations it solves are possible, particularly in the energy equation where it can add conduction, radiation and extra heating effects, however in our work we only examine the resistive MHD equations mentioned in Chapter 1.

Chapter 3

Particle acceleration and scattering in 1D

3.1 Introduction

We start our examination of the relationship between pitch angle scattering and acceleration due to parallel electric fields with a simple 1D model. We assume a homogeneous magnetic field in the $\hat{\mathbf{x}}$ direction with a sufficiently high field strength to ensure that the guiding centre approximation holds and that the particle gyrofrequency is higher than any scattering frequency the particle will encounter. Parallel to the magnetic field we apply an electric field which is proportional to a parameter representing the resistivity. Although the fields are artificial and unrealistic, this model will give us some indications about the interaction between particle acceleration and scattering associated with resistivity.

This 1D model is a greatly simplified model of the fields experienced by particles in regions of magnetic reconnection, however it is impossible to capture the effects of the field geometry in this model, which, as we will see later, play an important role in shaping particle energy spectra. Furthermore, since no energy is lost in the pitch angle scattering events, the energy of a given particle depends only on its initial energy and the potential drop it has traversed. If we restrict the spatial extent of the accelerating electric field and make sure that all particles simulated exit this 1D box (we refer to the 1D computational domain as a box as we would in 2D and 3D, however here this simply means the 1D spatial simulation domain), only the particle pitch angle at the end of the orbit, as well as the orbit duration will reflect the effects of particle acceleration and scattering. We also ignore the effects of perpendicular drifts (such as the $\mathbf{E} \times \mathbf{B}$ drift, although in any case our electric field is purely parallel to the magnetic field, so this component is zero). We proceed to give a detailed description of the field configuration used in Section 3.2, the

results of the simulations are presented, first with all test particles having the same initial conditions (Section 3.3), then with initial conditions having a Maxwellian distribution in energy and uniformly distributed in cosine of pitch angle (Section 3.4). A discussion of the results follows in Section 3.5.

3.2 1D field setup and code

Since we are solving a 1D problem, the equation of motion for a particle is,

$$\dot{x} = v_{\parallel} = \frac{u}{\gamma}. \tag{3.1}$$

Combining Equation 2.32 and the relevant terms from Equation 2.33 we get the evolution equation for the cosine of the pitch angle, β,

$$d\beta = \left(\frac{1}{U} \frac{dU}{dt} \beta \left(1 - \beta^2\right) - \beta\nu \right) dt + \sqrt{\nu \left(1 - \beta^2\right)} dW. \tag{3.2}$$

To obtain the energy we integrate Equation 2.34 with the relevant terms from Equation 2.37 resulting in

$$d\gamma = \dot{\gamma} dt = \frac{U}{c^2} \frac{dU}{dt} \left(1 + \frac{U^2}{c^2} + \frac{U_{\perp}^2}{c^2} \right)^{-1/2}, \tag{3.3}$$

where

$$\frac{dU}{dt} = \frac{qE}{m_e}. \tag{3.4}$$

We specify a current density J and a resistivity η (varied in the range of $10^{-3} - 10^{-8}$, in normalised units), which together specify an electric field

$$E = E_{\parallel} = \eta J,$$

such that when $\eta = 10^{-3}$ (in non-dimensional units) the electric field is $E = 10^3 \, \mathrm{V} \cdot \mathrm{m}^{-1}$. This parallel electric field strength was chosen for better comparison with the results of the 3D simulations that we go on to perform later in this thesis. Due to the nature of the 1D simulations, the imposed field is not self-consistent, in particular, there is no magnetic field gradient that would imply this current density. The range of values that the resistivity takes on is larger in this 1D case than in our 3D simulations, so smaller values of electric field can be obtained for smaller values of resistivity in comparison to the 3D MHD results. We use the following normalising scales for the magnetic field strength, length and time

respectively: $B_0 = 0.01\,\mathrm{T}, L_0 = 1\,\mathrm{m}, T_0 = 10^{-9}\,\mathrm{s}$. This gives the resistivity scaling $\eta_0 = \mu_0 L_0^2/T_0 \simeq 1.26 \times 10^3 \Omega\,\mathrm{m}$ (where μ_0 is the magnetic permeability). These values were chosen so that the scattering frequency was also comparable to the 3D simulations, but again it takes on much smaller values also. It should be noted that the 1D CUDA code does not specify a magnetic field strength (as stated before), simply assuming that it is sufficiently high for the guiding centre approximation to hold, which in this case requires that the gyration frequency is higher than the scattering frequency. We define the scattering frequency as,

$$\nu = \frac{v}{\lambda_0 \kappa}, \tag{3.5}$$

where $\kappa = \frac{\eta_{sp}}{\eta}$ (recall that η_{sp} is the Spitzer resistivity, and we set λ_0 to be a typical collisional mean free path in solar coronal plasma). In this case η is a parameter we input into our model, which also determines the electric field strength, but the Spitzer resistivity is calculated at a temperature of 10^7 K (this temperature is chosen to resemble the temperatures observed in our MHD simulations in Chapters 4 and 5).

A finite extent of the reconnection region is simulated by cutting off the integration after the particle reaches a particular distance, d, from $x = 0$ (in this case we set $d = 10^2\,\mathrm{m}$), at which point the time taken for the particle to reach this distance is recorded. A maximum orbit duration is also specified and particle orbits are computed until they exceed this specified time limit, although we try to pick a time limit such that all particles exit the computational box first (the time limit is needed for this particular implementation of the code to run on GPUs).

3.3 Particle orbit duration and cosine of pitch angle distributions

To investigate the effects of scattering on a large population of particles we integrate 5024 particle orbits multiple times subject to the conditions stated in Table 3.1. We start by comparing orbit duration and pitch angle distributions for different values of η for fixed initial energy values (20 keV in Figure 3.1, chosen so that particle orbit computation takes a reasonable amount of time for the domain size used) and cosine of pitch angle $\beta = 0.1$ (note that we are integrating electrons, so since the electric field is in the positive x direction, particles are going to be accelerated towards $-x$, however their initial velocity is in the $+x$ direction since $\beta > 0$). The results are shown in Figures 3.1 and 3.3. Here for runs 1 to 6 the resistivity

	η	notes
run 1	10^{-3}	initial energy $20\,\mathrm{keV}$, initial $\beta = 0.1$
run 2	10^{-4}	initial energy $20\,\mathrm{keV}$, initial $\beta = 0.1$
run 3	10^{-5}	initial energy $20\,\mathrm{keV}$, initial $\beta = 0.1$
run 4	10^{-6}	initial energy $20\,\mathrm{keV}$, initial $\beta = 0.1$
run 5	10^{-7}	initial energy $20\,\mathrm{keV}$, initial $\beta = 0.1$
run 6	10^{-8}	initial energy $20\,\mathrm{keV}$, initial $\beta = 0.1$
run 7	10^{-3}	initial energy $40\,\mathrm{keV}$, initial $\beta = 0.1$
run 8	10^{-3}	initial energy $60\,\mathrm{keV}$, initial $\beta = 0.1$
run 9	10^{-3}	initial energy Maxwellian at $20\,\mathrm{keV}$, initial β uniformly distributed
run 10	10^{-4}	initial energy Maxwellian at $20\,\mathrm{keV}$, initial β uniformly distributed
run 11	10^{-5}	initial energy Maxwellian at $20\,\mathrm{keV}$, initial β uniformly distributed
run 12	10^{-6}	initial energy Maxwellian at $20\,\mathrm{keV}$, initial β uniformly distributed
run 13	10^{-7}	initial energy Maxwellian at $20\,\mathrm{keV}$, initial β uniformly distributed
run 14	10^{-8}	initial energy Maxwellian at $20\,\mathrm{keV}$, initial β uniformly distributed

TABLE 3.1: Parameters used in simulations

progressively decreases by factors of 10 starting from an initial non-dimensional value of 10^{-3}. Since the current density parameter is held fixed, the electric field weakens proportionally to the resistivity. Similarly, κ increases with decreasing resistivity, resulting in less scattering.

In the absence of scattering a particle's orbit duration will be exclusively determined by the box size, the initial conditions (that is its pitch angle, energy and position in the box) and the applied electric field. Naturally if the electric field strength is increased, particles will exit the box quicker. The addition of pitch angle scattering will tend to spread out the distribution of orbit durations as some particles take longer than others to exit the box (this is the stochastic nature of the process). It would be particularly interesting to examine the effect of scattering at a rate tied to the resistivity, and hence the electric field strength, as these are competing processes in terms of their effect on orbit durations. There is also a physical motivation for studying the orbit duration as it affects the rate of energetic particles exiting the reconnection region in the context of solar flares. Having said that, the model presented here is a proof of concept only, so the results are not directly applicable to real flares. In Figure 3.1a we see that higher resistivity results in shorter orbit durations, but only to a point. In particular for the case when $\eta = 10^{-3}$ (black line, run 1) the orbits are generally longer than for $\eta = 10^{-4}$ (red line). If we count the proportion of short duration orbits for each run performed,

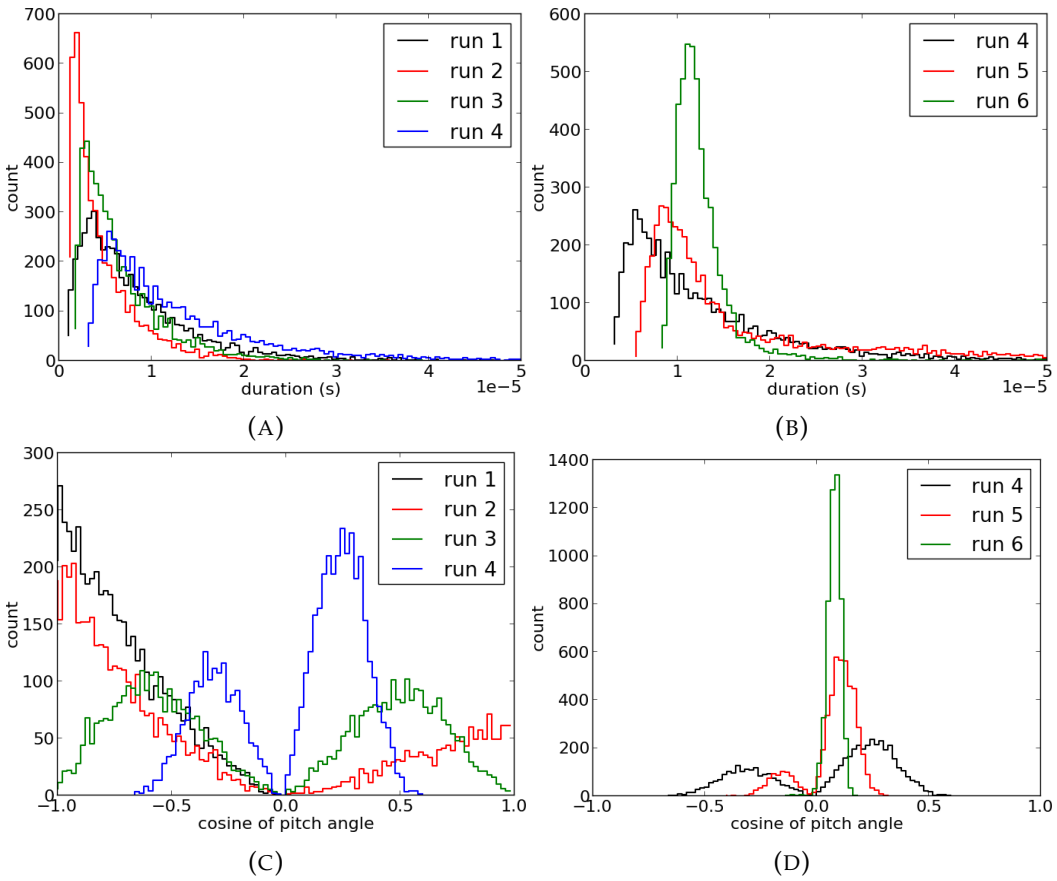

FIGURE 3.1: Particle orbit duration distributions (top row) and final cosine of pitch angle distributions (bottom row) with different resistivities (see Table 3.1). Initial particle energy is $20\,\mathrm{keV}$ and $\beta = 0.1$. (Note: time axis in top row is in units of $10^{-5}\,\mathrm{s}$, indicated by the 1e-5 in bottom right corner)

we get that for run 1 ($\eta = 10^{-3}$) 70.0% have orbits shorter than $10^{-5}\,\mathrm{s}$ in duration, while for runs 2, 3, and 4 (each with resistivity decreasing by a factor of 10 relative to run 1) the proportions are 90.6%, 81.6%, and 49.2% respectively. This implies that for some resistivity between $\eta = 10^{-4}$ and $\eta = 10^{-3}$ there is an optimal value for which the orbit durations are shortest. In Figure 3.1b we examine still lower resistivities and find that the orbit durations keep increasing with only 30.0% and 11.3% of orbits having durations shorter than $10^{-5}\,\mathrm{s}$ for runs 5 and 6 (resistivities $\eta = 10^{-7}$ and 10^{-8}) respectively. This can be further emphasized by looking at the height and location of the peak in the orbit duration distribution histogram for each of the different simulation runs. In particular, in Figure 3.2 we plot the maximum value of the histogram against the time at which it occurs for each of the runs performed above. Here we clearly see that the simulation with the greatest amount of short duration particle orbits is run 2. Furthermore, there are three regimes evident. For resistivities below 10^{-8} particle orbit durations are long due to little scattering and little accelerating electric field, which results in particles propagating with whatever initial conditions they were set up with. With increasing resistivity the electric field and scattering both increase, creating the second regime. Here the effects of the electric field seem to dominate over scattering, evidenced by the shortening orbit durations. Finally, for resistivities higher than 10^-4 the orbit duration once again increases, forming the third regime in which scattering plays an even more important role.

Since the particle energy and position at the end of the simulation is identical for all particles due to conservation of energy (strictly speaking the energy depends on which end of the box the particles exit, but that still only gives two different energies and positions that the particles could have), the only remaining variable directly obtained from the simulation that is left is the cosine of the pitch angle. In Figure 3.1c the cosine of pitch angle distribution shows marked differences between the different runs as the resistivity is progressively lowered. For the highest resistivity ($\eta = 10^{-3}$, run 1) all particles have $\beta < 0$ and 82.6% of particles have $\beta < -0.5$. This is not unexpected since we are accelerating electrons, and the electric potential drop in the $\eta = 10^{-3}$ case is $100\,\mathrm{kV}$, so particles should obtain energies of approximately $100\,\mathrm{keV}$. If particles do not experience pitch angle scattering this energy will only contribute to increasing the particle's parallel velocity, which, for these parameters, will lead to a pitch angle cosine close to -1 (for these parameters the final pitch angle cosine for a single particle in the absence of scattering is $\beta = -0.92$, corresponding to approximately $157°$, which is obtained by running the simulation for a single particle in the absence of scattering). The

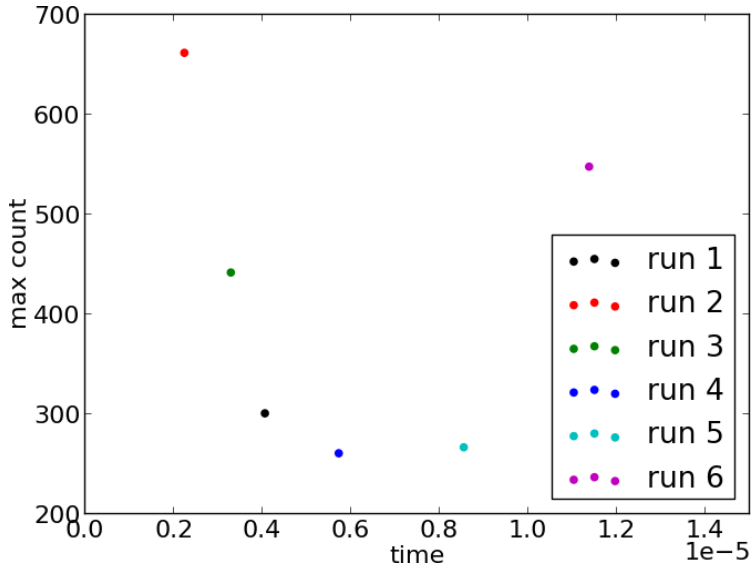

FIGURE 3.2: Scatter plot of the maximum value of the orbit duration histograms from Figures 3.1a and 3.1b against the duration for which this peak occurs (note: time axis is in units of 10^{-5} s, indicated by the 1e-5 in bottom right corner)

effect of scattering is to drive the β towards a uniform distribution, so the single maximum at $\beta = -0.92$ in the absence of scattering gets spread out. Clearly the cosine of the pitch angle is bounded by $-1 \leq \beta \leq 1$, so scattering will push the distribution is towards larger values of β. However, due to the strength of the electric field in run 1, particles do not manage to gain positive values of β (this would mean that particles are propagating in opposite direction to the force on them caused by the electric field). In runs 2 and 3 the proportion of particles with $\beta < -0.5$ decreases to 61.1% and 32.3% respectively due to the weakening electric field in comparison to run 1. The asymmetry in the β distribution slowly diminishes as the resistivity (and hence both scattering and accelerating electric field) decreases so that the distribution is roughly symmetrical when $\eta = 10^{-5}$ (run 3). In run 4 the distribution drastically changes, becoming double-peaked, as the electric field weakens further, with only 2.1% of particles accelerated to have $\beta < -0.5$. The asymmetry in the distribution for run 4 is due to the initial pitch angle being chosen to have $\beta = 0.1$. Decreasing the resistivity still further results in the distributions in Figure 3.1d, where the asymmetry in the distribution grows and fewer particles are able to reach pitch angles near to $\beta = \pm 1$. This is in part due to the weak strength of the electric field relative to the initial energy of the particle. Since J is held fixed, the potential drop is going to decrease proportionally to the

resistivity decrease, so in the case of run 6 where $\eta = 10^{-8}$ the potential drop is only $1\,\mathrm{V}$, which is negligible compared to the initial particle energy ($20\,\mathrm{keV}$), so even without scattering we would not expect any particles to have large absolute values of β. Also playing a role in the sharply peaked nature of the distribution is the weak scattering, as it is not able to cause the cosine of the pitch angle to become uniformly distributed by the time the particles have left the domain.

A relatively high initial energy of $20\,\mathrm{keV}$ was chosen for these simulations so as to ensure that they do not take too long to run (so that the particles exit the box sooner). Other alternatives could have been to decrease the box size, however, by looking at what happens for different initial energies we could hope to extrapolate to more reasonable initial conditions. To this end we ran simulations with initial energies of 40 and 60 keV with $\eta = 10^{-3}$, the results of which are shown in Figure 3.3. From Figure 3.3a we see that for higher initial energies (40 and $60\,\mathrm{keV}$ for runs 7 and 8) there are slightly more particles exiting earlier, however the difference in the distributions, at least for the distributions with a higher initial energy, is small (65.3% and 60.3% of particle orbits shorter than $10^{-5}\,\mathrm{s}$ respectively for runs 7 and 8, compared to 82.6% for run 1). This is because particles are initialised to propagate against the direction of the electric force on them, resulting in the electric field needing to take more time to slow down and reverse higher energy particles. As a result, a decrease in initial energy by a factor of 2 or so could result in the presence of more short duration orbits. On the other hand, Figure 3.3b shows there is almost no difference in the distribution of pitch angles with different initial energies.

3.4 Randomised initial conditions

The discrete initial conditions considered in the previous section are not very representative of any real plasma, so to have a more realistic setup we initialise the particles with a Maxwellian energy distribution and a uniform distribution in the cosine of the pitch angle. In Figure 3.4 we compare the orbit durations and pitch angle distributions for two of the runs to demonstrate the effect of initial conditions on runs with high ($\eta = 10^{-3}$) and low ($\eta = 10^{-6}$) resistivities. Black lines indicate discrete initial conditions (i.e. all particles have the same initial condition) while red lines indicate a distribution in both energy and cosine of pitch angle. For high resistivity (Figures 3.4a,3.4b) there is little difference between both the time and pitch angle distributions, while for low resistivity (Figures 3.4c,3.4d) particles

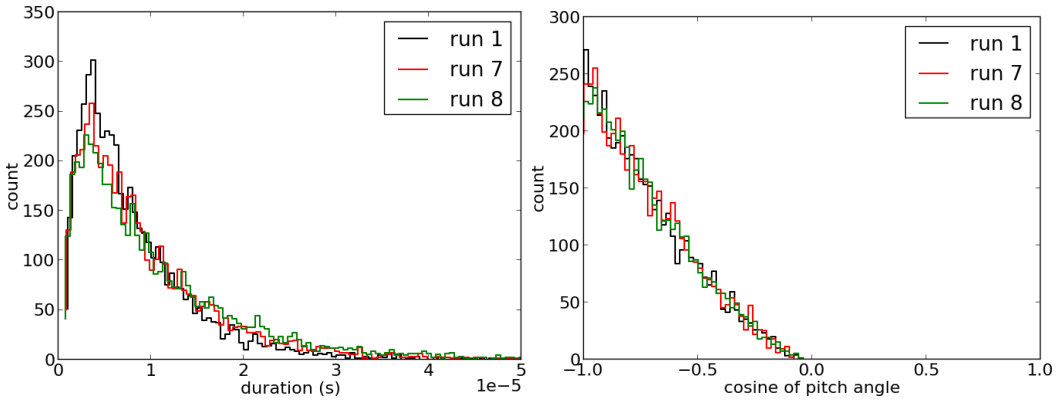

(A) (B)

FIGURE 3.3: Particle orbit duration distributions and final cosine of pitch angle distributions for initial particle energy $20\,\mathrm{keV}$ (black line), $40\,\mathrm{keV}$ (red line), and $60\,\mathrm{keV}$ (green line). Initial particle pitch angle cosine is $\beta = 0.1$, and $\eta = 10^{-3}$.

which have distributed initial conditions tend to have shorter orbit durations and a more uniform β distribution (apart from few particles near $\beta = 0$) when compared to particles with discrete initial conditions. This is likely due to the much stronger electric field and scattering in the high resistivity case having a strong effect on all particles, regardless of their initial conditions, whereas for lower resistivity the weaker electric field and scattering are unable to affect the initial distribution as much, hence the initial conditions are much more influential.

In Figure 3.5 we compare results from the same simulations as performed in Section 3.3, this time with randomised initial conditions. Figures 3.5a, and 3.5b suggest that particle orbit durations get shorter with decreased resistivity apart from the highest resistivity (run 9, $\eta = 10^{-3}$). Although if we look at the percentage of particle orbits shorter than $10^{-5}\,\mathrm{s}$ we get 69.4%, 92.2%, 89.5%, 86.5%, 86.2%, and 85.9% of particles for runs 9 through 14 respectively. Generally speaking particles tend to have shorter durations when compared to simulations where all the particles had identical initial conditions (especially for simulations with lower resistivities). In part this is because for our previous experiments (runs 1 to 8) initially all particles were moving against the direction of the force acting on them and had to wait to either be turned around by the electric force, or to be scattered in that direction. Since the randomised initial conditions have equally many particles

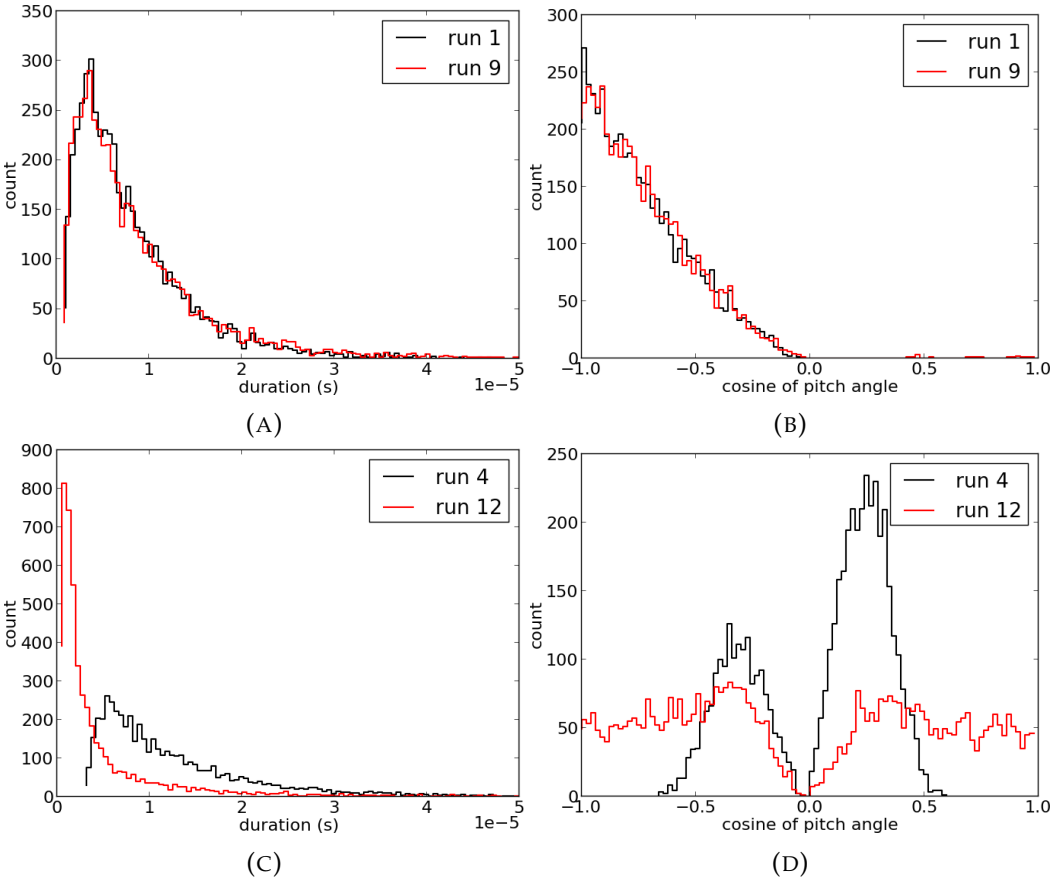

FIGURE 3.4: Comparing particle orbit duration distributions and final cosine of pitch angle distributions for discrete initial conditions (black lines) and initial conditions given by Maxwellian distributions in energy and uniform distribution in β (red line). Anomalous resistivity set to $\eta = 10^{-3}$ in the top row and $\eta = 10^{-6}$ in the bottom row (see also Table 3.1).

moving in the direction of the electric force as against, a larger portion of particles can exit the box quicker.

Figure 3.5c shows that for the two highest resistivities the pitch angle distribution is similar to what it was for discrete initial conditions (comparing runs 9 and 10 to runs 1 and 2 from Figure 3.1c), while decreasing the resistivity below 10^{-5} starts to result in distributions which are more symmetrical about $\beta = 0$, but also flatter towards $\beta = \pm 1$. Decreasing the resistivity further results in a pitch angle distribution that is almost uniform apart from a depletion of particles about $\beta = 0$, as shown in Figure 3.5d. For decreasing resistivity the width of the depletion region near $\beta = 0$ gets narrower. Since the associated electric field is very low for these cases it is not a surprise to see a final β distribution which is reasonably close to uniform, because the electric field is not strong enough to overcome scattering and cause a peak at $\beta = -1$. The depletion at $\beta = 0$ is also expected, because in order for a particle to cross the box boundary it must have some parallel component to its velocity. As the electric field gets weaker the probability of a particle having a value of β near zero gets higher, so the depletion region gets narrower. The effects of the randomised initial conditions are most noticeable for lower resistivities, with 82.1%,62.1%,42.2%,27.0%,26.9%, and 24.8% of particles having $\beta < -0.5$, which is similar to the fixed initial conditions for higher resistivities ($\eta = 10^{-3}, 10^{-4}$, runs 9,10), but there are many more particles for low resistivities than in the case with fixed initial conditions.

Once again we consider the location and height of the peaks in the orbit duration histograms (see Figure 3.6). This time we see much less variation, particularly for resistivities lower than $10^{-}3$. In particular, for runs 10-14 the peak of the distribution occurs for approximately the same orbit duration. Whereas in the case with discrete initial conditions the particle orbits were significantly influenced by their initial conditions for very low values of resistivity, this is not the case with uniformly distributed initial pitch angle cosine and Maxwellian energy distribution. In particular, for the very lowest values of resistivity (run 14) the randomised pitch angle ensures that particles exit the box quicker than if they had a single discrete value. This results in particles having much more similar typical orbit duration, with the effect of scattering only being noticeable for high resistivity ($\eta = 10^{-3}$).

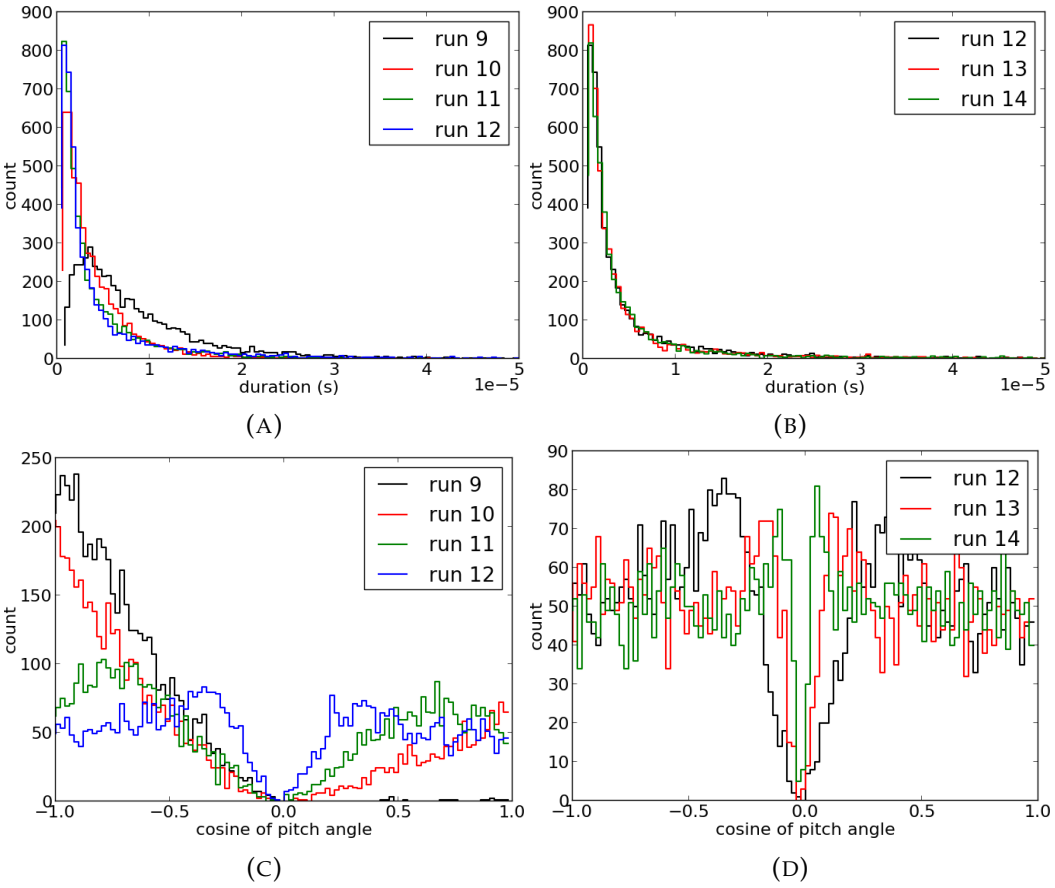

FIGURE 3.5: Particle orbit duration (top row) and final pitch angle cosine (bottom row) for simulations with Maxwellian distributed initial energy and uniformly distributed pitch angle cosine initial conditions. (Note: time axis in top row is in units of 10^{-5} s, indicated by the 1e-5 in bottom right corner)

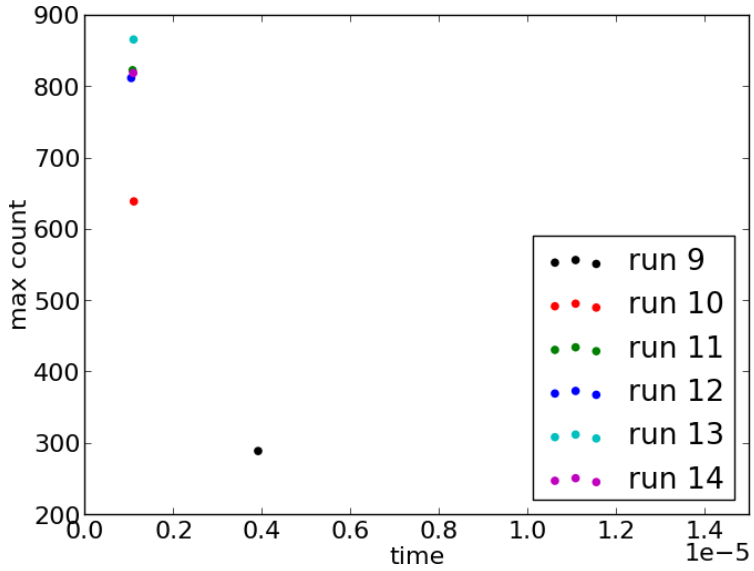

FIGURE 3.6: Scatter plot of the maximum value of the orbit duration histograms from Figures 3.5a and 3.5b against the duration for which this peak occurs (note: time axis is in units of 10^{-5} s, indicated by the 1e-5 in bottom right corner)

3.5 Discussion

This brief introduction to the interplay between pitch angle scattering and acceleration due to electric fields, with both tied to a resistivity parameter in this model, has yielded some interesting results. If the resistivity is high then scattering is stronger, which prevents particles from being accelerated and exiting the computational box as quickly. On the other hand if the resistivity is too low, the scattering does not impede the particles' progress, but the electric field is too weak to accelerate them as quickly (or to equally high energies). Hence, broadly, there are three regimes of interest in this setup. The first is when the resistivity is low, resulting in low scattering and low electric field. This means particles orbits are mainly determined by their initial conditions. The second regime is for medium values of resistivities, where the electric field and scattering are both higher, but the particle dynamics are dominated by the effects of the electric field. Finally for sufficiently high resistivity scattering becomes more important, slowing down the particles from exiting the box as quickly as for lower values of the resistivity. As a result, there appears to be an optimal level of resistivity which results in the particle orbits exiting the fastest (although, of course this is still generally longer than if there was no scattering). For these experiments the optimal level of

resistivity turned out to be between $\eta = 10^{-3}$ and 10^{-4} in non-dimensional units, although for a more physical experiment this may be different since the electric field and scattering rate are chosen arbitrarily here. For example, the electric field could easily be altered by choosing a different value for the current, J, and the scattering can be affected by choosing a different temperature to plug into the Spitzer resistivity.

This notion of an optimal electric field strength is reminiscent of what is known as the Dreicer field [Dreicer, 1959]. The Dreicer field is a critical value of the electric field above which Coulomb collisions become insufficient to slow particles down, resulting in the whole particle population being accelerated to arbitrarily high energies (bounded only by the amount of work the electric field can do on the particles). This occurs because the Coulomb collision frequency decreases with increasing energy. Our pitch angle scattering scenario is somewhat different. In our case, pitch angle scattering does not affect the energy of the particles, so particle energy gain will be dependent only on the potential drop. There are some similarities though, as both Coulomb collisions and pitch angle scattering cause an energetic beam of particles caused by an electric field to slow down. However, whereas Coulomb collisions do this up until the Dreicer field, our pitch angle scattering model shows the opposite behaviour with particle orbit durations decreasing up until a certain optimal field strength, then increasing again. The contrast between the Dreicer field and our optimal field strength is due to the Coulomb collision rate not influencing the value of the electric field (in models where the electric field is dependent on a specified resistivity), while our pitch angle scattering rate is tied to the electric field strength.

We also find that the final pitch angle distribution is severely affected by the resistivity. If the resistivity is high then the strong electric field causes all particles to move in one direction, however the strong scattering results in a distribution which is peaked at $\beta = -1$, decreasing all the way to $\beta = 0$. On the other hand, as the resistivity is lowered, particles can either be scattered in the direction opposite the electric force, or from their initial conditions, and as a result can exit the opposite side of the box to where the particles experiencing a high resistivity do. As a result of the low resistivity the low electric field and pitch angle scattering rate are less able to affect the initial pitch angle distribution. If starting the simulation with a Maxwellian energy distribution and uniform cosine of pitch angle distribution then the resulting orbit durations and final β distributions approach something resembling asymptotic distributions for small resistivity.

These simulations could be continued further, making more realistic

approximations for the electric field and Spitzer resistivity, as well as by investigating different expressions for each. Furthermore, these types of simulations could be extended to investigate the effect of pitch angle scattering in regions without an accelerating electric field when added onto a region with the electric field present. The aim of this would be to simulate what happens to particles as they pass from an acceleration region into the ideal corona where parallel electric fields are absent but pitch angle scattering may occur. This would allow the investigation of particle transport with additional pitch angle scattering similar to Bian et al. [2016]. However for the work in this thesis we instead move in the direction of considering more complicated geometries by way of examining the effects of pitch angle scattering in MHD simulations of magnetic reconnection.

Chapter 4

Particle acceleration and scattering in 2D MHD reconnection simulations[1]

4.1 Introduction

Clearly, the real world is not one-dimensional, and although 1D models can sometimes be very informative, they will often miss out on many important physical phenomena that occur in higher dimensions. As a result, although our 1D work shows that pitch angle scattering has an impact on particle orbit durations and pitch angle distributions, we move on to multi-dimensional models, where we examine whether or not these effects still apply in higher dimensions and if additional effects are found. As mentioned in Chapter 1, the simplest geometry where magnetic reconnection can occur is in a 2D x-point scenario, which we examine here with the addition of a guide field. Previous work on particle acceleration in 2D magnetic reconnection includes analytical studies [see e.g. Litvinenko, 1996], numerical simulations of test particles in analytical fields [e.g. Wood and Neukirch, 2005], numerical simulations of test particles in fields derived from MHD simulations [e.g. Gordovskyy et al., 2010a,b], and PIC simulations [e.g. Drake et al., 2006]. In this chapter we consider the effects of pitch angle scattering on test particle orbits in fields derived from MHD simulations of magnetic reconnection. In Section 4.2 we describe the MHD simulations we performed to obtain the background fields. Section 4.3 we describe the setup of the test particle code, including the scattering rate, particle orbit initial conditions, and the parameters used in the different simulation runs. Individual trajectories,

[1]The work in this chapter was performed in collaboration with Eduard Kontar and James Threlfall. Many of the results have been published in Borissov et al. [2017]

as well as energy spectra and distributions of other observables are described in Section 4.4. A discussion of these results follows in Section 4.5.

4.2 MHD simulations

As discussed in Chapter 2, to obtain our background electromagnetic fields we solve the standard resistive MHD equations [see e.g. Priest, 2014] given by Equations 1.7-1.11 using the *Lare2d* code [Arber et al., 2001]. We choose the normalising scales for length, magnetic field strength and density to be $\hat{L} = 10\,\mathrm{m}, \hat{B} = 0.03\,\mathrm{T}$ and $\hat{\rho} = 1.67 \times 10^{-12}\,\mathrm{kg \cdot m^{-3}}$ (for other normalising quantities that are derived from these see Table 4.1). The value of $\hat{\rho}$ is chosen to be representative of the coronal environment [Priest, 2014], while $\hat{B}$ is comparable to the normalising magnetic field strength used in other simulations of magnetic reconnection [e.g. Gordovskyy et al., 2010a] used to investigate particle acceleration and motivated by solar flares. The size of current sheets in the solar corona is not well constrained, so choosing a normalising length scale to be comparable to the current sheet size is difficult. Current sheet sizes similar to ours have been used [see e.g. Litvinenko, 1996, Wood and Neukirch, 2005], however so have much larger ones [e.g. Kliem, 1994, Gordovskyy et al., 2010a]. This lengthscale is on the lower limit of the applicability of MHD in the context of the solar corona, however this was necessary to achieve a compromise between the use of self-consistent electromagnetic fields, while also incorporating aspects of microscopic physics into the particle acceleration picture, and without using kinetic simulations. Since the energy of an electron accelerated by an electric field is $E_k = q_e \int_S \mathbf{E} \cdot d\mathbf{s}$, where S is the particle trajectory, and $d\mathbf{s}$ points along the trajectory, in the absence of scattering, test particle energies scale with the lengthscale. Therefore results from orbit calculations performed with a given choice of lengthscale can be extrapolated to represent orbits calculated in fields with other lengthscales by scaling the energies appropriately. This is not the case in general if particle orbits are affected by scattering, because the mean free path associated with the scattering introduces a scale independent of the MHD lengthscale, impacting the particle orbit trajectories, durations and energies. For instance, substantially increasing the lengthscale, without changing the scattering mean free path, would result in prohibitively expensive particle orbit computation because particles would experience more scattering events before exiting the computational box. Although this issue could be avoided by, for example, shrinking the domain size, doing so would restrict the effect of the geometrical configuration of the MHD fields on the particle simulation.

TABLE 4.1: Normalisation constants for Lare2d. Only the length, magnetic field, and density scaling are specified, while the rest are calculated. (For reference, normalising scales in the left column, top to bottom are: length, density, internal energy, current density, and resistivity. Right column: magnetic field strength, velocity, time, electric field strength, and temperature.)

Quantity	Normalising value	Quantity	Normalising value
$\hat{L}$	$10\ \mathrm{m}$	$\hat{B}$	$3 \times 10^{-2}\,\mathrm{T}$
$\hat{\rho}$	$1.67 \times 10^{-12}\,\mathrm{kg \cdot m^{-3}}$	$\hat{v}$	$2.07 \times 10^{7}\,\mathrm{m \cdot s^{-1}}$
$\hat{\varepsilon}$	$4.28 \times 10^{14}\,\mathrm{J \cdot kg^{-1}}$	$\hat{t}$	$4.83 \times 10^{-7}\,\mathrm{s}$
$\hat{j}$	$2.39 \times 10^{3}\,\mathrm{A \cdot m^{-2}}$	$\hat{E}$	$6.21 \times 10^{5}\,\mathrm{V \cdot m^{-1}}$
$\hat{\eta}$	$260\,\Omega \cdot \mathrm{m}$	$\hat{T}$	$6.23 \times 10^{10}\,\mathrm{K}$

It should also be noted that we assume the resistivity (η_a) is zero where the critical current is below a threshold value of $j_{\text{crit}} = 1$, while $\eta_a = 10^{-4}$ where the current exceeds j_{crit} (values of j_{crit} and η_a are given in normalised units). This results in pitch angle scattering only occuring within the current sheet.

Our simulation of 2D magnetic reconnection starts with an isothermal force-free Harris sheet whose magnetic field is perturbed in order to initiate reconnection. This Harris sheet is an equilibrium configuration with a sheared magnetic field given by $B_x \sim \tanh y$, $B_z \sim \operatorname{sech} y$. This ensures a constant magnetic pressure throughout, allowing the specification of a constant gas pressure (and using the ideal gas law, $p = nk_BT$ we can set constant (number) density and temperature). In this configuration there is a buildup of current near $y = 0$. To initiate reconnection a driving velocity at the boundaries may be imposed, which will enhance the current in the current sheet beyond the criticial threshold, triggering reconnection. Another way to initiate reconnection is to impose an additional perturbation to the fields, which is the method we use. The equations specifying the initial conditions for the MHD simulation are given in Equations 4.1-4.4:

$$\frac{B_x}{\hat{B}} = \tanh(y) - \frac{b_1}{b_0} k_y \cos(k_x x) \sin(k_y y), \tag{4.1}$$

$$\frac{B_y}{\hat{B}} = \frac{b_1}{b_0} k_x \cos(k_y y) \sin(k_x x), \tag{4.2}$$

$$\frac{B_z}{\hat{B}} = \operatorname{sech}(y), \tag{4.3}$$

$$\frac{\varepsilon}{\hat{\varepsilon}} = \frac{T_0/\hat{T}}{m_r(\gamma_p - 1)}, \tag{4.4}$$

where $b_1/b_0 = 0.3$ is the amplitude of the perturbation, $T_0 = 10^6\,\mathrm{K}$, $m_r = 1.2$ is the reduced mass for coronal plasma normalised to the proton mass, and $\gamma_p = 5/3$ is the ratio of specific heats. The initial density is specified to be $5\hat{\rho}$ uniformly throughout the domain. Our domain has size 15 in the x-direction and 30 in the y-direction so that our choices of $k_x = 2\pi/15$, $k_y = 2\pi/60$ ensure the perturbation has one period within the domain in x-direction and half a period in the y-direction. Periodic boundary conditions in the x-direction and closed boundary conditions in the y-direction are imposed. The magnetic field corresponding to the initial conditions is shown in Figure 4.1a.

We evolve the MHD simulation until the reconnection rate drops to near-zero and we use an individual snapshot from the simulation during the reconnecting phase into which we insert test particles to compute particle orbits (the magnetic energy within the simulation box is shown in Figure 4.1d, with the reconnection rate being the slope of the line, hence we wait until the magnetic energy stops decreasing). For simplicity, we pick a single MHD snapshot because the particle orbit lifespan is shorter than the electromagnetic field structure changes. Indeed, this is confirmed in Section 4.4.2 by the fact that most of the particle orbits' durations are shorter than $0.1\,\mathrm{ms}$, during which time the MHD fields do not vary a great deal because the main reconnection phase which lasts approximately $1\,\mathrm{ms}$ (this can be seen from the evolution of the magnetic energy in Figure 4.1d, which steadily decreases between 1 and $2\,\mathrm{ms}$).

4.3 Configuration of test particle code

To study the effect of pitch angle scattering on particle behaviour, we initialise test particle orbits in the MHD snapshot shown in Figure 4.1b, and integrate the governing equations for their evolution, detailed in Chapter 2, until the orbit leaves the computational domain. The scattering rate is modelled by

$$\nu = \frac{v_{tot}}{\lambda} \qquad \lambda = \lambda_0 \kappa \left(1 + \frac{v_{tot}}{v_{th}}\right)^{\alpha}, \tag{4.5}$$

where v_{tot} is the total particle velocity (i.e. not the velocity of the guiding centre), $v_{th} = \sqrt{3k_B T/m}$ is the thermal velocity at the temperature at the location of the particle, and $\lambda_0 = 2 \times 10^8\,\mathrm{m}$ is the collisional mean free path of an electron at

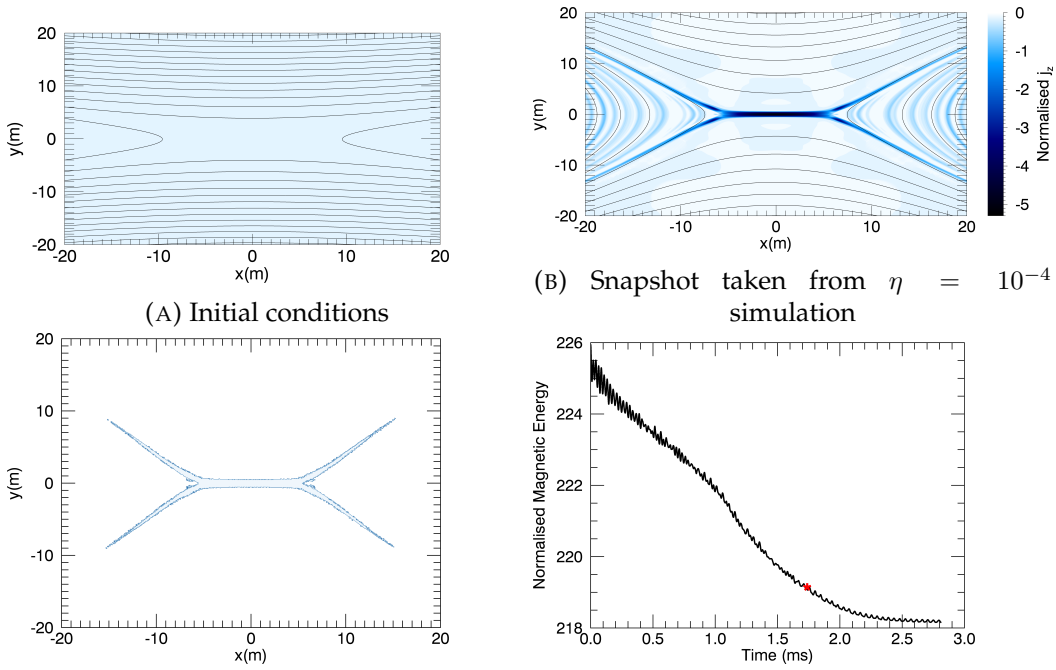

(A) Initial conditions

(B) Snapshot taken from $\eta = 10^{-4}$ simulation

(C) Contour of non-zero resistivity

(D) Time evolution of magnetic energy

FIGURE 4.1: Magnetic field lines (black) and out of plane electric field (colour) for the initial conditions of the MHD simulation (Panel A), and the chosen snapshot into which test particles are injected (Panel B). We present only the subset of the MHD simulation domain which is within the test particle computational box. Panel C shows the areas where current density exceeds the threshold value for triggering resistivity and coincides with the region where scattering takes place. Panel D presents the evolution of the magnetic energy in the simulation, with the red star indicating the time at which the snapshot used for the particle simulation is taken.

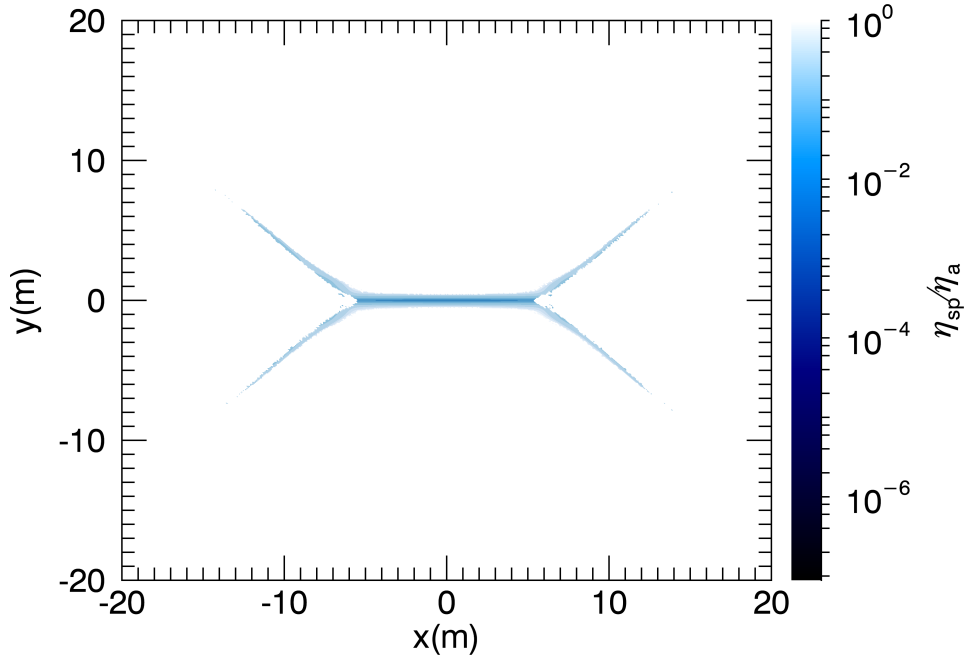

FIGURE 4.2: Spatial dependence of the ratio of Spitzer resistivity to MHD resistivity in the snapshot of the MHD simulation into which test particles are injected. White areas surrounding the current sheet do not have a specified MHD resistivity, hence the ratio is calculated only where $\eta_a \neq 0$.

$T = 5 \times 10^7$ K, in a plasma number density of $10^{15}\,\mathrm{m}^{-3}$. We compare the results of calculations in the presence of different scattering rates by varying the values of κ and α in Equation 4.5. The parameter α determines how the mean free path changes as a function of test particle velocity, with $\alpha > 0$ resulting in a longer mean free path (and hence less scattering) at higher particle velocities, while $\alpha < 0$ results in a decreasing mean free path for higher velocities. As before, a simple scaling of the mean free path can be applied by varying κ, with higher values leading to a longer mean free path and less scattering. Similarly, we introduce a dependence on the resistivity into the mean free path by setting $\kappa = \eta_{sp}/\eta_a$, where η_{sp} is the local Spitzer resistivity at the position of the guiding centre, although we also consider constant values of κ. To get an idea of the spatial dependence of the Spitzer resistivity on position in our MHD simulation, a contour plot of the ratio $\kappa = \eta_{sp}/\eta_a$ is shown in Figure 4.2. As expected, the strongest scattering is within the middle of the current sheet. It should be noted that the variability in the ratio η_{sp}/η_a is simply due to the variability of the calculated Spitzer resistivity (in this case mainly depending on the temperature), rather than the applied resistivity.

We perform test particle simulations with the following choices of parameters: to investigate the effect of velocity-dependent scattering we choose $\alpha = \pm 2, 0$, with $\kappa = \eta_{sp}/\eta_a$; to investigate the effect of resistivity we take $\alpha = 0$ and $\kappa = 10^{-5}, 10^{-6}, 2\times10^{-8}, \eta_{sp}/\eta_a$. In order for the guiding centre approximation to remain valid, the scattering frequency, $\nu = v_{tot}/\lambda$, must not exceed the gyrofrequency of the test particle. This restriction on the scattering frequency is dependent on the test particle gyrational velocity, as well as the local magnetic field strength. It is difficult to predict if a given test particle orbit will break this condition because it depends on many factors such as the particle's trajectory, energy gain and sequence of random numbers chosen for the scattering process, however we find that for values $\kappa < 5 \times 10^{-9}$ the scattering frequency starts to regularly exceed the gyrofrequency. In addition to performing test particle simulations with scattering included at different rates, we perform the same simulations without scattering using the variable timestep 4th order Runge-Kutta code. We refer to these simulations as the control cases.

To compute test particle energy spectra, we integrate 5×10^5 particle orbits for each of the parameter regimes mentioned above. The particle orbits are distributed with uniformly random initial positions inside a portion of the computation box. This portion is centred on the reconnection region and has a side length of 2 in normalised units (the whole computational box has a side length of 4, also centred on the reconnection region; see Figure 4.1b). The initial pitch angle takes on 100 evenly distributed values between 10° and 170° and the initial energy takes on 50 evenly distributed values between $10\,\mathrm{eV}$ and $320\,\mathrm{eV}$ (this energy range covers over 90% of the maxwellian at $10^6\,\mathrm{K}$). These choices mean that there are 100 particle orbits for every combination of initial pitch angle and energy, each having a different (uniformly random) initial position.

The final energy and position of each orbit is recorded as it exits the computational box. Each orbit is weighted in proportion to the plasma density at its initial position, so that the initial particle energy distribution is approximately a Maxwellian at a temperature of 10^6 K and the initial distribution of the cosine of the pitch angle is uniform. The resulting energy spectra are discussed in Section 4.4.2.

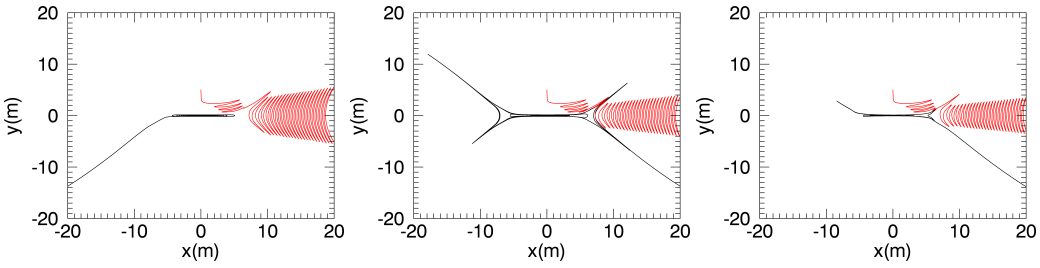

FIGURE 4.3: Orbit trajectories for test particles initialised at $(x, y) = (0, 0), (0, 5)\,\mathrm{m}$ (black and red trajectories respectively) within the MHD snapshot. The initial pitch angle is $90°$ and kinetic energy $320\,\mathrm{eV}$. Test particle orbit calculations were performed without scattering (Panel A), with scattering where $\kappa = 10^{-6}$ (Panel B), and where $\kappa = \eta_{sp}/\eta_a$ (Panel C).

4.4 Results of test particle calculations

4.4.1 Selected trajectories

We are primarily interested in the energy spectra that can be obtained by integrating large numbers of particle orbits, however first we examine selected orbit trajectories, energy, and pitch angle evolution, and how these are affected by pitch angle scattering. To do so test particles are initialised in two initial positions, $y_0 = 0$ and $5\,\mathrm{m}$, in both cases with $x = 0\,\mathrm{m}$, initial pitch angle $\theta_0 = 90°$, and kinetic energy $320\,\mathrm{eV}$, into the fields produced by the MHD simulation. This way the effect of scattering will be evident for orbits starting within the reconnection region, as well as for those that drift into it due to the $\mathbf{E} \times \mathbf{B}$ drift. The particle trajectories are calculated as described in Chapter 2 with no scattering, scattering with $\kappa = 10^{-6}$ in Equation 4.5, and with $\kappa = \eta_{sp}/\eta_a$. The resulting trajectories, energy evolution, and pitch angle evolution are shown in Figures 4.3 - 4.5.

Since the conservation of the magnetic moment is violated in the presence of pitch angle scattering, the orbit trajectories in Figures 4.3b and 4.3c differ from the control case (Figure 4.3a). The cause of this is due to terms in the guiding centre equations (Equations 2.20,2.21) proportional to μ having a randomising effect on the particle drifts where scattering is turned on (since μ is no longer constant). This is particularly evident for particle orbits initialised within the current sheet, with the more chaotic evolution of the pitch angle when $\kappa = \eta_{sp}/\eta_a$ (see green curve in Figure 4.4b in comparison to the red and black curves) suggesting that this choice of κ produces stronger scattering within the diffusion region than if $\kappa = 10^{-6}$.

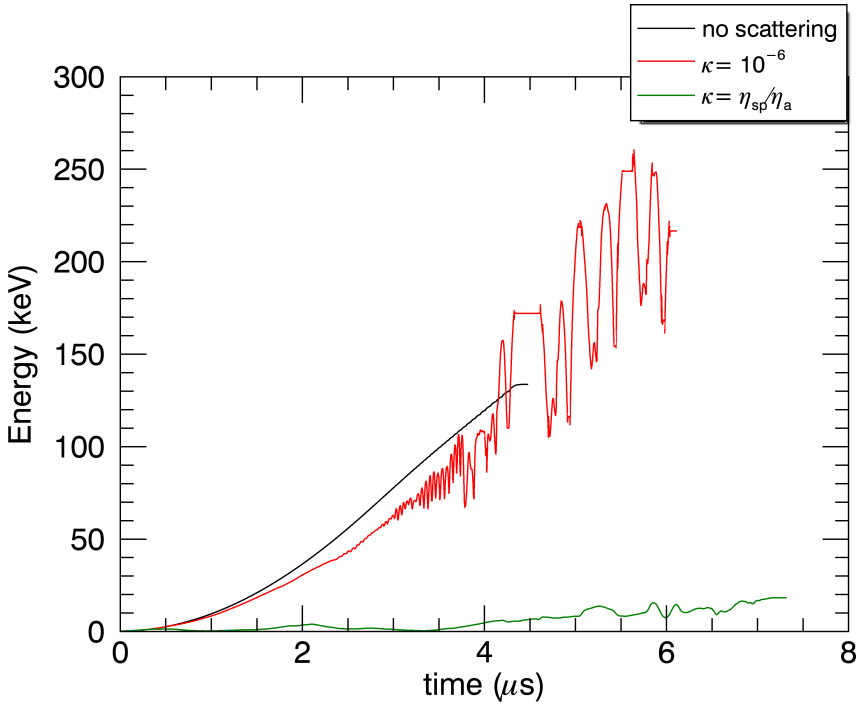

(A)

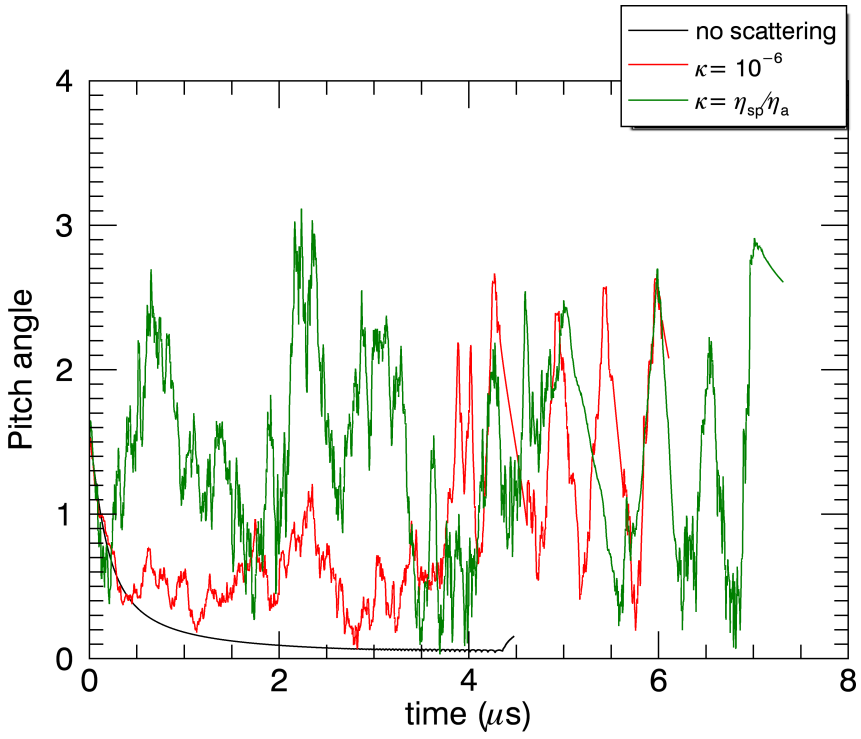

(B)

FIGURE 4.4: Orbit energy and pitch angle evolution for the trajectories calculated above which are initialised inside the current sheet. Black line for particle trajectory without scattering, red line for scattering at constant rate with $\kappa = 10^{-6}$ and green line has scattering at the variable rate, with $\kappa = \eta_{sp}/\eta_a$.

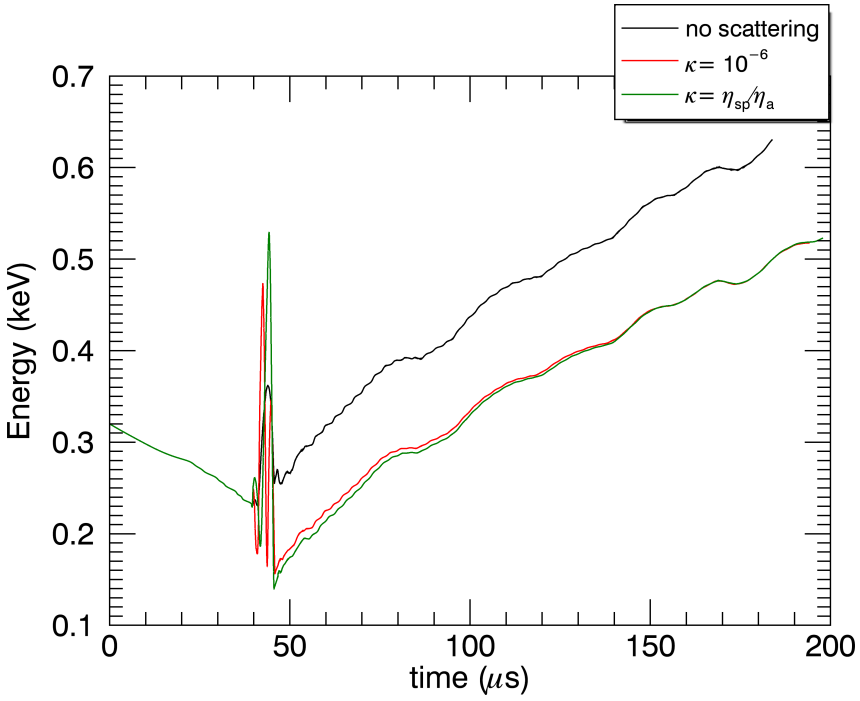

(A)

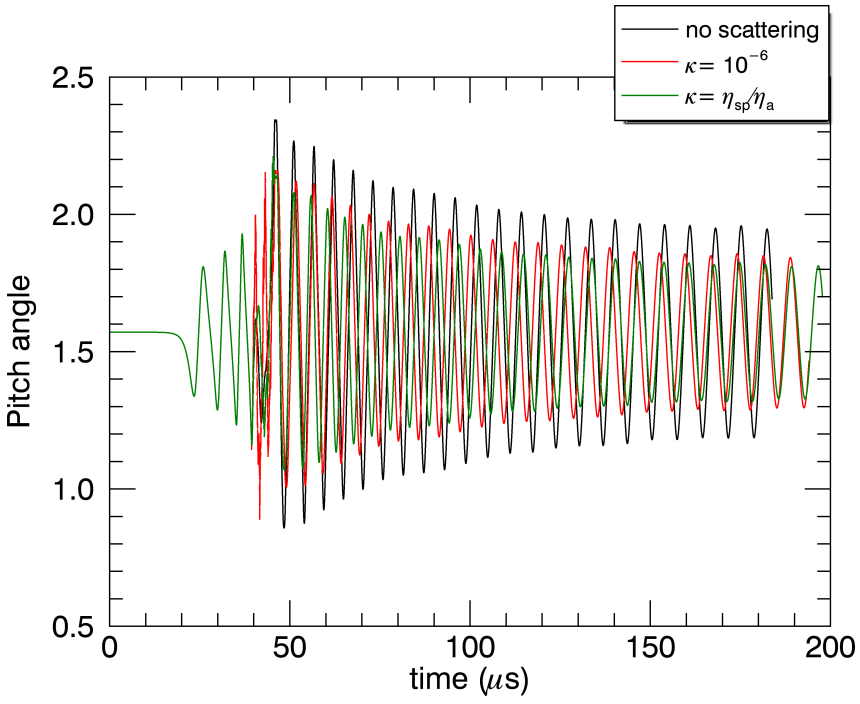

(B)

FIGURE 4.5: Orbit energy and pitch angle evolution for the trajectories calculated above which are initialised outside of the current sheet (at $y = 5\,\mathrm{m}$). Black line for particle trajectory without scattering, red line for scattering at constant rate with $\kappa = 10^{-6}$ and green line has scattering at the variable rate, with $\kappa = \eta_{sp}/\eta_a$.

Nevertheless, for $\kappa = 10^{-6}$ (but also in principle for any orbit with sufficient scattering), the particle orbit crosses the reconnection region multiple times (see black particle orbits in Figures 4.3b and 4.3c), as has been reported previously [see e.g. Burge et al., 2014]. This is not an effect that is seen in the absence of scattering. The electric field can do more work on (and thus accelerate to higher energies) the particles that traverse the reconnection region multiple times, rather than those orbits which only traverse a single time. It should be noted that due to the stochastic nature of the scattering process, such behaviour and associated increased energy is not guaranteed even with identical orbit initial conditions. This suggests that the presence of scattering will yield energy spectra containing higher maximum energies than the case without scattering, as a result of particle trajectories traversing the reconnection region multiple times.

Orbits which start outside of the reconnection region are not subject to as much scattering and acceleration if they drift into the separatrices rather than the central current sheet, since there is no scattering or acceleration possible in the ideal region where $\eta = 0$. Thus, even though some scattering is present in the trajectory (red lines in Figure 4.3) and pitch angle evolution (Figure 4.5b) of particle orbits initialised at $y = 5\,\mathrm{m}$, energy changes at the end of the orbit are much less evident than for the particle orbits initialised inside the current sheet.

To gain some understanding of the dynamics of large numbers of orbits we run 100 particles initialised in the middle of the current sheet (i.e. with $x = y = 0\,\mathrm{m}$), with initial pitch angle 90° and energy $320\,\mathrm{eV}$. This is done for the scattering rates $\kappa = 10^{-6}, 2 \times 10^{-8}, \eta_{sp}/\eta_a$. We then overplot the trajectories and energy evolution of the particles (with a high transparency for each line so that they are all visible) to examine the behaviour of multiple particle orbits at once. These results are shown in Figure 4.6. By comparing Figures 4.6a-4.6e we see that for the higher scattering rates ($\kappa = 2 \times 10^{-8}, \eta_{sp}/\eta_a$) there are more particles exiting within the reconnection outflows as compared to the lowest scattering rate, $\kappa = 10^{-6}$. Furthermore particles travel in a narrower stream when exiting the outflow region to the left than to the right. This indicates a pitch angle closer to 90° when exiting to the left compared to exiting to the right. Careful examination of the figures also suggests that there are more particle orbits very close to the outflow region of the current sheet in the $\kappa = 2 \times 10^{-8}$ simulation than in the $\kappa = \eta_{sp}/\eta_a$ simulation. This could be due to the scattering rate being higher in the separatrices for the constant κ simulation than when κ is calculated based on the local Spitzer resistivity, causing more particles to be scattered into this region and ultimately into either the outflow or back into the current sheet. Particle scattering out of the separatrices into the

reconnection outflow region contributes to the lower enegy gain seen for orbits with $\kappa = 2 \times 10^{-8}$ (compare Figure 4.6d with 4.6b and 4.6f), however, as we will see soon, the particle energy spectra in fact reach higher energies with scattering included. From Figures 4.6c, 4.6b, and 4.6f we see that particles do indeed gain higher energy in the presence of scattering (red lines) than without scattering (black line). However, with increasing scattering rate (lower κ) the time taken to achieve higher energies is longer. This is to be expected as a higher scattering rate results in particles taking longer to traverse the reconnection region due to multiple changes of direction, hence taking longer to complete multiple traverses of the reconnection region.

To check that it is indeed the case that particle scattering is weaker in the separatrices, we compute the value of κ and plot it with respect to y for the above orbits. The result is shown in Figure 4.7. The current sheet is located between $-1\,\mathrm{m} \leq y \leq 1\,\mathrm{m}$, so from Figure 4.7 we see that although the minimum value of κ is in some cases as low as 10^{-8} in the current sheet and not far into the separatrices, when the particles travel further into the separatrices the value of κ is approximately in the range $10^{-6} - 10^{-5}$, which implies less scattering further into the separatrices, something that does not occur for the constant κ simulations.

4.4.2 Energy spectra

In Figure 4.8a we compare the spectra produced by the control case (without scattering, black curve), with the scattering cases where $\kappa = 10^{-5}, 10^{-6}$ (in both of these we set $\alpha = 0$). In the control case there is a break in the spectrum at approximately $10\,\mathrm{keV}$. A small population of particles are able to achieve energies of approximately 100 keV (about 0.3% of the total number of orbits, after weighting, we refer to this part of the spectrum as the "spike"). The particles in this spike originate from throughout the inflow regions and have a wide range of initial conditions, so the reason for the spike is to do with the specific characteristics of the MHD fields used in the simulation, such as the thickness of the acceleration region. One way to address the spike could be to use a smoother profile for the resistivity, which would result in a smoother electric field seen by particles entering the reconnection region. In the presence of scattering, with $\kappa = 10^{-5}$ (red curve in Figure 4.8a), highly energised particles orbits are more spread out, both to higher and lower energies when compared to the control case, however the general shape of the energy spectrum remains unchanged. However, when $\kappa = 10^{-6}$ (green curve in Figure 4.8a) the resulting energy spectrum is smoother, and without any breaks. This suggests that scattering is much more effective for smaller values of

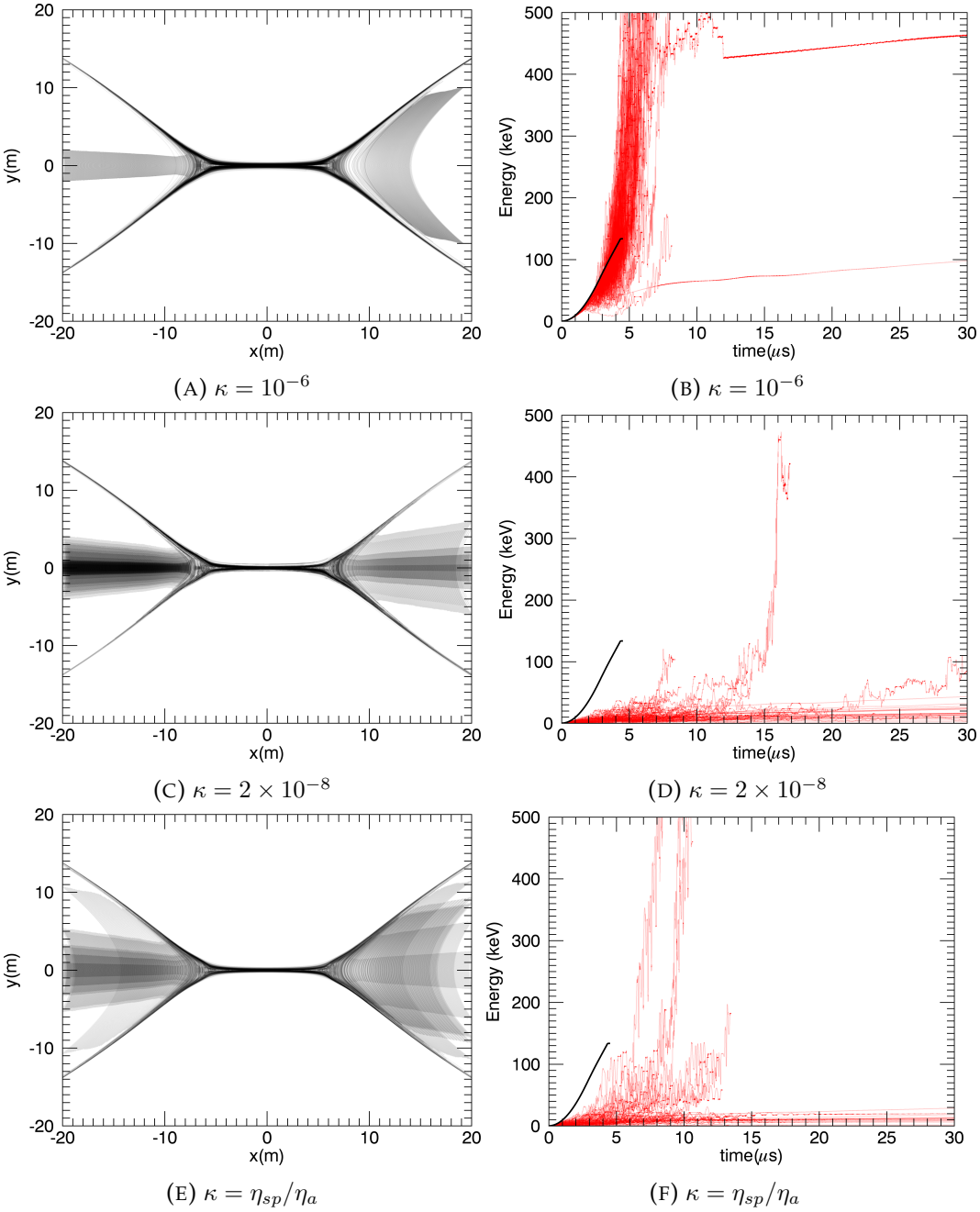

(A) $\kappa = 10^{-6}$ (B) $\kappa = 10^{-6}$

(C) $\kappa = 2 \times 10^{-8}$ (D) $\kappa = 2 \times 10^{-8}$

(E) $\kappa = \eta_{sp}/\eta_a$ (F) $\kappa = \eta_{sp}/\eta_a$

FIGURE 4.6: Left column: orbit trajectories for 100 particles started at $x = y = 0\,\mathrm{m}$ with pitch angle $90°$ and energy $320\,\mathrm{eV}$ for three different scattering rates. Right column: corresponding energy evolution (in red). Black line corresponds to energy evolution of unscattered particle with the same initial conditions

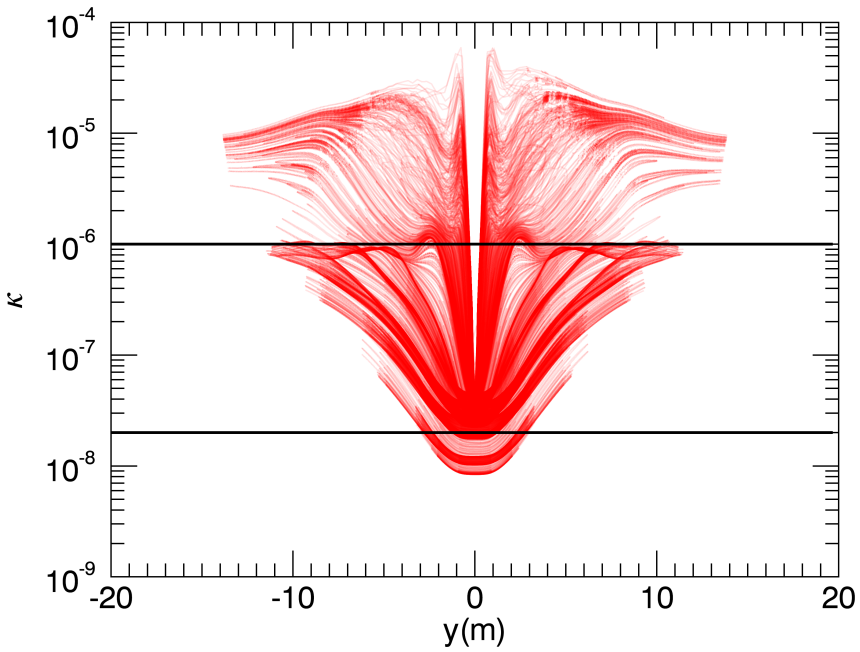

FIGURE 4.7: Value of κ (red lines) with respect to y for 100 orbits started at $x = y = 0\,\mathrm{m}$ with pitch angle $90°$ and energy $320\,\mathrm{eV}$ for simulation with $\kappa = \eta_{sp}/\eta_a$. Black lines indicate constant values of κ used in other simulations.

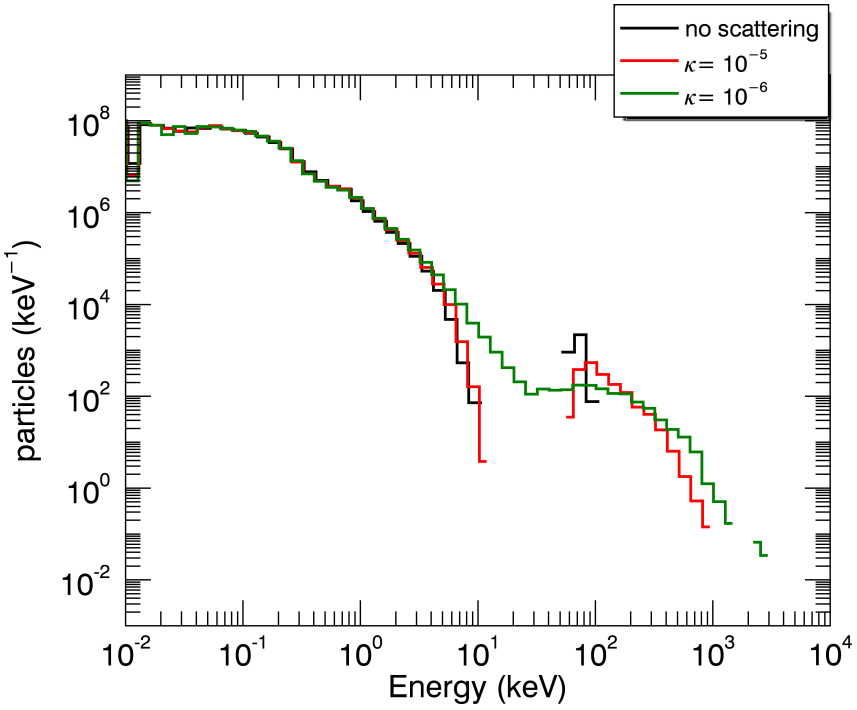

(A)

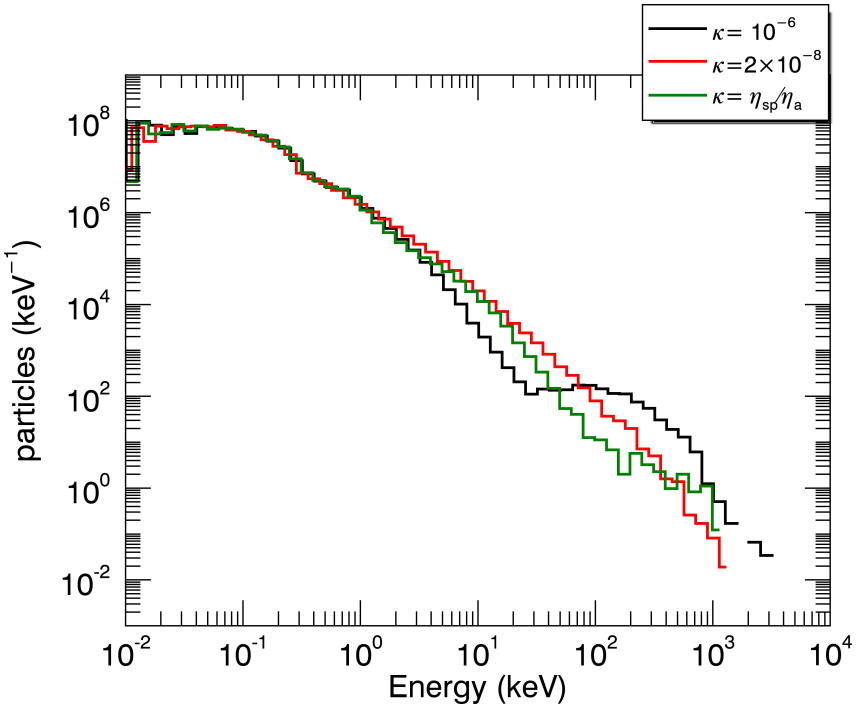

(B)

FIGURE 4.8: Final test particle energy spectra for scattering models with varying values of κ. In all cases 5×10^5 test particle orbits are calculated, then each orbit is weighted in proportion to the local density at the initial position of the orbit to ensure the initial energy distribution is a Maxwellian at $T = 10^6$ K, and that the initial pitch angle cosine distribution is uniform. Subsection 4.3 discusses the initial conditions of the simulations.

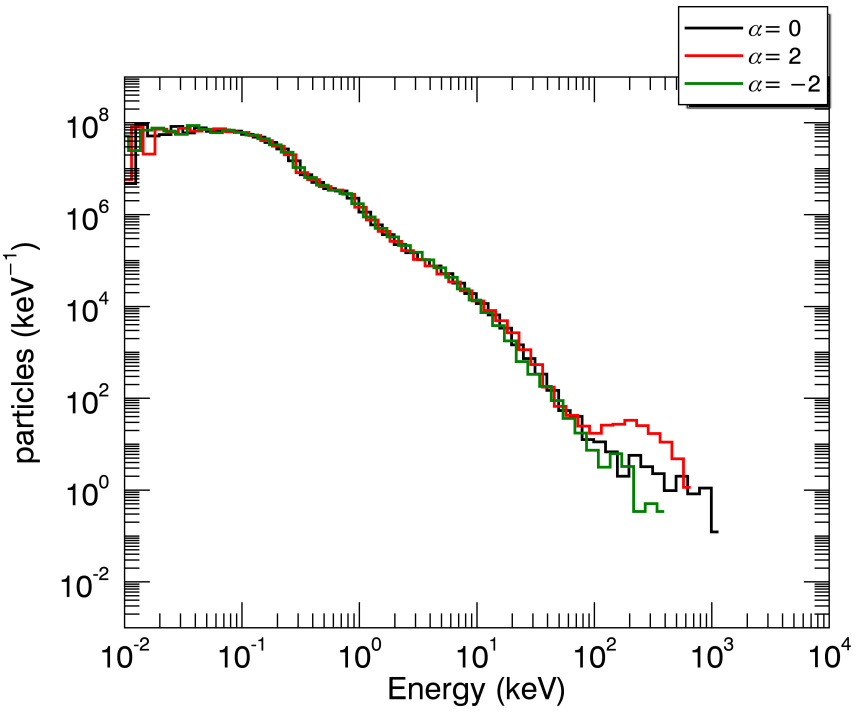

(A)

FIGURE 4.9: Final test particle energy spectra for scattering models with $\kappa = \eta_a/\eta sp$ and varying values of α. Again, 5×10^5 test particle orbits are calculated, then each orbit is weighted in proportion to the local density at the initial position of the orbit to ensure the initial energy distribution is a Maxwellian at $T = 10^6$ K, and that the initial pitch angle cosine distribution is uniform. Subsection 4.3 discusses the initial conditions of the simulations.

κ. Both scattering cases also contain significant numbers of particle orbits which obtain energies that are much greater than the maximum energy achieved by any particle orbit in the control case (in both scattering regimes approximately 0.15% of particle orbits achieve energies higher than any unscattered orbit, corresponding to approximately half of the population of the spike in the control case).

In Figure 4.8b we compare energy spectra produced with scattering at a rate given by $\kappa = \eta_{sp}/\eta_a$ to the constant $\kappa = 10^{-6}$ and $\kappa = 2 \times 10^{-8}$ cases, again with $\alpha = 0$. As seen in Figure 4.7, the value $\kappa = 2 \times 10^{-8}$ was specifically chosen to be comparable to the minimum value of η_{sp}/η_a. Since $\eta_{sp} \propto T^{-3/2}$ this corresponds to the locations in the MHD simulation which had the highest temperatures, i.e. in the middle of the current sheet. Furthermore, since all three cases examined here have strong scattering rates, there are no breaks in any spectrum, and there are more particles with energies of approximately 10 keV in the case when $\kappa = \eta_{sp}/\eta_a$ and $\kappa = 2 \times 10^{-8}$ than when $\kappa = 10^{-6}$. In particular 1.6% of the total particle orbits have energies between 5 and 30 keV for the case $\kappa = \eta_{sp}/\eta_a$, compared to 2.3% for the $\kappa = 2 \times 10^{-8}$ case, while only 0.5% of particles are in this range for the $\kappa = 10^{-6}$ simulation. We also note that the dependency of the mean free path on the resistivity leads to lower maximum energies than what is observed for a constant but lower value of κ. This is due to the ratio η_{sp}/η_a increasing in the separatrices where the temperature is lower, resulting in fewer particles being scattered. The absence of scattering within the separatrices means that fewer orbits are able to repeatedly cross the acceleration region, resulting in lower energies. We also note that scattering with $\kappa = 2 \times 10^{-8}$ yields fewer particles at energies above $100\,\mathrm{keV}$ when compared with the $\kappa = 10^{-6}$ case. In both cases, the maximum energy obtained by particles is still higher than for the case without scattering.

By introducing a velocity dependence into the scattering model we obtain the energy spectra shown in Figure 4.9a. In Figures 4.8a and 4.8b we fixed $\alpha = 0$ in Equation 4.5 and varied values of κ. Now we set $\kappa = \eta_{sp}/\eta_a$ and perform simulations with $\alpha = \pm 2$, which we then compare to the case $\alpha = 0$. There is a very small difference in the spectra above $1\,\mathrm{keV}$, with the $\alpha = -2$ case producing slightly more lower energy particle orbits, with 8.1% of all particle orbits had energies between 1 and 10 keV, compared to 7.9% and 7.6% for the $\alpha = 0$ and $\alpha = 2$ cases respectively. Fewer higher energy orbits are also observed, with 0.004% of all particle orbits had energies greater than 100 keV in the $\alpha = -2$ case, compared to 0.01% and 0.04% for the $\alpha = 0$ and $\alpha = 2$ cases respectively. Although large negative α causes a shorter mean free path and, as a result, more scattering, the effect on energy spectra is the opposite of what is seen when there

is no dependence of the mean free path on velocity. If there is no dependence on velocity particles tend to gain more energy with increased scattering. However, the differences between the energy spectra for the three values of α examined are very small when compared to varying κ. This is because the factor $1 + v_{tot}/v_{th}$ only varies from about 1 to 6 (for test particle orbits originating from the centre of the current sheet, where the temperature is at its maximum). Varying κ by several orders of magnitude, as done here, results in variation of the mean free path by the same amount, thus having a much greater impact on the scattering rates and energy spectra compared to changing the velocity dependence.

Pitch angle scattering should decrease the rate at which particles are accelerated, because in this model particles gain energy due to motion parallel to the electric field, which scattering inhibits. In Figure 4.10a we plot a histogram of orbit durations in cases without scattering (black curve), with scattering where $\kappa = 2 \times 10^{-8}$ (red curve) and $\kappa = \eta_{sp}/\eta_a$ (green curve, in both of the scattering cases $\alpha = 0$). Significant differences between the three cases arise only for orbits with duration longer than $0.1\,\mathrm{ms}$. In the absence of scattering the number of particle orbits with duration greater than $0.1\,\mathrm{ms}$ is about 14%, when $\kappa = \eta_{sp}/\eta_a$ this figure rises to 16% and to 22% when $\kappa = 2 \times 10^{-8}$, confirming that more scattering results in particle orbits with longer durations. Figures 4.10b - 4.10f show cumulative energy spectra for orbits with progressively longer durations (that is to say energy spectra from all the particle orbits with durations shorter than a given time). From Figure 4.10 we see that for progressively longer durations the energy spectra extend to progressively higher energies. This is a result of the particle orbits needing multiple traverses of the current sheet in order to gain energies higher than those possible in the absence of scattering, which takes more time than if the particles were directly accelerated out of the computation box. The portion of the spectra in Figures 4.10b-4.10e below approximately 320 eV is due to the particle orbits which exit the computational box without having encountered the reconnection region. This happens relatively quickly (the exact orbit duration would depend on the initial pitch angle, position, and kinetic energy of each particle orbit, but in all cases occurs faster than $0.1\,\mathrm{ms}$) and, as such, these particle orbits are not present in Figure 4.10f, resulting in a much smoother spectrum. We also observe the presence of a distinct shoulder in the energy spectra for particles with orbits longer than $0.1\,\mathrm{ms}$ for particles experiencing scattering parametrised by $\kappa = \eta_{sp}/\eta_a$. This shoulder starts at energies of approxmately $20\,\mathrm{keV}$ in Figure 4.10f, and is only seen for this scattering regime, with stronger scattering resulting in a spectrum more reminiscent of a power law at these energies. Given that very few particles have

orbits with a duration longer than $0.1\,\mathrm{ms}$, it is not surprising that this feature is not observed in the full spectrum in Figure 4.8b.

4.4.3 Particle orbit escape positions

We now examine the impact of pitch angle scattering on the distribution of test particle orbit positions upon exiting the computational box. Figure 4.11 shows the distributions of the final z and y orbit positions. This is done for the scattering model when $\kappa = \eta_{sp}/\eta_a$ (green curve) and $\kappa = 2 \times 10^{-8}$ (red curve), in both cases with $\alpha = 0$, in addition to the case without scattering (black curve). Without scattering the highly accelerated particle population primarily escapes the simulation domain between $z = 200$ and $z = 300\,\mathrm{m}$ causing a prominent increase seen on the right hand side of Figure 4.11a (note that the remaining particles exit with z close to zero and correspond to the particles which do not experience any acceleration). In contrast, scattering results in more spread in the distribution of final z-positions, with scattering in the $\kappa = \eta_{sp}/\eta_a$ model resulting in a narrower range of exit locations, compared to the stronger scattering case, with $\kappa = 2 \times 10^{-8}$, seen in the broader red curve in Figure 4.11a.

Similarly, in Figure 4.11b we present a histogram of the y-value at the point where the particles exit the computation box. The two tallest peaks, at approximately $y = \pm 15\,\mathrm{m}$, correspond to the separatrices, with $\|y\| < 15$ corresponding to particles exiting in the reconnection outflow region. The $\kappa = \eta_{sp}/\eta_a$ scattering model and the control case (without scattering) give very similar results, with 14% and 12% of the total particle orbits exiting within the outflow region respectively. The much stronger scattering case with $\kappa = 2 \times 10^{-8}$ has significantly more orbits exit within the outflow region (20% of total). This is likely due to stronger scattering in the separatrices (in the case of the $\kappa = 2 \times 10^{-8}$ case), which causes more particle orbits to be scattered from the separatrices into the outflow region. Since no scattering takes place in this region and the $\mathbf{E} \times \mathbf{B}$ drift is directed outward, the test particles are unable to re-enter the current sheet and exit the simulation box in the outflow region. We have already seen this phenomenon when we examined the trajectories of 100 test particle orbits, which all started in the current sheet in Figure 4.6a, 4.6c and 4.6e. For higher values of κ, or for $\kappa = \eta_{sp}/\eta_a$, scattering is much weaker in the separatrices, resulting in a distribution of final y-values much closer to that of the control case.

Finally, we consider the pitch angle distribution of particle orbits when they exit the computational box, which are shown in Figure 4.12. Firstly we note that there are 4 peaks in the pitch angle distribution, two near $\theta = 0, \pi$ and two more

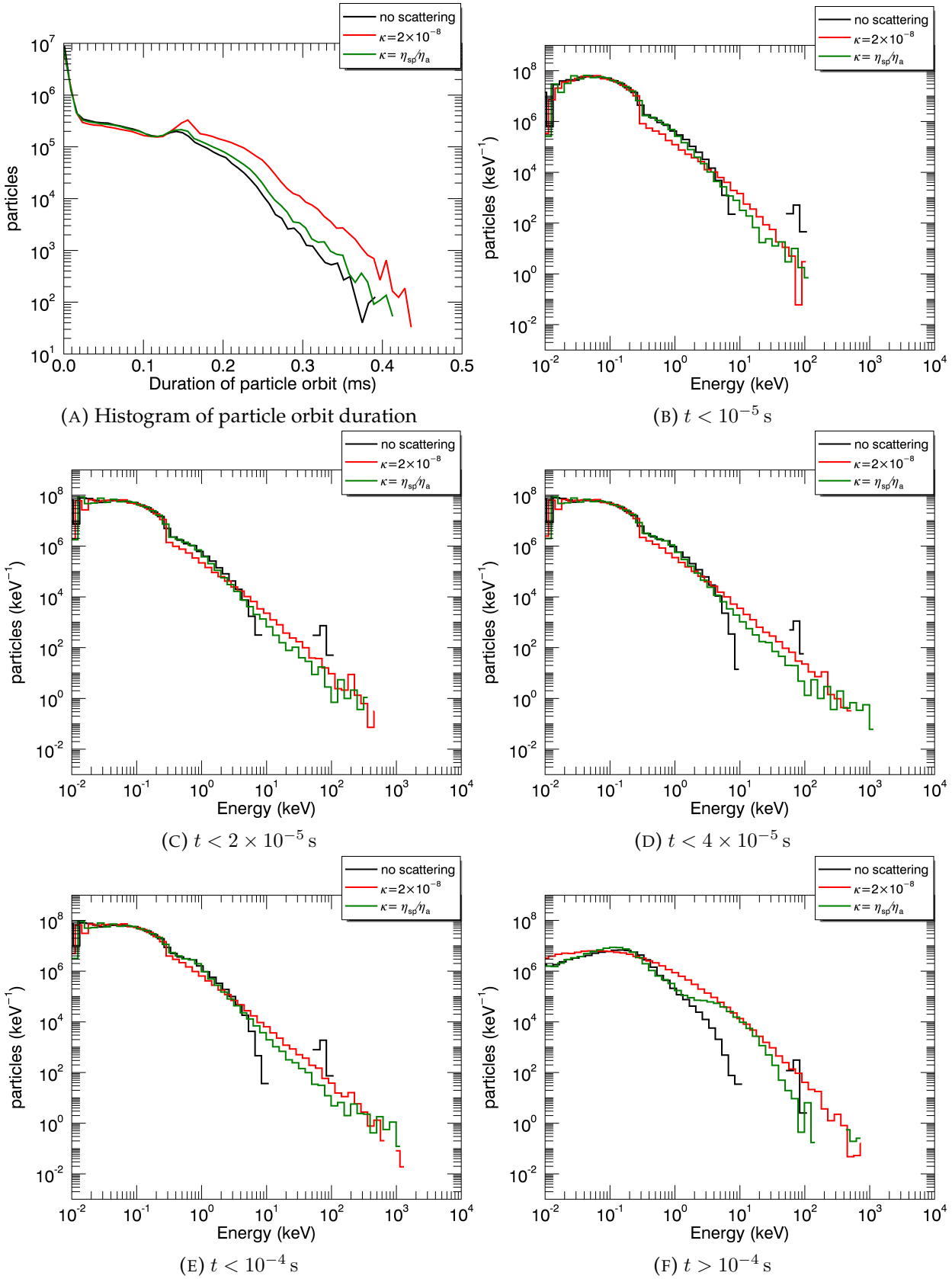

(A) Histogram of particle orbit duration

(B) $t < 10^{-5}$ s

(C) $t < 2 \times 10^{-5}$ s

(D) $t < 4 \times 10^{-5}$ s

(E) $t < 10^{-4}$ s

(F) $t > 10^{-4}$ s

FIGURE 4.10: Panel A shows a histogram of the duration of the particle orbits for the simulations without scattering (black lines), with scattering where $\kappa = 2 \times 10^{-8}$ (red lines), and $\kappa = \eta_{sp}/\eta_a$ (green lines). Panels B-F show spectra consisting of particle orbits with durations for the indicated time range in the same scattering regimes.

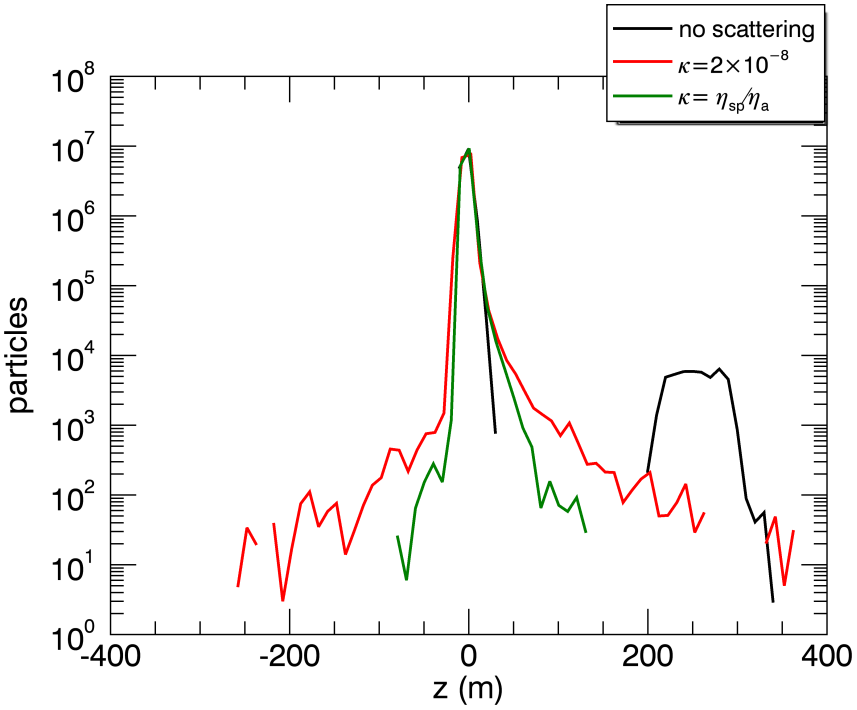

(A)

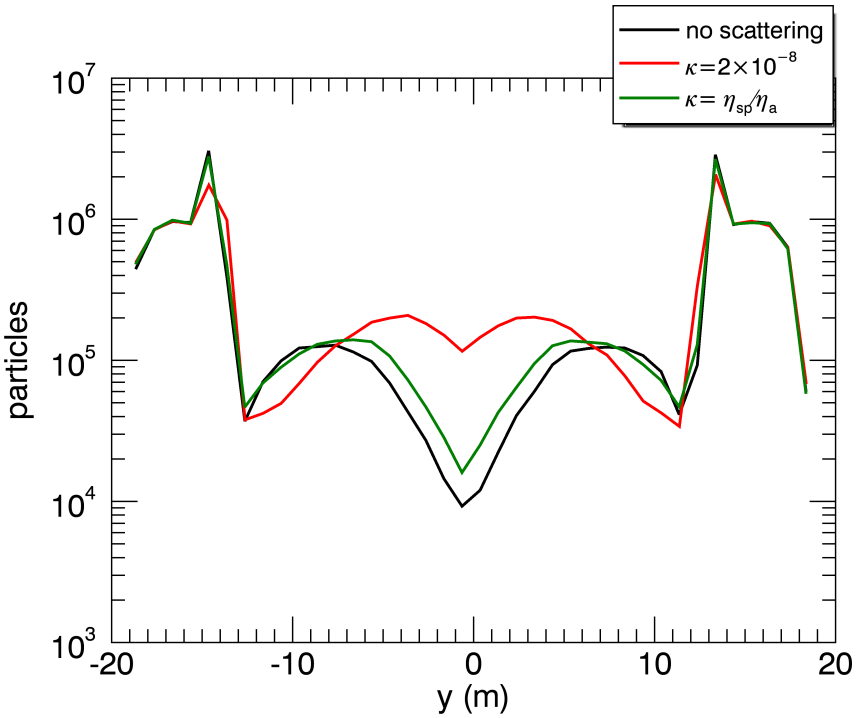

(B)

FIGURE 4.11: Histograms of the y-, and z-positions of particle orbit escape from computational box in the absence of scattering (black lines), and for the $\kappa = 2 \times 10^{-8}$ (red lines) and $\kappa = \eta_{sp}/\eta_a$ (green lines) scattering regimes. In both scattering cases, α is set to zero.

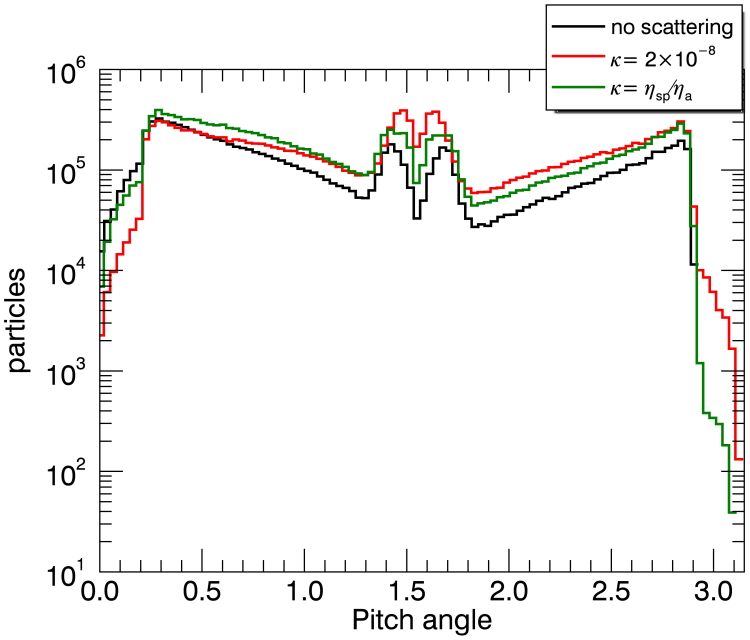

FIGURE 4.12: Pitch angle distributions in the absence of scattering (black line), and for the $\kappa = 2\times10^{-8}$ (red line) and $\kappa = \eta_{sp}/\eta_a$ (green line) scattering regimes. In both scattering cases, α is set to zero.

near $\theta = \pi/2$. The peaks near $\theta = 0, \pi$ are created by particles escaping along the separatrices, while the peaks near $\theta = \pi/2$ are created by particles trapped in the reconnection jet outflow. This is supported by looking at the percentage of particles with pitch angle $1.25 \leq \theta \leq 1.75$, which is 15.3% in the absence of scattering, 24.2% for scattering with $\kappa = 2 \times 10^{-8}$ and 18.1% for $\kappa = \eta_{sp}/\eta_a$, which roughly agrees with what was found for the final y-position of the particle orbits. Furthermore, looking at the proportion of particles with pitch angle $\theta < 0.5$ we have 27.7% if there is no scattering, 16.4% with $\kappa = 2 \times 10^{-8}$ and 21.9% with $\kappa = \eta_{sp}/\eta_a$. On the other hand, if considering particles with pitch angle $\theta > \pi - 0.5$ then the proportions are 12.9% without scattering, 14.3% with $\kappa = 2 \times 10^{-8}$ and 13.1% with $\kappa = \eta_{sp}/\eta_a$. This is to be expected as scattering will tend to create pitch angle distributions that are more uniform, hence there is a smaller difference between the sizes of the $\theta < 0.5$ and $\theta > \pi - 0.5$ populations when scattering is included, particularly when it is included at a constant, high rate of $\kappa = 2 \times 10^{-8}$.

4.5 Discussion

In our simple model for pitch angle scattering associated with resistivity in 2D magnetic reconnection we find a significant impact on test particle energy spectra and trajectories. Previous work including the collisional scattering [e.g. Numata and Yoshida, 2002, Burge et al., 2014] has found that repeated crossings of the reconnection region by test particles could lead to a higher energy gain than in the absence of scattering. In contrast to our work, the effect of repeated crossings of the reconnection region on energy spectra in these studies was not significant. On the other hand, pitch angle scattering at a rate many orders of magnitude higher than the Coulomb collision rate is the main aspect of the model which affects the energy spectra and box escape positions. Due to this strong scattering, the energy spectra we obtain show a significant number of orbits gaining energies higher than what would be possible without scattering, which is something not observed in Burge et al. [2014], due to their use of a much lower scattering rate.

By interpreting κ from Equation 4.5 as the dependence of the mean free path on the resistivity, the differences between constant and spatially varying ($\kappa = \eta_{sp}/\eta_a$) values of κ are mainly a result of their behaviour outside of the central current sheet. Since our MHD simulations involved a constant resistivity in regions where the current exceeded a critical threshold, whereas the Spitzer resistivity calculated at the location of the guiding centre is dependent on temperature, our choice of $\kappa = \eta_{sp}/\eta_a$ resulted in the scattering rate decreasing with temperature (this is a result of $\eta_{sp} \propto T^{-3/2}$). The case $\kappa = \eta_{sp}/\eta_a$ had weaker scattering in the separatrices due to the lower temperature (in comparison to the temperature inside the central current sheet) when compared to spatially constant values of κ. Less scattering in the separatrices resulted in fewer orbits re-entering the current sheet multiple times. Thus the main effect we saw from higher scattering rates was the extension of the energy spectra to higher energies and slight hardening (i.e. shallower slope). In addition, higher scattering caused more particles exiting for y near zero, and longer overall orbit durations.

In our model, the temperatures calculated in the MHD simulations has a significant effect on particle dynamics and energy spectra. In our MHD simulations the temperatures achieved are somewhat unrealistic, with a maximum temperature of 4.2×10^9 K. This is a result of a lack of thermal conduction and radiation used in our simulations, leading to the small values of $\eta_{sp}/\eta_a \approx 10^{-8}$ in the current sheet. This could be remedied, for example, by including thermal conduction and radiation in future MHD simulations. However, Bian et al. [2016] showed that

thermal conduction can be significantly reduced in coronal loops due to pitch angle scattering resulting from turbulence within the loops, leading to temperatures of the order of $10^8\,\mathrm{K}$. The reduced thermal conductivity means it is reasonable that there is a large difference in temperature between the current sheet and the separatrices, which leads to correspondingly large differences in the scattering rates and associated particle dynamics.

The energies we obtain in our simulations are relatively small compared to previous work on particle acceleration in 2D reconnection [e.g. Gordovskyy et al., 2010a, achieve energies of the order $1\,\mathrm{MeV}$ compared to our approximately $100\,\mathrm{keV}$]. This is due to our use of relatively small lengthscales resulting in small electric field strengths and a small reconnection region. For a given particle, the energy gain depends entirely on the work done by the electric field on the particle, which is itself dependent only on the trajectory of the particle (although it is possible that energy losses may occur in scattering processes, for example in Coulomb collisions). Scattering introduces an additional lengthscale, the mean free path, so it is no longer possible to scale the energy spectra obtained using one set of normalising parameters to adapt the results to other normalising scales. In our model of pitch angle scattering changes in the energy spectra are purely due to the different trajectories that particles take and the work that the electric field does on the particles throughout the course of their trajectories.

Possible extensions to the scattering model, such as the inclusion of energy loss terms, can be easily accommodated by adding stochastic terms to the energy evolution equation (Equation 2.34), or by specifying other models for the scattering rate. In particular, adding in energy loss terms may lead to an optimal value of the resistivity for the acceleration of charged particles. More complicated magnetic field topologies are also likely to impact the results obtained in this chapter with regards to particle trajectories and possibly energy spectra. It would be worth investigating how test particle acceleration is modified by pitch angle scattering in coronal structures such as in flux tubes [see e.g. Gordovskyy et al., 2014, Threlfall et al., 2018], however for the purposes of this thesis we move on instead to considering the effects of pitch angle scattering in 3D separator reconnection.

Chapter 5

Particle acceleration and scattering in 3D MHD simulations of separator reconnection

The natural extension of our work in 2D is to examine particle scattering in 3D models of reconnection. Previously particle acceleration has been examined in multiple 3D configurations which involve magnetic reconnection, for example the context of null points [e.g. Dalla and Browning, 2005, 2006, 2008, Browning et al., 2010, Stanier et al., 2012], reconnecting flux tubes [e.g. Gordovskyy et al., 2013, 2014, Threlfall et al., 2018], and in separator reconnection [Threlfall et al., 2015, 2016b]. In line with our strategy in Chapter 4, we repeat the 3D MHD simulations of separator reconnection, as performed in Stevenson and Parnell [2015a], and compute test particle trajectories and energy spectra in the resulting fields, again adding in test particle pitch angle scattering.

In addition to investigating a new geometry in which particle acceleration occurs, further motivation for performing these particle simulations comes from the fact that in this reconnection model different reconnection rates (and hence different parallel electric fields) can be obtained for different values of the resistivity [these MHD simulations are discussed in great detail in Stevenson and Parnell, 2015a,b]. In contrast, in 2D reconnection the reconnection rate is independent of the applied resistivity [Cargill et al., 2012], which prevented us from investigating the relationship between acceleration and scattering for different values of resistivity in Chapter 4. In Chapter 3 we were able to show that different resistivities did indeed have an effect on particle dynamics, however the 1D results did not include any geometrical effects, which we found to be important in the energisation of particles in the 2D case. As a result these 3D simulations combine multiple aspects of the investigations performed in the previous chapters to further examine the

relationship between acceleration and scattering caused by resistivity.

5.1 MHD setup

To obtain the background fields for our particle simulation we use the technique (and some of the data) from Stevenson and Parnell [2015a]. This means that the resulting fields from a numerical equilibrium [see Stevenson et al., 2015] containing a magnetic separator are induced to reconnect by specifying a non-zero constant resistivity wherever the current exceeds a specified threshold. The resulting fields consist of a separator connecting two nulls located at $x = y = 0, z = 0, 3$ (in normalised units) with the normalising scales taken to be $L_0 = 100\,\mathrm{m}$, $B_0 = 0.12\,\mathrm{T}$ and $\rho_0 = 1.67 \times 10^{-7}\,\mathrm{kg \cdot m^{-3}}$. Since heat conduction and radiation are not used in these simulations an elevated density is used to ensure realistic temperatures during reconnection, which is necessary so that the calculation of the Spitzer resistivity is representative of the value in the solar corona. In our case we use a critical current $j_{max} = 7.5$ and resistivity of $10^{-3}, 10^{-4}, 10^{-5}$ all in normalised units. To ensure that the highest parallel electric field is used the first output snapshot of the simulation is taken into which particles are injected. The resulting field structure, including the locations of the nulls is shown in Figure 5.1a

5.2 Particle Simulations

As before, we inject test particles into the simulation, with scattering occuring in regions of non-zero resistivity. The trajectories are integrated until the test particle exits the computational box, which is $x, y \in [-25, 25]\,\mathrm{m}, z \in [-100, 400]\,\mathrm{m}$, or the simulation time exceeds $10^4\,\mathrm{s}$.

One difference to previous calculations is that the scattering rate, in some cases, is calculated slightly differently. As before, we solve the SDE for the evolution of the pitch angle (Equation 2.32) with the mean free path given by $\nu = \frac{v_{tot}}{\lambda}$. We consider two cases. Firstly, $\lambda = \lambda_0 \kappa$ (note, in contrast to Equation 4.5 we do not consider any velocity dependence as it was found to have negligible effect in Chapter 4), with $\lambda_0 = 2 \times 10^8\,\mathrm{m}$ (corresponding to the collisional mean free path of an electron at coronal density ($10^{15}\,\mathrm{kgm^{-3}}$) and temperature $5 \times 10^7\,\mathrm{K}$), which is the same as in previous chapters. We also perform simulations where $\nu = \nu_{ei}\rho'/\kappa$, with $\nu_{ei} = 2.91 \times 10^{-6} n \log \Lambda T^{-3/2}\,\mathrm{s^{-1}}$, using *cgs* units, with temperature in eV [Huba et al., 1998], $\rho' = 10^{-3}, 10^{-5}$ to adjust density to something closer to coronal conditions, and $\kappa = \eta_{sp}/\eta_a$. This was done to accurately define the scattering rate

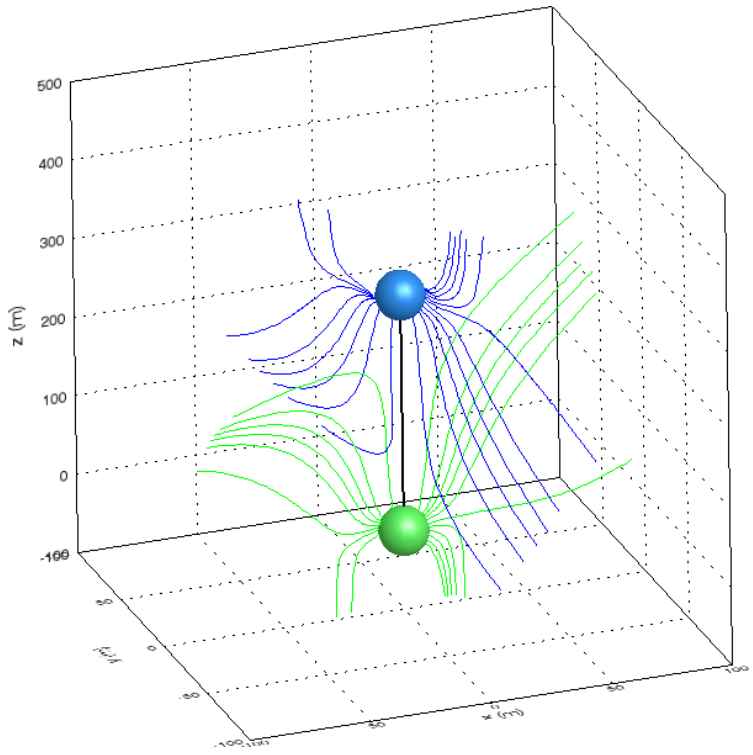

(A) 3D separator and field lines

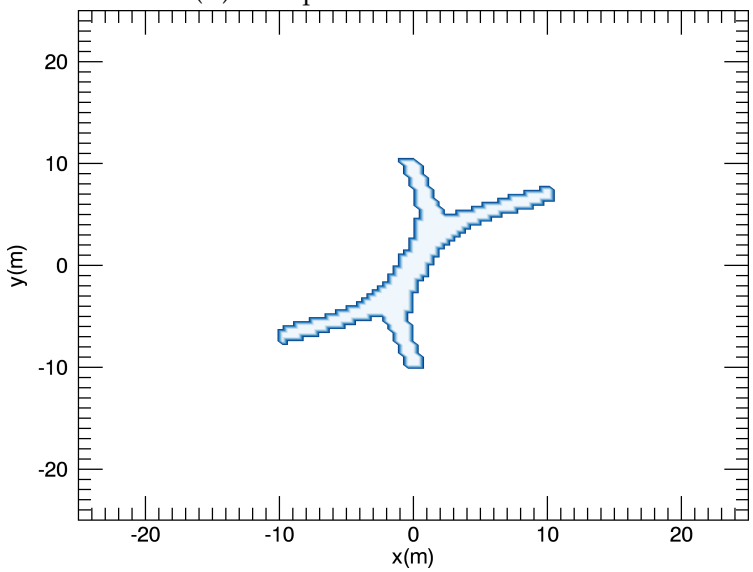

(B) Contour of non-zero resistivity

FIGURE 5.1: Separator magnetic field lines 3D structure (panel A) and non-zero resistivity contour in 2D slice parallel to the xy-plane halfway up the separator (panel B). Magnetic null points are represented by coloured spheres in panel A, with field lines coloured correspondingly to the null which they are connected to. Separator coloured black.

at the location of the test particle. In previous simulations ν_{ei} was calculated from $\lambda_0 = 2 \times 10^8\,\mathrm{m}$, and was taken to be constant throughout the simulation domain. This approach gives a more accurate reflection of the scattering rate at the location of the test particle. Throughout we will refer to the scattering rates as specified by κ, and ρ' if necessary.

5.2.1 Single particle results

As before, we first examine the orbits of individual particles to get an idea for the effect of pitch angle scattering on orbit trajectories, energy gain and pitch angle evolution. To do so we initialise individual test particles with energy 320 eV, an initial pitch angle of 90° and positions given by $y_0 = 0\,\mathrm{m}$, $z_0 = 150\,\mathrm{m}$ and $x_0 = 0.01, 0.1, 1\,\mathrm{m}$ in the simulation with $\eta_a = 10^{-3}$. The results of the calculations are shown in Figure 5.2. In the absence of scattering the particles are accelerated down along the separator and exit the computational box approximately along a field line (see Figure 5.2a). On the other hand, the presence of scattering causes the particle orbit which is started nearest to the separator (at $x = 0.01\,\mathrm{m}$, in black) to have a significantly perturbed orbit (see Figure 5.2b). Orbits initialised further from the separator experience significantly less scattering. We can also see this from the energy and pitch angle evolution (Figures 5.2c-5.2f). In Figures 5.2c and 5.2e we see that the particle initialised at $x_0 = 0.01\,\mathrm{m}$ experiences large jumps in energy as well as pitch angle throughout its evolution in the presence of pitch angle scattering (red line) when compared to the simulation of the same particle orbit without scattering. Although in this particular instance the scattered particle orbit does not obtain a final energy higher than what is possible without scattering, in other orbits it occurs (see Figures 5.4b,5.4d,5.4f). In Figures 5.2d and 5.2f we also see differences to the energy and pitch angle evolution of the orbit initialised at $x_0 = 0.1\,\mathrm{m}$, the changes are much less dramatic and the resulting orbit trajectories (see red lines in Figures 5.2a and 5.2b) hardly change and the energy gains are similar. We do not show here the trajectories obtained in the simulations with lower resistivity, however we do note that the maximum electric field strengths encountered by particles are approximately 1300 $\mathrm{V/m}$, 150 $\mathrm{V/m}$ and $15\,\mathrm{V/m}$ for $\eta_a = 10^{-3}, 10^{-4}$ and 10^{-5} respectively, allowing us to examine the relationship between particle acceleration and pitch angle scattering for different values of resistivity.

Just as in Chapter 4, we run 100 particles, overplot their trajectories and energy evolution to give a better idea of how particles tend to behave. In Figure 5.3 we plot 3D orbit trajectories, as well as projections of the trajectories onto the xy-plane. We note that the scattered trajectories only differ significantly once they are near the

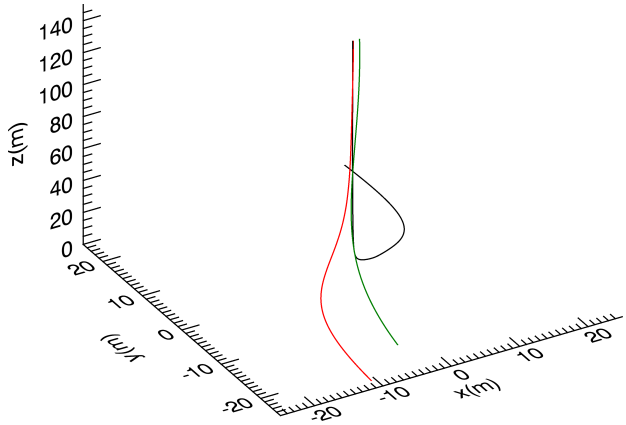

(A) Orbit trajectories without scattering

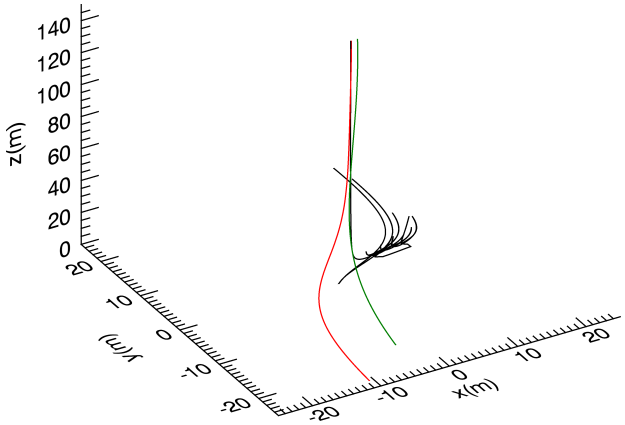

(B) Orbit trajectories with scattering ($\kappa = \eta_{sp}/\eta_a$)

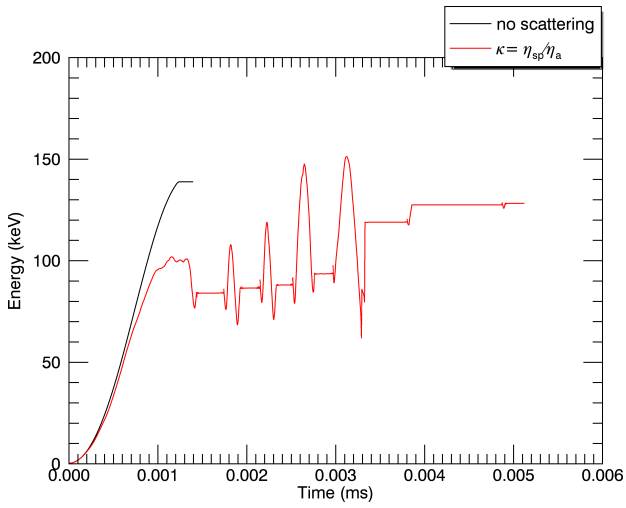

(C) Orbit energy evolution for $x_0 = 0.01\,\mathrm{m}$

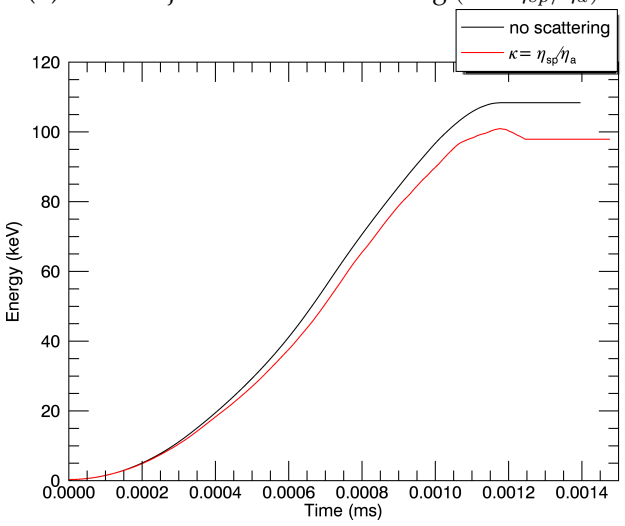

(D) Orbit energy evolution $x_0 = 0.1\,\mathrm{m}$

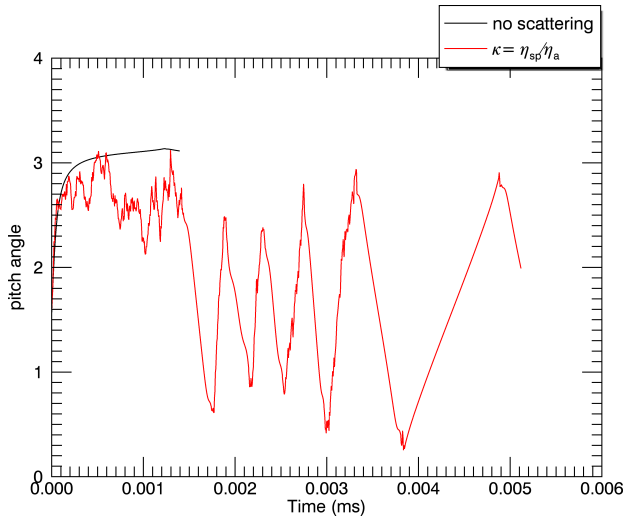

(E) Orbit pitch angle evolution $x_0 = 0.01\,\mathrm{m}$

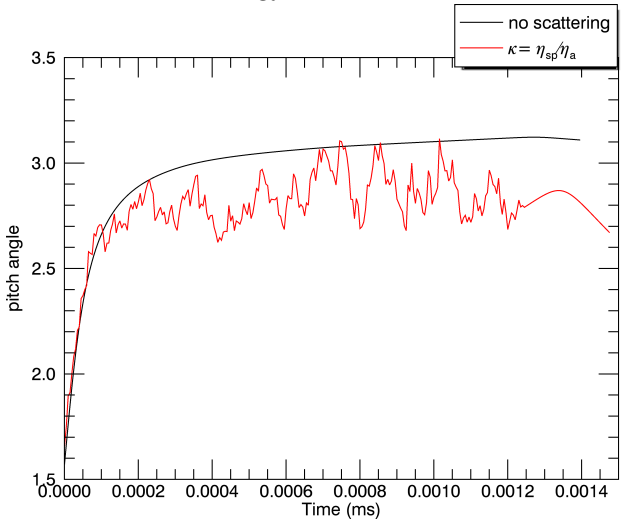

(F) Orbit pitch angle evolution $x_0 = 0.1\,\mathrm{m}$

FIGURE 5.2: Orbit trajectories (panels A and B, colours simply used for distinguishing different orbits) for three particles initialised halfway up the separator, for $x_0 = 0.01, 0.1, 1\,\mathrm{m}$, $y = 0\,\mathrm{m}$, and pitch angle $90°$, both with and without scattering. Panels C to F compare the energy and pitch angle evolution for particle orbits with $x_0 = 0.01, 0.1\,\mathrm{m}$ (corresponding to black and red lines in panels A and B).

xy-plane (this is seen in Figure 5.2 where particle trajectories generally all lie along the separator until reaching the xy-plane); along the separator they all follow the same path. For the higher resistivity simulations ($\eta_a = 10^{-4}, 10^{-3}$, Figures 5.3c,5.3e) it is just possible to tell that not all the orbits exit the computational domain with $z \approx 0$. By looking at the projections of the orbits on the xy-plane (Figures 5.3b, 5.3d, and 5.3f) we see that higher resistivity results in more scattering because the orbit tracks are more spread out in this plane, as expected.

The time evolution of z and the energy evolution of the same 100 particles are shown in Figure 5.4. With progressively higher resistivity the number of times that a particle gets scattered up the separator increases, as does the distance that particles are scattered upward by. It appears that the majority of scattering occurs in the xy-plane, as particles follow parabolic trajectories in z when they are scattered upwards, indicating a constant electric field accelerating them downward, without significant scattering. In general it is seen that particles also gain more energy than they would do in the absence of scattering for all levels of resistivity (energy evolution of unscattered orbits with the same initial conditions as the scattered ones are shown by the black lines in second column, note also the energy range changes to accomodate for different parallel electric fields). It is interesting to note that the energy evolution of many orbits in Figure 5.4f seems to have a small dip at approximately $1\,\mu\mathrm{s}$, which could be due to particles being scattered up the separator before they have reached the xy-plane for the first time, thus slowing the rate at which energy is gained.

5.2.2 Particle energy spectra and distributions

As usual, we are interested in the effect of scattering on test particle energy spectra and distributions of pitch angle and orbit duration. We first integrate the orbits of 10^4 particles with initial positions uniformly distributed in $x, y \in [-10, 10]\,\mathrm{m}$ and $z \in [100, 200]\,\mathrm{m}$, corresponding to a box encompassing the central part of the separator (recall that the null points are at $z = 0, 300\,\mathrm{m}$). The pitch angle takes on 100 values between 10° and 170°, and the initial energy 25 values between $10\,\mathrm{eV}$ and $320\,\mathrm{eV}$. The particle orbits are weighted when producing the spectra so that the initial energy distribution is Maxwellian and the initial cosine of pitch angle distribution is uniform. We perform these particle calculations in the MHD fields from the $\eta_a = 10^{-3}$ simulation. The resulting spectra and pitch angle and orbit duration distributions are shown in Figures 5.5a-5.5c. In contrast to the results of Chapter 4, the energy spectra for particle orbits both with and without scattering are almost identical (see Figure 5.5a). The orbit durations are also very nearly

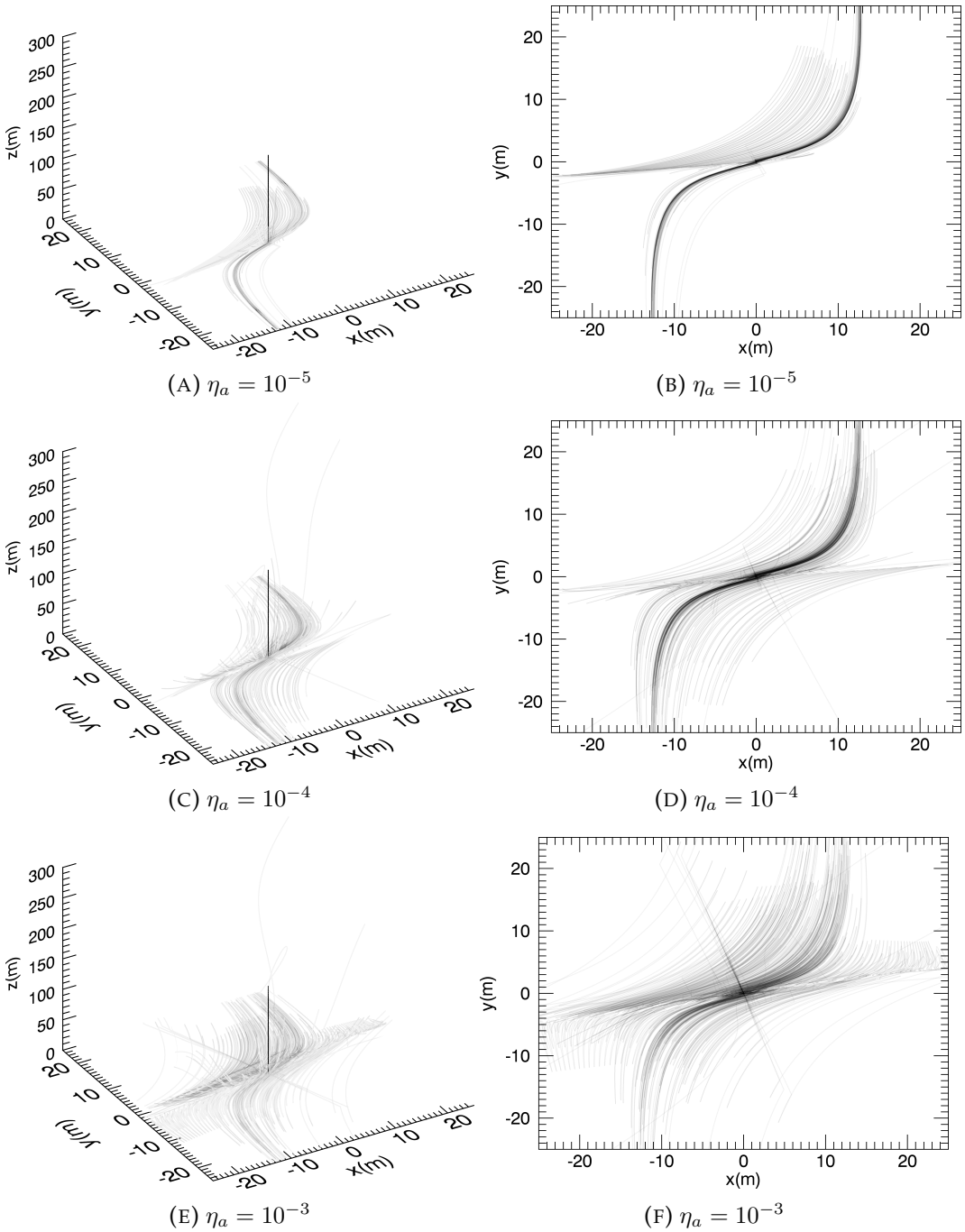

(A) $\eta_a = 10^{-5}$ (B) $\eta_a = 10^{-5}$

(C) $\eta_a = 10^{-4}$ (D) $\eta_a = 10^{-4}$

(E) $\eta_a = 10^{-3}$ (F) $\eta_a = 10^{-3}$

FIGURE 5.3: Particle orbit trajectories for 100 particles initialised half-way up the separator with pitch angle $90°$, kinetic energy $320\,\mathrm{eV}$, and $x, y = 0\,\mathrm{m}$ for three MHD simulations with different non-dimensional resistivities $\eta_a = 10^{-5}, 10^{-4}, 10^{-3}$. Trajectories are presented both in 3D (panels A,C,E) and their projections onto the xy-plane (panels B,D,F).

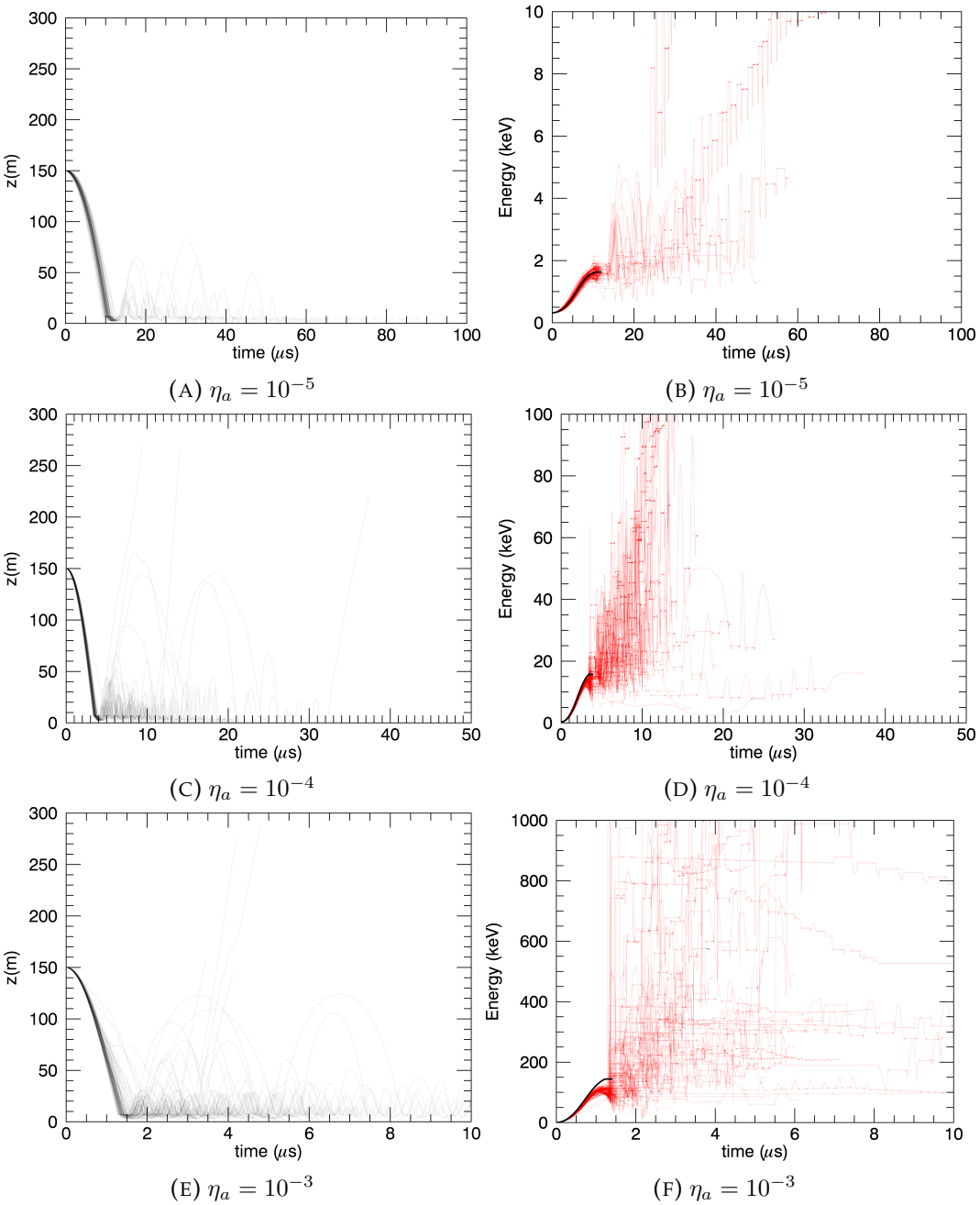

(A) $\eta_a = 10^{-5}$ (B) $\eta_a = 10^{-5}$

(C) $\eta_a = 10^{-4}$ (D) $\eta_a = 10^{-4}$

(E) $\eta_a = 10^{-3}$ (F) $\eta_a = 10^{-3}$

FIGURE 5.4: Particle z-coordinate and energy evolution for the same particle orbits computed in Figure 5.3.

Initial conditions used in simulation	5 – 30 keV	30 – 100 keV	100 – 200 keV	200 – 300 keV	> 300 keV	maximum energy (keV)
IC: $x, y \in [-10, 10]$ m, $z \in [100, 200]$ m, no scattering	9.1	2.9	2.4	0	0	157
IC: $x, y \in [-10, 10]$ m, $z \in [100, 200]$ m, $\kappa = 10{-}8$	10.5	2.7	1.4	0	5×10^{-3}	507
IC: $x, y \in [-10, 10]$ m, $z \in [100, 200]$ m, $\kappa = \eta_{sp}/\eta_a$	10.3	3.1	1.2	0.02	0	270
IC: $x, y \in [-1, 1]$ m, $z \in [100, 200]$ m, no scattering	34.6	34.2	9.4	0	0	180
IC: $x, y \in [-1, 1]$ m, $z \in [100, 200]$ m, $\kappa = 10{-}8$	36.7	38.9	3.9	0	0.06	2414
IC: $x, y \in [-1, 1]$ m, $z \in [100, 200]$ m, $\kappa = \eta_{sp}/\eta_a$	36.3	38.0	3.5	0	0.09	3693
IC: $x, y \in [-1, 1]$ m, $z \in [1, 299]$ m, no scattering	28.7	34.3	5.8	6.3	0	258
IC: $x, y \in [-1, 1]$ m, $z \in [1, 299]$ m, $\kappa = 10{-}8$	27.7	34.4	5.6	1.1	0.09	3113
IC: $x, y \in [-1, 1]$ m, $z \in [1, 299]$ m, $\kappa = \eta_{sp}/\eta_a$	27.8	33.5	5.5	1.7	0.4	3809
IC: $x, y \in [-1, 1]$ m, $z \in [1, 100]$ m, no scattering	34.5	4.7	0	0	0	67
IC: $x, y \in [-1, 1]$ m, $z \in [1, 100]$ m, $\kappa = 10{-}8$	34.5	3.5	0.1	0.03	0.01	675
IC: $x, y \in [-1, 1]$ m, $z \in [1, 100]$ m, $\kappa = \eta_{sp}/\eta_a$	34.1	2.5	0.1	0.089	0.21	2973
IC: $x, y \in [-1, 1]$ m, $z \in [200, 299]$ m, no scattering	19.9	58.0	9.8	3.0	0	263
IC: $x, y \in [-1, 1]$ m, $z \in [200, 299]$ m, $\kappa = 10{-}8$	19.8	59.4	11.1	3.3	0.22	2751
IC: $x, y \in [-1, 1]$ m, $z \in [200, 299]$ m, $\kappa = \eta_{sp}/\eta_a$	19.8	59.8	11.1	0.5	0.35	4122
IC: $x, y \in [-2.5, 2.5]$ m, $z \in [1, 299]$ m, no scattering	21.6	14.2	2.2	0.35	0	267
IC: $x, y \in [-2.5, 2.5]$ m, $z \in [1, 299]$ m, $\kappa = 10{-}8$	21.0	15.4	2.0	0.08	0.02	2344
IC: $x, y \in [-2.5, 2.5]$ m, $z \in [1, 299]$ m, $\kappa = \eta_{sp}/\eta_a$	20.7	15.3	2.0	0.15	0.12	3909

TABLE 5.1: Percentage of particle orbits in each energy band for different particle orbit simulations. All particle simulations run in fields from MHD simulation with $\eta_a = 10^{-3}$.

identical (Figure 5.5c), however the pitch angle distribution shows fewer particles with pitch angles $\theta > 3$ (note that all angles given in this chapter are in radians, unless otherwise specified), with 20% of the non-scattered particles achieving these pitch angles, compared to about 2% in each of the scattering cases. On the other hand 63% of all particle orbits (regardless of scattering rate, or in the absence of scattering) have final pitch angles $\theta > 2$, so scattering ensures approximately a 50% increase (from 43% of total to 61%) of particle orbits in the range $2 \leq \theta \leq 3$ from no scattering. It is still somewhat surprising to see no change in the energy spectra, so we consider particle orbits with initial conditions starting closer to the separator.

In Figures 5.6a-5.6c we use $x, y \in [-1, 1]\,\mathrm{m}$. As opposed to the first set of initial conditions, all particles with these initial positions start within the reconnection region. Here we start to see small differences in the energy spectra. From the energy spectra shown in Figure 5.6a, the portion of particles achieving energy more than $100\,\mathrm{keV}$ is 9% in the absence of scattering, and only about 4% for each of the scattering cases. However, if we examine the portion of particles obtaining energies more than $200\,\mathrm{keV}$, the proportion is 0.01% in the absence of scattering, 0.05% with scattering at a constant $\kappa = 10^{-8}$ and 0.1% with $\kappa = \eta_{sp}/\eta_a$. Considering the pitch angle distribution it is easy to see the large differences between the scattered and unscattered simulations. Whereas without scattering almost all (99.95%) of particles have final pitch angle $\theta > 2.5$, only 75% do for scattering with $\kappa = 10^{-8}$ and 72% for scattering with $\kappa = \eta_{sp}/\eta_a$. This clearly indicates scattering having a strong effect on at least the final pitch angle distribution, if not the energy spectra. Finally, the orbit duration distribution shows smaller differences, but still noticeable, with only 3.5% of particles having an orbit duration greater than $0.01\,\mathrm{ms}$ in the absence of scattering, comparing to 4.9% with $\kappa = 10^{-8}$ and 9.2% for $\kappa = \eta_{sp}/\eta_a$.

On the other hand, when also extending the range of the initial positions in the z direction so that $x, y \in [-1, 1]\,\mathrm{m}$ and $z \in [1, 299]\,\mathrm{m}$ (Figures 5.7a-5.7c), a larger difference in the energy spectra is observed, with the portion of particles achieving energy more than $100\,\mathrm{keV}$ being approximately 6% in all cases. This is due to some particles travelling further along the separator, having resulting in more energy gain from the electric field. However, the portion of particles obtaining energies more than $200\,\mathrm{keV}$ is 0.6% in the absence of scattering, 0.2% with scattering at a constant $\kappa = 10^{-8}$ and again 0.6% with $\kappa = \eta_{sp}/\eta_a$. If we further look at particles gaining energies more than $300\,\mathrm{keV}$, it is 0.03% in the absence of scattering, 0.09% for $\kappa = 10^{-8}$ and 0.4% for $\kappa = \eta_{sp}/\eta_a$. This suggests that scattering plays an important role in the energisation of a few particles to very

high energies. Considering the pitch angle distribution, the differences between the scattered and unscattered simulations is slightly smaller than in Figures 5.6a-5.6c. Without scattering most (93%) of the particles have final pitch angle $\theta > 2.5$, only 67% do for scattering with $\kappa = 10^{-8}$ and 58% for scattering with $\kappa = \eta_{sp}/\eta_a$. Finally, the orbit duration distribution shows small differences again, this time with 6% of particles having an orbit duration greater than $0.01\,\mathrm{ms}$ in the absence of scattering, comparing to 9% with $\kappa = 10^{-8}$ and 16% for $\kappa = \eta_{sp}/\eta_a$.

These results suggest that there are contributions to the final energy spectra by the orbits of particles initialised at the ends of the separator, near the null points. To investigate this we consider $x, y \in [-1, 1]\,\mathrm{m}$ and $z \in [1, 100]\,\mathrm{m}$. The results of these simulations are shown in Figures 5.8-5.10. Here we also run particles in fields from MHD simulations with different resistivities, as opposed to what has been presented so far, which only uses the results from the simulations with resistivity $\eta_a = 10^{-3}$ (in non-dimensional units). We note that for the simulation with $\eta_a = 10^{-3}$ (Figures 5.10a-5.10c) the maximum achieved energy is lower than if the initial conditions span a larger range of z values (see also Table 5.1, where the maximum energy of the unscattered particles in these simulations is only $67\,\mathrm{keV}$ compared to approximately $180\,\mathrm{keV}$ if the initial z range was $100\,\mathrm{m}$ to $200\,\mathrm{m}$). This is not surprising since we are running electrons, which get accelerated downward in this set of MHD fields, so particles starting higher up get accelerated more by the electric field. The shape of the energy spectra is also significantly different (comparing Figures 5.10a with 5.7a), with the spectrum for the larger range in z initial condition having a power law shape above approximately $30\,\mathrm{keV}$ (Figure 5.7a), whereas for a narrower range of z initial conditions the spectrum drops off rapidly (Figure 5.10a). It should be noted that the effect of scattering is qualitatively the same in both cases, leading to a small number of particle orbits achieving energies significantly higher than in the absence of scattering. With these initial conditions the pitch angles are also not as anti-aligned with the field as was the case for the wider initial z range, with 89.6% of the orbits having final pitch angle greater than 2.5 in the unscattered simulation, 68.4% if $\kappa = 10^{-8}$ and 48.1% for $\kappa = \eta_{sp}/\eta_a$. This is to be expected since the electric field has a greater distance over which it accelerates the particles. On the other hand, the orbit durations get slightly longer in general, with 8.8% of the particles exiting the box after $0.01\,\mathrm{ms}$ with out scattering, 11.8% with $\kappa = 10^{-8}$ and 24.1% with $\kappa = \eta_{sp}/\eta_a$.

In Figures 5.11-5.13 we plot the energy spectra, pitch angle and orbit duration distributions for particles initialised in $x, y \in [-1, 1]\,\mathrm{m}, z \in [200, 299]\,\mathrm{m}$ in the three MHD snapshots we have been using above. Qualitatively, the energy spectra differ

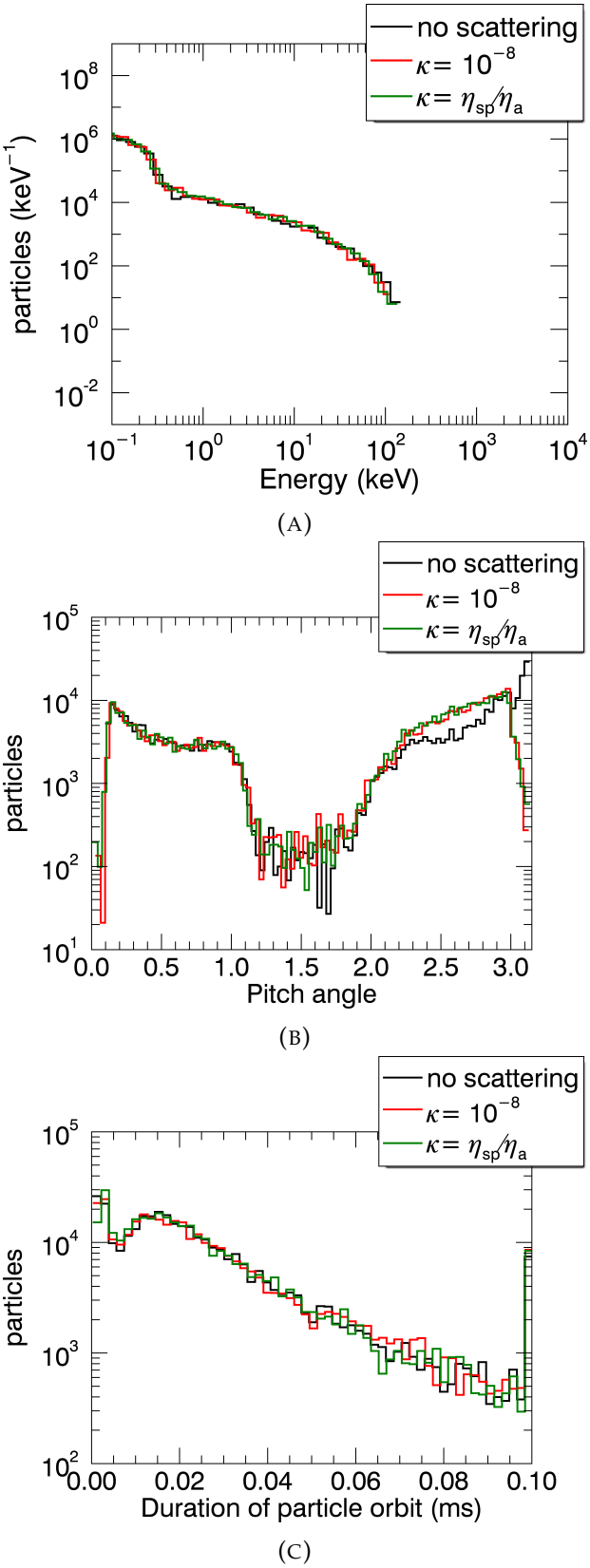

FIGURE 5.5: Particle energy spectra, pitch angle and orbit duration distributions for runs without scattering, with scattering at a rate $\kappa = 10^{-8}$, and $\kappa = \eta_{sp}/\eta_a$ in fields from MHD simulation with $\eta_a = 10^{-3}$. Particles are initialised with initial energies between $10\,\mathrm{eV}$ to $320\,\mathrm{eV}$, initial pitch angles are between $10°$ and $170°$. Particle initial positions $x, y \in [-10, 10]\,\mathrm{m}$, and $z \in [100, 200]\,\mathrm{m}$.

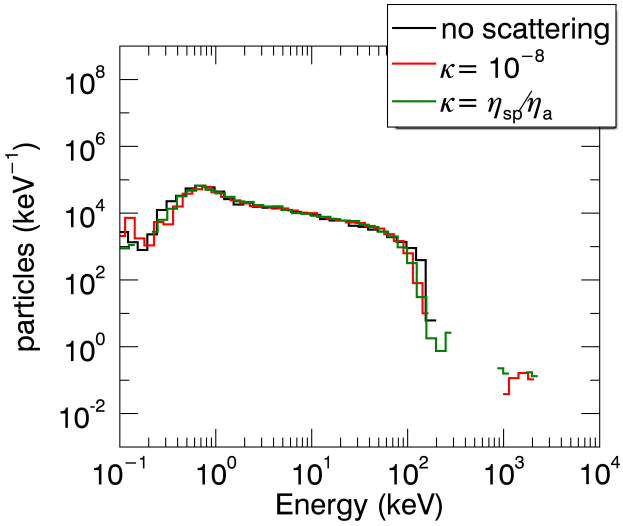

(A)

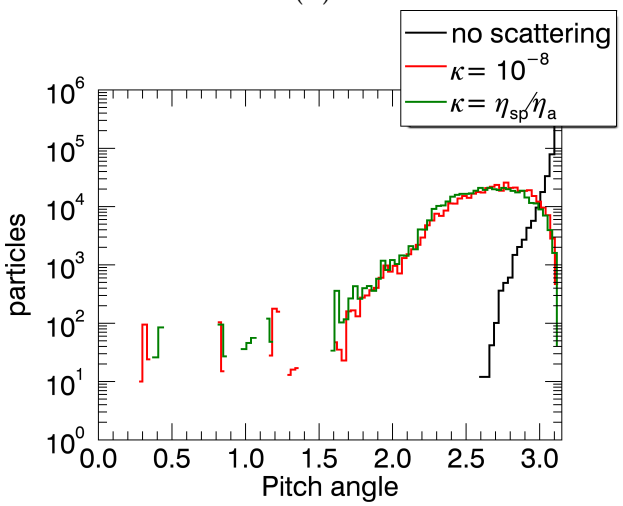

(B)

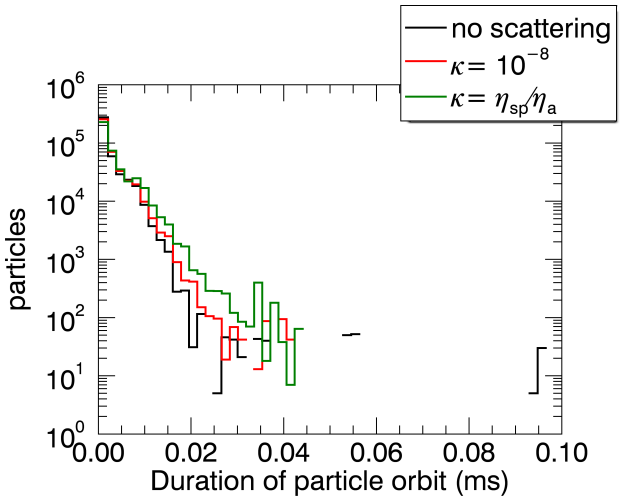

(C)

FIGURE 5.6: Particle energy spectra, pitch angle and orbit duration distributions for particle runs without scattering, with scattering at a rate $\kappa = 10^{-8}$, and $\kappa = \eta_{sp}/\eta_a$ in fields from MHD simulation with $\eta_a = 10^{-3}$. Particles are initialised with initial energies in the range 10 eV to 320 eV, initial pitch angles are between 10° and 170°. Particles have initial positions $x, y \in [-1, 1]$ m, and $z \in [100, 200]$ m.

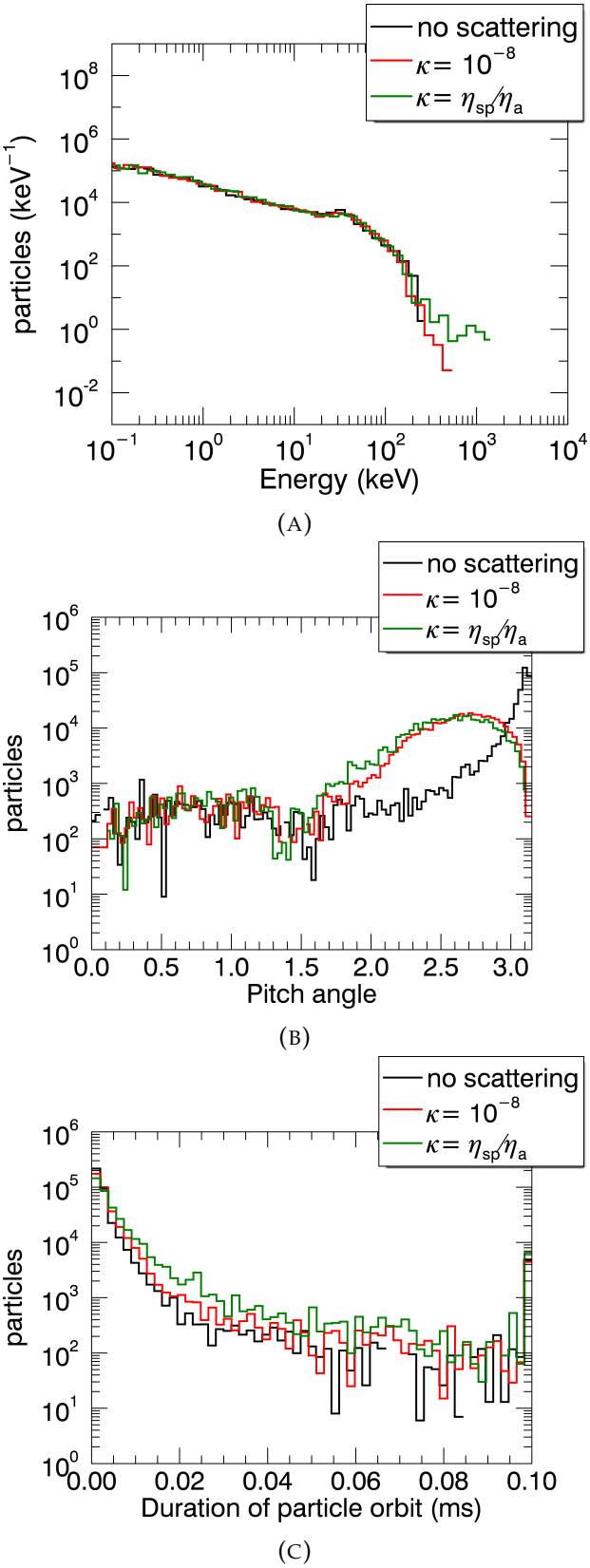

FIGURE 5.7: Particle energy spectra, pitch angle and orbit duration distributions for particle runs without scattering, with scattering at a rate $\kappa = 10^{-8}$, and $\kappa = \eta_{sp}/\eta_a$ in fields from MHD simulation with $\eta_a = 10^{-3}$. Particles are initialised with initial energies in the range $10\,\mathrm{eV}$ to $320\,\mathrm{eV}$, initial pitch angles are between $10°$ and $170°$. Particles have initial positions $x, y \in [-1, 1]\,\mathrm{m}$, and $z \in [1, 299]\,\mathrm{m}$.

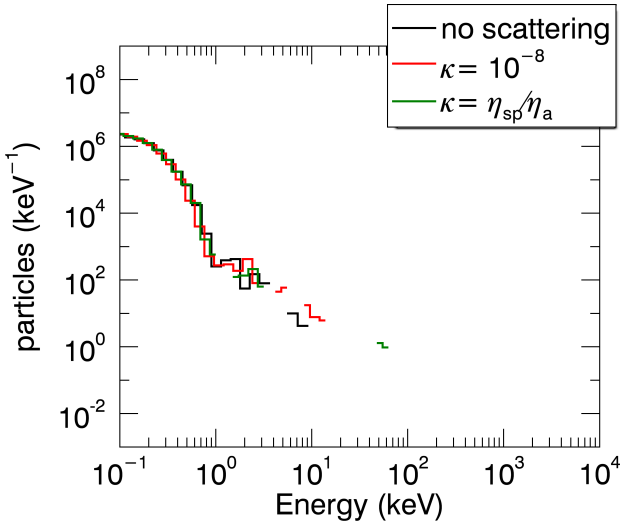

(A)

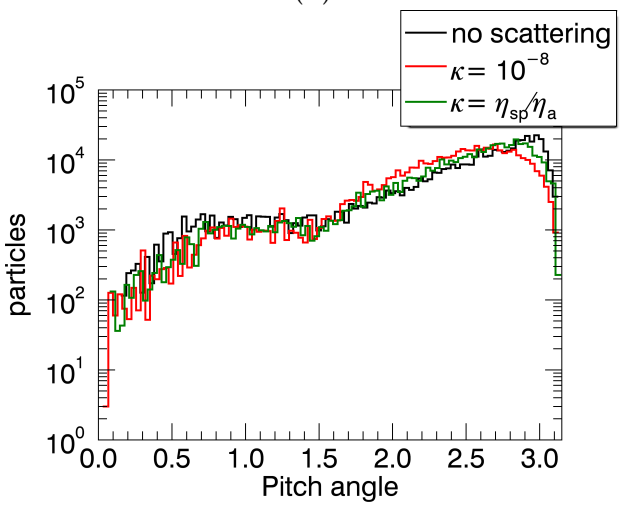

(B)

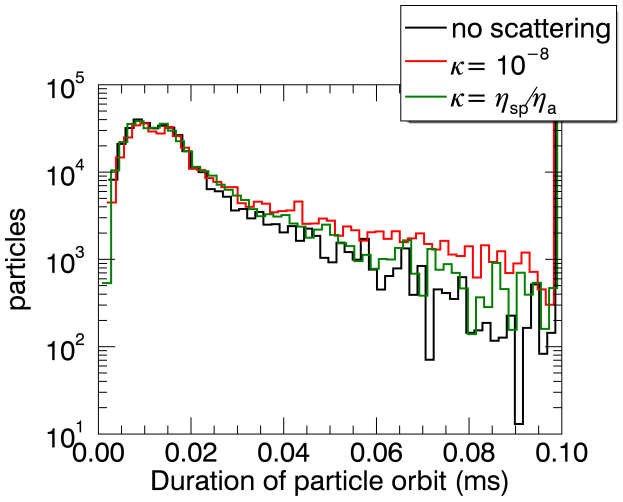

(C)

FIGURE 5.8: Energy spectra, pitch angle and orbit duration distributions for particles initialised in $x, y \in [-1, 1]\,\mathrm{m}, z \in [1, 100]\,\mathrm{m}$. Fields from $\eta_a = 10^{-5}$ simulation.

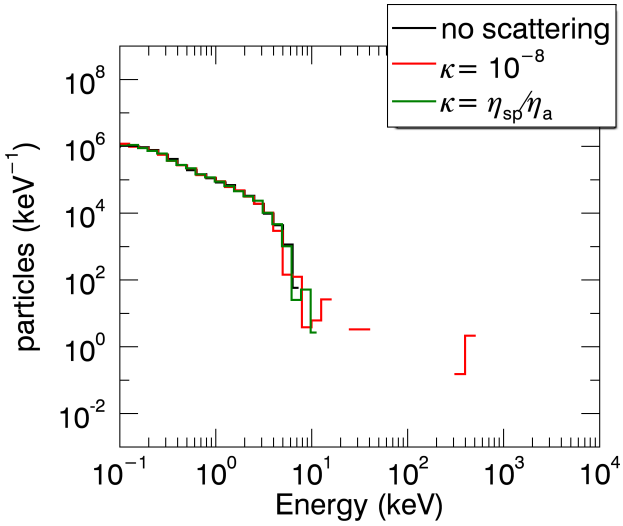

(A)

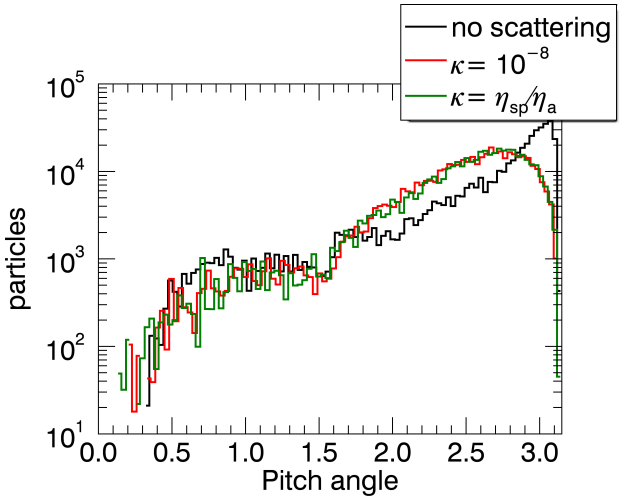

(B)

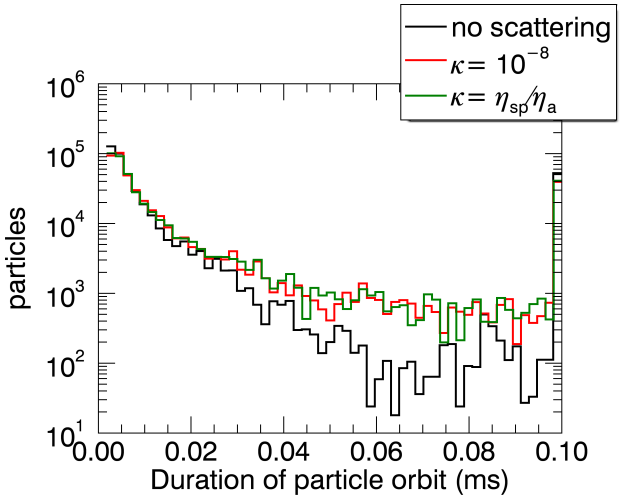

(C)

FIGURE 5.9: Energy spectra, pitch angle and orbit duration distributions for particles initialised in $x, y \in [-1, 1]\,\mathrm{m}, z \in [1, 100]\,\mathrm{m}$. Fields from $\eta_a = 10^{-4}$ simulation.

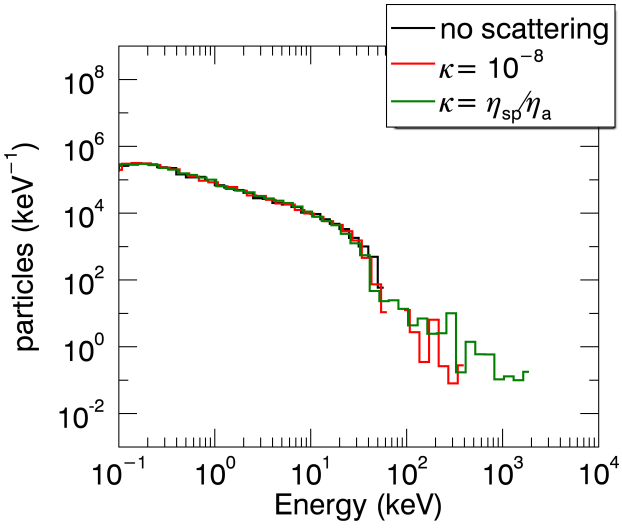

(A)

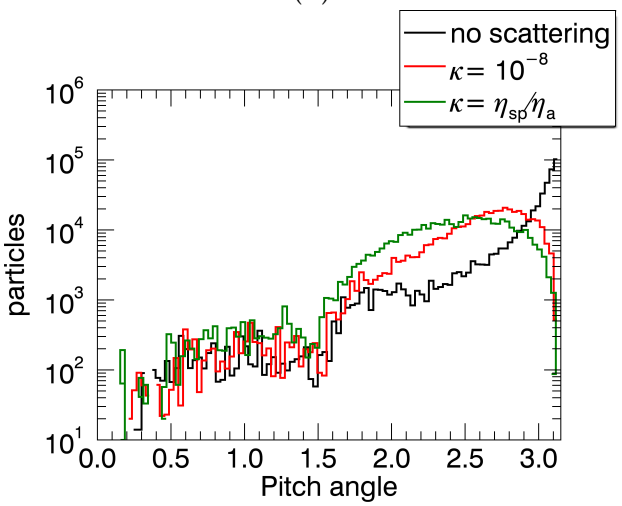

(B)

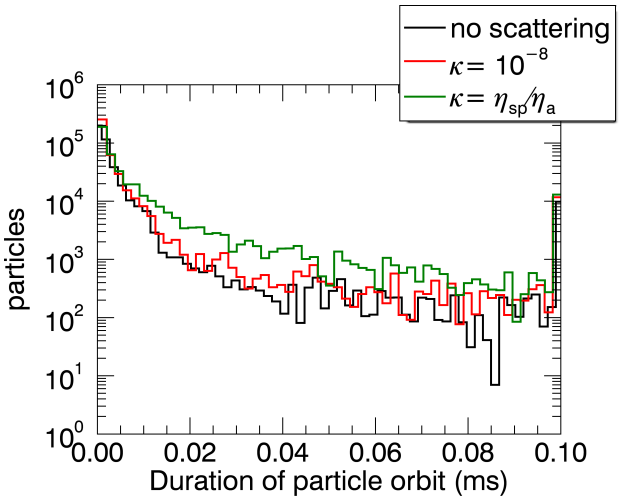

(C)

FIGURE 5.10: Energy spectra, pitch angle and orbit duration distributions for particles initialised in $x, y \in [-1, 1]\,\mathrm{m}, z \in [1, 100]\,\mathrm{m}$. Fields from $\eta_a = 10^{-3}$ simulation.

significantly from those in Figures 5.8 - 5.10, particularly in Figures 5.12a and 5.13a having peaks at approximately 4 and 40 keV respectively. From Table 5.1 it is clear that more particle orbits achieve higher energies, with approximately 60% reaching $30 - 100\,\mathrm{keV}$ compared to approximately 3% reaching these energies if the initial positions are lower along the separator. Furthermore, maximum energies achieved are higher, up to $4\,\mathrm{MeV}$ when $\kappa = \eta_{sp}/\eta_a$ compared to only about $2.7\,\mathrm{MeV}$ if the initial positions are lower along the separator for the same scattering rate. This difference is perhaps less than it should be considering the much wider range of maximum energies for unscattered orbits (again see Table 5.1, where the maximum energy of particles without scattering, starting at the top of the separator is about $260\,\mathrm{keV}$, and only $67\,\mathrm{keV}$ when starting at the bottom). This could be due to the scattering causing individual particle orbits to be scattered further up the separator and be accelerated more even though they start lower in the separator.

The pitch angle distributions also look somewhat different when comparing to starting particles low in the separator. In this case, 90.9% of particles have pitch angle $\theta > 2.5$ without scattering, 62.2% if $\kappa = 10^{-8}$ and 63.1% if $\kappa = \eta_{sp}/\eta_a$. These figures are reasonably similar to those obtained when starting particles low down along the separator, however the shape of the distribution, particularly below $\theta = \pi/2$ is very different. Indeed, this is reflected in the proportion of particles with final pitch angles less than $\pi/2$ being near 9% in the case when particles are initialised high up along the separator, compared to only $2 - 3\%$ if initialised low down. This is to be expected because negatively charged particles accelerated out of the bottom of the separator tend to pitch angles close to π, whereas negatively charged particles leaving the top of the box travelled generally along the electric field, thus reducing their pitch angle. Particles started at the top of the box, particularly in the presence of pitch angle scattering have a higher probability of exiting out of the top, compared to particles started at the bottom.

Finally, considering the orbit durations, we get slightly smaller proportions of particles exiting the box after $0.01\,\mathrm{ms}$, with 5.1% doing so without scattering, 8.7% with $\kappa = 10^{-8}$ and 11.9% with $\kappa = \eta_{sp}/\eta_a$.

We can also compare the effect of changing resistivity across one type of scattering model. In particular we are interested in examining the effect ofvarying the resistivity while scaling the scattering rate proportionally to this change, which is accomplished with the $\kappa = \eta_{sp}/\eta_a$ model. The results from the simulations are taken from Figures 5.11-5.13, however this time are plotted on one common set of axes in Figures 5.14-5.15. The most evident differences are found in the energy spectra (Figures 5.14a, 5.15a) where we see that increased resistivity

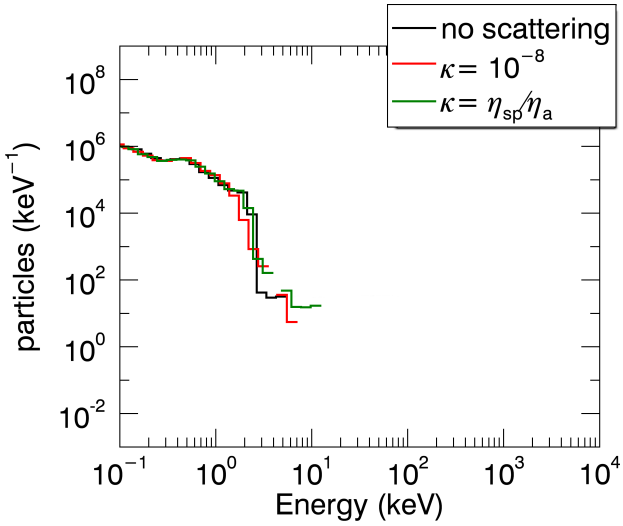

(A)

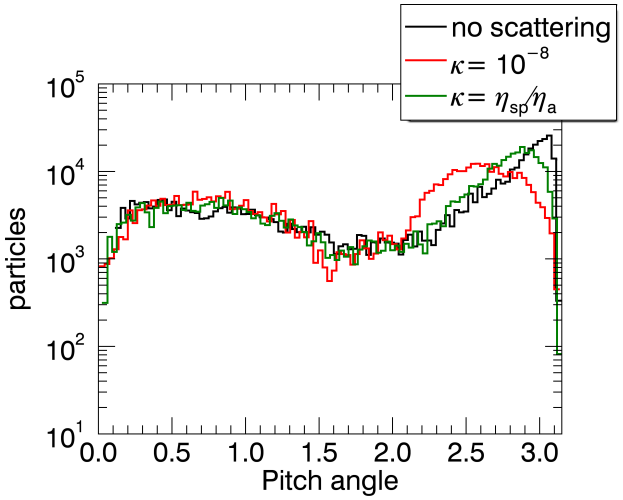

(B)

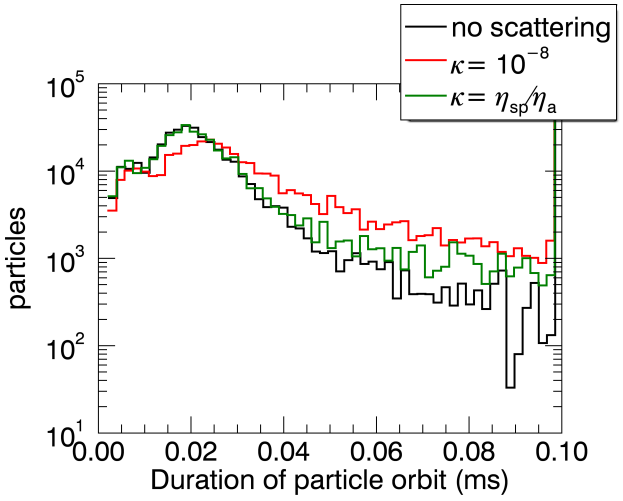

(C)

FIGURE 5.11: Energy spectra, pitch angle and orbit duration distributions for particles initialised in $x, y \in [-1, 1]\,\mathrm{m}, z \in [200, 299]\,\mathrm{m}$. MHD fields from $\eta_a = 10^{-5}$ simulation.

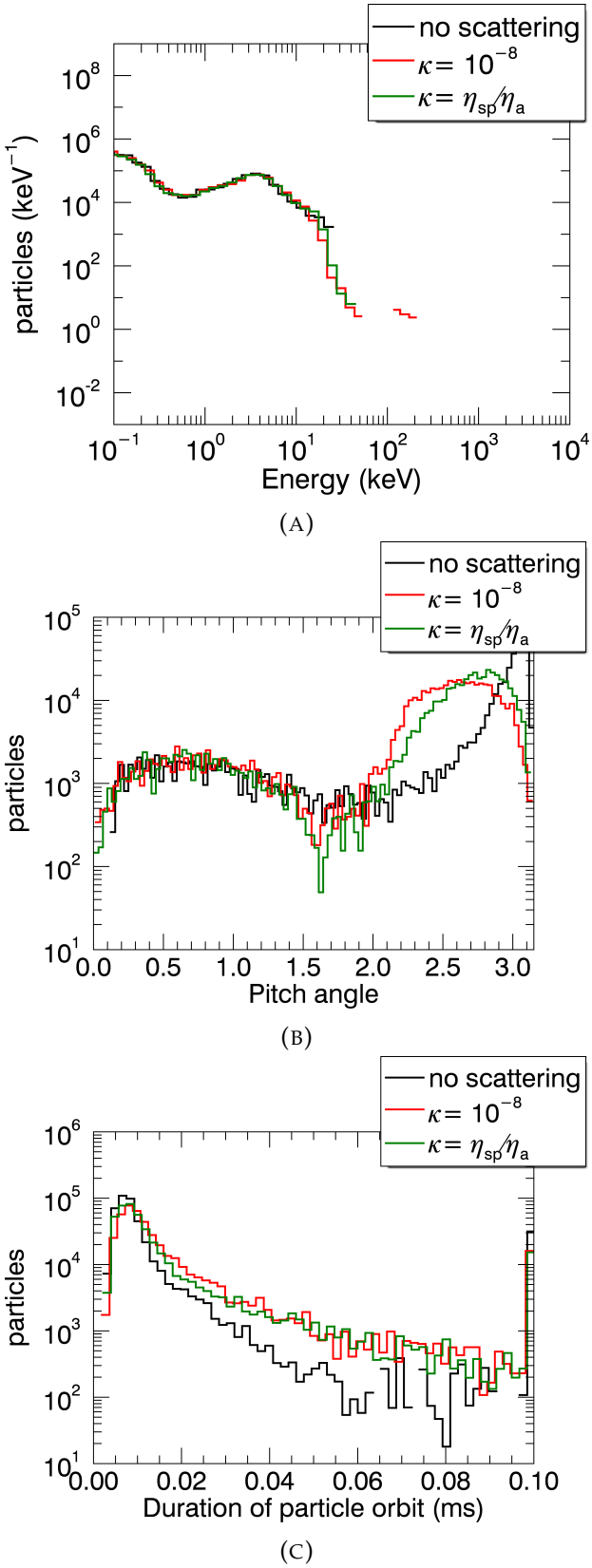

FIGURE 5.12: Energy spectra, pitch angle and orbit duration distributions for particles initialised in $x, y \in [-1, 1]\,\mathrm{m}, z \in [200, 299]\,\mathrm{m}$. MHD fields from $\eta_a = 10^{-4}$ simulation.

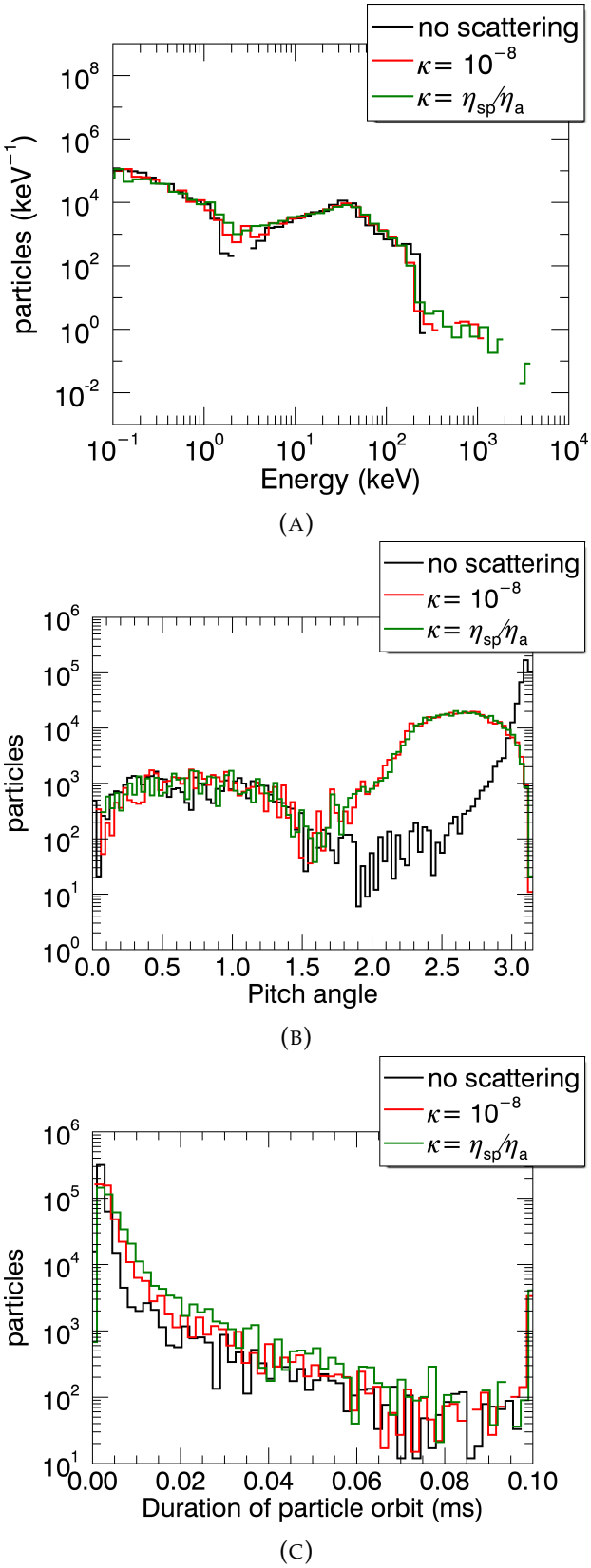

FIGURE 5.13: Energy spectra, pitch angle and orbit duration distributions for particles initialised in $x, y \in [-1, 1]\,\mathrm{m}, z \in [200, 299]\,\mathrm{m}$. MHD fields from $\eta_a = 10^{-3}$ simulation.

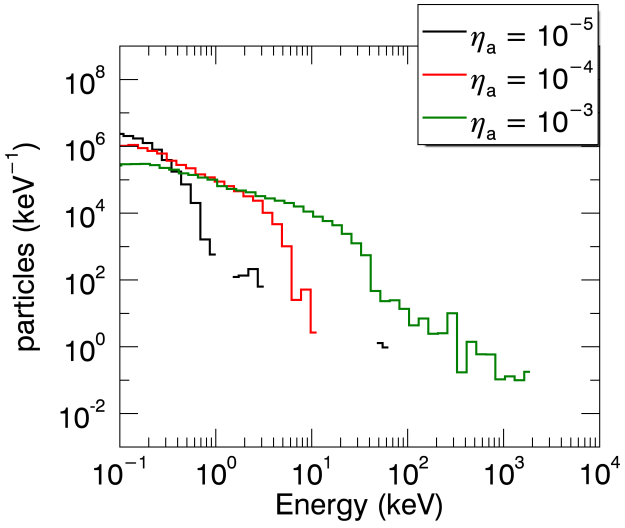

(A)

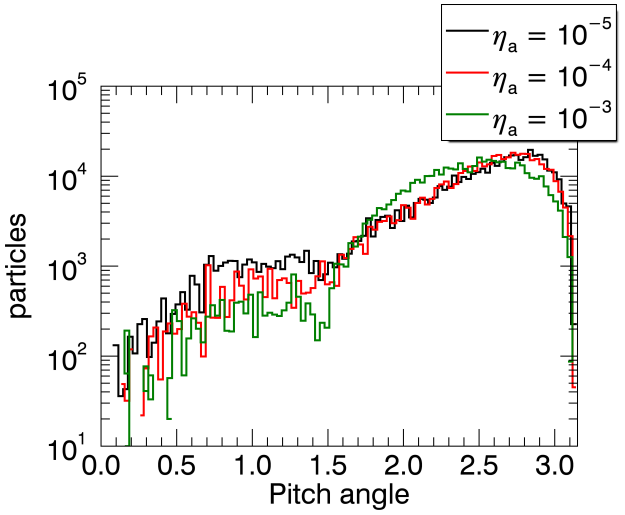

(B)

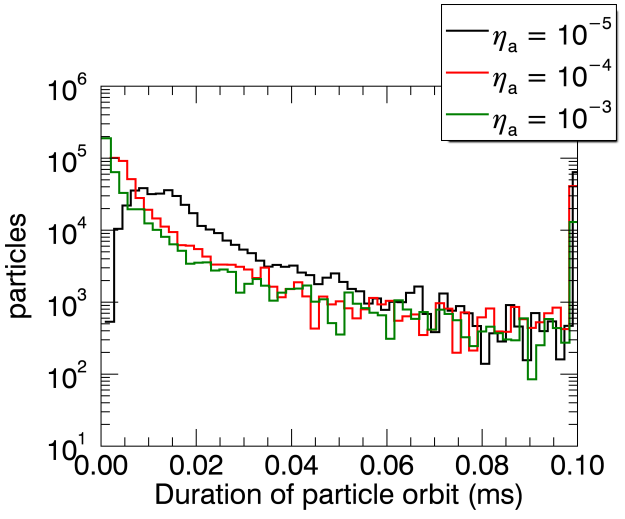

(C)

FIGURE 5.14: Energy spectra, pitch angle and orbit duration distributions for particles with scattering at a rate of $\kappa = \eta_{sp}/\eta_a$, in MHD simulations with resistivity $\eta_a = 10^{-5}, 10^{-4}, 10^{-3}$. Particles with initial positions $x, y \in [-1, 1]\,\mathrm{m}, z \in [1, 100]\,\mathrm{m}$.

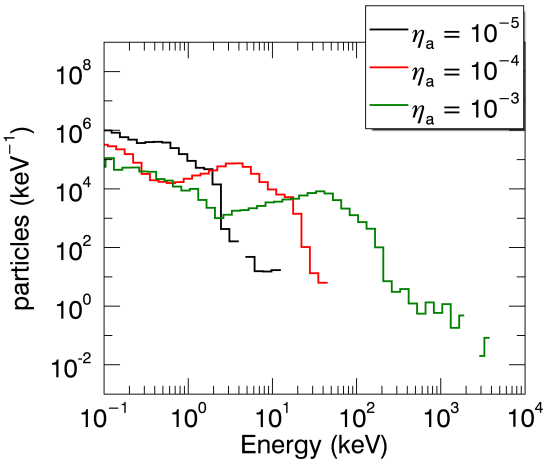

(A)

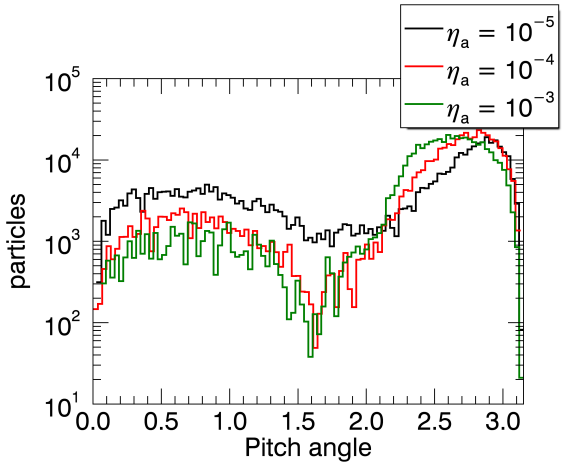

(B)

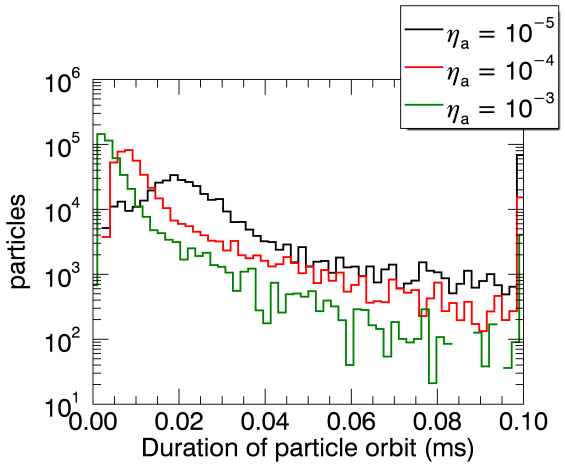

(C)

FIGURE 5.15: Energy spectra, pitch angle and orbit duration distributions for particles with scattering at a rate of $\kappa = \eta_{sp}/\eta_a$, in MHD simulations with resistivity $\eta_a = 10^{-5}, 10^{-4}, 10^{-3}$. Particles with initial positions $x, y \in [-1, 1]$ m, $z \in [200, 299]$ m.

results in greater energy gains. As demonstrated previously this is mainly due to the increased electric field strength and increased scattering is not able to make significant differences in the energy spectra. The pitch angle distributions, however, show the effects of increased scattering at higher resistivities, particularly in Figure 5.15b we see that increased resistivity results in the peak of the pitch angle distribution move to slightly lower values as a result of increased scattering. At the same time, however the distribution is lower for values $\theta < \pi$ as a result of the increased electric field strength. Finally, the orbit durations tend to get shorter with increased resistivity, reflecting some of the trend we saw in Chapter 3, however we do not see the multiple regimes that we saw in 1D. This is likely due to a more complex geometry and a narrower range of values of resistivity tested.

We also performed a larger simulation with 25000 particles (instead of the 10000 we had been using before) in the $\eta_a = 10^{-3}$ MHD snapshot with the following initial positions: $x, y \in [-2.5, 2.5]\,\mathrm{m}$ and $z \in [1, 299]\,\mathrm{m}$. The results are shown in Figure 5.16. The reason for this is to perform a run with a larger initial position range, while not lowering the initial particle position density too much (although the domain size increased by a factor 2.5^2, the number of particles increased by a factor of 2.5). This is useful since restricting $x, y \in [-1, 1]\,\mathrm{m}$ results in nearly all of the particles starting within a region of non-zero resistivity, which is no longer the case with $x, y \in [-2.5, 2.5]\,\mathrm{m}$. There are still some differences in the energy spectra, with the portion of particles achieving energy greater than $100\,\mathrm{keV}$ being approximately 2% in all cases. The portion of particles obtaining energies more than $200\,\mathrm{keV}$ is 0.35% in the absence of scattering, 0.01% with scattering at a constant $\kappa = 10^{-8}$ and again 0.027% with $\kappa = \eta_{sp}/\eta_a$. If we further look at particles gaining energies more than $300\,\mathrm{keV}$, it is 0.017% in the absence of scattering, 0.019% for $\kappa = 10^{-8}$ and 0.12% for $\kappa = \eta_{sp}/\eta_a$. Considering the pitch angle distribution, there are still obvious differences between the scattered and unscattered simulations, however these are smaller than they were for the simulations discussed above. Without scattering 70% of the particles have final pitch angle $\theta > 2.5$, only 54% do for scattering with $\kappa = 10^{-8}$ and 51% for scattering with $\kappa = \eta_{sp}/\eta_a$. The orbit duration distribution shows almost no differences between the scattered and unscattered distributions again.

In Figure 5.17 we plot the positions of the particle orbits at the end of the simulation for the unscattered case (Figure 5.17a) as well as including scattering at the rate $\kappa = \eta_{sp}/\eta_a$ (Figure 5.17b) for these larger simulations. There is little obvious difference between the two spatial distributions, and overplotting the two distributions (Figure 5.17c) does not reveal significant differences either.

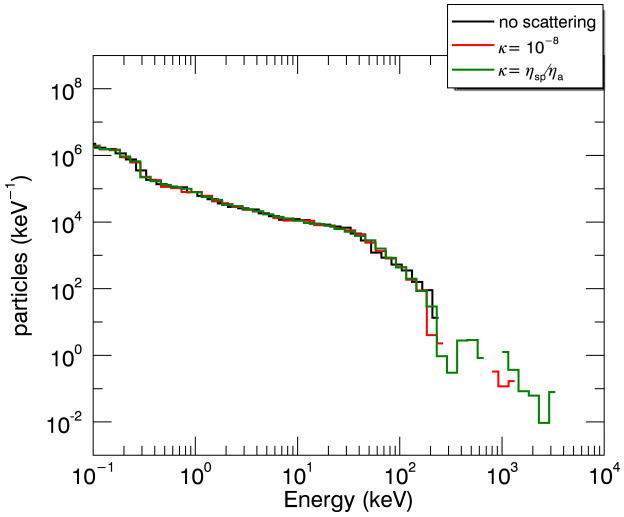

(A)

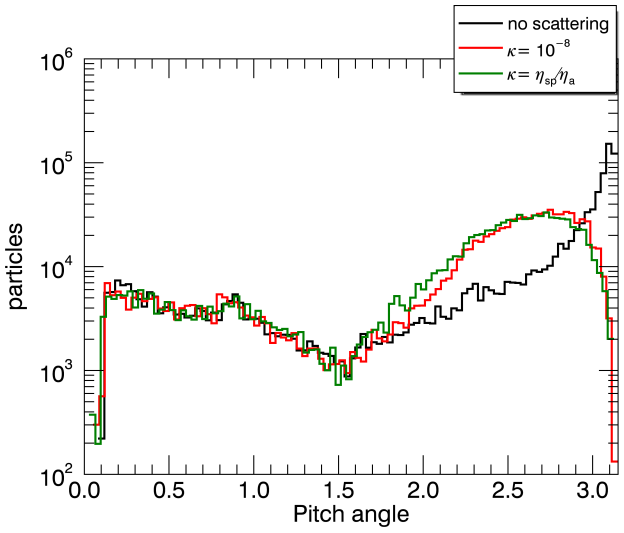

(B)

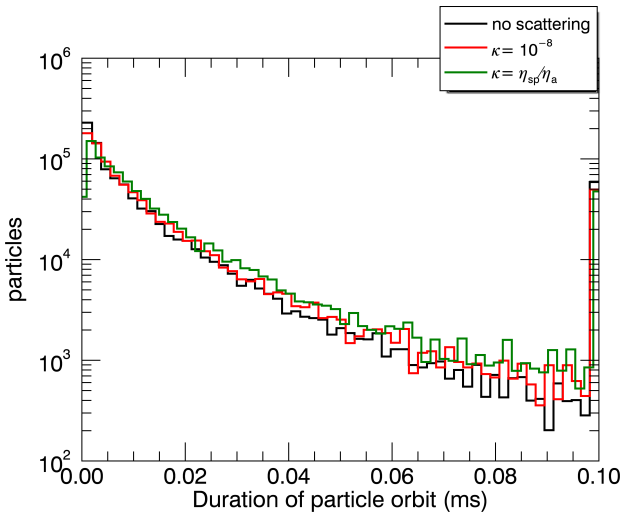

(C)

FIGURE 5.16: Energy spectra, pitch angle and orbit duration distributions for particles with scattering at a rate of $\kappa = \eta_{sp}/\eta_a$ in MHD simulation with $\eta_a = 10^{-3}$. Particle initial positions $x, y \in [-2.5, 2.5]$ m, $z \in [1, 299]$ m, 25000 particles orbits computed in total before weighting.

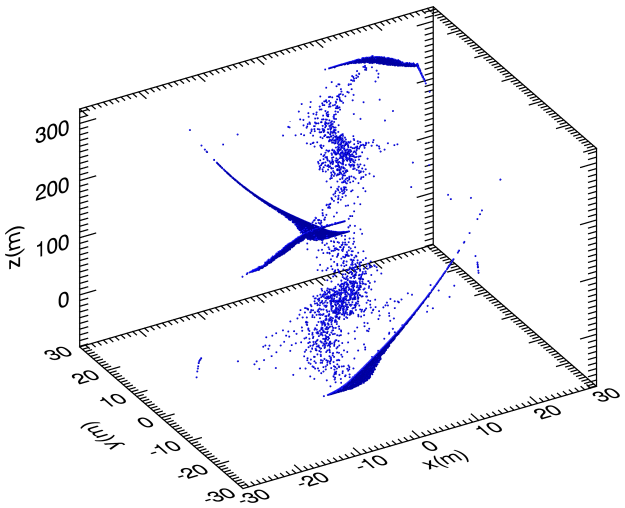

(A) No scattering

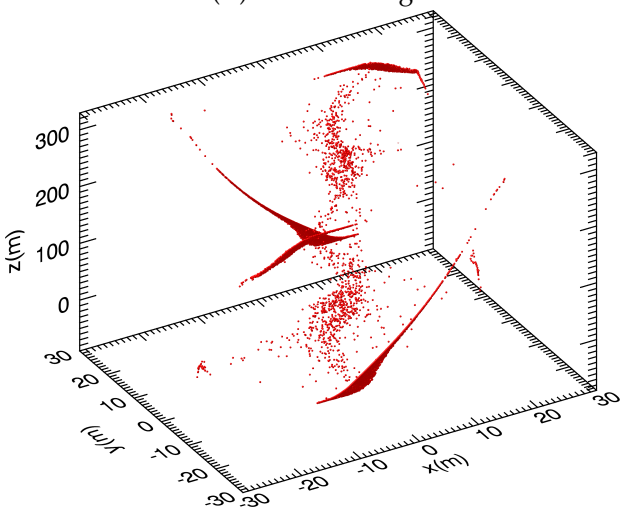

(B) Scattering with $\kappa = \eta_{sp}/\eta_a$

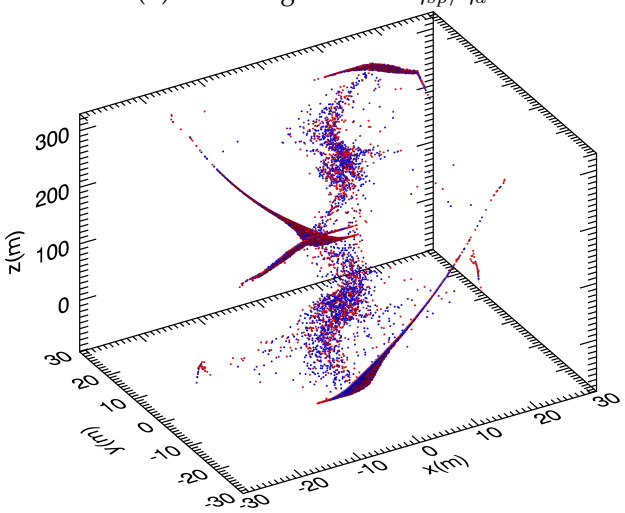

(C) Comparison of panels A and B

FIGURE 5.17: Final positions of particle orbits computed in Figure 5.16. MHD simulations used $\eta_a = 10^{-3}$.

5.3 Comparison with 1D and 2D results

Pitch angle scattering linked to resistivity clearly has an effect on particle orbit trajectories, and to varying degrees on the orbit energy gain, pitch angle evolution, and orbit duration. The relationship between the acceleration as a result of the parallel electric field and the pitch angle scattering is more complicated. In the 1D simulations we performed we found three regimes - one in which the acceleration was dominant, one in which scattering was dominant, and one in which the initial conditions dominated over the electric field and scattering. Since pitch angle scattering conserves energy in our implementation, energy spectra are somewhat meaningless in the 1D simulations we performed, because the energy of a given orbit will depend only on the work done by the electric field on the particle, which in turn will only depend on which side of the (1D) box the orbit exits. As a result, we only examined the final pitch angle and orbit duration distributions. We found that for a sufficiently high resistivity the pitch angle distribution approached a distribution which was peaked at $\cos\theta = -1$ (of course this could also be +1 if the electric field was directed in the opposite direction), with a smaller peak at $\cos\theta = 1$. In the absence of scattering an electric field acting over a fixed length will tend to make the particle have a pitch angle closer to $|\cos\theta| = 1$, depending on the direction and extent of the field, relative to the particle charge and initial pitch angle. For the strong fields employed in these simulations, in the absence of scattering, we would expect a single value of the cosine of the pitch angle very near -1, whereas with scattering we obtain what seems to be an asymptotic distribution with some particles exiting with $\cos\theta = 1$. Here, although the electric field is the dominant factor affecting the direction particles end up travelling in, scattering plays a non-negligible role. On the other hand, decreasing the resistivity results in scattering dominating the pitch angle distribution, which approaches becoming uniform in cosine of the pitch angle (with a depletion at $\cos\theta = 0$).

There are similarities between the 1D and the 3D cases. For instance, the pitch angle distributions are peaked toward anti-parallel values of pitch angle (this is dependent on the orientation of the electric field), although the shape of the distribution is much more complicated in the 3D case because the magnetic field geometry can also affect the pitch angle. There is also some similarity in the trend for increased resistivity to lead to shorter orbit durations in 3D, which is also seen in the regime where the effects of the electric field dominate in 1D. However, as for the pitch angle distributions, we do not see a regime where scattering dominates in 3D, likely due to the narrower range of values examined and more complex geometry.

The comparison with the 2D results is a bit more difficult. The parameter regimes of the 2D simulations are comparable with those of the 3D simulations. The resistivity (in physical units this time) in the 2D case was $2.6 \times 10^{-2}\,\Omega \cdot \mathrm{m}^{-1}$, while for the 3D cases it ranged between $3.2 \times 10^{-2} - 3.2 \times 10^{-4}\,\Omega \cdot \mathrm{m}^{-1}$. The peak electric field strength reached in the 2D simulation was $300\,\mathrm{V} \cdot \mathrm{m}^{-1}$, compared to ranging between $1300 - 15\,\mathrm{V} \cdot \mathrm{m}^{-1}$ for the 3D simulation. Maximum scattering rates were also comparable, being of the order of $10^6\,\mathrm{s}^{-1}$ for the 2D case and ranging between $10^6 - 10^3\,\mathrm{s}^{-1}$ in the 3D case.

There are broad similarities in the results also, with the energy spectra reaching similar maximum energies (of order MeV) and the orbit durations are also similar (of order $0.1\,\mathrm{ms}$). In both cases scattering tends to produce more energetic particles compared to the unscattered simulations, although this is more effective in the 2D case, and tends to lengthen orbit duration.

Furthermore, because of the geometrical differences between 2D and 3D simulations, direct comparisons of the orbits is difficult. We observe that there are more deviations (in terms of final position) from the unscattered orbits when including scattering in the 2D case than in the 3D case. In particular scattering in the 2D case results in particles exiting in the reconnection outflow regions more often than in the absence of scattering, whereas for the 3D case the particle exit positions remain roughly similar regardless of the presence of scattering. As a result of different field geometries, scattering affects particle trajectories, and hence energy gains, in different ways for the two different types of simulations, which could explain the result that there are large differences in the energy spectra for the 2D case, but not the 3D case. From Figure 5.3 we see that most of the scattering for the 3D case results in particles making multiple traverses of the fields near the xy-plane. In the 2D case (Figure 4.6) the particles are scattered in the separatrices and reenter the current sheet along a different trajectory. On the other hand, in the 3D case, due to the electric field dominating particle trajectories along the separator, scattering is unable to make the particles traverse the reconnection region multiple times such that the energy gained when going down the separator is not lost on the way up. As a result there is less impact on the energy spectra from scattering. This may partly explain the differences in the energy spectra, however without looking at individual trajectories this is difficult to tell. The trajectories used in Figures 4.6 and 5.3 are from only 100 orbits initialised with identical initial conditions, a more realistic distribution of initial conditions may yield a different result.

Since our scattering model does not include energy losses due to scattering events, any differences in energy spectra must occur due to changes in particle

orbit trajectories through the reconnection region, as has been discussed at length in Chapter 4. This is also true for the particle orbits in the 3D separator reconnection simulations. However, unlike in the 2D case, we do not see large differences in energy spectra between simulations which include scattering at various rates and those that do not. Although in Figure 5.4 we can see that in the presence of scattering energies can be achieved that are greater than in the absence of scattering, this does not translate to significantly higher energies achieved in the energy spectra. This is likely due to the fact that the accelerating parallel electric field is concentrated close around the separator and particles which are scattered back up the separator lose the same amount of energy as they gained going down. This is in contrast to the 2D case where particles scattered in the separatrices took a different path through the reconnection region (for example being advected with the $\mathbf{E} \times \mathbf{B}$ drift) resulting in energy gain each time they passed. In the 3D case particles have much less variation in their trajectories along the separator (see Figure 5.3) which does not allow for the same phenomenon as in 2D. Additional factors that influence energy gain are geometric differences between the 2D and 3D MHD simulations. In particular, in the 2D case particles are allowed to travel arbitrarily far along the invariant direction (out of plane, in our case labeled z), which in theory allows an arbitrarily high energy gain. In our simulations the most energetic particles travelled approximately $400\,\mathrm{m}$ in this direction (see Figure 4.11). This is however of the same order of magnitude as the length of the 3D separator (which is $300\,\mathrm{m}$, although many particles would have traversed a much shorter range), so determining if this effect is significant requires further investigation. Furthermore variations in the flows advecting particles into the reconnection region between the 2D and 3D cases may have an effect, since in the 2D case particles that get scattered to small distances outside of the reconnection region may be advected back in, resulting in more energy gain. This effect may be lessened in the 3D case due to different reconnection geometry which may allow particles to escape more easily. As a result, the dominant factor in determining the shape and extent of the energy spectra is the strength of the electric field, rather than scattering.

One key difference between the particle orbits in the 2D and 3D cases is that in the 3D case the final pitch angle of the particles tended to be anti-aligned with the magnetic field, with significantly fewer particles with pitch angle $\theta < \pi/2$. On the other hand, there were roughly comparable amounts of particles both aligned and anti-aligned to the magnetic field in the 2D case. This is also a consequence of the geometry, with particles exiting along all the separatrices in the 2D case, whereas particle orbits are predominantly accelerated in only one direction in the

3D separator case. In the 2D case there was also a population of particles which had a final pitch angle near $\theta = \pi/2$. These particles exited the domain the the reconnection outflow region. In the 3D case, though, there was no equivalent analogue to this, and in fact there was a depletion of particles with pitch angle $\theta = \pi/2$, generally speaking.

Although the nature of the reconnection processes is very different between the 2D and general 3D geometries, 3D separator reconnection has a number of similarities to 2D guide field reconnection. In particular, in a cut perpendicular to the separator the shape of the 3D field lines is similar to the 2D case if a guide field is included. In fact, the 2D guide field reconnection scenario could be thought of as a 3D separator with null points infinitely far apart. However there are differences also, for example as mentioned before, because of the way the parallel electric field reacts to different values of resistivity. In the 2D MHD simulations that we performed the electric field is generally independent of the resistivity because a lower resistivity will simply result in a higher current which will restore the reconnection rate, and hence, parallel electric field, to a similar value that was the case for a higher resistivity (this is because $\mathbf{j} \propto \nabla \times \mathbf{B}$, a lower resistivity will result in a thinner current sheet with a higher current). In addition, the narrower current sheet caused by a low resistivity may affect the particle trajectories slightly when compared to a larger current sheet associated with a higher resistivity. The 2D reconnection scenario is a model in which the reconnection rate is determined by the initial and boundary conditions of the simulation, and is suited to examining steady state reconnection.

As discussed previously, in the solar corona the dominant term in the magnetic induction equation (Equation 1.10) is the $\nabla \times (\mathbf{u} \times \mathbf{B})$, meaning that in order to get reconnection to occur large current gradients need to build up before reconnection can proceed. This process is better approximated by the approach we took for the 3D reconnection models, with a period of ideal relaxation during which currents build up around the separator, followed by switching on the resistivity where the current density exceeds a specified threshold, allowing reconnection to occur. In this case it is possible to get different values of the parallel electric field because the currents initially built up during the relaxation remain when the resistivity is switched on, so if different values of resistivity are used, different values of the parallel electric field will result. This allowed us to study the interaction between the particle acceleration due to the parallel electric field and the pitch angle scattering, both caused by the resistivity. As a result, the 3D simulations are a more appropriate model of reconnection in the solar corona, however, because

of the complex nature of the magnetic field geometry for 3D reconnection, further, more detailed studies of particle acceleration in 3D fields are required to better understand the particle dynamics in 3D magnetic reconnection.

Throughout this chapter we have considered the effects of different levels of resistivity on particle acceleration, however in all cases the resistivity, where it was non-zero, was always a constant value. Physically we should expect a more complex dependence of resistivity on current density due to the multiple instabilities which can cause it. Since our approach fundamentally relies on performing single fluid MHD simulations, it may be difficult to determine which instabilities contribute to resistivity at any given point in the simulation. On the other hand, a simple extension to the work already done here would be to consider a model of resistivity which depends on the current in a more complex way than just as a step function. For instance setting $\eta = j^{\alpha}$ for values of $j > j_{crit}$ and for positive values of α. This approach would produce more acceleration and more scattering in regions of higher current, however from the perspective of the MHD simulations it would prevent excessively high current from building up and dissipate it more rapidly if it does, thereby giving a better approximation of the physical processes in reconnection. It would be interesting to see how particles behave in such a model as the electric field will rise faster than the scattering rate with increasing current (since $E_{\parallel} = \eta j_{\parallel}$). The scattering model may also need to be made more complex (i.e. current dependent) to better reflect the changing scattering rate caused by current driven instabilities.

Chapter 6

Particle acceleration in a CMT with a braking plasma jet[1]

6.1 Introduction

Throughout this thesis we have been concerned with particle acceleration by DC electric fields, in particular by the coupling between pitch-angle scattering and the parallel electric field caused by anomalous resistivity. However, in addition to acceleration, particle trapping may be important in explaining other phenomena observed in solar flares, such as loop-top HXR emission [e.g. Somov and Kosugi, 1997]. There may be multiple ways of achieving trapping of charged particles, for example due to regions of anti-aligned parallel electric field occuring on the same field line [Threlfall et al., 2016a], however the one which is most commonly discussed is due to converging magnetic field lines and the conservation of the magnetic moment.

As discussed in Chapter 2 the conservation of the magnetic moment is due to the rapid gyrational motion of charged particles in strong magnetic fields. To illustrate the concept of particle trapping in converging magnetic fields consider a region of homogeneous magnetic field which is bounded on two sides by regions of stronger field (see Figure 6.1). Since the definition of the magnetic moment is $\mu = \frac{mv_{rot}^2}{2B}$, given a constant magnetic moment and an increasing magnetic field strength, a particle's perpendicular velocity must increase proportionally to the square root of the magnetic field. Due to the conservation of energy, the parallel velocity must thus decrease, causing the particle to slow its propagation along the field toward the strong field region and eventually return the other way. This effect is called magnetic mirroring and the combination of two magnetic mirrors as in Figure 6.1 is called a magnetic bottle or a magnetic trap. In the context of solar flares

[1]The work in this chapter was performed in collaboration with James Threlfall, and the many of the results have been published in Borissov et al. [2016]

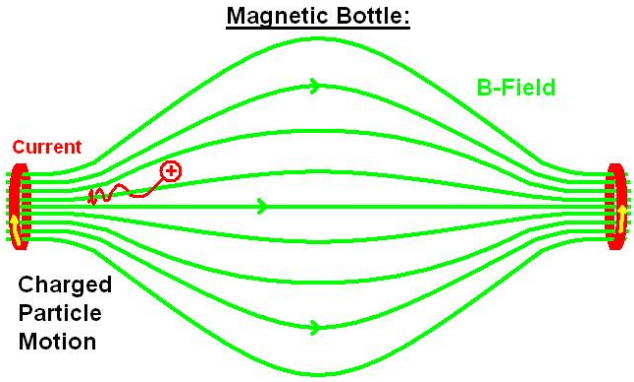

FIGURE 6.1: Configuration magnetic fields illustrating trapping of charged particles between converging field regions. (Credit: https:commons.wikimedia.orgwikiFile:Fields_in_magnetic_bottles.jpg, retrieved 12022018.)

trapping of particles can occur in a loop which is anchored in the chromosphere, where the magnetic field strength increases. This process may occur within the framework of the standard model for solar flares [see e.g. Shibata and Magara, 2011, or Chapter 1] when highly stretched reconnected loops collapse to form post-flare loops, leading to what is known as a collapsing magnetic trap (CMT).

Previous works [see e.g. Somov and Kosugi, 1997, Bogachev and Somov, 2001, 2005, 2007, 2009, Somov and Bogachev, 2003, Karlický and Kosugi, 2004, Karlický and Bárta, 2006, Grady and Neukirch, 2009, Minoshima et al., 2010, 2011, Grady et al., 2012, Eradat Oskoui et al., 2014, Eradat Oskoui and Neukirch, 2014] have shown that in a CMT both particle acceleration and trapping is possible. The particles are trapped between mirror points above the footpoints of the loops, with the exact location of the mirror points affecting a particular particle depending on the particle's magnetic moment. As the field lines contract the distance between the mirror points for individual particles gets shorter and the magnetic field strength increases. The decrease in distance between mirror points leads to what is known as Fermi acceleration [Fermi, 1954, Somov and Kosugi, 1997], wherein the particles gain energy every time they are reflected by the converging mirror points. The increasing magnetic field strength causes what is known as betatron acceleration. This can be seen in a simple model where a charged particle is located in a homogeneous magnetic field with steadily increasing field strength. Due to the conservation of the magnetic moment the particle's perpendicular velocity needs to increase also [this is similar to the magnetic mirror argument, however, here we do not require conservation of energy and allow the increase in the magnetic field

to do work on the particle Somov and Bogachev, 2003].

Collapsing magnetic traps are applicable to not only solar flares, but are also relevant for substorms in the Earth's magnetosphere, where reconnected field lines starting out in a highly stretched state relax to a dipole-like configuration [e.g. Birn et al., 2012]. In this context, observations [Imada et al., 2007, Fu et al., 2013] and numerical simulations [Sitnov and Swisdak, 2011] suggest that the outflow from the reconnection region forms a jet, which is characterized by a large increase in the magnetic field strength [for instance, in 2D reconnection simulations by Sitnov and Swisdak, 2011, there is an increase of the vertical component of the magnetic field by approximately a factor of two which moves outward from the reconnection site as the simulation progresses]. As the jet front propagates Earthward it encounters stronger magnetic fields, which causes it to slow down and stop [Khotyaintsev et al., 2011]. As it does so particle acceleration has been shown to occur [Artemyev, 2014], in a process called jet braking.

In this chapter we present an analytical model that combines the braking jet with a CMT along with results from test particle simulations in the model. In this model the contracting loops are compressed at the looptop due to their interaction with the braking jet. In Section 6.2 we introduce the equations which we use to define our analytical CMT model. In Section 6.3 we discuss the different types of test particle orbits that are possible in our model. The relative abundances of each type of orbit are investigated in Section 6.4.

6.2 Analytical Model for a CMT with a Braking Jet

To define the electromagnetic fields analytically we follow the transformation method of Giuliani et al. [2005]. This approach assumes that the evolution of the CMT occurs in a region of the corona where ideal MHD holds. Ideal MHD implies that the magnetic field is frozen to the plasma flow, which means that the fields may be calculated from a specified flow. Integration of the plasma flow velocity leads to an expression for the position of a fluid element at the final time (at the end of the simulation) as being a function of the position of the fluid element at an earlier time, that is $\mathbf{x}_\infty = \mathbf{G}(\mathbf{x}, t)$. Alternatively, instead of choosing the position of the fluid element at the final time being a function of its position at an initial time, we can specify the position of a fluid element at any time within the simulation as being a function of its position at the final time. We choose our model to be

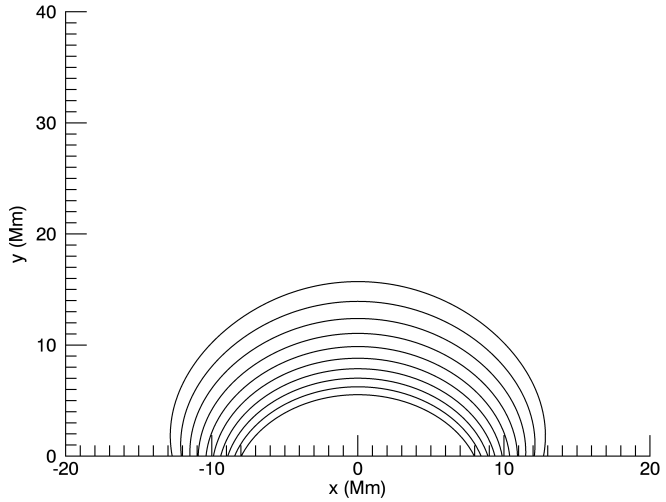

FIGURE 6.2: Magnetic field lines corresponding to the final field configuration given by the flux function in equation 6.2

two-dimensional, so we can write

$$\mathbf{B} = \nabla A(x, y, t) \times \mathbf{e}_z + B_z \mathbf{e}_z. \tag{6.1}$$

We specify the flux function, A, (and hence the electromagnetic fields) at $(\mathbf{x}, t)$ by choosing a final flux function, $A_0(\mathbf{x})$ and a coordinate transformation $\mathbf{x}_\infty(\mathbf{x}, t)$ so that $A(\mathbf{x}, t) = A_0\left[\mathbf{x}_\infty(\mathbf{x}, t)\right]$. In the present investigation we set $B_z = 0$.

Following Giuliani et al. [2005], we choose a bipolar configuration for the final flux function of the form

$$A_0(\mathbf{x}) = c_1 \left[\arctan\left(\frac{y+1}{x+0.5}\right) + \arctan\left(\frac{y+1}{x-0.5}\right)\right], \tag{6.2}$$

where x is the spatial coordinate parallel to the solar surface, y is the coordinate normal to the solar surface, and c_1 determines the strength of the bipole. The final field configuration is shown in Figure 6.2.

In our model we will only work with a transformation of the y coordinate and leave $x_\infty = x$. The basic idea behind the choice of transformation is as follows: regions where $y_\infty < y$ correspond to vertical stretching, while regions with $y_\infty > y$ correspond to vertical compression. Our goal is to develop a time-dependent transformation which deforms space (and hence the magnetic field lines) in such a

way as to reproduce a CMT [see Giuliani et al., 2005] and to incorporate a vertical compression and pileup of the field lines, modelling the region where the jet interacts with the lower lying loops. The y-component of the transformation we use, restricted to $x = 0\,\mathrm{Mm}$ is presented in Figure 6.3 for various time values.

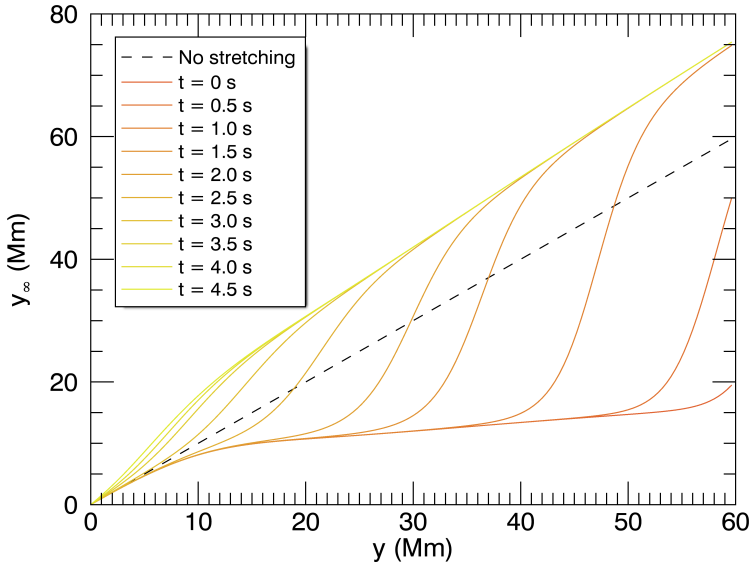

FIGURE 6.3: Transformation with $x = 0\,\mathrm{Mm}$ (in centre of CMT). Regions for which $y_\infty < y$ correspond to stretching, while regions with $y_\infty < y$ correspond to compression. For a fixed time, the front is located in the region where y_∞ increases rapidly. The dashed line is a visual aid, set at $y_\infty = y$.

Figure 6.3 shows that when $t = 0\,\mathrm{s}$ and $y < 60\ \mathrm{Mm}$, $y_\infty < y$, corresponding to a vertical stretching. The interaction of the jet with the stronger field in the lower loops creates a pileup of magnetic field, which we may call the jet front. For a given y value the passage of the front is caused by a large increase in the transformation, which causes a compression. After the passage of the front the transformation becomes less steep, reducing the compression. The functional form of the transformation shown in Figure 6.3 is given by

$$y_\infty = S + y\frac{1+\tanh\phi}{2}, \tag{6.3}$$

where the first term, S, determines the shape of the field before the passage of the front. The second term determines the shape of the front, with $\phi = 0$ giving the location of the front. We define our stretching to be of the form $S = s\log(1 + y/s)$ where s determines the amount of stretching for large values of y. The initial

justification for using this choice is that for small values of y, $S \approx y$, hence there is no distortion near the bottom of our domain. In order to have more control over the region without deformation we chose

$$\begin{aligned} S &= s\log\left(1+\frac{y}{s}\right)\left(1-\frac{1-\tanh(y-y')}{2}\cdot\frac{\tanh(x+x')-\tanh(x-x')}{2}\right) \\ &\quad +y\left(\frac{1-\tanh(y-y')}{2}\cdot\frac{\tanh(x+x')-\tanh(x-x')}{2}\right). \end{aligned} \tag{6.4}$$

This choice explicitly restricts $S = y$ for values of $y \ll y'$ and for $|x| \ll x'$. The restriction in the x-direction is unused in this work and we take $x' = 100$, which is outside of the simulation domain.

To determine the position of the front we set:

$$\phi = y - v_\phi \sigma \tanh(t/\sigma) - y_0. \tag{6.5}$$

Since the location of the front is given by $\phi = 0$, for small t the front is located at $y = y_0 + v_\phi\sigma\tanh(t/\sigma) \simeq y_0 + v_\phi t$, which means that initially the front propagates with a constant speed. For larger t, the term $\tanh(t/\sigma)$ tends to a constant, meaning that the speed of the front decreases. Calculating the limit as $t \to \infty$ gives,

$$\lim_{t\to\infty}\left(y_0 + v_\phi\sigma\tanh(t/\sigma)\right) = y_0 + v_\phi\sigma \tag{6.6}$$

which shows that the parameter σ can be used to determine the final location of the front.

The steepness of the front (which affects the strength of the electromagnetic fields in the front) may be modified by changing the gradient of ϕ, with a higher gradient implying a stronger magnetic field. We multiply the expression from equation (6.5) by $\alpha\left((y+1)\left(s_o x^2+1\right)\right)^\beta$. The transformation is steepened by the factor $(y+1)^\beta$ for larger values of y. Unfortunately doing so changes the shape of the loops, so the factor $\left(s_o x^2+1\right)^\beta$ is added to compensate. We add the functions J and T (given in Equation (6.7)) to further modify the shape of the CMT:

$$J = d\mathrm{e}^{-x^2 y/w}, \qquad T = k\tan\left(\frac{\pi}{2}\frac{x^2}{w_2}\right)\tanh y. \tag{6.7}$$

In this case J produces an indentation in the jet braking region see Figure 6.5, where d and w determine the depth and width of the indentation. T is further used to modify the shape of the CMT for large values of $|x|$ to maintain the shape of the loops after all the previous modifications.

It is suggested in Artemyev [2014] that during the propagation of the braking jet the front may steepen. In the transformation described above the front becomes shallower as the jet propagates towards the solar surface. The reason for this is that as the braking jet approaches the lower loops it is travelling slow enough that the magnetic flux that piled up previously spreads out. The spreading out of the magnetic flux causes the front to become less steep and eventually disappear. Nevertheless, closer to the reconnection region the outflow is faster and the magnetic field not as strong, so we expect to see a steepening front. To incorporate this steepening into our model, ϕ and T are multiplied by the factor $1+\frac{1}{2}\left[\chi\sin\left(\pi y/y_0\right)-1\right]\left[1-\tanh(\zeta(t-t'))\right]$. This corresponds to multiplying ϕ and T by $\chi\sin\left(\pi y/y_0\right)$ when $t \ll t'$, producing a steepening of the transformation near $y = y_0$. The result is the transformation presented in Equations (6.8) – (6.12).

$$y_\infty = \left[s\log\left(1+\frac{y}{s}\right)\left(1-F(y)G(x)\right)+yF(y)G(x)+y\frac{1+\tanh\phi}{2}\right]f(t)+yg(t), \tag{6.8}$$

$$x_\infty = x, \tag{6.9}$$

where

$$f(t) = \frac{1-\tanh(t-t_0)}{2}, \quad g(t) = 1-f(t),$$
$$F(y) = \frac{1-\tanh(y-y')}{2}, \quad G(x) = \frac{\tanh(x+x')-\tanh(x-x')}{2},$$

$$\begin{aligned}\phi &= \alpha\left(1+\left(\chi\sin\left(\frac{\pi y}{y_0}\right)-1\right)\frac{1-\tanh(\zeta(t-t'))}{2}\right) \\ &\quad\cdot\left(\left(y+1\right)\left(s_o x^2+1\right)\right)^\beta\left(y-v_\phi\sigma\tanh\left(\frac{t}{\sigma}\right)-y_0+J\right)+T,\end{aligned} \tag{6.10}$$

and

$$J = de^{-x^2y/w}, \tag{6.11}$$

$$T = k\left(1+\left(\chi\sin\left(\frac{\pi y}{y_0}\right)-1\right)\frac{1-\tanh(\zeta(t-t'))}{2}\right)\tan\left(\frac{\pi}{2}\frac{x^2}{w_2}\right)\tanh(y). \tag{6.12}$$

Note that the functions $f(t)$ and $g(t)$ are added to equation 6.8 so that the transformation smoothly becomes the identity transformation, $y_\infty = y$ for $t > t'$.

There are numerous parameters in the model which control everything from the width and depth of the deformation due to the jet impacting the lower loops to the time at which the deformations of space dissipate. Although some of these values have very clear physical interpretations, and may be modified with an easily predictable effect on the transformation (such as d and w controlling the depth and width of the jet braking region), others (such as w_2, which influences the shape of the loops at the edge of the CMT) are used to compensate for effects introduced by other parts of the transformation and are left unchanged throughout this investigation. In particular, the parameters $d, w, \beta, w_2, k, x', y', s$ and s_o are chosen so that the shape of the field lines resembles that found in MHD simulations, for example by Karlický and Bárta [2006]. The steepness of the front is controlled primarily by α. The parameters χ, ζ and t' influence the height and time at which the front changes from steepening to becoming shallower during its propogation. These parameters are chosen so that the gradient of the magnetic field at the jet braking region is initially increasing (when magnetic flux is piling up), and later decreasing (when the jet is being slowed by the stronger magnetic field in the lower loops). Of the remaining parameters, the initial speed of the front is determined by v_ϕ, the initial position of the front by y_0, σ controls the distance to which the front propagates, and the time at which the front dissipates is given by t_0.

The value of α is set by balancing the deceleration of the jet with deceleration forces due to both curvature of the field lines at the centre of the braking jet region and magnetic pressure. In the frame of reference of the jet the acceleration is $\frac{\partial v}{\partial t}$. By assuming a normalising timescale of $\hat{T} = 10\,\mathrm{s}$, the acceleration in the frame of reference of the jet is approximately $\frac{\hat{L}}{\hat{T}^2} = 10^5\,\mathrm{m\ s^{-2}}$. This can also be related to the forces acting on the plasma in the jet as follows

$$\frac{\partial v}{\partial t} \simeq \frac{1}{\rho}\left(\frac{B^2}{\mu_0 R_c} - \nabla\frac{B^2}{2\mu_0}\right). \tag{6.13}$$

The two terms on the right hand side of Equation (6.13) are the magnetic tension and pressure terms respectively. Assuming a mass density of $\rho = 10^{-10}\ \mathrm{kg\ m^{-3}}$ magnetic field of the order $\hat{B} = 10^{-2}\ \mathrm{T}$ in the CMT, radius of field line curvature $R_c \simeq 10^7\,\mathrm{m}$ in the jet braking region and approximating the magnetic permeability as $\mu_0 \simeq 10^{-6}\ \mathrm{H\ m^{-1}}$, requires a magnetic field strength gradient $\nabla\left(B^2\right) \simeq 10^{-11}\ \mathrm{T^2\ m^{-1}}$. To ensure that this is in fact the case in our model, the magnetic field strength was plotted along a cut through $x = 0$ and the gradient was confirmed to be of the correct order of magnitude (see Figure 6.4).

One set of non-dimensional parameters reproducing the properties of the CMT

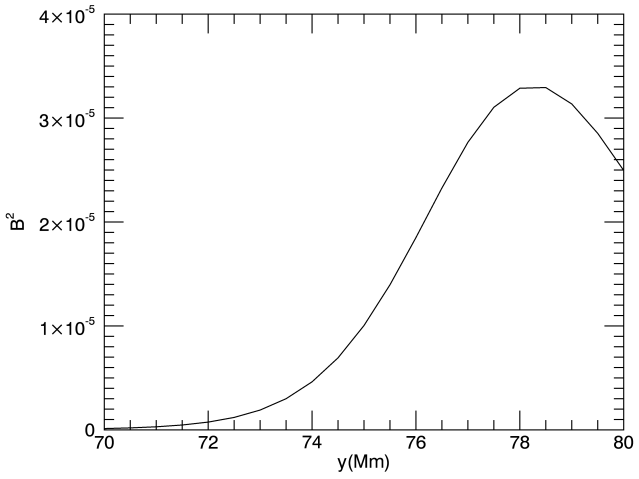

FIGURE 6.4: Squared magnetic field strength along a vertical cut through the braking jet region. Resulting gradient is of the order of $10^{-11}\,\mathrm{T^2 m^{-1}}$.

model we require is given in Table 6.1. We refer to this set of parameters as the basic parameters, and we shall investigate modifications to this parameter set later on. The magnetic field lines and out-of-plane electric field given by our CMT model using the basic parameters at various times are shown in Figure 6.5. The desired features, in particular, pileup of magnetic flux, indentation due to the braking jet deforming field lines, and slowing and dissipation of the jet front are clearly evident in Figure 6.5. Extraneous patches of strong electric field for large values of horizontal distance from the centre of the trap ($|x| \gtrsim 15\,\mathrm{Mm}$) and early times ($t < 1\,\mathrm{s}$) are undesirable, however, they do not affect particle orbits because test particles are initialized on field lines that do not cross this region.

The resulting transformation is shown in figure 6.5

6.3 Particle trajectories

As in previous chapters, we initialise a population of test particles within the specified fields, and integrate their trajectories based on the guiding centre equations (Equations 2.20-2.21). Since no reconnection is involved we do not take into account any pitch angle scattering. Previous work by Bogachev and Somov [2009] has taken into account Coulomb collisions within the context of a simpler

Shape				Front structure		Front propagation			
d	0.3	k	7	α	1	σ	4	x'	100
w	0.1	s	0.7	χ	1	v_ϕ	-2	y'	1
w_2	2.3	s_0	0.5	ζ	0.3	y_0	7	t'	5
β	0.5							t_0	100

TABLE 6.1: Basic parameters used in CMT model (Equations (6.8)-(6.12)) which control the shape of the trap, the steepness of the front, and the propagation of the front. The appendix details how these parameters affect the CMT model.

CMT model, however since we are focussing on the effects of the interaction of the braking jet with the CMT, for simplicity we neglect this type of scattering. Note also that although the relativistic form of the guiding centre equations are used for this study, even though relativistic energies were not expected (as the computational requirements for solving either set of equations is the same, it makes sense to use the more robust relativistic formulation). In fact the highest energy observed was approximately 100 keV, for a particle with a starting energy of 5.5 keV, which may be mildly relativistic and could cause some small errors if a non-relativistic code was used [see Eradat Oskoui and Neukirch, 2014].

The guiding centre equations are solved (subject to the normalising $\hat{L}, \hat{B}$, and $\hat{T}$, specified above) using an adaptive timestep 4th order Runge-Kutta code (specifically the Cash-Karp scheme, see). This approach compares the 4th and 5th order Runge-Kutta solutions and adjusts the timestep so that the difference between the two solutions is below a specified threshold. Since Equation (2.22) defines γ, it does not need to be integrated, however it is used to update the value of γ at the beginning of each timestep. Test particle orbits are initialized in the CMT with a specified position, kinetic energy and pitch angle. We refer to pitch angles near $\theta = 90^\circ$ as high pitch angles, and pitch angles near $\theta = 0^\circ$ or $\theta = 180^\circ$ as low pitch angles. We illustrate the most common particle trajectories in sections 6.3.1-6.3.3. Section 6.3.1 describes particle orbits which are dominated by trapping in the jet braking region near the centre of the CMT (these orbits we will define as type 1 orbits), particle orbits dominated by trapping in the sides of the CMT are described in section 6.3.2 (we define these as type 2 orbits, and introduce three subcategories of these in section 6.5), while orbits which escape the CMT are described in section 6.3.3 (we define these orbits as type 3).

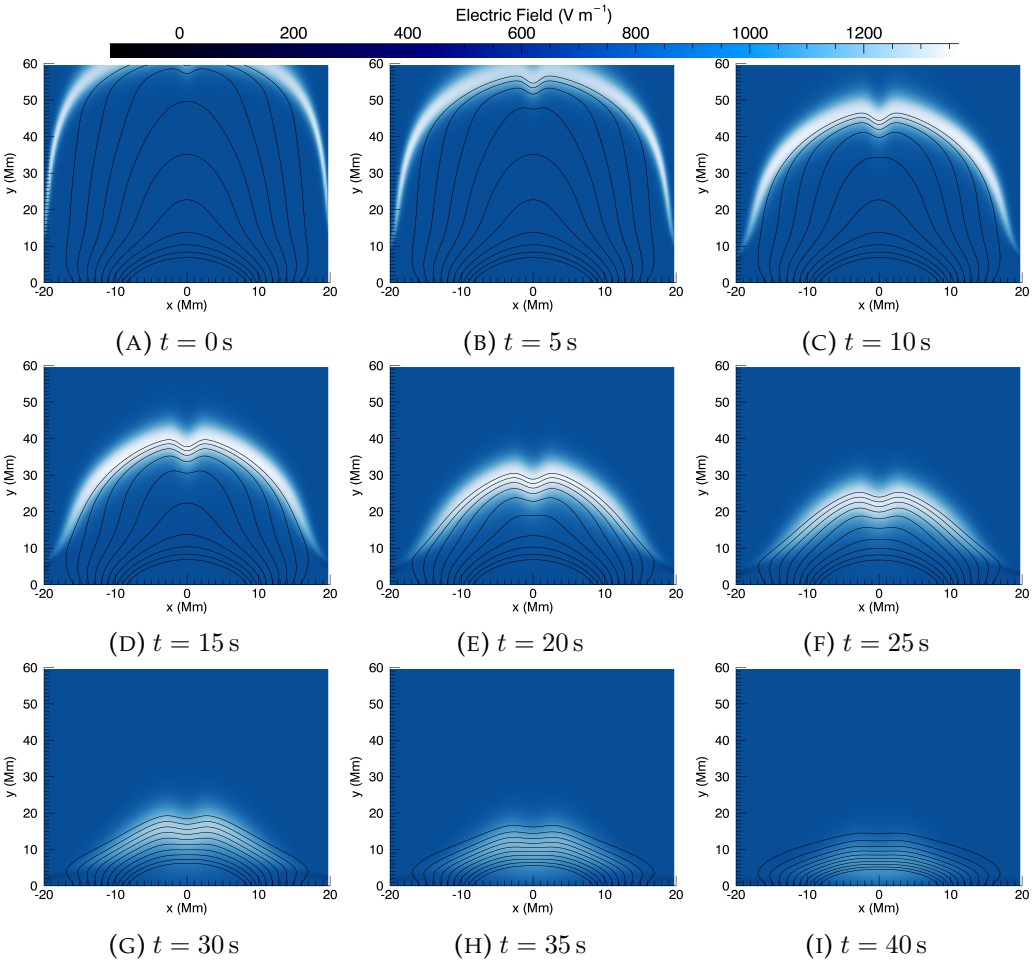

FIGURE 6.5: Panels A-I outline the temporal evolution of a collapsing magnetic trap which incorporates jet braking and flux pileup. The evolution of the electric field is seen in colour and overlaid with magnetic field lines (black) to illustrate the evolution of the magnetic field.

6.3.1 Trapping in braking jet region (type 1)

Test particle orbits starting in the centre of the trap with a high pitch angle are trapped near the centre in the jet braking region. To demonstrate this effect, four orbits are initialized at different vertical positions in the middle of the trap with a starting pitch angle of $\theta = 75°$. These initial conditions ensure that the orbits are trapped by the braking jet. The particle orbit trajectories and kinetic energies are shown in Figure 6.6. Test particle orbits with a lower initial vertical position

experience more acceleration and propagate further down in the magnetic trap. Towards the end of the simulation time, as the jet front weakens, the test particles exit the braking jet and become trapped in a wider region. Although, by definition type 1 orbits are dominated by trapping in the jet braking region, more complicated behaviour is also possible. One example of this is shown by the particle orbit started at $55\ \mathrm{Mm}$, which is briefly trapped in the curved field lines beside the jet braking region before the front dissipates. For this test particle orbit, trapping in this region produces a small energy gain of approximately $3\,\mathrm{keV}$ starting at $t \approx 30\,\mathrm{s}$. Test particle orbits with higher initial vertical positions do not exhibit this behaviour and hence do not gain any energy from trapping in the loop sides.

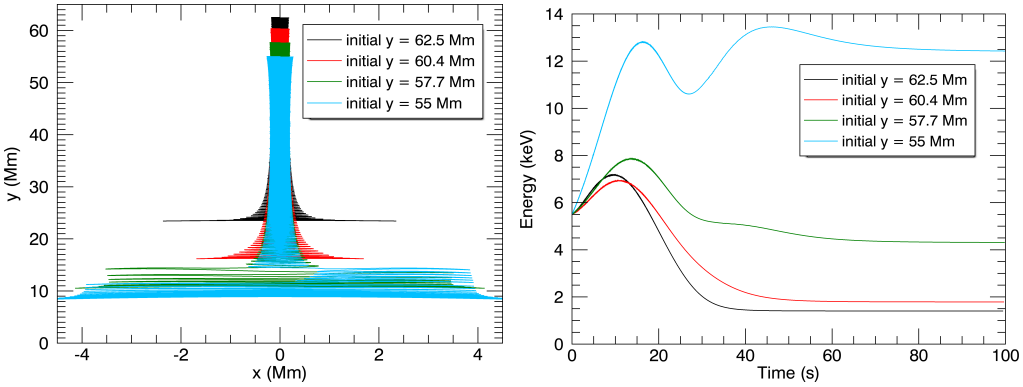

(A) Test particle trajectory (B) Test particle energy

FIGURE 6.6: Test particle trajectories (a) and kinetic energies (b) in cases where orbits become trapped in the jet braking region of a CMT (type 1 orbits). The initial conditions for these orbits are $x = 0\,\mathrm{Mm}, \theta = 75°, E_{k0} = 5.5\,\mathrm{keV}$. Initial vertical positions given in the legend.

6.3.2 Trapping in loop legs (type 2)

Test particle orbits with a lower initial pitch angle will not be trapped in the braking jet. For a low initial pitch angle and with initial horizontal position $x = 0\ \mathrm{Mm}$, orbits initialized high in the trap, inside the front, escape the trap after few or no bounces. These orbits are discussed in section 6.3.3. In this section we focus on orbits that are initialized below the jet braking region. As the front passes, these orbits become trapped between a mirror point near to the footpoint of the loop and the braking jet. We refer to these orbits as trapped at the sides of the loop, or type 2 orbits.

To demonstrate typical type 2 behaviour we again initialize four test particle orbits with varying initial vertical position at the centre of the CMT ($x = 0$ Mm), and an initial pitch angle of $\theta = 40°$. The resulting particle orbits and kinetic energies are presented in Figure 6.7. Test particles are initialized on a field line which has only one bend in it prior to the passage of the jet front. Test particles on such a field line travel between two mirror points on either side of $x = 0$ Mm. As the jet front approaches, the field lines start to curve and compress. This compression increases the magnetic field strength at the braking jet leading to particle orbits becoming confined away from the jet centre. As the trap collapses particle orbits gain energy. Towards the end of the simulation, the field lines straighten again and the test particles no longer mirror at the jet centre, but instead have access to a larger portion of the lower loop.

The energy gains of type 2 orbits do not follow the simple pattern of type 1 orbits. Very little energy is gained before the jet front passes the field line along which the test particle is orbiting. Once the jet reaches the test particle orbit location, the test particle experiences significant acceleration while trapped in the side of the loop. Furthermore we see that there are slightly different locations where orbits are trapped at the side of the loop. For instance, the orbit started at 49.5 Mm gets trapped lower in the loop leg and as a result gains energy without interruption (in comparison to the orbit started at 44.2 Mm which changes locations where it is trapped more often).

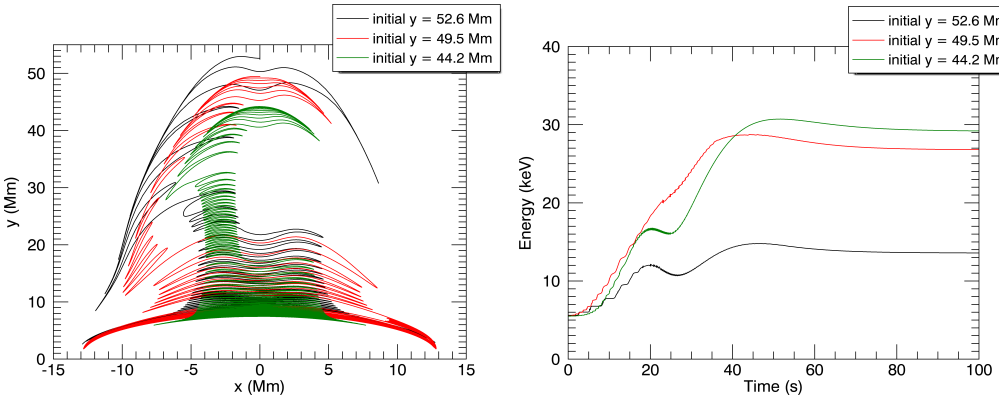

(A) Test particle trajectory (B) Test particle energy

FIGURE 6.7: Test particle trajectories (a) and kinetic energies (b) in cases where orbits become trapped in the loop legs of a CMT (type 2 orbits). The initial conditions for these orbits are $x = 0$ Mm, $\theta = 40°$, $E_{k0} = 5.5$ keV. Initial vertical positions are given in the legend.

Of the categories of orbits found in this CMT, type 2 motion shows the largest

energy gains. By varying the trap parameters it is possible to obtain energies of ~ 100 keV for electrons (see Section 6.5 for effects of trap parameters on particle motion). An example of an orbit achieving such energies is shown in Figure 6.8, which is achieved by setting $v_\phi = -3$, $\sigma = 3$, and $y_0 = 10$, resulting in a faster initial jet flow speed.

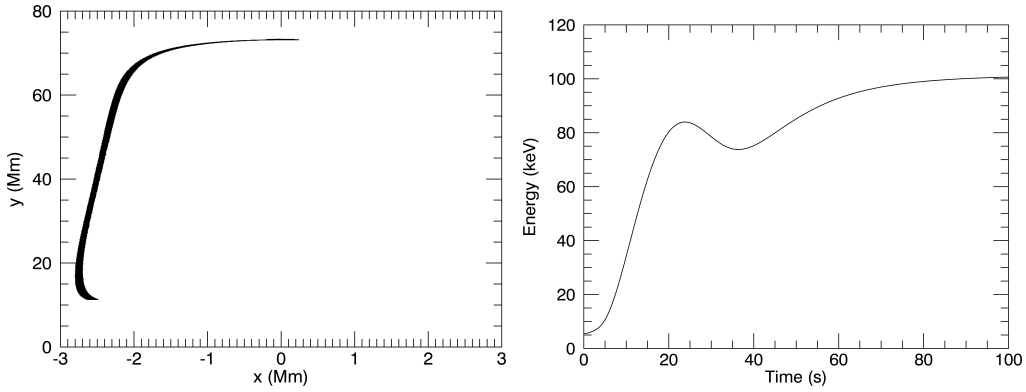

(A) Test particle trajectory (B) Test particle energy

FIGURE 6.8: Test particle orbit (a) and kinetic energy (b) for an orbit achieving kinetic energies higher than 100 keV. The trap parameters used in this simulation are the same as given in Table 6.1 with the following parameters modified: $v_\phi = -3$, $\sigma = 3$, and $y_0 = 10$. The initial conditions of the test particle orbit are: $y = 73.3\,\mathrm{Mm}, x = 0\,\mathrm{Mm}, \theta = 85°, E_{k0} = 5.5\,\mathrm{keV}$.

6.3.3 EARLY ESCAPE (TYPE 3)

As discussed in section 6.3.2, test particle orbits initialized with a low pitch angle near the jet front are unlikely to be trapped for more than a few bounces; as a result these orbits escape much earlier and do not gain as much energy as type 2 orbits or some type 1 orbits. We refer to these as type 3 orbits. To demonstrate the dependence of the type of orbit on the initial conditions, we present four orbits starting at the same position in the CMT, with varying initial pitch angle in Figure 6.9. Test particles with initial pitch angle $\theta = 15° - 20°$ develop type 3 orbits and all escape the CMT by about 20 seconds. By increasing the initial pitch angle, test particle orbits execute increasing numbers of bounces, until at $\theta = 30°$ they no longer exit the CMT within the simulation time. This is reminiscent of the findings of Eradat Oskoui et al. [2014], albeit in the context of a different CMT model. Further increases in initial pitch angle for the same initial position yield type 2 orbits and, for sufficiently high pitch angles, type 1 orbits. Among type 3 orbits, particles that are trapped longer are able to gain more energy.

In Figure 6.9, the particle orbit with initial pitch angle $\theta = 30°$ is more appropriately classified as a type 2 orbit because it remains trapped throughout the simulation time and for a portion of the orbit is confined to the loop leg. Test particles with a lower initial pitch angle have type 3 orbits. This shows that small changes in initial conditions can cause an orbit to entirely change classification.

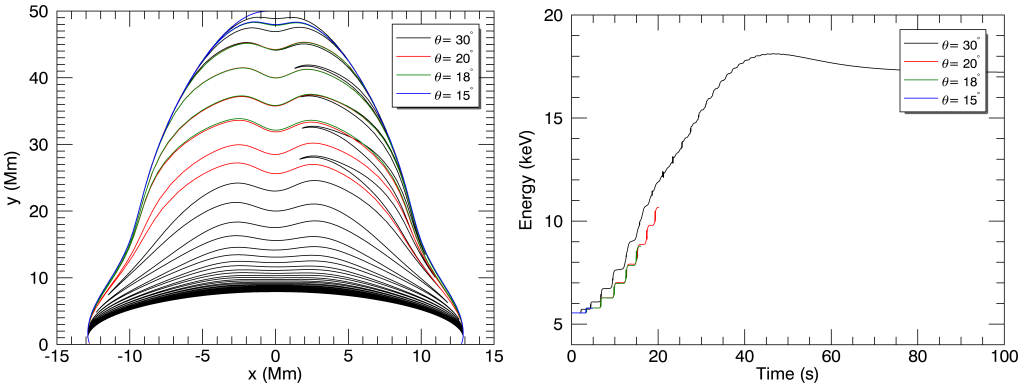

(A) Test particle trajectory (B) Test particle energy

FIGURE 6.9: Test particle trajectories (a) and kinetic energies (b) in cases where orbits exit the CMT within the simulation time (type 3 orbits), with the exception of the orbit shown in black, which is a type 2 orbit, shown for comparison. The initial conditions of the test particle orbit are: $y = 50\,\mathrm{Mm}, x = 0\,\mathrm{Mm}, E_{k0} = 5.5\,\mathrm{keV}$. The initial pitch angles are given in the legend.

Although we have presented a way of classifying particle orbits into three different types, we have also seen glimpses of when this classification method does not work as well as hoped. In particular the orbit mentioned in this section (black trajectory in Figure 6.9), as well as the highest energy orbit presented in section 6.3.1 (light blue line in Figure 6.6) both exhibit behaviour that does not quite make them fit directly into any of the categories. As shall be discussed in Section 6.4 the reasons for a given particle to be of one type rather than another depends on whether or not different parts of the CMT manage to trap the particle in a particular region. This is highly dependent on the initial conditions of the test particle orbit as well as the CMT model parameters. Nevertheless, many orbits will still be readily categorised into one of the three types of orbits described above, and as such we can investigate the effect of varying trap parameters on the different orbit types (which we will do in Section 6.5).

6.4 Discussion of Test Particle Motion and Acceleration Mechanisms

6.4.1 Trapping locations

The behaviour of particle orbits outlined in section 6.3 may be explained by considering the positions of possible mirror points within the CMT. Mirroring of a particle occurs due to terms on the right hand side of Equation (2.21). In our model mirror points can occur due to field line curvature (first term on the right hand side of Equation (2.21)) and strengthening of the magnetic field (third term on the right hand side of Equation (2.21) [2]). For a given test particle orbit, mirror points may be located on either side of the indentation caused by the braking jet (regions labelled a in Figure 6.10), further up the loop legs just below the front (regions labelled b in Figure 6.10) as well as near the footpoints of the loops (regions labelled c in Figure 6.10).

Type 1 orbits are trapped between two mirror points located on either side of the indentation around the region of the braking jet (labelled a in Figure 6.10). Type 2 motion is caused by mirroring between points in regions c and b, c and a, or b and a. For example, trapping between mirror points in regions b and c occurs for the orbit started at $49.5\,\mathrm{Mm}$ (red line) in Figure 6.7, whereas the test particle orbit initialized at $44.2\,\mathrm{Mm}$ (green line) in Figure 6.7 mirrors between points in regions a and b. As the jet progresses downward, the magnetic field strength increases, causing some particle orbits to be trapped outside of the jet braking region, resulting in type 2 motion. In order to see an appreciable front in this CMT model the magnetic field strength in the front needs to be comparable to the magnetic field near the footpoints. As a result, test particle orbits with a sufficiently small initial pitch angle to escape the jet braking region gain enough energy within a few bounces to escape the trap.

6.4.2 Acceleration mechanisms

As discussed previously, there are two mechanisms that can help explain particle acceleration in CMTs: betatron acceleration and Fermi acceleration. In this section we investigate the energy evolution of two particle orbits and whether we can attribute most of the acceleration of particular types of orbits to either of these

[2] There are no contributions to the parallel guiding centre velocity by parallel electric field since $E_{\parallel} = 0$ in ideal MHD. This means that mirroring due to the parallel electric field cannot occur [see Threlfall et al., 2016a].

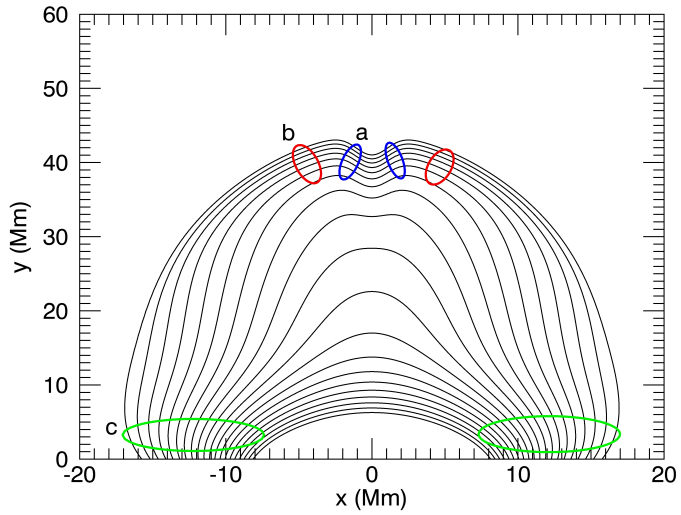

FIGURE 6.10: Approximate locations of possible mirror points for particles trapped in our CMT model are circled. The test particle orbit's initial conditions determine in which regions it is mirrored. Black lines are magnetic field lines. Regions a and b may contain mirror points because of the higher magnetic field strength associated with the braking jet. Mirror points located in the region c occur due to the stronger magnetic field at the solar surface.

acceleration mechanisms. We first consider Figure 6.11, which shows how the energy of two test particles (of type 1 and 2) changes throughout their respective orbits. The type 1 orbit (Figure 6.11a) corresponds to the orbit started at 55 Mm (light blue line) in Figure 6.6. This orbit demonstrates the typical motion of type 1 particles when trapped in the braking jet, in addition to showing some trapping in the loop sides lower in the orbit. Type 1 orbits experience an initial increase, followed by a decrease of energy when trapped in the braking jet. This is caused in part by initially increasing magnetic field strength while the jet is propagating through regions of low background field, followed by decreasing magnetic field strength when the front encounters regions of stronger field in the lower loops causing the front to dissipate. If the particle orbit exits the braking jet before the jet dissipates then the particle orbit can gain energy in the loop sides, as shown in Figure 6.11a.

The type 2 orbit (Figure 6.11b) corresponds to the orbit started at 44.2 Mm (green line) in Figure 6.7. In this case most of the energy is gained in two regions of the particle orbit. The first region occurs when the particle is confined to the side of the loop for $40\,\mathrm{Mm} \geq y \geq 30\ \mathrm{Mm}$, while the second occurs when it is trapped lower down for $15\,\mathrm{Mm} \geq y \geq 9\,\mathrm{Mm}$ (although less dramatic increases are also present at other times when trapped in the loop sides). Similar to the type 1 orbit, the energy gains are partially caused by increases of the magnetic field, however there is no substantial decrease in magnetic field strength when the front dissipates due to the particle being trapped outside of the braking jet.

Despite the importance of the magnetic field strength in determining the energy of the test particle orbit, Fermi acceleration can also play a role. In Figure 6.12 the distance travelled by the particle orbit along a field line between mirror points is compared to the energy for type 1 and 2 particle orbits. The bounce distance of the type 1 orbit decreases for $t < 10\ \mathrm{s}$ during which time the orbit energy increases, indicating possible Fermi acceleration. The same is true for the type 2 orbit for $t < 25\,\mathrm{s}$, indicating Fermi acceleration may be important in this case also. Increases in the distance between mirror points for $t > 40\ \mathrm{s}$ for both orbits may contribute to the energy loss in these time periods.

As a result of the complicated nature of our model, it may be difficult to directly attribute energy gains or losses to a single mechanism. Significant changes in distance between mirror points (indicative of Fermi acceleration) may be accompanied by changing magnetic field strength due to the orbit entering a different region of the CMT. This results in energy changes that are difficult to attribute to either Fermi acceleration or the betatron effect alone.

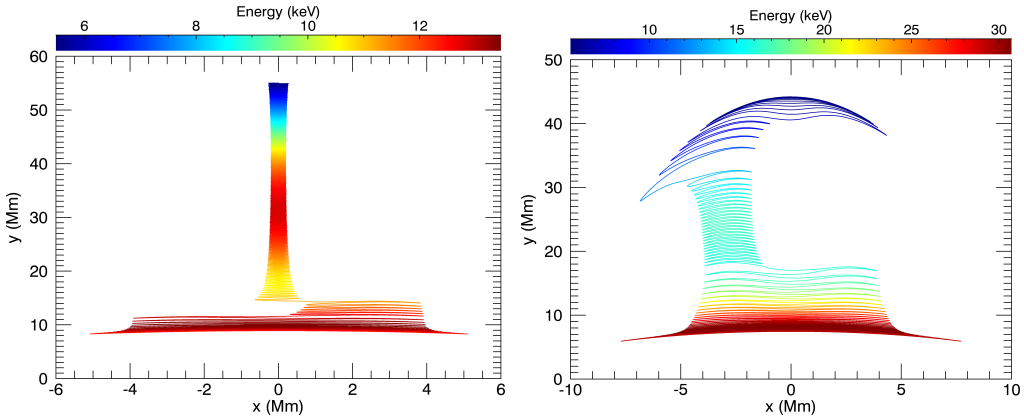

(A) Type 1 orbit (B) Type 2 orbit

FIGURE 6.11: Particle orbit energy, indicated in colour, with respect to position for type 1 and 2 orbits. The type 1 and 2 orbits correspond to orbits started at 55 Mm (light blue curve) in Figure 6.6 and at 44.2 Mm (green curve) in Figure 6.7 respectively. The type 1 orbit shows an initial increase in energy, followed by a decrease while trapped in the braking jet. When the orbit escapes the jet and becomes trapped in the side of the loop there is an associated increase in energy. The type 2 orbit shows sharp increases in energy for $40\,\mathrm{Mm} \geq y \geq 30$ Mm and for $15\,\mathrm{Mm} \geq y \geq 9\,\mathrm{Mm}$.

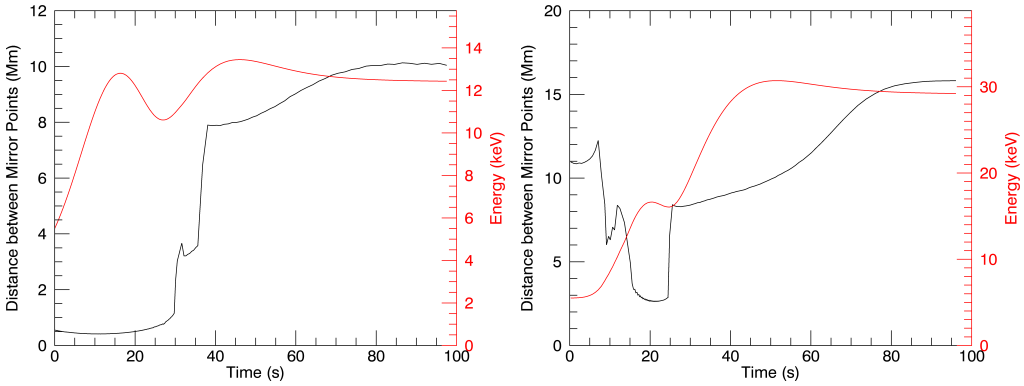

(A) Type 1 orbit (B) Type 2 orbit

FIGURE 6.12: Distance between bounces (black) and kinetic energy (red) with respect to time of type 1 and 2 particle orbits. The type 1 and 2 orbits correspond to orbits started at 55 Mm (light blue curve) in Figure6.6 and at 44.2 Mm (green curve) in Figure 6.7 respectively. We see that the distance between bounces decreases in the early stages of the type 1 orbit (for $t < 10\,\mathrm{s}$) and for a significant portion of the type 2 orbit ($t < 25\,\mathrm{s}$), which may be indicative of Fermi acceleration affecting the energy in addition to the betatron effect.

6.5 Effect of Varying Parameters on Particle Orbits

To analyze the effect of changing parameters in the CMT model on the types of particle orbits, in this section we investigate the connections between the orbit classification and the average position of the test particle orbit. The average position is determined by the integral

$$\overline{\mathbf{x}} = \frac{1}{t_{\text{final}}} \int_0^{t_{\text{final}}} \mathbf{x} dt, \tag{6.14}$$

where t_{final} is the time of the test particle's escape from the trap, or the simulation time (if the orbit remains trapped). In this section $\overline{x}$ and $\overline{y}$ refer to the average position in the x and y directions respectively, while $\overline{\mathbf{x}} = (\overline{x}, \overline{y})$. Type 1 orbits are symmetric about $x = 0\,\text{Mm}$ for most of their duration, which restricts the average x-position to $\overline{x} \approx 0\,\text{Mm}$. This is not the case for type 2 orbits, which spend significant amounts of time in the loop legs, slightly displaced from the centre of the trap resulting in $|\overline{x}| > 0\,\text{Mm}$. Type 3 orbits (particularly those which exit the trap after few or no bounces) have $|\overline{\mathbf{x}}| \gg 0\,\text{Mm}$. These orbits are also identifiable by their small maximum energies. It is important to note that $\overline{\mathbf{x}}$ is a proxy for determining the general behaviour of particle orbits and does not correspond to the location that the orbits spend most of their time at.

The initial conditions used in the investigation are presented in Table 6.2. These values are chosen to represent a meaningful part of the parameter space for the initial conditions, which also return behaviour of interest. These values are not intended to be an accurate description of the distribution of particles in the coronal plasma during a solar flare, but are meant to illustrate how changes in trap parameters influence orbit behaviour. The results are shown in Figure 6.13. In Figure 6.13a, type 1 orbits are clearly identifiable as the peak near $x = 0\,\text{Mm}$. The two peaks on either side of $x = 0\,\text{Mm}$ correspond to type 2 orbits.

Figure 6.13b shows that type 2 motion can be divided into two different categories whose average positions are fairly distinct. We label these subcategories 2a and 2b for decreasing $\overline{y}$ respectively. For certain choices of trap parameters these sub-categories may disappear (see Figure 6.14c) or another category may appear (see Figure 6.14b), which we will call 2c. Type 2c particles have average positions satisfying $\overline{y} < 20\,\text{Mm}$ and $|\overline{x}| > 13\,\text{Mm}$. For parameters and initial conditions for each of the following runs see Table 6.3.

The results of our test runs are shown in Figures 6.14 and 6.15, as well as in Tables 6.4 and 6.5. Figure 6.14 illustrates how the results shown in Figure 6.13b

Label	x	y	θ	E_{k0}
IC1	0, 2 Mm	[45,60] Mm	$[25°, 75°]$	5.5 keV
IC2	0, 2 Mm	[60,90] Mm	$[25°, 75°]$	5.5 keV
IC3	0, 2 Mm	[40,55] Mm	$[25°, 75°]$	5.5 keV

TABLE 6.2: Initial conditions used in different runs for investigating the effects of varying trap parameters on particle orbit behaviour. In each case x takes on two values, y takes on 15 evenly spaced values in the indicated range, and θ takes on 20 evenly spaced values in the indicated range. Initial conditions IC1 are used in conjunction with the run using basic trap parameters (see Table 6.1) and the run with a steeper front. Conditions IC2 are used in the case of a faster initial jet, while IC3 are used with a larger braking jet.

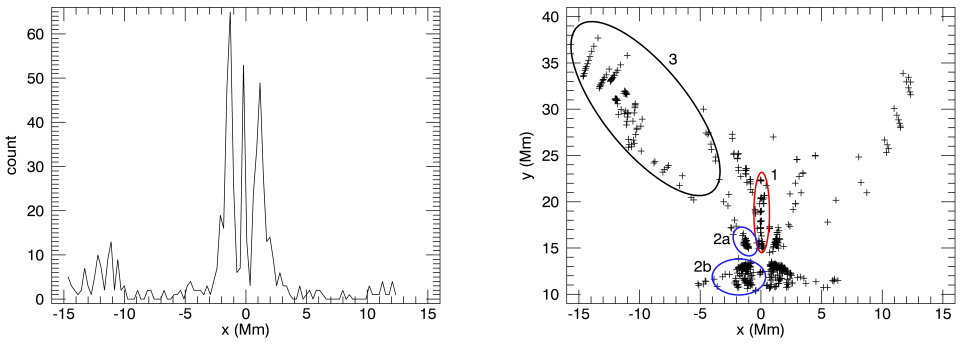

(A) Histogram of average x position (B) Average position

FIGURE 6.13: Histogram of average x position (a) and the average coordinate $\overline{\mathbf{x}} = (\overline{x}, \overline{y})$ (b) for 600 particle orbits computed with the initial conditions IC1 given in Table 6.2 for the trap parameters given in Table 6.1. The distinction between type 1 and type 2 orbits is clearly visible in panel A, with type 2 orbits having an $|\overline{x}|$ between 1 and 5 Mm, while type 1 orbits have an $|\overline{x}|$ less than 1 Mm. Panel B shows the regions different orbit classifications occupy when their average coordinates are computed.

	Parameters	Initial conditions
Figure 6.14a	Basic	IC1
Figure 6.14b	Basic except $v_\phi = -3, \sigma = 3$	IC2
Figure 6.14c	Basic except $d = 0.8, w = 0.5$	IC3
Figure 6.14d	Basic except $\alpha = 2.0$	IC1

TABLE 6.3: Trap parameters and test particle orbit initial conditions used to examine the effect of changes in trap parameters on particle orbits. The basic parameters are given in Table 6.1

change when parameters are varied according to the categories in Table 6.3. Figure 6.15 shows histograms of the number of particle orbits per given energy. Table 6.4 counts the number of times at which each type of orbit is observed in each test run. Table 6.5 shows the maximum energy obtained by any orbit for each orbit classification in each test run, as well as the average of the maximum energy values.

Figure 6.14a shows the average test particle orbit positions from Figure 6.13b, where the maximum energy of each orbit defines the colour of each point. The highest energies are achieved by particle orbits of type 2a, followed by type 2b and type 1. Type 2b orbits show higher average maximum energies than type 1, although the most energetic orbit in both categories achieves a kinetic energy of approximately 50 keV. This indicates that type 1 orbits are not as efficient at energizing particles as type 2 orbits are. Type 2a orbits are similar to that shown in Figure 6.8 (in that they are trapped between mirror points in regions a and b in Figure 6.10). In contrast, type 2b orbits are similar to those started at $52.6\,\mathrm{Mm}$ and $49.5\ \mathrm{Mm}$ from Figure 6.7, and are trapped further down the loop leg.

Increasing the initial flow velocity of the braking jet from its value in the basic parameters (see Table 6.3) accelerates test particle orbits to higher energies, as can be seen in Figure 6.14b, and from the red curve in Figure 6.15. Table 6.5 shows increases in the maximum and average kinetic energy obtained by the orbits, with the most energetic particles reaching up to $95.2\ \mathrm{keV}$ in comparison to $65.4\ \mathrm{keV}$ obtained with the basic trap parameters. Figure 6.14b shows a new subset of type 2 particles with $|\overline{x}| > 10\,\mathrm{Mm}$ and $\overline{y} < 20\,\mathrm{Mm}$, which we refer to as type 2c (labeled in Figure 6.14b). Type 2c orbits correspond to particles trapped very low in the loop legs and also show high energy gains. These orbits remain confined in the loop leg at the end of the simulation after the jet front has dissipated (between mirror points b and c in Figure 6.10, albeit with mirror point b being located very close to the location of mirror point c). This is due to the increased compression of the lower loops caused by the faster jet front. A rebounding of the lower loops after the dissipation of the front could make the average position of these particle orbits

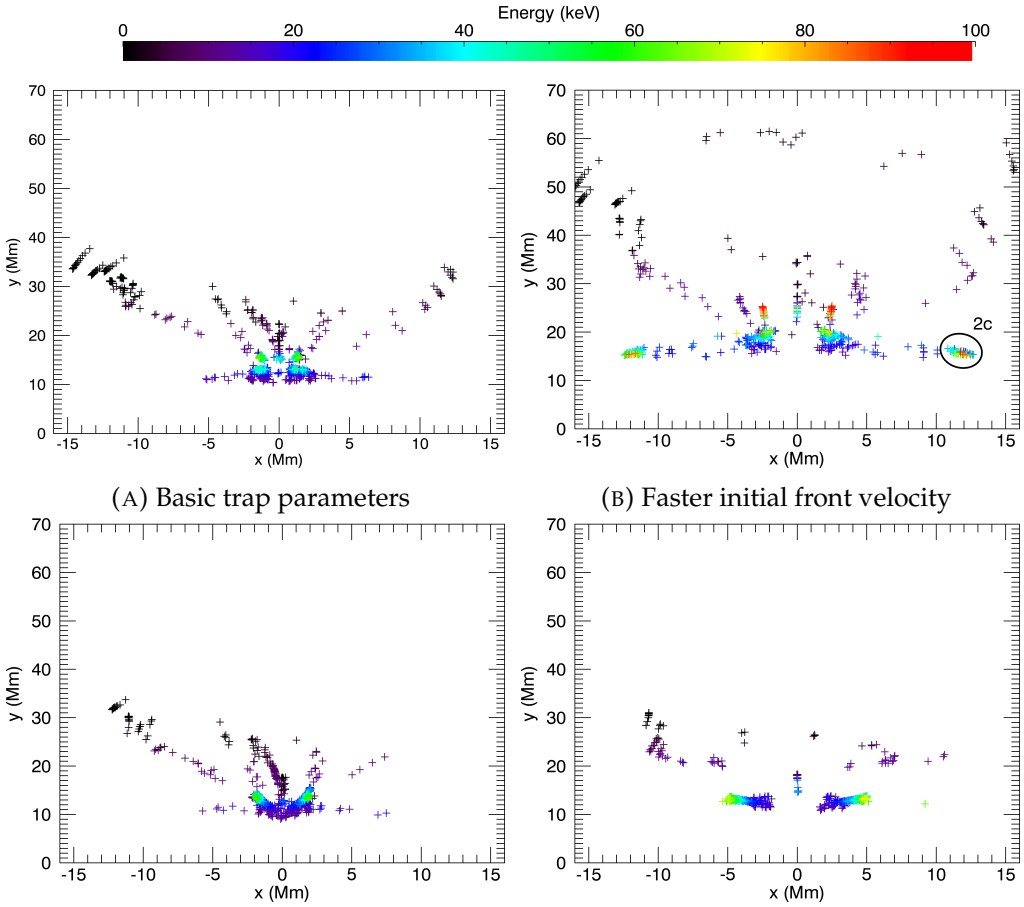

(A) Basic trap parameters

(B) Faster initial front velocity

(C) Larger jet braking region

(D) Steeper front

FIGURE 6.14: Average position (crosses) and energy (colour) of 600 particle orbits for various trap parameters. Trap parameters and test particle orbit initial conditions are given in Table 6.3.

much more similar to those of type 2b, as they would no longer be confined to a small region in one of the loop legs. In addition to a new subcategory of particle orbits, an increase in initial flow velocity results in the particle orbit categories being more spread out in terms of average position. This indicates particle orbit categories are more distinct, with less overlap between categories. There is a general increase in $\overline{y}$ for particle orbits of type 3 (seen in Figure 6.14b). This is due to the orbits and the braking jet being initialized at a higher position so that the jet front would have more time to come to a stop. For orbits which remain trapped throughout the simulation $\overline{y}$ does not change as much because σ is adjusted so that the front stops at a similar height as in the basic parameter case. Table 6.4 shows

that a faster front is more efficient at trapping particles, particularly in type 2 orbits, in comparison to a slower front.

Increasing the size of the jet braking region results in less distinction between orbits of type 2a and 2b (see in Figure 6.14c). The maximum energy achieved by type 1 particles is also reduced by a larger jet braking region; the energy gains made by all other orbits remain relatively unchanged from those seen in the case with basic trap parameters (as can be seen in Table 6.5).

Finally, increasing the steepness of the front caused by the braking jet results in a stronger magnetic field in the jet braking region. The stronger magnetic field in the braking jet region causes trapping of particle orbits in this region to become much less frequent (see Table 6.4), which results in type 2 orbits becoming more frequent. In particular, all type 2 orbits obtained are of type 2b. We also see a modest rise in maximal energy of type 2 orbits compared to the case with basic trap parameters. The maximum energy achieved by a type 1 orbit is lower, only $38.6\ \mathrm{keV}$, in comparison to $50.9\ \mathrm{keV}$ for the basic parameter case. The average of the maximum energies of type 1 orbits is slightly higher ($22\ \mathrm{keV}$ compared to $18.1\ \mathrm{keV}$ for the basic parameters). Type 3 orbits show small increases in energy (both maximum and average over all type 3 orbits) in comparison with the basic parameter case.

In each of the cases outlined above the populations of particle orbits generated depend both on the magnetic field structure of the CMT and also on the initial conditions of the test particle orbits. The structure and evolution of the magnetic field is of great importance for the possibility of different populations of particle orbits occuring. For instance, the presence of different subcategories of type 2 orbits depends on the velocity and shape of the front. For slower jet fronts it is not possible to obtain populations of particle orbits of type 2c. Conversely, increasing the steepness of the front causes the type 2a orbits to disappear, leaving type 2b orbits the dominant behaviour in this test run. The initial conditions of the test particles also strongly influences particle orbit behaviour. For an individual particle orbit, small changes in initial conditions (such as its initial position with respect to the front) can result in significantly different behaviour. For example, for a given pitch angle, horizontal displacement of the initial position can change the field line orbited by the particle, together with the location of possible mirror points. This may cause particles to change trapping behaviour. These findings suggest that it may be very difficult to predict the behaviour of a given particle orbit based on initial conditions alone, particularly when trying to differentiate between different subcategories of type 2 orbits.

The effect of different parameter regimes on test particle orbit energies is shown in a histogram of maximum orbit energies for each of the runs discussed previously (see Figure 6.15). In comparison to the basic parameters, Figure 6.15 shows that increasing the speed of propagation of the jet front causes an increase in the number of high energy orbits. A larger jet braking region causes more trapping and accelerates more particle orbits to modest energies in the range of 10 keV to 20 keV, however fewer orbits gain energies beyond 35 keV. Finally a steeper front produces a dramatic increase in test particle orbits with energies in the range of 15 to 50 keV. Few orbits are left that have energies less than 15 keV.

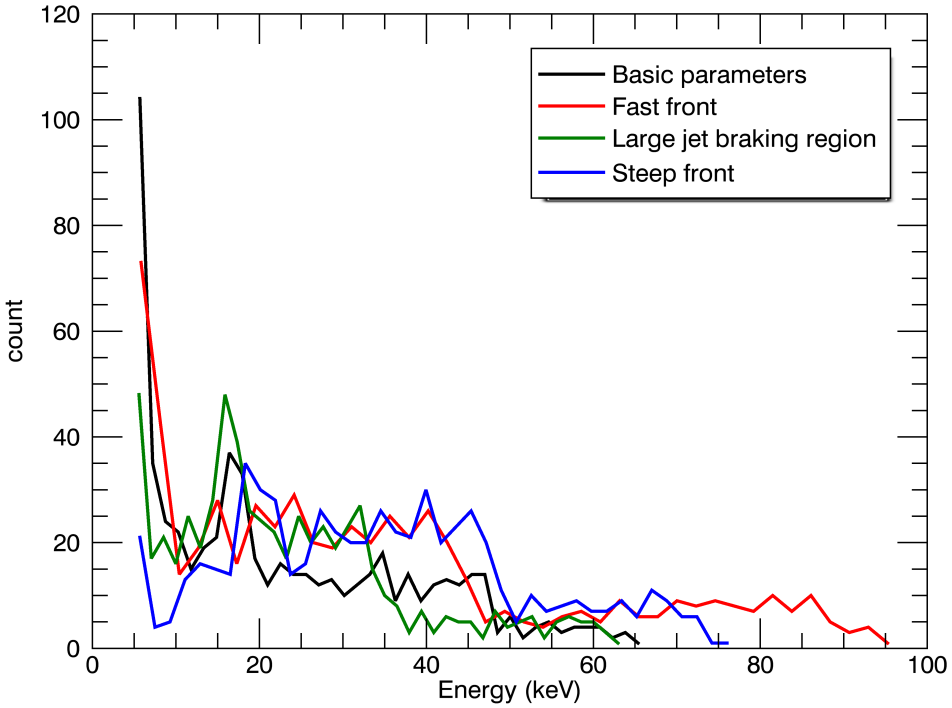

FIGURE 6.15: Particle orbit energy frequency for trap parameters given in Table 6.3. The maximum kinetic energy of each particle orbit is counted.

Our results may be explained as follows. A faster jet results in more pileup of magnetic flux at the jet front, producing more energy gain and altering the trapping characteristics to favour type 2 motion more than with a slower jet. A larger braking jet region results in more trapping, however with no increase in magnetic field

	Basic	Fast Front	Large jet braking region	Steep Front
type 1	78	52	99	21
type 2a	75	66	362	
type 2b	260	205		497
type 2c		127		
type 3	187	150	139	82

TABLE 6.4: Particle orbit frequencies for different test runs.

Orbit type	Basic		Fast front	
	maximum	average	maximum	average
1	50.9	18.1	73.1	17.5
2a	65.4	45.4	95.2	74.5
2b	49.4	29.4	86.2	34.6
2c			93.3	49.1
3	17.2	8.9	21.7	11.1
Orbit type	Large jet braking region		Steep front	
	maximum	average	maximum	average
1	34.5	17.2	38.6	22.0
2a	63.0	31.1		
2b			76.0	39.8
2c				
3	16.9	10.5	19.0	12.4

TABLE 6.5: Maximum and average kinetic energies (in keV) obtained for each type of particle orbit for parameter values and initial conditions shown in Table 6.3. Average energies are calculated by averaging the maximum energies achieved by each particle orbit for each orbit type.

strength, the orbits do not gain as much energy as in the case of the faster jet or the steeper front, yielding many orbits with small energy gains. An increase in the steepness of the front results in a significantly greater magnetic field strength, which produces much less trapping in the jet braking region. This is because the magnetic field strength is more uniform between the centre of the trap and region a in Figure 6.10. In this scenario test particle orbits are more efficiently trapped in the loop legs, resulting in type 2 orbits.

6.5.1 Many more particles

This investigation has been primarily targeted at investigating the effect of modifying parameters on the types of orbits observed, and we are not trying to accurately model the non-thermal particle population within the CMT. For these

purposes the 600 particles used in each simulation run are sufficient to get a good idea of what the particle behaviour is. Nevertheless, it would be nice to have a bigger sample to check that our classification has captured all the orbit behaviour that can occur in this CMT model. To do so we ran 25000 orbits in the fast front CMT setup (same as for Figure 6.14b, see also Table 6.3). A plot of the resulting average positions is shown in Figure 6.16a. We note that although the distribution of average positions is more continuous than it was for a lesser number of particles, the maximum energy particles can obtain remains the same. Furthermore, there may be a lot of overlap if we are plotting individual particles, so to get an idea of the relative frequency of orbits we plot a 2D histogram of the number of particles per average position bin in Figure 6.16b. Here we see that the most common particle orbit types (type 2b, and c), when examining the simulation with only 600 particles, are also the most common when running 250000 particles. This confirms that the orbits we found when running only 600 particles represent an accurate description of the types of orbits which are possible in this CMT model.

6.6 Conclusion

The addition of a braking jet to previously studied CMT models has resulted in new types of particle orbits being observed. Whereas in the absence of a braking jet particle orbits were confined between a pair of mirror points located at varying distances, but symetrically along the loop legs [see e.g. Giuliani et al., 2005], the presence of the indentation at the looptop caused by the braking jet results in the possibility of additional mirror points appearing on either side of this indentation. This results in the possibility of particles being trapped on one side of the CMT, or within the jet region. The relative frequency of each type of behaviour is dependent on the trap parameters. The largest energy gains are observed for faster initial front velocities. A larger indentation caused by the jet results in more particles being trapped within the indentation, but lower maximum energies. On the other hand, a steeper front results in more particles being trapped in the sides of the loop legs instead of the indentation region, and somewhat higher maximum energies.

Although the contribution of particles in CMTs to overall energy spectra is likely very small [see Birn et al., 2017], as they tend to be trapped in the solar corona rather than precipitating at the loop footpoints and their energy gains are generally not all that high, they may nevertheless contribute to looptop emission [e.g. Somov and Kosugi, 1997]. Therefore, since the presence of indentations caused by reconnection outflows has been observed in other studies [see e.g. Karlický and

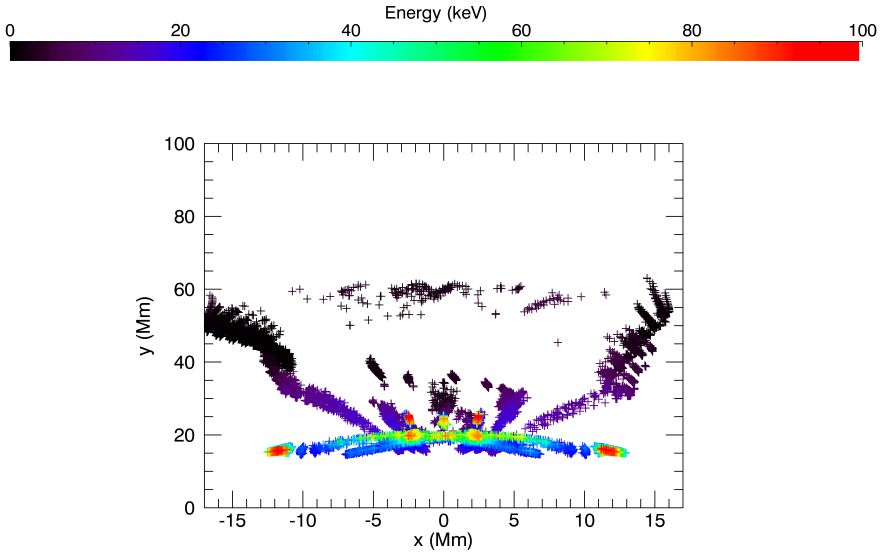

(A) Scatterplot of the average positions and energies

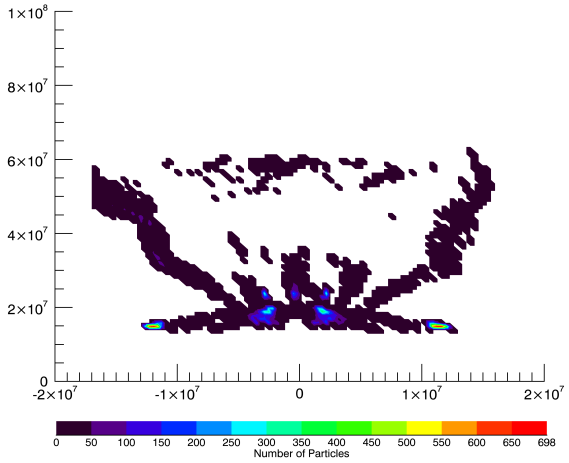

(B) 2D histogram of average positions

FIGURE 6.16: Panel A: Average position (crosses) and energy (colour) of 25000 particle orbits for fast front trap parameters (see Table 6.3). Panel B: 2D histogram of average positions showing that the most commonly observed orbit types are also found when only running 600 particles, since the particles still tend to be clustered where particles clustered when fewer orbits were run.

Bárta, 2006, Birn et al., 2017], the behaviour observed here may indeed occur and be of relevance to the overall picture of particle dynamics in large solar flares.

Chapter 7

Conclusion

Understanding particle acceleration is key to understanding solar flares. Multiple mechanisms are capable of accelerating particles to energies sufficient to produce observed HXR emission during solar flares. In this thesis we primarily focused on investigating the parallel electric field approach, however we also studied particle acceleration and dynamics in a new analytical model of collapsing magnetic traps.

Parallel electric fields are generated during the process of magnetic reconnection through non-ideal terms in Ohm's law. Although there exist multiple non-ideal terms, one of the most commonly used terms is the resistivity term, ηj. Collisions between particles imply a Spitzer resistivity, η_{sp}, which for typical values in the corona is many orders of magnitude too low to produce a sufficiently high reconnection rate (and hence a sufficiently high parallel electric field). As a result, wave-particle interactions are postulated to produce an anomalous resistivity several orders of magnitude higher than the Spitzer resistivity. Anomalous resistivity is often used in simulations of magnetic reconnection, including ones which are subsequently used to study particle acceleration [such as Gordovskyy et al., 2010a,b, Threlfall et al., 2016b]. However, despite performing simulations where the resistivity is fundamentally caused by particle scattering, test particle simulations typically do not incorporate scattering, and for the ones that do it is usually at the Coulomb collision rate which is responsible for the much weaker Spitzer resistivity [e.g. Gordovskyy et al., 2014, Burge et al., 2014]. In this thesis we examined how scattering at much higher rates due to anomalous resistivity affects particle acceleration in multiple reconnection scenarios.

We first examined a simple 1D scenario which involved acceleration and scattering, with both being proportional to a parameter, which we called the anomalous resistivity. Here particles were accelerated by an imposed electric field, while scattering affected the particle's motion along the one coordinate by scattering the pitch angle, while also conserving energy. Clearly there are significant consistency issues with this approach, chiefly that the fields imposed

are unrealistic, however this exercise was meant to demonstrate that there might be some interaction between the electric field accelerating the particles, and the scattering slowing their progress (if not decreasing their energy). We found that there is an optimal resistivity, in the sense of the resulting particle orbit duration distribution, which results in particles exiting the box at the highest rate. We also found a dependence of the pitch angle distribution at the end of the particle orbits on the anomalous resistivity. Generally, higher resistivity resulted in a pitch angle distribution which was peaked towards $\cos\theta = -1$ (due to our choice of electric field direction), whereas lower resistivities were unable to impact the initial pitch angle distribution very much. This resulted broadly in three regimes: when the resistivity was very low particle behaviour was most influenced by their initial conditions (this is to say they propagated with whatever parallel velocity they were initialised with); medium resistivities resulted in particles being accelerated by the parallel electric field, and although the effects of scattering were noticeable, the electric field dominated resulting in progressively shorter orbit durations with increasing resistivity; and finally for very high resistivity the scattering played an important role in particle dynamics, preventing ever shorter particle orbit durations and causing longer orbit durations once more. A more detailed study of the relationship between scattering and acceleration could be performed in the context of this model, for example by incorporating energy loss terms into the scattering process. This model could also be extended in a very straightforward fashion to include regions without an electric field, but still with scattering. This is inspired by work done on pitch angle scattering inhibiting particle transport through flare loops [Bian et al., 2016, Bian et al., 2017]. Here a region without an electric field could be appended to a region with an electric field representing the flare loops below the reconnection region. This would allow an investigation into the effects different scattering rates within the flare loops have on the final particle pitch angle and orbit duration distributions.

Although our 1D model was useful for establishing that pitch angle scattering could play an important role in particle dynamics, more realistic fields need to be considered. To do so, we performed 2D MHD simulations of x-point magnetic reconnection into which test particles were injected. Significant differences were found between scattered and unscattered orbits, with scattering leading to multiple transits of the reconnection region. This effect produced energy spectra that extended to higher energies in the presence of pitch angle scattering compared to without it. We also examined the differences in the scattering rates between spatially dependent scattering (where the rate was proportional to η/η_{sp}, with the

Spitzer resistivity being calculated based on local plasma parameters). We found that this way particles experience less scattering away from the central current sheet region, resulting in fewer very high energy orbits compared to a high rate of scattering throughout. However, if scattering occurs at a constant rate which is lower in the current sheet but higher in the separatrices when compared to the spatially dependent scattering, observed energies are lower. Like in the 1D case, we find that scattering results in longer orbit durations, as well as some differences in the pitch angle distribution, however because the geometry of the experiment is much more complicated, and the range of scattering rates much lower, than in the 1D case, the differences in the pitch angle distribution are much smaller also. Finally, large differences are observed in the final exit position of the particles, with more scattering leading to more particles exiting in the reconnection outflow region.

In comparison to previous work on particle acceleration in fields derived from 2D MHD reconnection simulations [such as Gordovskyy et al., 2010a,b], the kinetic energies we obtain are lower due to a smaller length scale used and thus a smaller region which accelerates particles. Normally the results could still be compared because the particle energies could be scaled to account for different lengthscales, however because scattering introduces an additional lengthscale, namely the particle mean free path, this is no longer possible. Previous work on particle acceleration in the presence of scattering has been performed [see e.g. Burge et al., 2014], however the pitch angle scattering rate was at the Coulomb collision rate. Since our pitch angle scattering rate is motivated by an anomalous resistivity, it is several orders of magnitude higher than the Coulomb collision rate. Burge et al. [2014] did find particles traversing the reconnection region multiple times, but the effect on energy spectra was not as pronounced as in our case.

There are multiple possible extensions to these 2D experiments such as more complex field geometries, for example fragmenting current sheets [such as in Gordovskyy et al., 2010b]. A more realistic temperature profile giving a better approximation of the Spitzer resistivity could also help to give a more accurate picture of the scattering rate. The use of scattering rates which are motivated by specific plasma instabilities would also give a more accurate picture of the scattering that the particles experience. This may be difficult to do in the single fluid MHD picture, because the plasma instabilities are dependent on the electron and ion temperatures. This could be addressed by looking at multi-fluid simulations, or PIC simulations to derive scattering rates which are more representative of the plasma processes going on in the reconnection region.

Another possible extension is to consider the same particle scattering model, but in the context of 3D reconnection simulations. This is the approach we took, and it involved investigating particle acceleration and pitch angle scattering in the context of 3D separator reconnection, similar to Threlfall et al. [2016a]. In this case pitch angle scattering again affected the particle trajectories, however there was very little effect on the particle energy spectra when compared to the 2D simulations. This is likely due to geometrical differences between the 2D and 3D experiments (for instance, size of the reconnection region, different plasma flow patterns, and length of the separator). On the other hand, scattering produced a significant change in the pitch angle distribution with significantly fewer particles at pitch angles near $180°$. Similar to the previous cases, scattering tended to make orbit durations longer. One significant difference between the 2D and 3D simulations is that for the 3D case it is possible to obtain reconnection rates, and hence parallel electric fields that are not constant with respect to the applied resistivity, which was impossible in our 2D simulations. This way we could investigate the effect of different anomalous resistivities on particle acceleration and scattering. We found relatively little difference between the final pitch angle distributions for different resistivities, however there were significant changes to the energy spectra and orbit duration distributions. A higher resistivity tended to cause higher observed particle energies, as well as shorter orbit durations. More complex and realistic models of resistivity, specifically a current dependent resistivity, would be interesting to investigate. This is particularly important in the 3D context as these simulations are a more accurate representation of the gradual buildup followed by explosive release of energy which characterizes solar flares (in contrast to the steady state picture presented here for the 2D case).

Previous work by Threlfall et al. [2015, 2016a] suggested that particles could be accelerated at 3D magnetic separators to energies sufficient to produce HXR emission in solar flares. Because the work performed in these papers does not take into account particle scattering, the energy spectra produced can be scaled to account for different separator lengths. As mentioned before, in our work the scattering mean free path introduces an additional length scale so it is not possible to simply rescale the particle energies to account for different separator lengths. It may be worthwhile to examine different separator lengths, however it is important to pick an appropriate scattering model, since increasing the size of the separator will necessarily increase the orbit duration if the scattering rate is unchanged.

Further extensions to this work could involve using scattering rates motivated by, for example, PIC simulations of 2D reconnection to specify a more realistic

scattering rate in the 3D separator case. It is also important to examine the effect (if any) that pitch angle scattering has on particle acceleration in other configurations pertaining to solar flares such as kinking flux tubes [e.g Gordovskyy et al., 2013, 2014, Threlfall et al., 2018].

In addition to examining particle acceleration and scattering by parallel electric fields, we also examined particle dynamics and trapping in collapsing magnetic traps. CMTs are one possible method of accelerating and trapping an energetic particle population which could produce looptop HXR emission in solar flares [e.g. Somov and Kosugi, 1997]. Previous numerical studies [e.g. Grady et al., 2012, Eradat Oskoui et al., 2014] have shown that particles become trapped in the flare loop between mirror points located towards the footpoints of the loop (this would depend on their pitch angle, so for instance particles with a pitch angle near 90° would get trapped very near the loop apex, while those with pitch angle near to $\theta = 0, 180^\circ$ might mirror at the footpoints, or escape the trap through the footpoints altogether). Separate work in the context of dipolarisation fronts in the Earth's magnetotail, that similar loop-like structures are deformed by a reconnection outflow [e.g. Sitnov and Swisdak, 2011, Khotyaintsev et al., 2011], and particle acceleration is observed to occur in these scenarios [Artemyev, 2014]. In our work we combined these two models, introducing into the CMT a region of strong compression of the field along with an indentation in the loop apex, both caused by a jet outflow. We found that particles can gain energies up to $100\,\mathrm{keV}$, from an initial energy of $5.5\,\mathrm{keV}$. This is broadly consistent with the findings of Grady et al. [2012], who found increases in energy of factors up to 50. We additionally find new types of trapped orbits, ones which are trapped within indentation, and ones which might start out in the indentation, but quickly escape and are instead trapped on one side of the loop. The relative frequency of the types of orbits observed changes for different trap parameters.

Since this work was published, similar orbits have been observed in test particle simulations performed in background fields from MHD simulations [Birn et al., 2017], however they also found that the energy gain was not significant enough to produce high energy power-law tails in the energy spectrum. Nevertheless, the collapsing trap mechanism may be able to enhance fluxes of a power-law seed population.

As mentioned regarding extensions to the 1D model, pitch angle scattering in flare loops can affect particle transport from the flaring region to the chromosphere [see e.g. Bian et al., 2016]. The same principle could be applied to CMTs by examining the effect of pitch angle scattering on particle transport. In this case

the scattering will not be connected to the same plasma instabilities that we had in mind in the reconnection case, but will arise due to turbulence in the flare loops. Particle transport in CMTs has already been examined taking into account Coulomb collisions [Bogachev and Somov, 2009], and has been shown to affect particles with energies less than $10\,\mathrm{keV}$. Since Coulomb collisions become less effective on particles with higher energies, they do not significantly affect particles with energies higher than $10\,\mathrm{keV}$. It would be thus be worthwhile comparing the effects of pitch angle scattering and Coulomb collisions on particle behaviour.

Appendices

Appendix A

Connection between Fokker-Planck equation and stochastic differential equations

To establish the connection between the Fokker-Planck equation and stochastic differential equations we will need to first examine some results from Ito calculus. Here we follow Gardiner [2004] to give an overview of the results we need, however this will necessarily be a very brief description and more detail can be found in, for example, the aforementioned reference.

The Fokker-Planck equation is useful for describing Brownian motion, which is the random motion of macroscopic particles suspended in a fluid. It was observed by Robert Brown in 1827, and the mathematics behind it were subsequently developed by Einstein and Smoluchowski [Gardiner, 2004]. Brownian motion can include both a systematic drift caused by fluid motion (or also drag causing the particles to slow down due to interaction with the fluid), as well as a stochastic component leading to the random motion. The general formulation is:

$$\frac{\partial}{\partial t}p\left(\mathbf{x},t|\mathbf{y},t'\right)=-\sum_i\frac{\partial}{\partial z_i}\left[A_i(\mathbf{x},t)p\left(\mathbf{x},t|\mathbf{y},t'\right)\right]+\frac{1}{2}\sum_{i,j}\frac{\partial^2}{\partial z_i\partial z_j}\left[B_{ij}(\mathbf{x},t)p\left(\mathbf{x},t|\mathbf{y},t'\right)\right], \tag{A.1}$$

where $p\left(\mathbf{x},t|\mathbf{y},t'\right)$ is the probability density function at point $\mathbf{x}$ at time t given being at point $\mathbf{y}$ at time $t'<t$, and A,B are the drift vector and diffusion matrices respectively (in our case the distribution function will eventually take the place of the probability density). To begin with, let us consider the the one-dimensional case when $A=0$ and $B=1$. This simplifies to

$$\frac{\partial}{\partial t}p\left(x,t|x_0,t_0\right)=\frac{1}{2}\frac{\partial^2}{\partial x^2}p\left(x,t|x_0,t_0\right). \tag{A.2}$$

For the initial condition $p\left(x,t_0|x_0,t_0\right)=\delta\left(x-x_0\right)$ the solution to Equation A.2 is,

$$p\left(x,t|x_0,t_0\right)=\frac{1}{\sqrt{2\pi\left(t-t_0\right)}}\exp\left[-\frac{\left(x-x_0\right)^2}{2\left(t-t_0\right)}\right],$$

which is a Gaussian centred at x_0 with standard deviation $t-t_0$. This solution is often denoted $W(t)$ and refered to as a Wiener process.

We wish to connect the Fokker-Planck equation to something which is easily solved numerically. To do so we introduce the Ito SDE for a quantity $x(t)$:

$$dx=A(x(t),t)dt+B(x(t),t)dW, \tag{A.3}$$

where $dW=\lim_{t'\to t^+}W(t')-W(t)$, and A and B are functions of x and t. We aim to show that this SDE corresponds to the one-dimensional version of the Fokker-Planck equation given in Equation A.1. To do so we need an analogue to the chain rule for stochastic variables as well as the identity $dW^2=dt$. First we show the latter.

A nonanticipating function $G(t)$ is one which is is independent of $W(s)-W(t)$ for $t<s$. For one such nonanticipating function, $G(t)$, denote $G_i=G(t_i)$, where $\{t_i\}_{i=1}^{\infty}\subset[0,T]$, $\Delta W_i=W(t_{i+1})-W(t_i)$ and $\Delta t_i=t_{i+1}-t_i$. Then let

$$\begin{aligned}
I&=\lim_{n\to\infty}\left\langle\left[\sum_{i=1}^{n}G_{i-1}\left(\Delta W_i^2-\Delta t_i\right)\right]^2\right\rangle\\
&=\lim_{n\to\infty}\left\langle\sum_{i=1}^{n}G_{i-1}^2\left(\Delta W_i^2-\Delta t_i\right)^2+\sum_{i<j}2G_{i-1}G_{j-1}\left(\Delta W_i^2-\Delta t_i\right)\left(\Delta W_j^2-\Delta t_j\right)\right\rangle\\
&=\lim_{n\to\infty}\sum_{i=1}^{n}\left\langle\left(\Delta W_i^2-\Delta t_i\right)^2\right\rangle\left\langle G_{i-1}^2\right\rangle\\
&=\lim_{n\to\infty}2\sum_{i=1}^{n}\Delta t_i\left\langle G_{i-1}^2\right\rangle.
\end{aligned}$$

Here we used the fact that G is nonanticipating, hence all terms inside the summations are independent and the expectation can be taken of all the terms individually when going from the second line to the third. Furthermore, from the standard deviation of a Wiener process $\left\langle\Delta W_i^2\right\rangle=\Delta t_i$ and $\left\langle\left(\Delta W_i^2-\Delta t_i\right)^2\right\rangle=2\Delta t_i^2$, resulting in the second term in the second line being zero, and giving us the

final result. If we assume that $\Delta t_i < 1/n$ and that $\left\langle G_{i-1}^2 \right\rangle$ is bounded then

$$I = \lim_{n\to\infty} 2\sum_{i=1}^{n} \Delta t_i \left\langle G_{i-1}^2 \right\rangle = 0.$$

Since the mean square limit, $\lim_{n\to\infty} \sum_{i=1}^{n} G_{i-1}\Delta t_i = \int_{t_0}^{t} G(t')dt'$, we have,

$$\int_{t_0}^{t} G(t') \left(dW(t')\right)^2 = \int_{t_0}^{t} G(t')dt'. \tag{A.4}$$

Hence we get the identity

$$dW^2 = dt \tag{A.5}$$

The reason for needing this identity is to derive an analogue of the chain rule for stochastic variables called Ito's formula. For an arbitrary function $f\left(x(t)\right)$ where x is such that $dx = a\left(x(t),t\right)dt + b\left(x(t),t\right)dW$ we have

$$\begin{aligned} df &= f\left(x+dx\right) - f(x) \\ &= f'(x)dx + \frac{1}{2}f''(x)dx^2 + \ldots \\ &= f'(x)a\left(x(t),t\right)dt + b\left(x(t),t\right)dW + \frac{1}{2}f''(x)\left[a\left(x(t),t\right)dt + b\left(x(t),t\right)dW\right]^2 \\ &= \left(f'(x)a\left(x(t),t\right) + \frac{1}{2}f''(x)b\left(x(t),t\right)\right)dt + b\left(x(t),t\right)dW \end{aligned} \tag{A.6}$$

We can now show that a Fokker-Planck equation has a direct analogue in the form of an SDE. For an arbitrary function $g(x(t))$ we have:

$$\frac{d\left\langle g(x(t))\right\rangle}{dt} = \left\langle \frac{dg(x(t))}{dt} \right\rangle = \frac{d}{dt}\left\langle g(x(t))\right\rangle = \left\langle A(x(t),t)\frac{\partial g}{\partial x} + \frac{1}{2}B(x(t),t)^2\frac{\partial^2 g}{\partial x^2}\right\rangle. \tag{A.7}$$

The expected value of g can be written as

$$\frac{d}{dt}\left\langle g\right\rangle = \frac{d}{dt}\int g(x)p(x,t)dx = \int g(x)\frac{\partial p}{\partial x}dx. \tag{A.8}$$

Combining the results fo Equations A.7 and A.8 we get

$$\int g(x)\frac{\partial p}{\partial t}dx = \int \left(A(x(t),t)\frac{\partial g}{\partial x} + \frac{1}{2}B(x(t),t)^2\frac{\partial^2 g}{\partial x^2}\right)p(x,t)dx. \tag{A.9}$$

Using integration by parts on the right hand side we get

$$\int g(x)\frac{\partial p}{\partial t}dx = \int g(x)\left(-\frac{\partial}{\partial x}\left[A(x,t)p(x,t)\right] + \frac{1}{2}\frac{\partial^2}{\partial x^2}\left[B(x,t)^2 p(x,t)\right]\right)dx \quad \text{(A.10)}$$

Since the function g is arbitrary we obtain the Fokker-Planck equation assosciated with the SDE for x:

$$\frac{\partial p}{\partial t} = -\frac{\partial}{\partial x}\left[A(x,t)p(x,t)\right] + \frac{1}{2}\frac{\partial^2}{\partial x^2}\left[B(x,t)^2 p(x,t)\right] \quad \text{(A.11)}$$

List of Figures

Bibliography

TD Arber, AW Longbottom, CL Gerrard, and AM Milne. A staggered grid, lagrangian–eulerian remap code for 3-d mhd simulations. *Journal of Computational Physics*, 171(1):151–181, 2001.

V. Archontis. Magnetic flux emergence in the Sun. *Journal of Geophysical Research (Space Physics)*, 113:A03S04, March 2008. doi: 10.1029/2007JA012422.

A. V. Artemyev. Charged-particle acceleration in braking plasma jets. *Physical Review E*, 89:033108, Mar 2014. doi: 10.1103/PhysRevE.89.033108. URL http://link.aps.org/doi/10.1103/PhysRevE.89.033108.

G. Aulanier, E. Pariat, and P. Démoulin. Current sheet formation in quasi-separatrix layers andÂăhyperbolicÂăfluxÂătubes. *Astronomy & Astrophysics*, 444(3):961–976, 2005. doi: 10.1051/0004-6361:20053600. URL https://doi.org/10.1051/0004-6361:20053600.

G. Aulanier, E. Pariat, P. Démoulin, and C. R. Devore. Slip-running reconnection in quasi-separatrix layers. *Solar Physics*, 238(2):347–376, Nov 2006. ISSN 1573-093X. doi: 10.1007/s11207-006-0230-2. URL https://doi.org/10.1007/s11207-006-0230-2.

L. Ball and D. B. Melrose. Shock Drift Acceleration of Electrons. *Publ. Astron. Soc. Australia*, 18:361–373, 2001. doi: 10.1071/AS01047.

A. O. Benz. Flare Observations. *Living Reviews in Solar Physics*, 5:1, February 2008. doi: 10.12942/lrsp-2008-1.

N. H. Bian, A. G. Emslie, and E. P. Kontar. The Role of Diffusion in the Transport of Energetic Electrons during Solar Flares. *Astrophysical Journal*, 835:262, February 2017. doi: 10.3847/1538-4357/835/2/262.

Nicolas H. Bian, Eduard P. Kontar, and A. Gordon Emslie. Suppression of parallel transport in turbulent magnetized plasmas and its impact on the non-thermal and thermal aspects of solar flares. *The Astrophysical Journal*, 824(2):78, 2016. URL http://stacks.iop.org/0004-637X/824/i=2/a=78.

J. Birn, A.V. Artemyev, D.N. Baker, M. Echim, M. Hoshino, and L.M. Zelenyi. Particle acceleration in the magnetotail and aurora. *Space Science Reviews*, 173 (1-4):49–102, 2012. ISSN 0038-6308. doi: 10.1007/s11214-012-9874-4. URL http://dx.doi.org/10.1007/s11214-012-9874-4.

J. Birn, M. Battaglia, L. Fletcher, M. Hesse, and T. Neukirch. Can Substorm Particle Acceleration Be Applied to Solar Flares? *Astrophysical Journal*, 848:116, October 2017. doi: 10.3847/1538-4357/aa8ad4.

D. Biskamp. *Magnetic Reconnection in Plasmas*. September 2000.

S. A. Bogachev and B. V. Somov. Acceleration of Charged Particles in Collapsing Magnetic Traps During Solar Flares. *Astronomy Reports*, 45:157–161, February 2001. doi: 10.1134/1.1346724.

S. A. Bogachev and B. V. Somov. Comparison of the Fermi and Betatron Acceleration Efficiencies in Collapsing Magnetic Traps. *Astronomy Letters*, 31: 537–545, August 2005. doi: 10.1134/1.2007030.

S. A. Bogachev and B. V. Somov. Formation of power-law electron spectra in collapsing magnetic traps. *Astronomy Letters*, 33:54–62, January 2007. doi: 10.1134/S1063773707010070.

S. A. Bogachev and B. V. Somov. Effect of Coulomb collisions on the particle acceleration in collapsing magnetic traps. *Astronomy Letters*, 35:57–69, January 2009. doi: 10.1134/S1063773709010071.

A. Borissov, T. Neukirch, and J. Threlfall. Particle Acceleration in Collapsing Magnetic Traps with a Braking Plasma Jet. *Solar Physics*, 291:1385–1404, May 2016. doi: 10.1007/s11207-016-0915-0.

A. Borissov, E. P. Kontar, J. Threlfall, and T. Neukirch. Particle acceleration with anomalous pitch angle scattering in 2D magnetohydrodynamic reconnection simulations. *Astronomy & Astrophysics*, 605:A73, September 2017. doi: 10.1051/0004-6361/201731183.

T. J. M. Boyd and J. J. Sanderson. *The Physics of Plasmas*. January 2003.

D. S. Brown and E. R. Priest. The topological behaviour of 3D null points in the Sun's corona. *Astronomy & Astrophysics*, 367:339–346, February 2001. doi: 10.1051/0004-6361:20010016.

J. C. Brown. The Deduction of Energy Spectra of Non-Thermal Electrons in Flares from the Observed Dynamic Spectra of Hard X-Ray Bursts. *Solar Physics*, 18: 489–502, July 1971. doi: 10.1007/BF00149070.

J. C. Brown, R. Turkmani, E. P. Kontar, A. L. MacKinnon, and L. Vlahos. Local re-acceleration and a modified thick target model of solar flare electrons. *Astronomy & Astrophysics*, 508:993–1000, December 2009. doi: 10.1051/0004-6361/200913145.

P. K. Browning, S. Dalla, D. Peters, and J. Smith. Scaling of particle acceleration in 3D reconnection at null points. *Astronomy & Astrophysics*, 520:A105, September 2010. doi: 10.1051/0004-6361/201014964.

C. A. Burge, A. L. MacKinnon, and P. Petkaki. Effect of binary collisions on electron acceleration in magnetic reconnection. *Astronomy & Astrophysics*, 561:A107, January 2014. doi: 10.1051/0004-6361/201322199.

P. J. Cargill, L. Vlahos, G. Baumann, J. F. Drake, and Å. Nordlund. Current Fragmentation and Particle Acceleration in Solar Flares. *Space Science Reviews*, 173:223–245, November 2012. doi: 10.1007/s11214-012-9888-y.

J.R. Cash and A.H. Karp. A variable order Runge-Kutta method for initial-value problems with rapidly varying right-hand sides. *ACM Transactions on Mathematical Software*, 16:201–222, September 1990. doi: 10.1145/79505.79507.

P. Charbonneau, S. W. McIntosh, H.-L. Liu, and T. J. Bogdan. Avalanche models for solar flares (Invited Review). *Solar Physics*, 203:321–353, November 2001. doi: 10.1023/A:1013301521745.

D. P. Choudhary, A. Ambastha, and G. Ai. Emerging Flux and X-class Flares in NOAA 6555. *Solar Physics*, 179:133–140, 1998. doi: 10.1023/A:1005063609450.

I. J. D. Craig, R. B. Fabling, S. M. Henton, and G. J. Rickard. An exact solution for steady state magnetic reconnection in three dimensions. *The Astrophysical Journal Letters*, 455(2):L197, 1995. URL `http://stacks.iop.org/1538-4357/455/i=2/a=L197`.

S. Dalla and P. K. Browning. Particle acceleration at a three-dimensional reconnection site in the solar corona. *Astronomy & Astrophysics*, 436:1103–1111, June 2005. doi: 10.1051/0004-6361:20042589.

S. Dalla and P. K. Browning. Jets of Energetic Particles Generated by Magnetic Reconnection at a Three-dimensional Magnetic Null. *Astrophysical Journal letters*, 640:L99–L102, March 2006. doi: 10.1086/503302.

S. Dalla and P. K. Browning. Particle trajectories and acceleration during 3D fan reconnection. *Astronomy & Astrophysics*, 491:289–295, November 2008. doi: 10.1051/0004-6361:200809771.

William Daughton, Giovanni Lapenta, and Paolo Ricci. Nonlinear evolution of the lower-hybrid drift instability in a current sheet. *Physical Review Letters*, 93: 105004, Sep 2004. doi: 10.1103/PhysRevLett.93.105004. URL `https://link.aps.org/doi/10.1103/PhysRevLett.93.105004`.

J. F. Drake, M. Swisdak, H. Che, and M. A. Shay. Electron acceleration from contracting magnetic islands during reconnection. *Nature*, 443:553–556, October 2006. doi: 10.1038/nature05116.

H. Dreicer. Electron and ion runaway in a fully ionized gas. i. *Physical Review*, 115: 238–249, Jul 1959. doi: 10.1103/PhysRev.115.238. URL `https://link.aps.org/doi/10.1103/PhysRev.115.238`.

L. O. Drury. An introduction to the theory of diffusive shock acceleration of energetic particles in tenuous plasmas. *Reports on Progress in Physics*, 46:973–1027, August 1983. doi: 10.1088/0034-4885/46/8/002.

A. G. Emslie. The collisional interaction of a beam of charged particles with a hydrogen target of arbitrary ionization level. *Astrophysical Journal*, 224:241–246, August 1978. doi: 10.1086/156371.

S. Eradat Oskoui and T. Neukirch. Particle energisation in a collapsing magnetic trap model: the relativistic regime. *Astronomy & Astrophysics*, 567:A131, July 2014. doi: 10.1051/0004-6361/201423886.

S. Eradat Oskoui, T. Neukirch, and K. J. Grady. Loss cone evolution and particle escape in collapsing magnetic trap models in solar flares. *Astronomy & Astrophysics*, 563:A73, March 2014. doi: 10.1051/0004-6361/201322519.

E. Fermi. Galactic Magnetic Fields and the Origin of Cosmic Radiation. *Astrophysical Journal*, 119:1, January 1954. doi: 10.1086/145789.

R. Fitzpatrick. *Plasma Physics: An Introduction*. Taylor & Francis, lecture notes version used , 2014. ISBN 9781466594265. URL `https://books.google.co.uk/books?id=0RwbBAAAQBAJ`.

H. S. Fu, J. B. Cao, Y. V. Khotyaintsev, M. I. Sitnov, A. Runov, S. Y. Fu, M. Hamrin, M. André, A. Retinò, Y. D. Ma, H. Y. Lu, X. H. Wei, and S. Y. Huang. Dipolarization fronts as a consequence of transient reconnection: In situ evidence. *Geophysical Research Letters*, 40:6023–6027, December 2013. doi: 10.1002/2013GL058620.

C. W. Gardiner. *Handbook of stochastic methods for physics, chemistry and the natural sciences*, volume 13 of *Springer Series in Synergetics*. Springer-Verlag, Berlin, third edition, 2004. ISBN 3-540-20882-8.

R. Giacconi. History of X-ray telescopes and astronomy. *Experimental Astronomy*, 25:143–156, August 2009. doi: 10.1007/s10686-009-9139-8.

P. Giuliani, T. Neukirch, and P. Wood. Particle Motion in Collapsing Magnetic Traps in Solar Flares. I. Kinematic Theory of Collapsing Magnetic Traps. *Astrophysical Journal*, 635:636–646, December 2005. doi: 10.1086/497366.

N. Gopalswamy. Low-Frequency Radio Bursts and Space Weather. *ArXiv e-prints*, May 2016.

M. Gordovskyy, P. K. Browning, and G. E. Vekstein. Particle acceleration in a transient magnetic reconnection event. *Astronomy & Astrophysics*, 519:A21, September 2010a. doi: 10.1051/0004-6361/200913569.

M. Gordovskyy, P. K. Browning, and G. E. Vekstein. Particle Acceleration in Fragmenting Periodic Reconnecting Current Sheets in Solar Flares. *Astrophysical Journal*, 720:1603–1611, September 2010b. doi: 10.1088/0004-637X/720/2/1603.

M. Gordovskyy, P. K. Browning, E. P. Kontar, and N. H. Bian. Effect of Collisions and Magnetic Convergence on Electron Acceleration and Transport in Reconnecting Twisted Solar Flare Loops. *Solar Physics*, 284:489–498, June 2013. doi: 10.1007/s11207-012-0124-4.

M. Gordovskyy, P. K. Browning, E. P. Kontar, and N. H. Bian. Particle acceleration and transport in reconnecting twisted loops in a stratified atmosphere. *Astronomy & Astrophysics*, 561:A72, January 2014. doi: 10.1051/0004-6361/201321715.

K Grady. *Solar flare particle acceleration in collapsing magnetic traps*. PhD thesis, University of St Andrews, College Gate, St Andrews, Fife, Scotland, UK. KY16 9AJ, 2012.

K. J. Grady and T. Neukirch. An extension of the theory of kinematic MHD models of collapsing magnetic traps to 2.5D with shear flow and to 3D. *Astronomy & Astrophysics*, 508:1461–1468, December 2009. doi: 10.1051/0004-6361/200913230.

K. J. Grady, T. Neukirch, and P. Giuliani. A systematic examination of particle motion in a collapsing magnetic trap model for solar flares. *Astronomy & Astrophysics*, 546:A85, October 2012. doi: 10.1051/0004-6361/201218914.

M. J. Hagyard, P. Venkatakrishnan, and J. B. Smith, Jr. Nonpotential magnetic fields at sites of gamma-ray flares. *Astrophysical Journal Supplement*, 73:159–163, June 1990. doi: 10.1086/191447.

V. H. Hansteen, V. Archontis, T. M. D. Pereira, M. Carlsson, L. Rouppe van der Voort, and J. Leenaarts. Bombs and Flares at the Surface and Lower Atmosphere of the Sun. *Astrophysical Journal*, 839:22, April 2017. doi: 10.3847/1538-4357/aa6844.

M. Hesse. Three-Dimensional Magnetic Reconnection in Space- and Astrophysical Plasmas and its Consequences for Particle Acceleration. In G. Klare, editor, *Reviews in Modern Astronomy*, volume 8 of *Reviews in Modern Astronomy*, pages 323–348, 1995.

M. Hesse and K. Schindler. A theoretical foundation of general magnetic reconnection. *Journal of Geophysical Research*, 93:5559–5567, June 1988. doi: 10.1029/JA093iA06p05559.

M. Hesse, T. Neukirch, K. Schindler, M. Kuznetsova, and S. Zenitani. The Diffusion Region in Collisionless Magnetic Reconnection. *Space Science Reviews*, 160:3–23, October 2011. doi: 10.1007/s11214-010-9740-1.

A. W. Hood, P. J. Cargill, P. K. Browning, and K. V. Tam. An MHD Avalanche in a Multi-threaded Coronal Loop. *Astrophysical Journal*, 817:5, January 2016. doi: 10.3847/0004-637X/817/1/5.

J.D. Huba, United States. Office of Naval Research, and Naval Research Laboratory (U.S.). *NRL Plasma Formulary*. NRL publication. Naval Research Laboratory, 1998. URL `https://books.google.co.uk/books?id=7lHMrQEACAAJ`.

S. Imada, R. Nakamura, P. W. Daly, M. Hoshino, W. Baumjohann, S. Mühlbachler, A. Balogh, and H. Rème. Energetic electron acceleration in the downstream reconnection outflow region. *Journal of Geophysical Research (Space Physics)*, 112: A03202, March 2007. doi: 10.1029/2006JA011847.

C. D. Johnston, A. W. Hood, P. J. Cargill, and I. De Moortel. A new approach for modelling chromospheric evaporation in response to enhanced coronal heating. I. The method. *Astronomy & Astrophysics*, 597:A81, January 2017a. doi: 10.1051/0004-6361/201629153.

C. D. Johnston, A. W. Hood, P. J. Cargill, and I. De Moortel. A new approach for modelling chromospheric evaporation in response to enhanced coronal heating. II. Non-uniform heating. *Astronomy & Astrophysics*, 605:A8, August 2017b. doi: 10.1051/0004-6361/201730486.

S. R. Kane and K. A. Anderson. Spectral Characteristics of Impulsive Solar-Flare X-Rays $\gtrsim$ 10 KeV. *Astrophysical Journal*, 162:1003, December 1970. doi: 10.1086/150732.

M. Karlický and M. Bárta. X-Ray Loop-Top Source Generated by Processes in a Flare Collapsing Trap. *Astrophysical Journal*, 647:1472–1479, August 2006. doi: 10.1086/505460.

M. Karlický and T. Kosugi. Acceleration and heating processes in a collapsing magnetic trap. *Astronomy & Astrophysics*, 419:1159–1168, June 2004. doi: 10.1051/0004-6361:20034323.

Yu. V. Khotyaintsev, C. M. Cully, A. Vaivads, M. André, and C. J. Owen. Plasma jet braking: Energy dissipation and nonadiabatic electrons. *Physical Review Letters*, 106:165001, Apr 2011. doi: 10.1103/PhysRevLett.106.165001. URL `http://link.aps.org/doi/10.1103/PhysRevLett.106.165001`.

A. L. Kiplinger. Comparative Studies of Hard X-Ray Spectral Evolution in Solar Flares with High-Energy Proton Events Observed at Earth. *Astrophysical Journal*, 453:973, November 1995. doi: 10.1086/176457.

B. Kliem. Particle orbits, trapping, and acceleration in a filamentary current sheet model. *Astrophysical Journal Supplement*, 90:719–728, February 1994. doi: 10.1086/191896.

J. A. Klimchuk. On Solving the Coronal Heating Problem. *Solar Physics*, 234:41–77, March 2006. doi: 10.1007/s11207-006-0055-z.

V. A. Kovalev and B. V. Somov. On the Acceleration of Solar-Flare Charged Particles in a Collapsing Magnetic Trap with an Electric Potential. *Astronomy Letters*, 28:488–493, July 2002. doi: 10.1134/1.1491971.

S. Krucker, G. J. Hurford, and R. P. Lin. Hard X-Ray Source Motions in the 2002 July 23 Gamma-Ray Flare. *Astrophysical Journal letters*, 595:L103–L106, October 2003. doi: 10.1086/378840.

S. Krucker, M. D. Fivian, and R. P. Lin. Hard X-ray footpoint motions in solar flares: Comparing magnetic reconnection models with observations. *Advances in Space Research*, 35:1707–1711, 2005. doi: 10.1016/j.asr.2005.05.054.

A. Kuritsyn, M. Yamada, S. Gerhardt, H. Ji, R. Kulsrud, and Y. Ren. Measurements of the parallel and transverse spitzer resistivities during collisional magnetic reconnection. *Physics of Plasmas*, 13(5):055703, 2006. doi: 10.1063/1.2179416. URL `https://doi.org/10.1063/1.2179416`.

Y. E. Litvinenko. Particle Acceleration in Reconnecting Current Sheets with a Nonzero Magnetic Field. *Astrophysical Journal*, 462:997, May 1996. doi: 10.1086/177213.

D. W. Longcope, D. E. McKenzie, J. Cirtain, and J. Scott. Observations of Separator Reconnection to an Emerging Active Region. *Astrophysical Journal*, 630:596–614, September 2005. doi: 10.1086/432039.

N. F. Loureiro and D. A. Uzdensky. Magnetic reconnection: from the Sweet-Parker model to stochastic plasmoid chains. *Plasma Physics and Controlled Fusion*, 58(1): 014021, January 2016. doi: 10.1088/0741-3335/58/1/014021.

N. F. Loureiro, A. A. Schekochihin, and S. C. Cowley. Instability of current sheets and formation of plasmoid chains. *Physics of Plasmas*, 14(10):100703–100703, October 2007. doi: 10.1063/1.2783986.

M. A. Malkov and H. J. Völk. Diffusive ion acceleration at shocks: the problem of injection. *Advances in Space Research*, 21:551–554, 1998. doi: 10.1016/S0273-1177(97)00961-7.

S. Markidis, P. Henri, G. Lapenta, A. Divin, M. V. Goldman, D. Newman, and S. Eriksson. Collisionless magnetic reconnection in a plasmoid chain. *Nonlinear Processes in Geophysics*, 19:145–153, February 2012. doi: 10.5194/npg-19-145-2012.

S. Masuda, T. Kosugi, H. Hara, T. Sakao, K. Shibata, and S. Tsuneta. Hard X-Ray Sources and the Primary Energy-Release Site in Solar Flares. *Publ. Astron. Soc. Japan*, 47:677–689, October 1995.

V. F. Melnikov, K. Shibasaki, and V. E. Reznikova. Loop-Top Nonthermal Microwave Source in Extended Solar Flaring Loops. *Astrophysical Journal letters*, 580:L185–L188, December 2002. doi: 10.1086/345587.

T. R. Metcalf, D. Alexander, H. S. Hudson, and D. W. Longcope. TRACE and Yohkoh Observations of a White-Light Flare. *Astrophysical Journal*, 595:483–492, September 2003. doi: 10.1086/377217.

J. A. Miller, P. J. Cargill, A. G. Emslie, G. D. Holman, B. R. Dennis, T. N. LaRosa, R. M. Winglee, S. G. Benka, and S. Tsuneta. Critical issues for understanding particle acceleration in impulsive solar flares. *Journal of Geophysical Research*, 102: 14631–14660, July 1997. doi: 10.1029/97JA00976.

T. Minoshima, S. Masuda, and Y. Miyoshi. Drift-kinetic Modeling of Particle Acceleration and Transport in Solar Flares. *Astrophysical Journal*, 714:332–342, May 2010. doi: 10.1088/0004-637X/714/1/332.

T. Minoshima, S. Masuda, Y. Miyoshi, and K. Kusano. Coronal Electron Distribution in Solar Flares: Drift-kinetic Model. *Astrophysical Journal*, 732:111, May 2011. doi: 10.1088/0004-637X/732/2/111.

W. M. Neupert. Comparison of Solar X-Ray Line Emission with Microwave Emission during Flares. *Astrophysical Journal letters*, 153:L59, July 1968. doi: 10.1086/180220.

Theodore G. Northrop. *The Adiabatic Motion of Charged Particles*. John Wiley & Sons, Inc., New York, 1963.

Ryusuke Numata and Zensho Yoshida. Chaos-induced resistivity in collisionless magnetic reconnection. *Physical Review Letters*, 88:045003, Jan 2002. doi: 10.1103/PhysRevLett.88.045003. URL `http://link.aps.org/doi/10.1103/PhysRevLett.88.045003`.

E. N. Parker. Sweet's Mechanism for Merging Magnetic Fields in Conducting Fluids. *Journal of Geophysical Research*, 62:509–520, December 1957. doi: 10.1029/JZ062i004p00509.

E. N. Parker. Nanoflares and the solar X-ray corona. *Astrophysical Journal*, 330:474–479, July 1988. doi: 10.1086/166485.

G. K. Parks and J. R. Winckler. Sixteen-Second Periodic Pulsations Observed in the Correlated Microwave and Energetic X-Ray Emission from a Solar Flare. *Astrophysical Journal letters*, 155:L117, February 1969. doi: 10.1086/180315.

C. E. Parnell, J. M. Smith, T. Neukirch, and E. R. Priest. The structure of threeâĂŘdimensional magnetic neutral points. *Physics of Plasmas*, 3(3):759–770, 1996. doi: 10.1063/1.871810. URL https://doi.org/10.1063/1.871810.

C. E. Parnell, A. L. Haynes, and K. Galsgaard. Structure of magnetic separators and separator reconnection. *Journal of Geophysical Research (Space Physics)*, 115:A02102, February 2010a. doi: 10.1029/2009JA014557.

C. E. Parnell, R. C. Maclean, and A. L. Haynes. The Detection of Numerous Magnetic Separators in a Three-Dimensional Magnetohydrodynamic Model of Solar Emerging Flux. *Astrophysical Journal letters*, 725:L214–L218, December 2010b. doi: 10.1088/2041-8205/725/2/L214.

P. Petkaki and M. P. Freeman. Nonlinear Dependence of Anomalous Ion-Acoustic Resistivity on Electron Drift Velocity. *Astrophysical Journal*, 686:686-693, October 2008. doi: 10.1086/590654.

V. Petrosian. Stochastic Acceleration by Turbulence. *Space Science Reviews*, 173:535–556, November 2012. doi: 10.1007/s11214-012-9900-6.

V. Petrosian, T. Q. Donaghy, and J. M. McTiernan. Loop Top Hard X-Ray Emission in Solar Flares: Images and Statistics. *Astrophysical Journal*, 569:459–473, April 2002. doi: 10.1086/339240.

V. Petrosian, H. Yan, and A. Lazarian. Damping of Magnetohydrodynamic Turbulence in Solar Flares. *Astrophysical Journal*, 644:603–612, June 2006. doi: 10.1086/503378.

H. E. Petschek. Magnetic Field Annihilation. *NASA Special Publication*, 50:425, 1964.

D. I. Pontin. Theory of magnetic reconnection in solar and astrophysical plasmas. *Phil. Trans. Royal Soc. London (series A)*, 370:3169–3192, July 2012. doi: 10.1098/rsta.2011.0501.

D. I. Pontin, G. Hornig, and E. R. Priest. Kinematic reconnection at a magnetic null point: spine-aligned current. *Geophysical and Astrophysical Fluid Dynamics*, 98: 407–428, May 2004. doi: 10.1080/0309192042000272324.

D. I. Pontin, K. Galsgaard, G. Hornig, and E. R. Priest. A fully magnetohydrodynamic simulation of three-dimensional non-null reconnection. *Physics of Plasmas*, 12(5): 052307, May 2005a. doi: 10.1063/1.1891005.

D. I. Pontin, G. Hornig, and E. R. Priest. Kinematic reconnection at a magnetic null point: fan-aligned current. *Geophysical and Astrophysical Fluid Dynamics*, 99:77–93, January 2005b. doi: 10.1080/03091920512331328071.

D. I. Pontin, A. K. Al-Hachami, and K. Galsgaard. Generalised models for torsional spine and fan magnetic reconnection. *Astronomy & Astrophysics*, 533:A78, September 2011. doi: 10.1051/0004-6361/201117250.

E. Priest. *Magnetohydrodynamics of the Sun*. May 2014.

E. Priest and T. Forbes, editors. *Magnetic reconnection : MHD theory and applications*. 2000.

E. R. Priest and P. Démoulin. Three-dimensional magnetic reconnection without null points: 1. basic theory of magnetic flipping. *Journal of Geophysical Research*, 100(A12):23443–23463, 1995. ISSN 2156-2202. doi: 10.1029/95JA02740. URL `http://dx.doi.org/10.1029/95JA02740`.

E. R. Priest and T. G. Forbes. The magnetic nature of solar flares. *Astronomy & Astrophysics Review*, 10:313–377, 2002. doi: 10.1007/s001590100013.

E. R. Priest and V. S. Titov. Magnetic Reconnection at Three-Dimensional Null Points. *Proc. Royal Soc. London (series A)*, 354:2951–2992, December 1996.

J. W. Reep and A. J. B. Russell. Alfv\'enic Wave Heating of the Upper Chromosphere in Flares. *Astrophysical Journal letters*, 818:L20, February 2016. doi: 10.3847/2041-8205/818/1/L20.

K. Schindler, M. Hesse, and J. Birn. General magnetic reconnection, parallel electric fields, and helicity. *Journal of Geophysical Research*, 93:5547–5557, June 1988. doi: 10.1029/JA093iA06p05547.

K. Shibata and T. Magara. Solar Flares: Magnetohydrodynamic Processes. *Living Reviews in Solar Physics*, 8:6, December 2011. doi: 10.12942/lrsp-2011-6.

M. I. Sitnov and M. Swisdak. Onset of collisionless magnetic reconnection in two-dimensional current sheets and formation of dipolarization fronts. *Journal of Geophysical Research (Space Physics)*, 116:A12216, December 2011. doi: 10.1029/2011JA016920.

B. V. Somov and S. A. Bogachev. The Betatron Effect in Collapsing Magnetic Traps. *Astronomy Letters*, 29:621–628, September 2003. doi: 10.1134/1.1607500.

B. V. Somov and T. Kosugi. Collisionless Reconnection and High-Energy Particle Acceleration in Solar Flares. *Astrophysical Journal*, 485:859–868, August 1997.

A. Stanier, P. Browning, and S. Dalla. Solar particle acceleration at reconnecting 3D null points. *Astronomy & Astrophysics*, 542:A47, June 2012. doi: 10.1051/0004-6361/201218857.

J. E. H. Stevenson and C. E. Parnell. Spontaneous reconnection at a separator current layer: 1. Nature of the reconnection. *Journal of Geophysical Research (Space Physics)*, 120:10, December 2015a. doi: 10.1002/2015JA021730.

J. E. H. Stevenson and C. E. Parnell. Spontaneous reconnection at a separator current layer: 2. Nature of the waves and flows. *Journal of Geophysical Research (Space Physics)*, 120:10, December 2015b. doi: 10.1002/2015JA021736.

J. E. H. Stevenson, C. E. Parnell, E. R. Priest, and A. L. Haynes. The nature of separator current layers in MHS equilibria. I. Current parallel to the separator. *Astronomy & Astrophysics*, 573:A44, January 2015. doi: 10.1051/0004-6361/201424348.

P. A. Sweet. The Neutral Point Theory of Solar Flares. In B. Lehnert, editor, *Electromagnetic Phenomena in Cosmical Physics*, volume 6 of *IAU Symposium*, page 123, 1958.

K. V. Tam, A. W. Hood, P. K. Browning, and P. J. Cargill. Coronal heating in multiple magnetic threads. *Astronomy & Astrophysics*, 580:A122, August 2015. doi: 10.1051/0004-6361/201525995.

A. Tenerani, M. Velli, F. Pucci, S. Landi, and A. F. Rappazzo. 'Ideally' unstable current sheets and the triggering of fast magnetic reconnection. *Journal of Plasma Physics*, 82(5):535820501, October 2016. doi: 10.1017/S002237781600088X.

P. Testa, B. De Pontieu, J. Allred, M. Carlsson, F. Reale, A. Daw, V. Hansteen, J. Martinez-Sykora, W. Liu, E. E. DeLuca, L. Golub, S. McKillop, K. Reeves, S. Saar, H. Tian, J. Lemen, A. Title, P. Boerner, N. Hurlburt, T. D. Tarbell, J. P. Wuelser, L. Kleint, C. Kankelborg, and S. Jaeggli. Evidence of nonthermal particles in coronal loops heated impulsively by nanoflares. *Science*, 346:1255724, October 2014. doi: 10.1126/science.1255724.

J. Threlfall, T. Neukirch, C. E. Parnell, and S. Eradat Oskoui. Particle acceleration at a reconnecting magnetic separator. *Astronomy & Astrophysics*, 574:A7, February 2015. doi: 10.1051/0004-6361/201424366.

J. Threlfall, P.-A. Bourdin, T. Neukirch, and C. E. Parnell. Particle dynamics in a non-flaring solar active region model. *Astronomy & Astrophysics*, 587:A4, March 2016a. doi: 10.1051/0004-6361/201526657.

J. Threlfall, J. E. H. Stevenson, C. E. Parnell, and T. Neukirch. Particle acceleration at reconnecting separator current layers. *Astronomy & Astrophysics*, 585:A95, January 2016b. doi: 10.1051/0004-6361/201527381.

J. Threlfall, T. Neukirch, and C. E. Parnell. Particle Acceleration Due to Coronal Non-null Magnetic Reconnection. *Solar Physics*, 292:45, March 2017. doi: 10.1007/s11207-017-1060-0.

J. Threlfall, A. W. Hood, and P. K. Browning. Flare particle acceleration in the interaction of twisted coronal flux ropes. *ArXiv e-prints*, January 2018.

T. Török and B. Kliem. Confined and Ejective Eruptions of Kink-unstable Flux Ropes. *Astrophysical Journal letters*, 630:L97–L100, September 2005. doi: 10.1086/462412.

R. A. Treumann. Origin of resistivity in reconnection. *Earth, Planets, and Space*, 53: 453–462, June 2001. doi: 10.1186/BF03353256.

R. A. Treumann and W. Baumjohann. *Advanced space plasma physics*. 1997. doi: 10.1142/p020.

S. Tsuneta and T. Naito. Fermi Acceleration at the Fast Shock in a Solar Flare and the Impulsive Loop-Top Hard X-Ray Source. *Astrophysical Journal letters*, 495: L67–L70, March 1998. doi: 10.1086/311207.

P. O. Vandervoort. The relativistic motion of a charged particle in an inhomogeneous electromagnetic field. *Annals of Physics*, 10:401–453, July 1960. doi: 10.1016/0003-4916(60)90004-X.

P. Wood and T. Neukirch. Electron Acceleration in Reconnecting Current Sheets. *Solar Physics*, 226:73–95, January 2005. doi: 10.1007/s11207-005-5686-y.

P. F. Wyper, R. Jain, and D. I. Pontin. Spine-fan reconnection. The influence of temporal and spatial variation in the driver. *Astronomy & Astrophysics*, 545:A78, September 2012. doi: 10.1051/0004-6361/201219281.